

**THESE**  
présentée par

**Pradip XAVIER**

En vue de l'obtention du grade de **Docteur de Normandie Université**  
délivrée par **l'Institut National des Sciences Appliquées de Rouen**

Discipline : Physique  
Spécialité : Énergétique

**Investigation of Flame Stabilization Mechanisms  
in a Premixed Combustor using a Hot Gas  
Cavity-based Flame Holder**

soutenue le **09 Décembre 2014**

*Composition du Jury :*

Rapporteurs :

<b>Simone HOCHGREB</b>	Professeure, University of Cambridge, UK
<b>Thierry SCHULLER</b>	Professeur des Universités, École Centrale Paris, laboratoire EM2C

Examineurs :

<b>Christian CHAUVEAU</b>	Directeur de Recherche CNRS, laboratoire ICARE
<b>Laurent SELLE</b>	Chargé de Recherche CNRS, laboratoire IMFT
<b>Mourad A BOUKHALFA</b>	Professeur des Universités, INSA Rouen, laboratoire CORIA
<b>Michel CAZALENS</b>	Docteur Ingénieur de Recherche, SAFRAN

Directeurs de thèse :

<b>Bruno RENOUE</b>	Professeur des Universités, INSA Rouen, laboratoire CORIA
<b>Gilles CABOT</b>	Professeur des Universités, Université de Rouen, laboratoire CORIA



# Résumé

**Mots-clefs:** Trapped Vortex Combustor, combustion pauvre prémélangée, cavités, instabilités de combustion, diagnostics lasers rapides.

Ces travaux s'inscrivent dans le cadre de la réduction des émissions de polluants dans les foyers de combustion aéronautiques. Malgré l'optimisation des technologies actuelles, et ceci afin de répondre aux futures normes environnementales, certaines pistes mènent à considérer une rupture technologique au niveau de l'architecture entière de la chambre de combustion. Cette thèse décrit l'étude d'une chambre de combustion innovante de type Trapped Vortex Combustor (TVC): ce concept utilise des cavités de gaz chauds pour stabiliser des flammes prémélangées pauvres. Les performances de ce concept sont avérées très prometteuses [192, 215]. Cependant, très peu d'études se sont penchées sur les mécanismes physiques stabilisateurs et déstabilisateurs dans ce type de configurations. En effet, les écoulements passant au dessus de cavités sont connus pour présenter de nombreuses instabilités aérodynamiques et l'addition du processus chimique de combustion peut mener à l'apparition d'instabilités de combustion. L'objectif de cette thèse est d'étudier expérimentalement, à l'aide de diagnostics optiques, une condition fortement instable, afin de déterminer les mécanismes déstabilisateurs, de fournir des recommandations pour un meilleur dimensionnement, et être capable de prédire les gammes de fonctionnement stables de ce type de chambre de combustion.

A partir des études précédentes de Burguburu [26] et Merlin [160], l'étude globale d'un point de fonctionnement instable montre la nécessité de séparer l'impact de l'aérodynamique et du processus de combustion.

La structure de l'écoulement inerte montre les avantages d'injections de masse dans la cavité, tant au niveau de la turbulence et du mélange que des échanges de masses entre les différentes régions du brûleur. Cependant, ces injections sont aussi à l'origine de fortes instabilités qui perturbent la couche de mélange et détériorent ainsi la zone favorable d'accroche de la flamme. Il est montré qu'une augmentation de l'impulsion de l'écoulement principale permet un meilleur confinement de la dynamique de cavité.

Ensuite, une étude temporelle et spatiale est réalisée sur un point de fonctionnement instable, et ceci en conditions réactives. L'implémentation de diagnostics optiques couplés à haute cadence permet de comprendre les interactions entre la structure de la flamme, la topologie de l'écoulement et l'acoustique du brûleur. Cette étude confirme que les instabilités aérodynamiques couplées aux différences importantes de composition des gaz mènent à une fluctuation importantes du taux de dégagement de chaleur dans la cavité. L'expansion thermique des gaz qui s'en suit pilote le développement des instabilités de combustion.

Suite à ces études détaillées, une modification des systèmes d'injection montrent qu'il est possible

de supprimer ces instabilités en confinant l'aérodynamique de la cavité. Ces recommandations permettent une vérification *a posteriori*, notamment grâce à l'obtention de diagrammes de stabilité de flammes. Cette dernière étude montre aussi la difficulté de prédire un mode stable avec ce type d'architecture, principalement lié au nombre importants de paramètres inter-dépendants.



# Summary

**Keywords:** trapped vortex combustor, lean premixed combustion, cavities, combustion instabilities, high-speed laser diagnostics.

This study addresses the reduction of pollutant emissions in aero-engines. Despite numerous optimizations of actual technologies to meet future emission standards, many incentives encourage the continuous scientific effort to investigate disruptive technologies on new combustor architectures.

This thesis described an innovative trapped vortex model combustor (TVC): this concept uses recirculating hot gas flow trapped in cavities to stabilize lean flames. The effectiveness of this concept is promising [192, 215]. However, few studies have been focused on understanding mechanisms of flame stabilization in such geometries. In fact, flows passing past cavities are subject to aerodynamic instabilities, and addition of the combustion process can therefore lead to the occurrence of combustion instabilities. Therefore, the objective of this experimental study was to take advantage of optical diagnostics to: obtain an improved understanding of stabilization mechanisms during unstable operating conditions, provide some design recommendations, and predict the combustor stability.

Based on previous studies of Burguburu [26] and Merlin [160], a global analysis of one unstable operating condition showed the necessity to treat separately effects of the aerodynamics and combustion process.

Investigation of the inert flow structure highlighted benefits of adding mass injection systems in the cavity; that is, improvements of turbulence and mixing as well as mass exchanges between the different regions. However, these injection systems were also greatly affecting the shear layer region and therefore deteriorating the flame stabilization region. These instabilities were remarkably annihilated by increasing the mainstream momentum, which in turn improved confinement of the cavity dynamics.

Thus, a spatial and temporal analysis was performed on one reactive operating condition. Implementation of dual high-speed optical diagnostics enabled to assess the flame-flow-acoustic interactions. This study confirmed that aerodynamic instabilities, coupled with important differences in gas composition, were the primary reasons to large heat release fluctuations in the cavity. The resulting thermal gas expansion piloted the unsteady behavior of the combustor.

Based on these detailed measurements, an appropriate modification of the cavity injection systems revealed that it was possible to suppress these instabilities by confining the cavity. These recommendations were used to perform *a posteriori* validations, notably with the determination

of flame stability diagrams. The latter study also pinpointed difficulties to predict a stable combustion mode in this geometry, primarily due to the large amounts of dependant parameters.

# Contents

<b>Résumé</b>	<b>v</b>
<b>Summary</b>	<b>vii</b>
<b>List of figures</b>	<b>xv</b>
<b>List of tables</b>	<b>xvi</b>
<b>1 Introduction and Technological Review</b>	<b>1</b>
1.1 Driving forces in aviation . . . . .	1
1.2 Trapped vortex combustor: general background and previous works . . . . .	5
1.2.1 Conventional combustor . . . . .	5
1.2.2 Limitations of conventional aero-engines and need for new technologies . .	9
1.2.3 Trapped Vortex Combustor . . . . .	9
1.3 Thesis Goals . . . . .	20
1.3.1 CORIA laboratory research activities . . . . .	20
1.3.2 Thesis framework . . . . .	22
1.3.3 Thesis objectives and contents . . . . .	23
1.4 Experimental setup of the CORIA-TVC . . . . .	26
1.4.1 Objectives and constraints . . . . .	26
1.4.2 Description of the TVC . . . . .	27
<b>2 Preliminary Investigation of Combustion Instabilities in a TVC</b>	<b>33</b>
2.1 Background on flame stabilization and combustion instabilities . . . . .	34
2.1.1 Flame stabilization in premixed flows . . . . .	34
2.1.2 Combustion instabilities . . . . .	39
2.1.3 Difficulty to predict combustion instabilities mechanisms . . . . .	44
2.2 Diagnostics and Procedures . . . . .	45
2.2.1 Acoustic measurements . . . . .	45
2.2.2 CH*-Chemiluminescence . . . . .	47
2.2.3 OH planar laser induced fluorescence (OH-PLIF) . . . . .	49
2.2.4 Phase-averaged measurements . . . . .	52
2.3 Description of thermo-acoustic instabilities . . . . .	53
2.3.1 Operating conditions . . . . .	53
2.3.2 Pressure Dynamics . . . . .	54
2.3.3 Combustion dynamics . . . . .	55
2.3.4 Flame Structure Dynamics . . . . .	58
2.3.5 Rayleigh Index Distribution . . . . .	60
2.4 Concluding remarks . . . . .	62

<b>3</b>	<b>Aerodynamic stability of the shear layer in a TVC</b>	<b>64</b>
3.1	Background on cavity flows . . . . .	66
3.1.1	Free shear flows and associated instabilities . . . . .	66
3.1.2	Cavity flow dynamics . . . . .	69
3.1.3	Conclusion and challenging issues . . . . .	77
3.2	Experimental setup of the inert trapped vortex combustor . . . . .	77
3.3	High-speed particle image velocimetry (HS-PIV) . . . . .	78
3.3.1	Presentation of the technique . . . . .	78
3.3.2	Estimation of the accuracy of PIV . . . . .	79
3.4	Global flow topology . . . . .	85
3.4.1	Inlet flow characterization and operating conditions . . . . .	85
3.4.2	Qualitative description of the flow topology in an active and passive cavity . . . . .	87
3.4.3	Mass exchanges fluxes between the cavity and the mainstream flows . . . . .	89
3.4.4	Turbulent features . . . . .	94
3.4.5	Coherent Structures . . . . .	96
3.5	Characterization of the flow separation shear layer . . . . .	99
3.5.1	Self similar behavior . . . . .	99
3.5.2	Evolution of the shear layer thickness . . . . .	103
3.5.3	Effects of cavity flow injections on the shear layer location . . . . .	105
3.5.4	Momentum budget . . . . .	106
3.6	Conclusion . . . . .	108
<b>4</b>	<b>Temporal and Spatial analysis of Flow-Flame-Acoustic Interactions</b>	<b>111</b>
4.1	Experimental methods . . . . .	112
4.1.1	Advanced high-speed laser diagnostics . . . . .	112
4.2	Experimental methods . . . . .	113
4.2.1	10kHz OH-Planar Laser Induced Fluorescence system . . . . .	113
4.2.2	Reactive 2.5kHz Particle Image Velocimetry system . . . . .	115
4.2.3	Pressure and Photomultiplier . . . . .	115
4.2.4	Synchronisation and Measurement Duration . . . . .	116
4.3	Data Processing . . . . .	117
4.3.1	Flame front extraction . . . . .	117
4.3.2	Coherent velocity field filtering . . . . .	117
4.3.3	Proper orthogonal decomposition (POD) . . . . .	119
4.4	Mechanisms of combustion instabilities . . . . .	121
4.4.1	Global Rayleigh Index . . . . .	121
4.4.2	Phenomenological description of self-excited oscillations . . . . .	123
4.4.3	Effects of acoustics on the flow field . . . . .	126
4.4.4	Effects of flow dynamics on the unsteady combustion process . . . . .	131
4.4.5	Resulting mass transfers at the interface between the cavity and the mainstream . . . . .	133
4.5	Scenario for combustion instabilities in the present TVC . . . . .	136
4.6	Concluding Remarks . . . . .	137
<b>5</b>	<b>Global analysis of the TVC burner</b>	<b>139</b>
5.1	Experimental tools . . . . .	140
5.1.1	Pressure energy $E_p$ . . . . .	140
5.1.2	Pollutant emissions . . . . .	141
5.2	TVC performances . . . . .	142
5.2.1	Effect of the mainstream flow momentum . . . . .	142

5.2.2	Importance of the cavity for flame stabilization . . . . .	145
5.2.3	Cavity equivalence ratio $\phi_c$ . . . . .	146
5.2.4	TVC momentum ratio . . . . .	147
5.2.5	Conclusion of the sensitivity study . . . . .	149
5.3	Determination of criteria to predict flame stability . . . . .	149
5.3.1	Definition of stability transition . . . . .	150
5.3.2	Importance of the cavity power $P_c$ . . . . .	151
5.3.3	Mainstream-cavity interactions . . . . .	154
5.4	Characteristics of a stable point of operation . . . . .	156
5.5	Conclusion . . . . .	161
<b>6</b>	<b>Conclusion and recommendations for future works</b>	<b>163</b>
	<b>Appendices</b>	<b>168</b>
<b>A</b>	<b>Laser-Induced Fluorescence Spectroscopy</b>	<b>169</b>
A.1	Quantum Mechanics . . . . .	169
A.2	Transfer processes . . . . .	170
A.3	Laser excitation spectroscopy . . . . .	170
<b>B</b>	<b>Estimation of the local flame curvature</b>	<b>175</b>

# List of Figures

1.1	Comparison between several $NO_x$ emission standards and certification measurements in engines. Data are given as a function of the engine overall pressure ratio (OPR). Reproduced from [1]. . . . .	3
1.2	Emissions of a conventional combustor. T.O.: Take off. Reproduced from Wulff et al. [234] . . . . .	4
1.3	Left: Undamaged combustor. Right: Damaged combustor. Perforates have melted. Reproduced from Goy et al. [142] . . . . .	4
1.4	Schematic illustration of a two spool high by-pass turbofan [69] . . . . .	6
1.5	Schematic illustration of an annular combustor. Reproduced from Lefebvre [137].	7
1.6	Schematic illustration of (a) a multipoint injector [7], and (b) a lean premixed injection system from the TLC European project [26] . . . . .	8
1.7	Schematic illustration of the flow field topology in a TVC. . . . .	10
1.8	Laboratory-scale AFRL TVC. The 2P-2V configuration is presented: two passages in the mainstream and two vortices in the cavity. Reproduced from Burrus et al. [28] . . . . .	10
1.9	Laboratory-scale TVC of Hsu et al. [104] Reproduced from Sturgess et al. [215]. .	12
1.10	Laboratory-scale AFRL-TVC of Steele et al. Reproduced from Roquemore et al. [192] . . . . .	12
1.11	Laboratory GE TVC. The tri-pass configuration is shown on the left: three passages in the mainstream. . . . .	13
1.12	Desired $NO_x$ route in RQL combustors. Reproduced from [137]. . . . .	14
1.13	LBO limits of the 2 <sup>nd</sup> Generation TVC (only the cavity is fueled). Comparison with current and advanced combustors. Reproduced from Roquemore et al. [192]	15
1.14	Schematic illustration of the flow-induced resonance in a cavity ( $\delta$ : thickness boundary layer, $L$ : cavity length, $D$ : cavity depth, $\lambda$ : spatial wavelength of the instability). Reproduced from Cattafesta et al. [33] . . . . .	16
1.15	Example of a stability diagram. Mean $CH^*$ chemiluminescence when the main and cavity equivalence ratios were varied (mainstream flow rate of 20 g.s <sup>-1</sup> ). Reproduced from Burguburu [26]. . . . .	20
1.16	Comparison of pressure spectra for a stable and unstable operating conditions. reproduced from Burguburu [26]. . . . .	21
1.17	Instantaneous two-dimensional source term of the energy equation, for the unstable case. Reproduced from Merlin [160] . . . . .	22
1.18	Schematic illustration of the thesis content. . . . .	24
1.19	Schematic illustrations of different cavity injection systems resulting in different flow structures. Reproduced from Roquemore [192]. . . . .	27
1.20	Photography of the test bench. . . . .	27
1.21	Schematic illustration of the injection system. . . . .	27

1.22	3D Schematic illustration of the TVC . . . . .	28
1.23	(a) Schematic representation of the experimental setup. $\otimes$ : choked nozzle. (b) Details of the cavity region in the TVC ( $L_c = 22$ mm, $H_{aft} = 18.5$ mm). . . . .	29
1.24	Photography of the combustion chamber casing. The TVC combustion chamber was inserted in the chamber. Left: view from the inlet. The red circle corresponds to the igniter location. Right: view from the rear. The black circle depicts one dilution hole used to gather cold air with burned gases. . . . .	29
1.25	Details of the exhaust system. Left: overview. Right: sonic nozzle with the adjustable valve. . . . .	31
1.26	Left: schema of the TVC burner. right: details of the cavity region. $H_{aft} = 18.5$ mm. . . . .	31
1.27	Schematic illustration of the TVC instrumentation . . . . .	32
2.1	Combustion regimes in an aero-engine. Reproduced from [197]. . . . .	35
2.2	Schematic illustration depicting effects of kinematic balance between flow and flame velocities in a planar premixed flame propagating in a tube: (a) blowoff when $u_f > S_f$ , (b) flashback when $u_f < S_f$ , (c) stabilized when $u_f = S_f$ . . . . .	36
2.3	Schematic illustration of different methods used to stabilize flames. (a) splitter plate, (b) jet, (c) bluff body, (d) backward-facing step. Shear layer regions are depicted in gray. . . . .	37
2.4	Schematic illustration of a jet in cross-flow structure, including the counter-rotative pair (CVP). Reproduced from Fric and Roshko [74]. . . . .	38
2.5	Schematic illustration of processes involved in combustion instabilities. . . . .	40
2.6	Left: schematic illustration of the waveguide system. Right: schema depicting the phase shift between the pressure produced in the cavity and pressure measured by the sensor. . . . .	47
2.7	Schematic illustration of the phase-averaged procedure. Bins are depicted with grey filled rectangles (and numbering). . . . .	53
2.8	Time evolution of pressure fluctuations for an unstable condition (—) and a stable condition (....., additional details in Chap. 5). . . . .	54
2.9	Pressure fluctuation frequency spectrum of the unstable operating condition. . . . .	55
2.10	Phased-averaged $CH^*$ fields with values of phase angle marked. Only the upper-half of the burner is represented and corresponds to the spatial average of the lower and upper parts of the burner to take into account any possible assymetric effects. Pressure traces is shown at the bottom and also depicts the different bins used for the phase-averaged procedure. . . . .	56
2.11	Phase-averaged pressure fluctuations ( $\bullet$ ) and total $CH^*$ fluctuations ( $\blacksquare$ ). Informative dashed lines are depicted for clarity. . . . .	57
2.12	Instantaneous OH-PLIF images, illustrating specific instance of the combustion instability cycle. Phase angle values are identical to Fig. 2.10. . . . .	59
2.13	Example depicting the implementation of the Abel procedure. The image on the left corresponds to the volume averaged $CH^*$ field. The corresponding deconvoluted image is given on the right. . . . .	61
2.14	Rayleigh index distribution corresponding to the images show in Fig. 2.10. . . . .	61
3.1	Schematic illustration of a free shear layer flow with the different steps leading to the creation of vortices. . . . .	66
3.2	Shadowgraphs illustrating KH instabilities in a free shear layer (Nitrogen-Helium). Reproduced from Brown and Roshko [24]. . . . .	67

3.3	Superimposition of transverse and longitudinal rollers in a free shear flow. Reproduced from Bernal and Roshko [10]. . . . .	68
3.4	Autocorrelation functions of axial velocities measured in a free shear layer (backward-facing step flow). Reproduced from Rockwell & Knisely [189]. . . . .	68
3.5	Autocorrelation functions of axial velocities in a shear layer developing above a cavity. Reproduced from Rockwell & Knisely [189]. . . . .	69
3.6	Cavity classification of length $L$ , depth $D$ and with a free flow speed $U_\infty$ . (a): Deep cavity; (b): open cavity; (c): transitional cavity; (d): closed cavity. Reproduced from [34]. . . . .	70
3.7	Cavity classification for different $L/D$ , $W/D$ , and Mach numbers. Reproduced from Plentovich [176] . . . . .	71
3.8	Illustration of the flow-induced resonance in a cavity. Reproduced from Cattafesta et al. [33] . . . . .	72
3.9	Cavity region arrangement used for inert studies. The burner was operated at ambient pressure $P_{glob} = 0.1$ MPa. Two geometries were investigated: (a) a passive cavity with no mass injection systems in the cavity and, (b) an active cavity with two mass flow injection systems (by means of slots) . . . . .	78
3.10	One dimensional cut in the 2D averaged spectrum, for measured (—) and de-compensated (.....) spectra of the axial velocity fluctuation $u'$ . . . . .	81
3.11	1D cut in the 2D modeled transfer function energy spectra for two different interrogation windows (i.e., 16x16 and 32x32 $pix^2$ ) and for two overlap values (i.e., 50 and 75%). . . . .	83
3.12	Schematic illustration of the HS-PIV in inert conditions. (a) apparatus used to seed the flow; (b) A-A view (from the camera) . . . . .	84
3.13	Mainstream mass flow rate calculation $\dot{m}_m^o$ with PIV (Eq. 3.9). Comparison with theoretical values. . . . .	86
3.14	Mean velocity vector fields for the NF (top) and 2F (bottom). Mainstream mass flow rate $\dot{m}_m = 30g.s^{-1}$ . (left) Magnitude, (middle) $\bar{u}$ , (right) $\bar{v}$ . . . . .	88
3.15	Schema presenting the calculation principle of local mass transfers along the interfacial zone between the cavity and the mainstream. . . . .	89
3.16	Validation of the continuity equation along the interface between the cavity and the main channel (red line). left: NF; right: 2F. Mainstream flow rate $\dot{m}_o^m = 30 g.s^{-1}$ . . . . .	91
3.17	Normalized mean mass transfer profiles $\bar{Y}$ along the cavity interface ( $y = 0$ mm) for different mainstream flow rates $\dot{m}_m^o$ . NF configuration. . . . .	91
3.18	r.m.s of the mass transfer profile along the cavity interface ( $y = 0$ mm) for different mainstream flow rates. NF configuration. . . . .	92
3.19	Normalized mean mass transfer profiles $\bar{Y}$ along the cavity interface ( $y = 0$ mm) for different mainstream flow rates $\dot{m}_m^o$ . 2F configuration. . . . .	93
3.20	r.m.s of the mass transfer along the cavity interface ( $y = 0$ mm) for different mainstream flow rates. 2F configuration. . . . .	94
3.21	Isotropy coefficient $I_s = \overline{u'^2}/\overline{v'^2}$ for a mainstream mass flow rate $\dot{m}_m^o$ of $10g.s^{-1}$ . Left: NF; Right: 2F. . . . .	95
3.22	Turbulence intensity $I_t = (u'^2 + v'^2)^{0.5}/(u^2 + v^2)^{0.5}$ for the NF (left) and 2F (right) configuration and for a mainstream mass flow rate $\dot{m}_m^o$ of $10g.s^{-1}$ . . . . .	95
3.23	Scheme of the probe locations along the cavity interface. . . . .	97
3.24	FFTs for the 2F configuration, with a mainstream mass flow rate $\dot{m}_m^o$ of $10gs^{-1}$ . . . . .	97
3.25	Two instantaneous PIV measurements for the 2F configuration. Main flow rate of $10g.s^{-1}$ . . . . .	98



3.26	Evolution of the Strouhal number $St_{L_c}$ ( $1^{st}$ mode) with the main mass flow rate .	99
3.27	Mean axial velocity profiles $\bar{u}(x/L_c = 0.5)$ for the NF configuration and for several main flow rates. Profiles extracted at $x/L_c = 0.5$ . . . . .	100
3.28	Schematic illustration depicting a typical shear layer and notations used to define the self-similar concept. . . . .	101
3.29	Scaled mean axial profiles, according to Pope [179], for a mainstream mass flow rate of $30 \text{ g.s}^{-1}$ . . . . .	101
3.30	(Left) Axial mean velocity $\bar{u}$ profiles for the 2F configuration and for several mainstream flow rates. Profiles extracted at $x/L_c = 0.5$ . (Right) Scaled axial profiles for a main mass flow rate of $30 \text{ g.s}^{-1}$ , at different locations. . . . .	102
3.31	Evolution of the vorticity thickness $\delta_\omega$ along the cavity, for the NF configuration and for different mainstream mass flow rates $\dot{m}_m^o$ . . . . .	104
3.32	Evolution of the vorticity thickness $\delta_\omega$ along the cavity, for the 2F configuration and for different main mass flow rates. . . . .	104
3.33	Comparison of locus $y_{0.5}$ for the NF and 2F configurations, for a mainstream mass flow rate $\dot{m}_m^o$ of $10 \text{ g.s}^{-1}$ . . . . .	105
3.34	Different terms of the momentum equation budget for the NF configuration. Main flow rate of $30 \text{ g.s}^{-1}$ . . . . .	107
3.35	Different terms of the momentum equation budget for the 2F configuration. Main flow rate of $30 \text{ g.s}^{-1}$ . . . . .	108
4.1	Schematic representation of the dual measurement technique. . . . .	114
4.2	Triple decomposition principle. (a) Definition of variables. (b) Implementation procedure for the triple decomposition using an acoustic cutoff frequency $f_c$ . . . .	118
4.3	Schema illustrating the feedback process involved in combustion instabilities. $p'$ : unsteady pressure, $q'$ : unsteady heat release, $u'$ : velocity fluctuations. . . . .	121
4.4	(a) Pressure signal from dynamic sensor (left axis), and $\text{CH}^*$ radical intensity (right axis). . . . .	122
4.5	Pressure (left axis) and heat release (right) spectra. . . . .	123
4.6	Simultaneous OH traces and velocity measurements (colored according to magnitude) for an individual pressure cycle. . . . .	125
4.7	Power spectrum density of the axial velocity fluctuation $u'$ , taken in zone A (mainstream) and zone B (cavity). Refer to Fig. 4.6 for the nomenclature. . . . .	127
4.8	Comparison between total energy spectra ( $\tilde{u} + \tilde{u}'$ or $\tilde{v} + \tilde{v}'$ ) and filtered energy spectra ( $\tilde{u}'$ or $\tilde{v}'$ ) using triple decomposition. $R_{uv}$ corresponds to the ratio of the energy spectra of the axial component $u$ in the radial direction $\vec{y}$ . . . . .	127
4.9	Normalized energy of POD modes for the axial and radial velocity component . .	129
4.10	r.m.s velocity component fields, calculated from the first and second POD modes. Top: $1^{st}$ mode. Bottom: $2^{nd}$ mode. Left: $u_{rms}$ . Right: $v_{rms}$ . . . . .	130
4.11	Temporal history of the reduced pressure, heat release, and axial reconstructed velocity (with the two first modes). . . . .	130
4.12	Time series measurements of G parameter. . . . .	131
4.13	Phase shift between global heat release and velocity fluctuations: a) $\varphi_{u'-q'}$ (axial fluctuation). b) $\varphi_{v'-q'}$ (radial fluctuation). . . . .	132
4.14	Conditioned mean radial velocity $v_m(x, y = 0 \text{ mm})$ (red curve) superimposed on the corresponding mean progress variable $\bar{c}$ fields (grayscale). (a) $0^\circ < \varphi < 36^\circ$ . (b) $180 < \varphi < 216^\circ$ . (c) $288^\circ < \varphi < 324^\circ$ . The lower right pressure signal recalls the position of each graph along the combustion instability cycle (red dots). . . .	134

4.15	scatter plots of the spatially averaged progress variables with the corresponding averaged velocity component. 2000 instantaneous data. Left: data extracted in zone A and axial velocity. Right: data extracted in zone B and radial velocity . .	135
4.16	Schematic illustration of the mechanism of combustion instabilities encountered in the present TVC. . . . .	136
5.1	Schematic illustration of the two cavity injection systems $I_0$ (left) and $I_1$ (right). The cavity aspect ratio $L_c / H_{aft}$ was unchanged. . . . .	142
5.2	Pressure energy $E_p$ as a function of the mainstream temperature $T_{air}$ . Left: $\phi_m = 0.60$ , $\dot{m}_m^o = 28.7 \text{ g.s}^{-1}$ ; Right: $\phi_m = 0.80$ , $\dot{m}_m^o = 21.6 \text{ g.s}^{-1}$ . $P_g = 60\text{kW}$ , $\phi_c = 3.0$ , $\dot{m}_c^o = 0.7 \text{ g.s}^{-1}$ . Mass flow rates are given at ambient temperature. . .	143
5.3	Pressure energy $E_p$ as a function of the main bulk velocity $U_m$ . Corresponding main equivalence ratios $\phi_m$ are given on the secondary x-axis. $P_g = 60\text{kW}$ . $T_{air} = 413\text{K}$ , $\phi_c = 3.0$ , $\dot{m}_c^o = 0.7 \text{ g.s}^{-1}$ . . . . .	144
5.4	$\text{NO}$ emissions as a function of the main bulk velocity $U_m$ , for the two cavity injection systems. Corresponding main equivalence ratios $\phi_m$ are given on the secondary x-axis. $P_g = 60\text{kW}$ . $T_{air} = 413\text{K}$ , $\phi_c = 3.0$ , $\dot{m}_c^o = 0.7 \text{ g.s}^{-1}$ . . . . .	145
5.5	$\text{CO}$ and $\text{UHC}$ emissions as a function of the main bulk velocity $U_m$ , for two cavity injection systems. Corresponding main equivalence ratios $\phi_m$ are given on the secondary x-axis. $P_m = 50\text{kW}$ . $\phi_c = 3.0$ , $\dot{m}_c^o = 0.7 \text{ g.s}^{-1}$ . . . . .	146
5.6	Pressure energy $E_p$ as a function of the cavity equivalence ratio $\phi_c$ . $P_m = 50\text{kW}$ , $\phi_m = 0.7$ , $T_{air} = 413\text{K}$ . . . . .	147
5.7	Schematic illustration of the jet cross-flow like flow. Arrows represent the different flow pathlines. . . . .	147
5.8	Pressure energy $E_p$ as a function of the URF cavity bulk velocity. Results given for the $I_1$ injection system. . . . .	148
5.9	Example depicting the pressure energy criterion $E_{p,t}$ used to determine the transition to a stable regime. Pressure energy $E_p$ as a function of the main bulk velocity $U_m$ . $P_g = 15 \text{ kW}$ , $\phi_c = 3.0$ . . . . .	150
5.10	Stability map scaled with transitional jet momentum flux $J_t$ , for different power ratios $P_m / P_c$ while keeping fixed conditions in the cavity ( $P_c = 3.5 \text{ kW}$ , $\phi_c = 3.0$ , $U_c = 3.6 \text{ m.s}^{-1}$ ) . . . . .	152
5.11	Stability map scaled with transitional $S_t$ values, for different power ratios $P_m / P_c$ while keeping fixed conditions in the cavity ( $P_c = 3.5 \text{ kW}$ , $\phi_c = 3.0$ , $U_c = 3.6 \text{ m.s}^{-1}$ ) . . . . .	153
5.12	Stability map as a function of the power ratio $P_m / P_c$ and for different cavity equivalence ratios. Constant aerodynamics within the cavity, $U_c = 3.6 \text{ m.s}^{-1}$ . . .	154
5.13	Transitional cavity bulk velocities obtained for different mainstream velocities $U_m$ and for different power ratios $P_m / P_c$ . $P_c = 3.5 \text{ kW}$ . . . . .	155
5.14	Values of $S_t$ a function of the mainstream bulk velocity $U_m$ and for different power ratios . Values corresponding to transitional values obtained in Fig. 5.13 . . . . .	155
5.15	Simplified schematic illustration of a design procedure with a given cavity power $P_c^*$ . . . . .	156
5.16	Simultaneous OH traces and velocity measurements (colored according to magnitude). Time between two instantaneous records was $400\mu\text{s}$ . Left: rod middle plane RM; Right: rod center plane RC. • at the bottom represents rods and vertical line corresponds to the plane of interest. . . . .	157
5.17	Mean OH field for the stable configuration. Left: rod middle plane RM; Right: rod center plane RC. Flame regions are depicted with colored dashed rectangles. . . . .	159

5.18	Left: zones considered in the pilot and the main flame to estimate the spatial average of the progress variable $\langle c \rangle$ . Right: scatter plot of the progress variable $\langle c \rangle$ (spatially averaged) taken in the pilot and in the main region for 2000 instantaneous binarized OH-PLIF data. . . . .	160
5.19	Scatter plots of the spatially averaged progress variable with the corresponding averaged velocity components. Top: $\langle c_{pilot} \rangle$ ; Bottom: $\langle c_{main} \rangle$ . . . . .	161
A.1	Schematic illustration of a two-level energy diagram. Several transfer processes are presented. . . . .	170
A.2	Typical experimental arrangement for laser excitation spectroscopy. $\lambda_{exc}$ is the tunable wavelength of the dye laser, $S_f$ is the fluorescence signal collected on the intensified camera (cam.), and BD is a beam dump. . . . .	171
A.3	Influence of the temperature on the Doppler, collisional, and natural broadening widths. Results given for the OH molecule ( $Q_1(5)$ line). Reproduced from [22].	173
A.4	Experimental and theoretical laser excitation spectrum of the OH molecule in a laminar burner. $P = 1$ bar, $T = 2000$ K. The fluorescence signal was obtained by averaging 100 images and by taking the mean value of a defined region of interest ( $40 \times 40 \text{ pix}^2$ ). The wavelength interval between two measurements was 0.01nm. .	173
A.5	Theoretical emission spectrum of the OH molecule. $P = 1$ bar, $T = 2000$ K, and $\lambda_{exc} = 282.75 \text{ nm}$ [80]. . . . .	174
B.1	Schematic illustration of the curvature estimation procedure. . . . .	175
B.2	Extracted intensity profile of a raw and a filtered OH-PLIF image. . . . .	176
B.3	Procedure used to extract the flame front from a raw OH PLIF image. Tests were performed on a swirl combustor. left: corrected raw image; middle: image after the NLD filter; right: flame front (green line) superimposed on the corrected raw image. . . . .	177
B.4	Schematic illustration of pixel tracking procedure. . . . .	177
B.5	Schematic illustration of the curvature estimation procedure. (a) Example of fitting process on the discrete function $y(s)$ . (b) Automatic criterion used to determine the physical curvature $H$ , where BG are burned gases, FB are fresh gases, $\vec{G}$ is the local intensity gradient vector, and $\vec{R}$ is the local radius of curvature.	179
B.6	Sensitivity analysis based on the number of pixels used for the fit. . . . .	179

# List of Tables

1.1	Advanced Studies on TVC (experimental and numerical). Exp: Experiments, CFD: Computational Fluid Dynamics. RANS: Reynolds-Averaged Navier-Stokes, LES: Large Eddy Simulation . . . . .	19
1.2	Nomenclature used in the present study. . . . .	30
1.3	Nomenclature used in the present study. . . . .	30
2.1	Details of parameters used to correct pressure records. . . . .	46
2.2	TVC operating conditions. . . . .	54
3.1	Cavity classification in accordance with ratios $L/D$ and $W/L$ . . . . .	70
3.2	Nomenclature used for the inert investigation. <b>NF</b> : NOFLOWS (passive cavity); <b>2F</b> : 2FLOWS (active cavity). Reynolds numbers $Re_h$ are based on the slot height $h_m$ . $U$ is the bulk velocity. * These values have been chosen in accordance with the operating conditions given in Chap. 2 [235, 27]. . . . .	86
4.1	Acquisition rates and amount of processed data. . . . .	116
5.1	TVC operating conditions. * The mainstream air was heated up to 413K. . . . .	158
5.2	Pollutant emissions for the stable and unstable operating conditions. . . . .	162

# Nomenclature

This list of symbols is not exhaustive and symbols that are not mentioned below are explained when they appear.

## Abbreviations

$2F$  2FLOWS

*ACARE* Advisory council for aviation research and innovation in Europe

*CAEP* Committee on aviation environmental protection

$CH_4$  Methane

$CO$  Carbon monoxide

$CO_2$  Carbon dioxide

*DCA* Downstream cooling air

$I_0$  Historical injection system

$I_1$  Modified injection system

*LP* Lean premixed

*NF* NOFLOWS

$NO_x$  Nitrogen oxides

*OPR* Overall pressure ratio

*RC* Rod center

*RM* Rod middle

*RQL* Rich-quick/quick-mix/lean-burn

*TVC* Trapped vortex combustor

*URF* Upstream reactive flow

ICAO International civil aviation organization

IEA International energy agency

KH Kelvin Helmholtz

Mtoe Million of tonnes of oil equivalent

PIV Particle image velocimetry

PLIF	Planar laser induced fluorescence
POD	Proper orthogonal decomposition
PSD	Power spectral density
r.m.s	Root mean square
SPL	Sound pressure level

### Greek letters

$\lambda$	Eigenvalue	
$\Phi$	Space function	
$\phi$	Equivalence ratio	[-]
$\rho$	Gas density	[kg.m <sup>3</sup> ]
$\tau$	Characteristic time	[s]
$\varphi$	Phase angle	[°]

### Latin letters

$\Delta t$	Time delay	[s]
$\dot{m}$	Mass flow rate	[g.s <sup>-1</sup> ]
$\mathbf{u}$	Velocity vector field	[-]
$\mathcal{R}$	Rayleigh index	[a.u]
$a$	POD time coefficient	
$c$	Progress variable	[-]
$c^s$	Sound speed	[m.s <sup>-1</sup> ]
$E_p$	Pressure energy	[Pa <sup>2</sup> ]
$f$	Frequency	[Hz]
$f_0$	Fundamental acoustic frequency	[Hz]
$h_m$	Main channel height	[mm]
$H_{aft}$	Afterbody height	[mm]
$I$	Pixel intensity of an image	[a.u]
$I_s$	Isotropy coefficient	[-]
$I_t$	Turbulent intensity	[-]
$J$	Jet momentum flux	[-]
$k$	POD mode	
$L_c$	Cavity length	[mm]
$P$	Power	[kW]
$p'$	Pressure fluctuation	[Pa]

$p_{glob}$	Global pressure	[MPa]
$q'$	Heat release fluctuation	[V]
$R$	Spatial correlation matrix	
$Re$	Reynolds number	[-]
$S$	Stratification ratio	[-]
$S_w$	Swirl number	[-]
$t$	Time	[s]
$T_{air}$	Mainstream air temperature	[K]
$U$	Bulk velocity	[m.s <sup>-1</sup> ]
$u$	Axial velocity component	[m.s <sup>-1</sup> ]
$v$	Radial velocity component	[m.s <sup>-1</sup> ]
$x$	Axial coordinate	[mm]
$Y$	Local mass exchange	[-]
$y$	Radial coordinate	[mm]

### Subscripts and Superscripts

$\langle \cdot \rangle$	Spatial average operator
$\bar{\cdot}$	Temporal average operator
$c$	Cavity
$DCA$	Downstream cooling air
$F$	Fuel
$g$	Global
$m$	Mainstream
$o$	Oxidant
$t$	Transitional value





# Chapter 1

## Introduction and Technological Review

### Contents

---

<b>1.1</b>	<b>Driving forces in aviation . . . . .</b>	<b>1</b>
<b>1.2</b>	<b>Trapped vortex combustor: general background and previous works</b>	<b>5</b>
1.2.1	Conventional combustor . . . . .	5
1.2.2	Limitations of conventional aero-engines and need for new technologies .	9
1.2.3	Trapped Vortex Combustor . . . . .	9
<b>1.3</b>	<b>Thesis Goals . . . . .</b>	<b>20</b>
1.3.1	CORIA laboratory research activities . . . . .	20
1.3.2	Thesis framework . . . . .	22
1.3.3	Thesis objectives and contents . . . . .	23
<b>1.4</b>	<b>Experimental setup of the CORIA-TVC . . . . .</b>	<b>26</b>
1.4.1	Objectives and constraints . . . . .	26
1.4.2	Description of the TVC . . . . .	27

---

### 1.1 Driving forces in aviation

3.1 billion passengers have used the air transportation network in 2013. The international civil aviation organization (ICAO) reported that this figure increased by 5% for the year [37], and forecasts<sup>1</sup> made by the international energy agency (IEA) show that air transportation may grow

---

<sup>1</sup>Scenarios, recalibrations and assumptions are based on [60, 61].

four-fold between 2005 and 2050, with half of this growth in non-OECD countries (organisation for economic co-operation and development) [62]. These brief figures underline the dynamism of aviation sector, which is being diversified through new markets.

Because aircraft engines currently rely on fossil fuels, how aviation contribute to climate change and what are expectations in the future? On the one hand, since the invention of the airplane by the Wright brothers, important aircraft technology improvements have been achieved, leading to a reduction in energy intensity of 60% between 1960 and 1998<sup>2</sup> (energy used per passenger and kilometer). On the other hand, the energy footprint of aviation constantly increases and may triple in 2050 to about 750 Mtoe (Million Tonnes of Oil equivalent). These two opposite facts show the gap between improvements of aircraft efficiency and aviation activity growth rate. As a result, there is no doubt on the impact of aviation on climate change. Among others, carbon dioxide  $CO_2$ , nitrogen oxides  $NO_x$  or carbon monoxide  $CO$  mainly contribute to aircraft pollutant emissions.

As mentioned by Sawyer [202], establishment of stringent regulations is necessary and determine driving forces and means to reduce pollutant emissions in aero-engines. As an example, Fig. 1.1 depicts the evolution of several  $NO_x$  standards, given as a function of the engine overall pressure ratio (OPR). Colored lines correspond to several CAEP standards (committee on aviation environmental protection) whereas triangles represent  $NO_x$  emissions measured for different engines. Note that these regulations are dependent on the engine OPR [138] and that  $NO_x$  emissions of actual aero-engines are mostly below the latest standard shown in this graph (i.e., CAEP/6).

The primary reason for this trend is that standards are valid for all engines in operation. Consequently, older engines which do not satisfy new standards are subjected to an early retirement. It is then essential for manufacturers to meet the latest standards with a maximum margin in order to stay competitive. In Europe, the advisory council for aviation research and innovation in Europe (ACARE) recommends mid and long term goals in order to stimulate and structure research and development.

---

<sup>2</sup>US data only.

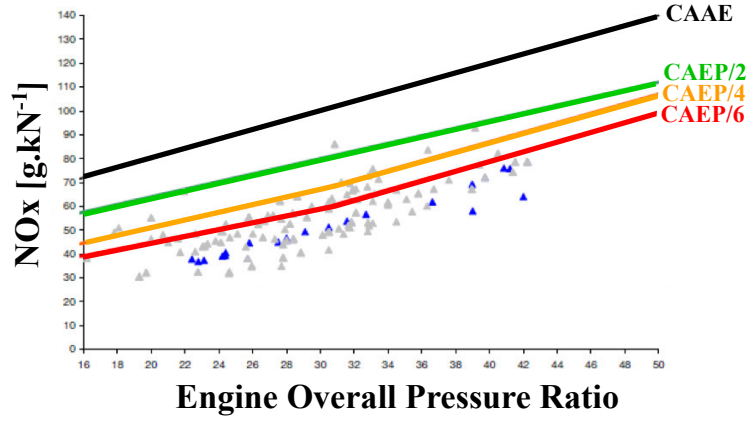


Figure 1.1: Comparison between several  $NO_x$  emission standards and certification measurements in engines. Data are given as a function of the engine overall pressure ratio (OPR). Reproduced from [1].

The 2020 ACARE targets recommend to reduce  $CO_2$  emissions by 50% and  $NO_x$  emissions by 80% in 2020 (compared to 2000). Because  $CO_2$  is a by-product of combustion, the only solution consists in reducing fuel consumption. Reduction of other pollutants raises many issues. Figure 1.2 depicts the evolution of  $NO_x$ ,  $CO$ , and unburned hydro-carbons (UHC) as a function of the equivalence ratio  $\phi$ . Typical corresponding flight operating conditions are also given for information.  $NO_x$  are generated near stoichiometry (i.e.,  $\phi \approx 1$ ), at high temperatures (e.g., take-off), whereas  $CO$  is created at low temperatures (e.g., idle) or when combustion is incomplete (e.g.,  $\phi \gg 1$  or  $\phi \ll 1$ ). Thus, an optimum zone has to be reached, and is referred to as the low emissions zone in Fig. 1.2.

However, several design constraints makes the operation in this zone more difficult for conventional combustors [234]. For instance, the constant air split between the primary and secondary zone (see Sec.1.2.1), coupled with the liquid fuel evaporation, creates a non-uniform temperature field in the primary zone, and which is even more not perfectly controlled. Moreover, constraints on weak extinction limits at low power avoid lean operating conditions at high power. Several alternative technologies have been developed for the course of several years, in order to extend the range of operating conditions. Variable geometry or staged combustors may be a solution but their mechanical integration is quite complex. Lean Premixed (LP) combustion is a promising technology to cut  $NO_x$ : the fuel is mixed with the air ahead of the combustion chamber, which results in a mixture with a perfectly controlled equivalence ratio. In addition, because air

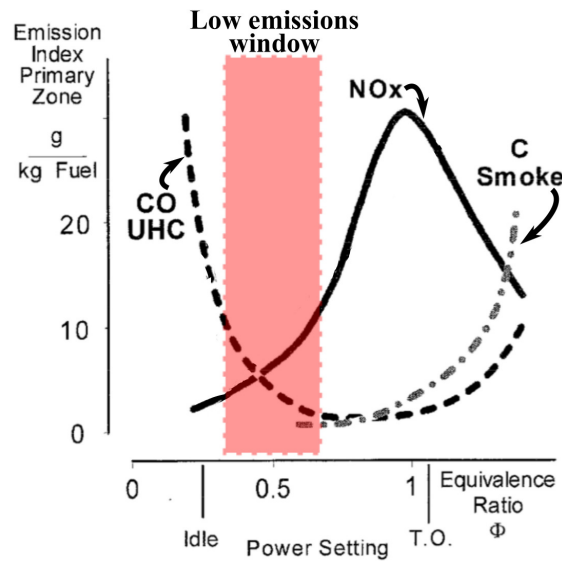


Figure 1.2: Emissions of a conventional combustor. T.O.: Take off. Reproduced from Wulff et al. [234]

is injected in excess, the adiabatic flame temperature is drastically reduced and can therefore prevent from thermal- $NO_x$  production.

Unfortunately, developments of LP combustion in combustors have also brought new technological challenges. Because the equivalence ratio is decreased, corresponding variations in temperatures and flame speeds are greater and make the flame to be more sensitive to external disturbances. In turn, the combustor is more prone to unsteady behaviors: local flame extinction, flame blow-off, flashback or even thermo-acoustic oscillations (see [142] for case studies). Unsteady combustion is problematic because it greatly affects the flame stabilization, reduces the combustion efficiency, induces severe material stresses and even deteriorates components prematurely, as shown in Fig. 1.3 [78, 143, 29].

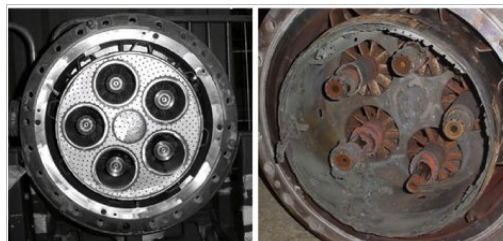


Figure 1.3: Left: Undamaged combustor. Right: Damaged combustor. Perforates have melted. Reproduced from Goy et al. [142]

A possible solution to prevent these undesired phenomena consists in integrating cavity flame

holders in the combustion chamber to improve flame stabilization. The effectiveness of this concept has been investigated over the course of several years in scramjet hypersonic combustors, and investigations for subsonic applications, known as the trapped vortex combustor (TVC), have been conducted since the early 1990s.

## **1.2 Trapped vortex combustor: general background and previous works**

We present in this section a review of research and progress of the TVC. In order to give a clearer context of the present study, a brief reminder on conventional combustors is provided to the reader.

### **1.2.1 Conventional combustor**

Pollutant emissions are key indicators of the combustion process and depends on many parameters such as geometry, inlet pressure, inlet temperature, evaporation of fuel droplets, turbulence, mixing, etc. It is important to understand how operates a classical gas turbine combustor to reveal limitations and possible improvements.

#### **Operation of a gas turbine**

The combustor is one of the key element of a gas turbine because it provides the thrust of an aircraft. A schematic illustration of a turbofan is shown in Fig. 1.4. A large fan at the front of the engine sucks a large quantity of air, which is divided into two parts: 8 to 12% goes through the core engine (compressor, combustor, turbine, and nozzle stages) whereas the remaining air bypasses the core engine and flows to the back of the engine. In the core engine, air is squeezed through the compressor and then forced in the combustor. It is then mixed with the fuel and ignited. The hot stream coming out of the combustor enters the turbine, where its kinetic energy is extracted to drive one or several shaft(s) connected to the compressor, the fan, and accessories. Finally, cold and hot flows pass a nozzle at the rear of the engine and provide a forward thrust. Note that more than 80% of the thrust is provided by the bypass flow.

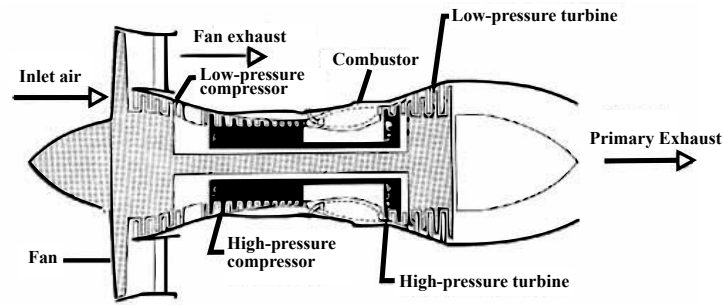


Figure 1.4: Schematic illustration of a two spool high by-pass turbofan [69]

### Conventional combustor architecture

Aero-engine combustors must satisfy several requirements in order to be safe and economically viable. Specifically, several constraints have to be taken into account during design processes:

- Size and weight.
- Small pressure loss.
- Efficient ignition or re-ignition at high altitude.
- Wide range of operating conditions in terms of pressure, temperature, and flow rates (e.g., cruise conditions vs. unexpected go-around).
- No self-induced pressure fluctuations (especially with lean premixed combustion).
- Appropriate outlet temperature (turbine inlet temperature TIT) with smooth spatial distribution (pattern factor).
- Efficient wall cooling.
- Fuel consumption and pollutant emissions.

Figure 1.5 depicts the typical architecture of an annular conventional combustor, which can be divided into three parts:

**Diffuser.** The airstream velocity exiting the compressor outlet guide vane stage must be lowered to a reasonable value. A diffuser is then used to reduce the airflow velocity through an expanding geometry. A minimum pressure loss must be obtained with this expansion, which makes its design complex. Figure. 1.5 also shows a snout, which splits the airstream to the liner

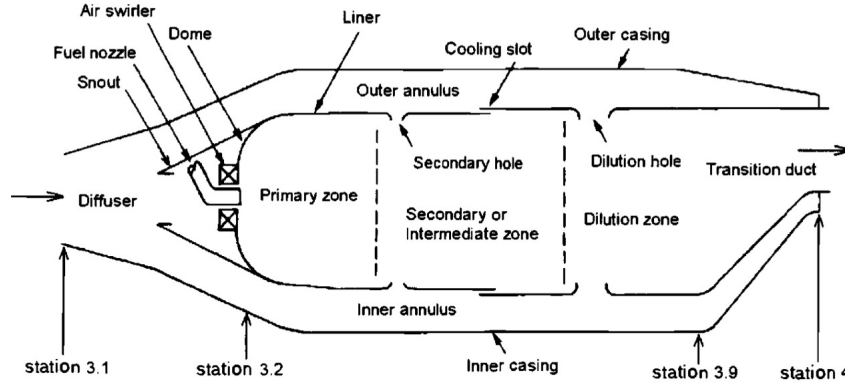


Figure 1.5: Schematic illustration of an annular combustor. Reproduced from Lefebvre [137].

or to the annulus. The former airstream flows through the air swirler and the latter enters the liner through dilution and cooling holes.

**Injector and primary zone.** The air passing through the snout is used to be mixed with the fuel and stabilize the flame in the primary zone. The design of the injector and the primary airflow pattern are paramount because they control the flame holding process. Swirl flow is commonly used in conventional combustors: it consists in adding a tangential velocity component to the incoming air flow, which in turn creates a toroidal flow reversal. Burned gases are then entrained back to the injector neck and ensure a continuous ignition and flame stabilization [81]. The swirl number is used to characterize this type of flow behavior, and is defined as

$$S_w = \frac{G_\theta}{G_x}, \quad (1.1)$$

where  $G_\theta$  is the axial flux of tangential momentum, and  $G_x$  is the axial flux of axial momentum. Liquid fuels are mostly used in aircraft and need to be atomized, evaporated and mixed with air in the primary zone. The better the atomization process is, the better the evaporation and mixing are. Several systems have been developed in order to improve efficiency of injection systems. Among others:

- **Multipoint injection systems.** The basic idea lies on adding secondary fuel injections to create a staged injection system, which can increase mixing and widen the range of operating conditions while maintaining good flame holding capabilities. A schematic illustration is given in Fig. 1.6-(a). The primary zone is located in the central zone whereas

secondary injections are added in the surroundings. This concept has the advantage to be compact, but also suffers from the large amounts of parameters which can affect its performances: location of the secondary injections, operating conditions, dependance with the geometry, etc., [136, 7].

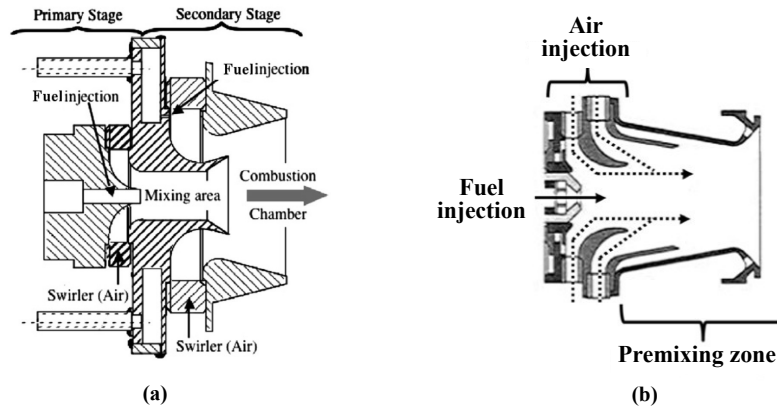


Figure 1.6: Schematic illustration of (a) a multipoint injector [7], and (b) a lean premixed injection system from the TLC European project [26]

- Lean premixed prevaporized injection systems are based on conventional injection systems but the mixing region is drastically increased to obtain a (partially) lean mixture at the exit (Fig. 1.6-(b)). Unfortunately, these types of injectors also suffer from many instabilities, such as combustion instabilities [29].

**Intermediate, dilution zone and combustor liner.** The air which is bypassed to the annulus is injected in the intermediate zone through secondary holes and cooling slots. This air is used to complete combustion of remaining rich-fuel pockets and to smoothly cool down the hot gas stream. The remaining air is finally injected through dilution holes. The function of the dilution zone is to lower temperatures to acceptable values for the turbine guide vane stage. Optimizing the design of these injections is paramount in order to achieve a rapid mixing and good temperature homogeneization.

Because the combustion process is contained in the liner, this part must withstand strong thermal and mechanical stresses. Thus, cooling walls is crucial. For example, use of angled effusion cooling (AEC) holes are widely used in modern aero-engines [137].



### 1.2.2 Limitations of conventional aero-engines and need for new technologies

Conventional combustors are still optimized to meet emission standards. However, technologies are more and more complex and results in longer design development times. Because injection of liquid fuels and the resulting mixing with air is directly achieved in the primary zone, several combustion regimes (lean or rich) and several types of flames (diffusive or premixed) are encountered. It implies that the local equivalence ratio is not controlled in this zone and that there are no possibilities to control production of pollutants. In addition, because swirl flows are extensively used, their range of operating conditions are greatly dependant on the incoming flow rate (see Eq. 1.1), and many instabilities can affect the combustion process and reduces the range of stable operating conditions.

Investigation of new combustor concepts is then crucial in order to make easier the implementation of new combustion regimes. Optimization of actual combustors is one solution which is nowadays adopted but a technological breakthrough has to be considered in view of future stringent standards. Note that several concepts are now investigated (constant volume combustion, rotating and pulsed detonation combustion [97, 113], etc.) and also embed the whole engine (e.g., open rotor [31]). This study is focused on the trapped vortex combustor and next section aims to introduce this concept.

### 1.2.3 Trapped Vortex Combustor

This section aims to introduce the trapped vortex combustor (TVC) concept. A brief review is provided to the reader in terms of global performances (pollutant emissions, flame stability, range of operating operations). Then, critical points when designing such a burner are presented in order to highlight the main issues and therefore reinforce the goal of the present study.

#### TVC Principle

TVC developments started in the 1990s at the Air Force Research Laboratory (AFRL) with experimental works of Hsu et al. [104] and numerical investigations of Katta and Roquemore [119,

118].

Figure 1.7 presents a schematic illustration of the general flow topology encountered in a TVC. A mainstream flows past a cavity, where one or several vortices are trapped. Note that this flow topology is quite different from conventional swirl-stabilized combustors.

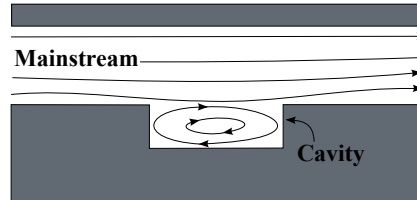


Figure 1.7: Schematic illustration of the flow field topology in a TVC.

Motivations in integrating cavities in combustors historically come from the aerodynamic community. Many studies were focused on performing an active control to reduce drag of many systems involving cavities: bomb bays, interstices between train carriages, landing gear doors, etc. [33]. Therefore, many studies attempted to assess instability mechanisms related to the presence of an interfacial shear layer at the flow separation between the cavity and the mainstream. Gharib et al. [75] found that when a stable vortex was established in the cavity, the drag was remarkably reduced. This observation was confirmed by other workers [149, 124]. Hsu et al. [104] took advantage of this flow stability to introduce the TVC.

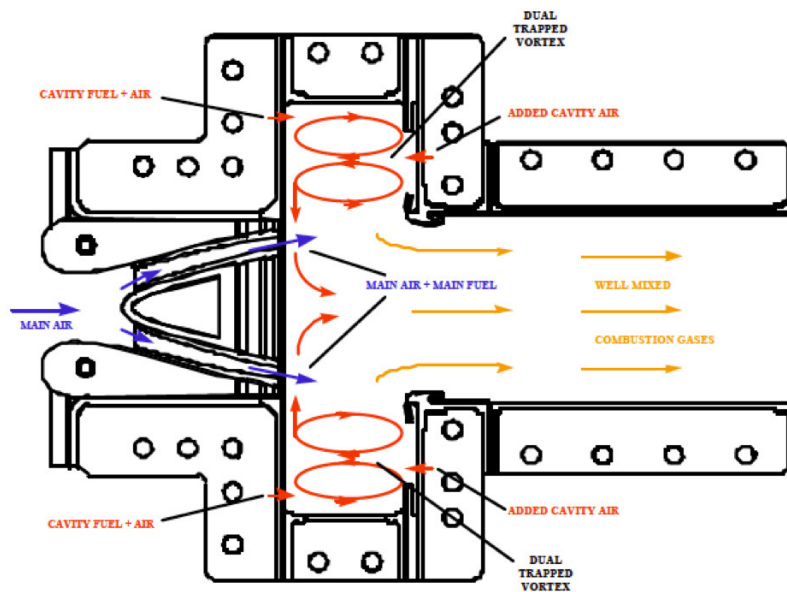


Figure 1.8: Laboratory-scale AFRL TVC. The 2P-2V configuration is presented: two passages in the mainstream and two vortices in the cavity. Reproduced from Burrus et al. [28]

The TVC concept uses a recirculating rich flow trapped in a cavity to create a stable pilot flame that continuously ignites a main lean mixture passing above the cavity. Recirculating zones of hot combustion products inside the cavity and their rapid mixing with the lean main mixture provide a continuous ignition source and stabilize the flame. In order to achieve an improved mixing between cavity products and the main flow, additional flame holders can be added in the main channel [2, 192].

A schematic illustration of the AFRL-TVC is shown in Fig. 1.8. Recirculation zones are created by means of two cavities, located around the mainstream (main flow passing from the left to the right). In the cavity, two injection systems bring primary air and fuel to establish a stable recirculation zone and produce combustion products, radicals, and heat needed for the stabilization process. This technology offers several attractive advantages for aero-engines:

- Because part of the combustion takes place inside the cavity, the natural confinement of this pilot region is less affected by sudden changes in the mainstream.
- Any turbulence occurring in the combustion chamber is trapped within the cavity where reactants can be mixed efficiently.
- The combustor can operate with high amounts of excess air in the premixed regime and can withstand high-speed flows while preventing flash-back.
- Extremely low  $NO_x$  emission levels are tolerated without any dilution or post-combustion stages.
- TVC is capable of operating as a staged combustor if the fuel is injected into the cavity and the mainstream. It can also be operated as a rich-burn/quick-quench/lean-burn (RQL) combustion concept when the fuel is injected into the cavity only. Thus, a wider range of operating conditions is achieved while retaining good flame holding capabilities.

Several types of TVC have been developed by the AFRL and General Electric (GE). They can be classified historically [192]:

- **First Generation.** Hsu et al. [104] studied the TVC to demonstrate the concept of trapping a flame within a cavity. A schema of the burner is shown in Fig. 1.9. The cavity was made of two disks mounted in tandem on a single shaft. The mainstream consisted in

pure air whereas primary fuel and air injection systems were located on the downstream face of the spindle. In addition, air and fuel were injected separately through rings of holes (see right part of Fig. 1.9). Katta et al. [118] performed numerical computations of this experiment.

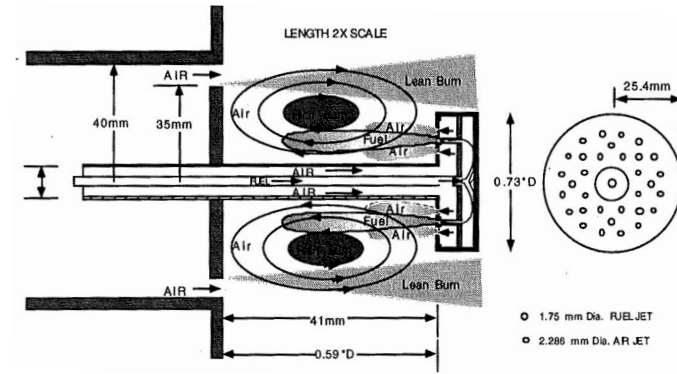


Figure 1.9: Laboratory-scale TVC of Hsu et al. [104] Reproduced from Sturgess et al. [215].

- **Second Generation.** This generation was mainly used to obtain global performance measurements (i.e., pollutant emissions, LBO limits, relight capabilities). The burner had a can-type architecture and the cavity was placed on the outer part of the mainstream flow. In contrast with the first generation, the mainstream flow was also fueled. In addition, struts were added in the mainstream to enhance mass transfers between the cavity and the mainstream.

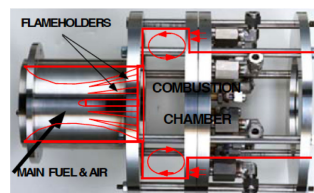


Figure 1.10: Laboratory-scale AFRL-TVC of Steele et al. Reproduced from Roquemore et al. [192]

- **Third Generation.** Capabilities to integrate a TVC in aircraft gas turbines were tested, especially through use of liquid fuels. The geometry consisted in a two-dimensional sector rig, with a full optical access to visualize the flame.
- **GE TVCs.** The TVC was similar to the 3<sup>rd</sup> generation. Liquid fuels were injected both in the cavity and in the mainstream. Additional air injection systems were added to cool

down walls. Hendricks et al. [94] studied more than 19 different configurations to determine the best strategy for cavity injection systems.

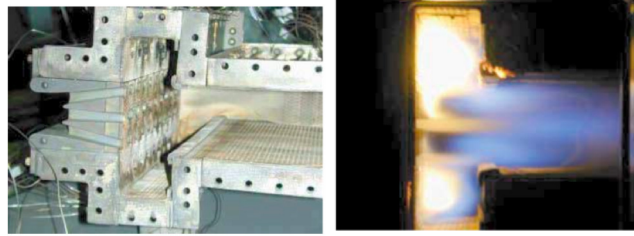


Figure 1.11: Laboratory GE TVC. The tri-pass configuration is shown on the left: three passages in the mainstream.

Today, many workers continue to investigate the TVC [14, 15, 108]. To our knowledge, no integration neither tests have been performed on real engines, but it is noted that many patents have been filed during the ten last years [64, 67, 63, 65, 66]. In addition, the complexity and specificity of the TVC geometry makes every study merely unique and limits possibilities to compare results.

### Rich-burn Quick-mix Lean-burn (RQL) and Low- $NO_x$ TVC

It is known that temperature and residence time have an important role in the production of thermal- $NO_x$  [137]. Therefore, obtaining an overall lean combustion regime necessarily reduces the adiabatic flame temperature. In addition, optimizing the mixing process also reduces the residence time in the combustor. The architecture of a TVC combustor is like an RQL combustor, in a more precise form:

- Rich-burn: fuel and air are first introduced to create a rich zone. The combustion is then incomplete and temperatures are lower than stoichiometric conditions. In the TVC, this stage corresponds to the cavity, where the equivalence ratio is usually higher than unity.
- Quick-mix: a large quantity of air is added to quench the rich mixture. Mixing yield is of great importance to prevent high temperature pockets (i.e., at stoichiometry) and rapidly brings the mixture to the lean region. Exchanges between the mainstream and the cavity represent this mixing process in a TVC. A schematic illustration of the normal and RQL like low- $NO_x$  paths are shown in Fig. 1.12

- Lean-burn: combustion of the resulting fuel-lean mixture can lead to a low- $NO_x$  condition. Lean conditions in the mainstream of a TVC enables to reduce the overall temperature and then prevent from the production of thermal  $NO_x$ .

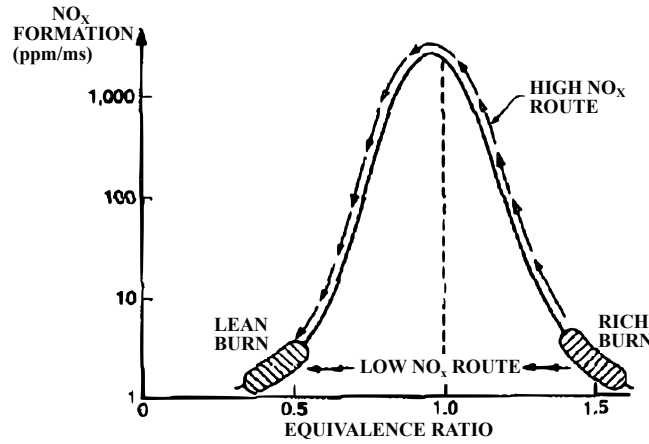


Figure 1.12: Desired  $NO_x$  route in RQL combustors. Reproduced from [137].

Burrus et al. [28] obtained pollutant emissions data on the GE TVC. Tests were carried out with JP-8 liquid fuel, with an inlet pressure of 20.7 bars and a temperature and 900K. He demonstrated a 40 to 60% reduction in  $NO_x$  emissions, compared to the 1996 ICAO standards. At the same time, the combustion efficiency was maintained above 99% over a range of operating conditions 40% wider.

Hendricks et al. [94] collected additional data on the GE TVC. Tests were done with liquid fuel, at low pressure (3-4 bar) and with inlet temperatures lying between 500 and 850 K. In this study, the cavity was only fueled. He found a 50% reduction in  $NO_x$  emissions compared to advanced gas turbines. Haynes et al. [90] developed a can-type TVC at GE Global Research for heavy-duty gas turbines. The gas turbine was studied at part/full-load on natural gas. The first prototype demonstrated a reduction of 60 to 75% in  $NO_x$  emissions while the second prototype showed a  $NO_x$  benefit of 60 to 80% compared to conventional engine emissions.

### Importance of the cavity-based flame holder on performances

Because the recirculation zone of a TVC is located in a cavity, the geometry acts as a natural shield and makes this zone quite stable, and even unaffected by the mainstream conditions. Therefore, it was expected to obtain a wider range of flame stability, lower LBO limits and better

altitude relight capabilities. Roquemore et al. [192] studied LBO limits of the 2<sup>nd</sup> generation TVC, when the cavity was only fueled. For several cavity air flow rates, the corresponding cavity fuel flow rate was reduced until flame extinction occurred. This operation was repeated for several mainstream air flow rates and for several inlet temperatures. Results are shown in Fig. 1.13 and exhibit significantly lower LBO values in comparison with conventional swirl-stabilized combustors. Moreover, these values appeared to be interestingly independent from the mainstream operating conditions, thus confirming benefits of using a cavity.

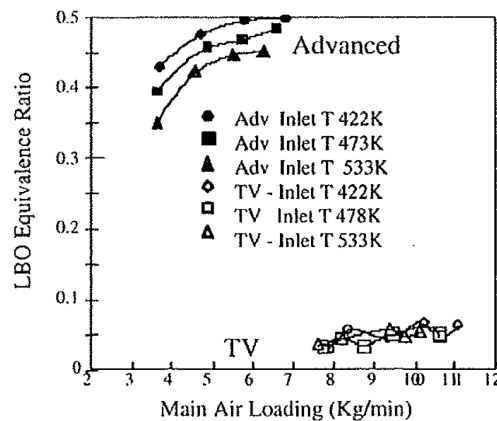


Figure 1.13: LBO limits of the 2<sup>nd</sup> Generation TVC (only the cavity is fueled). Comparison with current and advanced combustors. Reproduced from Roquemore et al. [192]

LBO results on the 3<sup>rd</sup> generation also gave good performances. When the cavity and the mainstream were fueled (liquid), Burrus et al. [28] found a 50% improvements of LBO margins compared to conventional combustors. Hendricks et al. [94] found a 25% LBO improvements at high-pressure (i.e., 20 and 50 bars) and ambient temperatures. More recent studies investigated LBO limits on a similar GE TVC at the Beijing University (Xing et al., [237, 236]). They found rather low LBO values and put in evidence the beneficial advantage of increasing the cavity airstream temperature.

### Critical features for a TVC design

Conditions for an efficient flame stabilization and a low- $NO_x$  burner rely on:

- a stable recirculation flow in the cavity.
- important exchanges between the mainstream and the cavity to increase mixing.

The main issue is that these two conditions are contradictory. In fact, this type of flow topology exhibits important aerodynamic instabilities for certain conditions. As mentioned previously, several works were carried out in the aerodynamic community [75, 189, 33] and put in evidence different cavity oscillation processes (see Chap. 3). An example is depicted in Fig. 1.14.

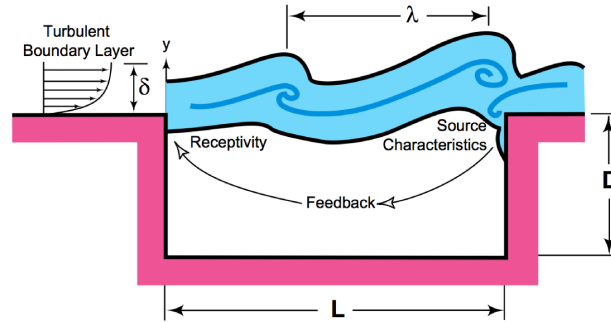


Figure 1.14: Schematic illustration of the flow-induced resonance in a cavity ( $\delta$ : thickness boundary layer,  $L$ : cavity length,  $D$ : cavity depth,  $\lambda$ : spatial wavelength of the instability). Reproduced from Cattafesta et al. [33]

The flow separation at the cavity leading edge naturally leads to the development of an interfacial shear layer, which in turn impinges on the cavity trailing edge. This impingement and reattachment region can create an acoustic or aerodynamic feedback which can sometimes leads to self-sustained flow oscillations. A proper design of the cavity (e.g., size, mainstream velocity, etc.) is of great importance to prevent these instabilities and achieve a stable recirculation zone.

When a stable vortex is established in the cavity with enough strength, the cavity flow is stable but very little main fluid enters the cavity. This can deteriorates the flame stabilization (and ignition). In the TVC concept, this issue was overcome by adding injection systems in the cavity and struts in the mainstream. However, differences appear as the cavity becomes active (i.e., mass injection) and with the addition of heat release. As a result, the stability criteria found for inert passive cavities (i.e. no mass injection) may change. Katta and Roquemore [117, 119] numerically investigated the inert flow dynamics when fuel and air were directly injected in the cavity and found different criteria compared to passive cavities. Non optimum cavity sizes led to an unstable recirculation zone an even occurrence of coherent structures. Therefore, they performed reacting flow calculations and showed that combustion was surprisingly stable even though criteria were based on inert conditions. More recent studies have been carried out by



Kumar et al. [128, 129]. He highlighted the importance of the cavity size, the injection strategy and interactions between the cavity and the mainstream flow.

Because fast mixing and capabilities to stabilize a flame are key parameters in a TVC, interactions (mass, heat, radicals, etc.) between the cavity and the mainstream are paramount. Sturgess et al. [215] and Katta et al. [119] experimentally and numerically investigated the cavity flow entrainment for different configurations in reactive conditions. Sturgess et al. [215] pointed out the difficulty to perform direct experimental measurements of mass exchanges between the mainstream and the cavity. Indeed, he introduced an alternative technique, based on the LBO measurements. However, his results were based on a strong assumption: air and fuel, which were separately injected in the cavity, were instantaneously mixed. Remarkably, Stone et al. demonstrated the contrary: location of mixing and reaction zones were highly dependant on the mainstream inlet velocity [212]. More recent works have been performed to assess the influence of adding flame holders in the mainstream flow to create larger wake regions and then increase mixing [192, 2].

In comparison with numerous performance studies, only few studies have been focused on understanding the fundamental mechanisms of flame stabilization in a TVC. Table 1.1 summarizes a list of advanced studies which attempted to investigate physical mechanisms in this type of configuration. Despite the complexity of such a geometry, this combustor concept can be associated to several existing concepts: stratified combustion [217], backward-facing step stabilization [76], RQL combustion, etc. Note that studies listed in Tab. 1.1 have almost the same strategy:

- investigation of the inert flow topology with a passive cavity.
- addition of mass in the cavity with several injection systems to evaluate optimal operating conditions (in inert conditions).
- investigation of performances in reactive conditions.

Remarkably, almost all studies in Tab. 1.1 were carried out on stable operating conditions (e.g., free of combustion instabilities) and to our knowledge, only two studies mentioned the existence of combustion instabilities in this type of concept. Roquemoire [192] observed instabilities, primarily due to the location of the fuel injection systems in the cavity. However, no additional

information were provided on these stringent conditions. Hsu et al. [103] investigated the appearance of combustion instabilities when this combustor was operating next to LBO limits. He found that the combination of cavity dimensions and cavity air flow rate were the main parameters controlling the appearance of combustion instabilities. In addition, he argued that the coupling with the unsteady flow dynamics next to the cavity trailing edge could also drive self-sustained oscillations.

To our knowledge, no detailed investigations have been performed to assess mechanisms of combustion instabilities occurring in this type of combustor, under full load operating conditions. In fact, the aim of most TVC studies were to demonstrate the capability to be more efficient than actual combustors. Naturally, positive results were put in evidence whereas issues could have been eluded.

References	TVC Generation	Technique	Study
Sturgess and Hsu (1997) [215]	1 <sup>st</sup>	Exp	Indirect measurements of mainstream flow entrainment. Introduction of the momentum flux ratio between the cavity and the mainstream.
Katta and Roquemore (1998) [119]	1 <sup>st</sup>	CFD (RANS)	Effects of adding jet injection systems in a cavity on the flow dynamics. Determination of an optimum cavity size with an active cavity.
Katta and Roquemore (1998) [118]	1 <sup>st</sup>	CFD (RANS)	Reactive calculations using an optimal cavity size. No instabilities found.
Stone and Menon (2000) [212]	1 <sup>st</sup>	CFD (LES)	Study on mixing and location of combustion reaction zones.
Meyer et al. (2002) [162]	3 <sup>rd</sup>	Exp / CFD	Preliminary implementation of laser diagnostics and validation with numerical computations.
Rongshun and Weijun (2002) [191]	3 <sup>rd</sup>	Exp / CFD	Indirect measurements of mainstream flow entrainment. Effects of mainstream velocities, cavity jet injection systems and shape of struts.
Kumar and Mishra (2012) [129]	1 <sup>st</sup>	CFD (RANS)	Influence of the momentum flux ratio between the cavity and the mainstream on the flow structure.
Burguburu et al. [27]	1 <sup>st</sup> / 2 <sup>nd</sup>	Exp	Analysis of the combustion dynamics.
Merlin et al. [161]	1 <sup>st</sup> / 2 <sup>nd</sup>	CFD (LES)	Optimization of numerical models and parametric study in inert and reactive conditions.
Agarwal et al. (2013) [2]	3 <sup>rd</sup>	Exp / CFD (RANS)	Addition of inclined struts in the mainstream and effects on mixing.

Table 1.1: Advanced Studies on TVC (experimental and numerical). Exp: Experiments, CFD: Computational Fluid Dynamics. RANS: Reynolds-Averaged Navier-Stokes, LES: Large Eddy Simulation

## 1.3 Thesis Goals

### 1.3.1 CORIA laboratory research activities

With all reasons mentioned previously, lowering  $NO_x$  implies developing new combustors using lean burn technologies. However, designing such combustors requires new methodologies and robust tools. Flame stabilization in turbulent lean premixed (prevaporized) burners is one research activity which has been developed at CORIA for many years [221, 156, 225, 73, 160, 26, 43]. Note that investigations of such flames are performed with numerical and experimental tools on well-controlled academic burners.

In 2008, the laboratory developed and commissioned its own TVC. This work was supported by the European TECC-AE project (Technologies Enhancement for Clean Combustion in Aero Engines). The purpose of this collaborative work was to develop and validate lean combustion systems (injectors) in accordance with the ACARE 2020 recommendations. The staged combustion concept was extensively studied, with the development of new injectors and new architectures. Two PhD were completed on the TVC. Burguburu [26] led an experimental work, consisting in determining a global range of flame stability and relevant parameters which could be used for a fast early-design. The research strategy was similar to the one presented previously; that is, after a characterization of the inert flow structure, he investigated effects of several parameters in reactive conditions (i.e., staging strategy). An example of his results is given in Fig. 1.15

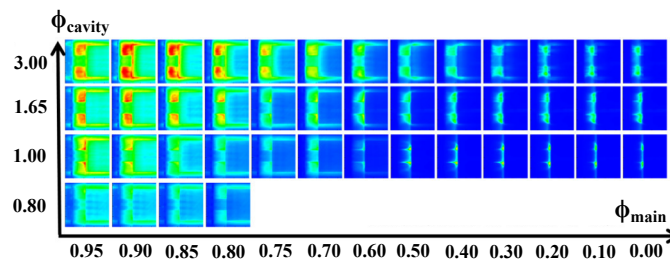


Figure 1.15: Example of a stability diagram. Mean  $CH^*$  chemiluminescence when the main and cavity equivalence ratios were varied (mainstream flow rate of  $20 \text{ g.s}^{-1}$ ). Reproduced from Burguburu [26].

Unfortunately, he observed for most of conditions the existence of strong thermo-acoustic

oscillations. An example of two opposite pressure spectra is shown in Fig. 1.16.

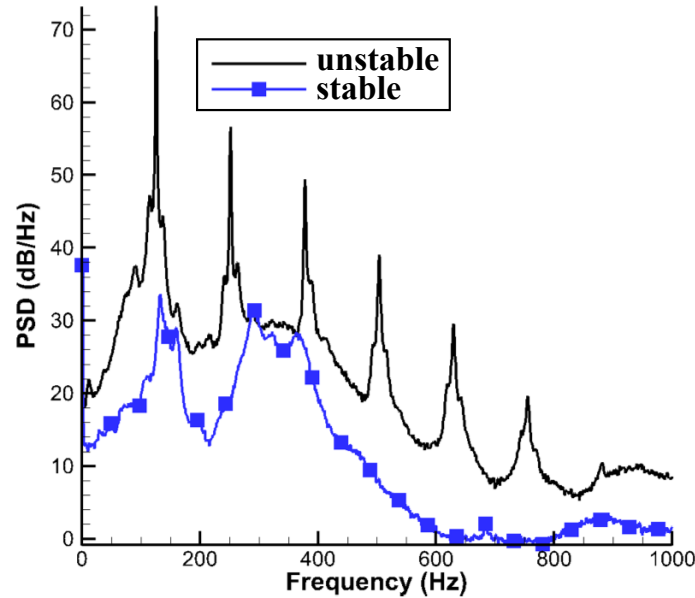


Figure 1.16: Comparison of pressure spectra for a stable and unstable operating conditions. reproduced from Burguburu [26].

Merlin [160] focused her study on developing an immersed boundary method to perform compressible flow calculations in complex geometries while keeping a structured code. Application of this method to cavities was motivated by the presence of several physical processes associated to different characteristic time scales (i.e., aerodynamics and acoustics, see Chap. 3). An example depicting the evolution of the source term of the energy equation is shown in Fig. 1.17.

TVC computations were performed in accordance with experimental tests of Burguburu [26]. Results put in evidence the existence of combustion instabilities, and an acoustic limit cycle. Flame dynamics was also studied in order to improve accuracy of turbulent combustion models. She finally demonstrated that pressure oscillations were directly related to strong variations of the progress variable and recommended (1) to improve stabilization methods by reducing the volume occupied by the flame, and (2) to generate more stable recirculation zones to reduce fluctuations of the progress variable.

The present study is related to these two previous PhD studies. While Merlin [160] and Burguburu [26] observed combustion instabilities and preponderant parameters controlling the combustor stability, we aim to have a more detailed physical understanding of the flame dynamics

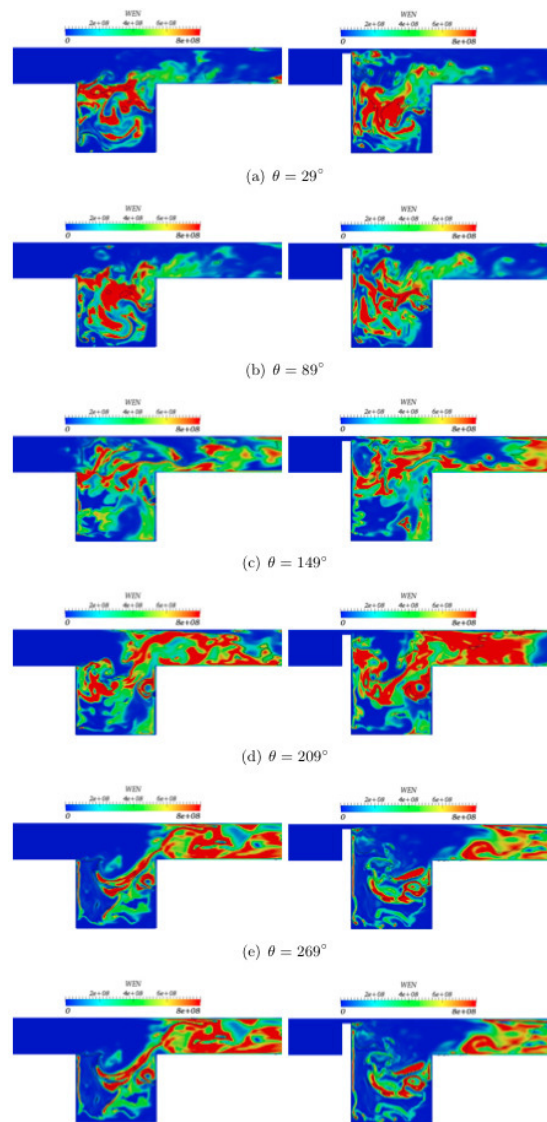


Figure 1.17: Instantaneous two-dimensional source term of the energy equation, for the unstable case. Reproduced from Merlin [160]

in this novel architecture and effects on flame stabilization.

### 1.3.2 Thesis framework

The present study is part of the intelligent design methodologies for low pollutant combustors for aero-engines European project (IMPACT-AE). It brings together a consortium of 18 partners (both industrials and academic institutions under the leadership of Rolls-Royce Deutschland) to lead a collaborative research for a 48 month period. It also supports the ACARE 2020 recommendations. The main objective is to develop and validate new tools to decrease substantially

development time cycles of promising concepts. With improved numerical models for heat transfers and  $NO_x$  production, it might be possible, from a preliminary rough combustor architecture to develop smart and complex low-pollutant engine architectures (see [50] for further details).

This study is part of the technical work package 4.3, which aims to provide detailed experimental database to validate these methods and tools. Note that Safran Snecma is performing numerical computations of this geometry<sup>3</sup>.

### 1.3.3 Thesis objectives and contents

The thesis objectives are:

- Understand flame dynamics and mechanisms leading to an efficient flame stabilization with a hot gas cavity-based flame holder. In fact, remarkably few papers [192, 103] are referenced on unstable conditions where the stabilization process is inefficient. It is then of great importance to obtain insights from these drastic conditions, to relate the unsteady heat release to any aerodynamic flow instabilities.
- With the detailed insights gained on the stabilization processes, extract some relevant parameters which could predict the flame stability and the corresponding stable range of operating conditions.
- Confirm *a posteriori* the different stabilizing mechanisms, and finally highlight benefits of this novel architecture.

A schematic illustration of our research strategy is shown in Fig. 1.18. The different chapters of the present study are recalled to give a clearer visibility to the reader.

Chapter 2 describes qualitatively one unstable operating condition. This chapter also introduces basic concepts of flame stabilization and their possible involvement in combustion instabilities. The different diagnostics are presented and then, a reconstruction of one cycle of instability is shown. Challenges are discussed as well as the research strategy adopted in the next chapters.

---

<sup>3</sup>Calculations should start in December 2014

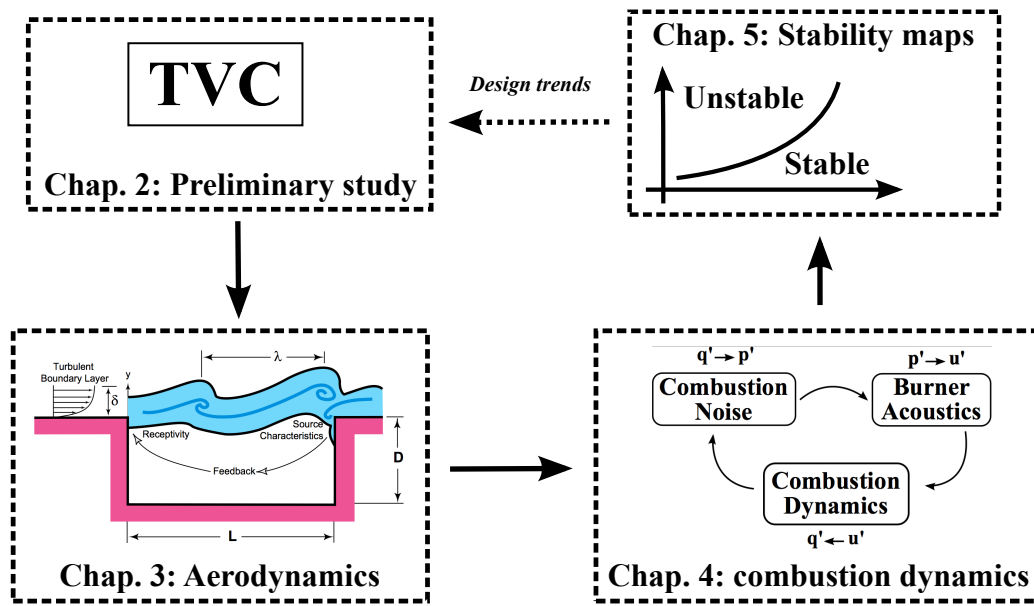


Figure 1.18: Schematic illustration of the thesis content.

From the preliminary analysis performed in Chapter 2, and because flows passing past cavities have been extensively studied in the literature, we separate physical contributions by considering only the inert flow dynamics. Chapter 3 is focused on the effects of direct mass injection in the cavity and the characterization of the shear layer region, initially used to mix hot gases from the cavity with the mainstream.

Because combustion instabilities can arise from a coupling between aerodynamic instabilities and the combustion process, Chapter 4 aims to gain information about the coupling and driving paths regarding the flame-flow-acoustic interactions in one unstable operating condition. For this reason, advanced coupled planar high-speed laser diagnostics are implemented to obtain temporal and spatial information. We then assess the contribution of acoustics with regards to turbulence levels, investigate the possible coherent structures responsible for these oscillations and resulting mass transfers between the cavity and the main channel. We finally propose a scenario for these combustion instabilities and the main parameters which may lead to a stable combustor.



Based on the detailed insights from previous chapters, Chapter 5 aims to determine some dimensionless parameters which could lead to smart and fast design rules. Effects of some parameters are globally investigated to validate conclusions of Chapter 4 and then, we present some control laws which may be suitable to predict the combustor stability. We discuss the validity of these findings and finally, we take advantage of these control laws to describe in details a stable operating condition.

## 1.4 Experimental setup of the CORIA-TVC

Because the geometry of the TVC is innovative in comparison to conventional combustors, this section gives a detailed description of the TVC. Note that the TVC was designed during the PhD of Burguburu [26].

### 1.4.1 Objectives and constraints

The experimental TVC burner was initially designed and built to have a full optical access and study fundamental mechanisms of flame stabilization. An academic-like combustor was therefore designed and commissioned with a maximum adjustable parameters. The combustor was integrated in an existing test-bench, which resulted in several constraints:

- Use of an existing test-bench, limiting the maximum power to 100kW.
- Use of an existing combustion chamber casing to control the absolute pressure. Thus, dimensions of the combustor were constrained to a maximum diameter of 80 mm and a maximum length of 250 mm.
- In order to obtain an axisymmetric burner and an optical access to implement laser diagnostics, the cavity was located in the inner part of the combustor, similarly to the 1<sup>st</sup> TVC generation (Fig. 1.9).

Previous section showed that many geometries were investigated in the literature, and that many parameters could be adjusted. In accordance with Hsu [104], injection systems within the cavity were unavoidable. In addition, several studies showed that the cavity flow structure presenting two counter-vortices was less sensitive to the location of injection systems and gave better performances at low combustor loads [192, 215]. An example is depicted in Fig. 1.19 and configuration (a) was chosen in the present study. Air injected from the downstream face of the cavity was primarily used to strengthen the double vortex topology but also cooled down the downstream cavity edge which was subject to high temperatures.

Use of circular jet rings within the cavity were replaced by slots in order to increase the burner axisymmetry. In addition, all injection systems were completely premixed in order to overcome issues related to *in situ* mixing; that is, fuel and air were mixed ahead of the combustor.

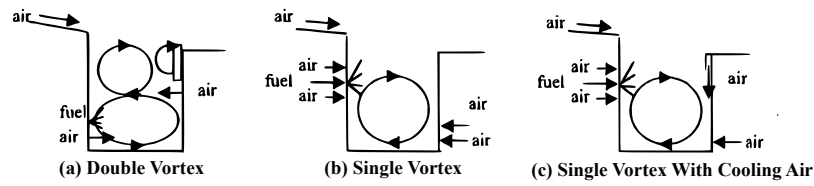


Figure 1.19: Schematic illustrations of different cavity injection systems resulting in different flow structures. Reproduced from Roquemore [192].

### 1.4.2 Description of the TVC

#### General overview

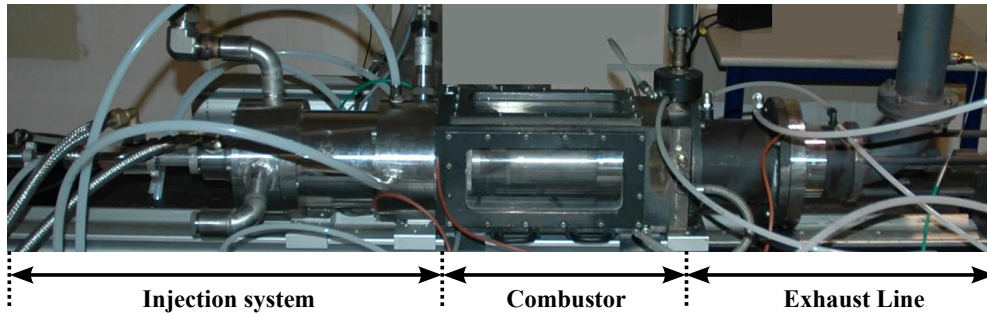


Figure 1.20: Photography of the test bench.

Figure 1.20 shows a photography of the entire test-bench which integrated the TVC combustor. It consisted of three portions:

- **Injection system.** It brought all fluids to the different injection systems, and included mixers and cooling water network. The mainstream injection system consisted in a stainless

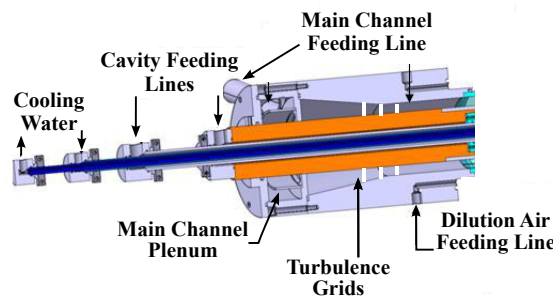


Figure 1.21: Schematic illustration of the injection system.

steel block with a circular air passage of 80 mm in diameter. The upstream part of the

combustor (orange piece in Fig. 1.21), named forebody, was inserted in this block and created an annular air passage for the mainstream flow, with an inner diameter of 59 mm and an outer diameter of 80 mm. Main air and fuel were premixed in a mixing box, upstream of the combustor and the mixture was tangentially discharged in a plenum (by means of three inlets). Three turbulence grids were added in the mainstream passage to break-up large structures.

The different cavity fluids were passing through the forebody. A stainless steel central shaft was made up of several tubes with several diameters. Annular passages between them were used to carry the different mixtures to the cavity (similar to Fig. 1.9). Two passages were used to circulate the cooling water (tubes with inner diameters of 6 mm and 8 mm). Two others were used for the two cavity injection systems (tubes with inner diameters of 16 mm and 25 mm).

- **Combustor.** Figure 1.22 depicts the combustor. It was located in a transparent quartz cylinder of inner diameter of 80 mm and 200 mm length, and made of Herasil to implement laser diagnostics.

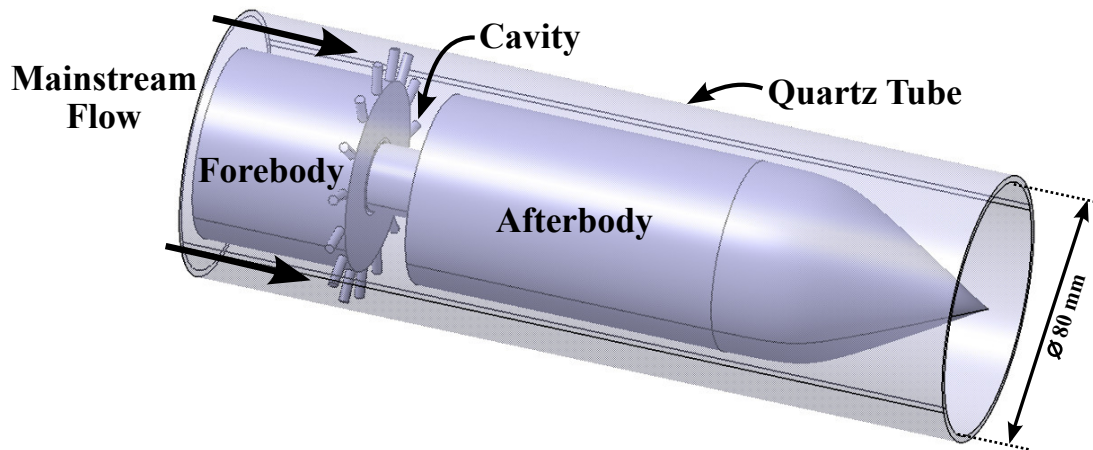


Figure 1.22: 3D Schematic illustration of the TVC

The combustor, which consisted of an assembly with cylindrical forebody and afterbody elements, had a diameter of 59 mm. A smaller tube passed through the forebody and was used to assemble the two pieces. In addition, this central shaft, made up of several tubes, was also used to carry fluids to the afterbody. At the end of the shaft was mounted an afterbody, primarily used to form the annular cavity. The cavity Length  $L_c$  was adjustable

by sliding the central shaft. In order to improve mass transfers between the cavity and the mainstream, a ring of 20 rods, each with a diameter of 3 mm, were positioned on the upstream cavity corner, and produced a blockage area of 23% in the mainstream. Wake regions produced by these secondary flame holders enabled to drain burned gases from the cavity to the mainstream. The cylindrical shape of these struts was chosen in order to obtain a blockage area which was not depending on the mainstream flow direction (e.g., with a swirl motion).

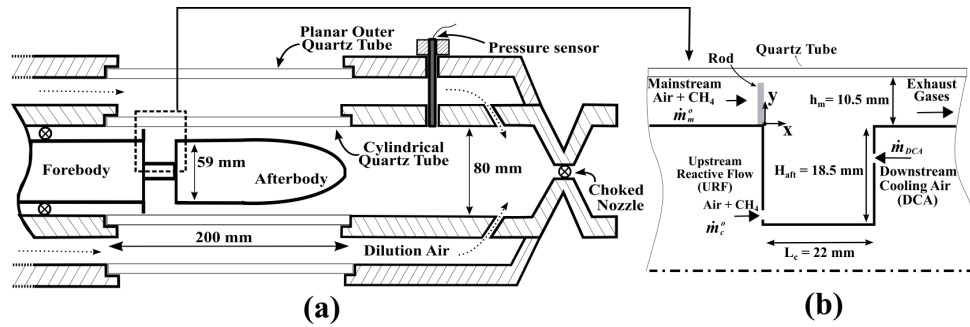


Figure 1.23: (a) Schematic representation of the experimental setup.  $\otimes$ : choked nozzle. (b) Details of the cavity region in the TVC ( $L_c = 22$  mm,  $H_{aft} = 18.5$  mm).

The quartz cylinder was surrounded by a second protective transparent casing equipped with planar quartz windows (Fig. 1.23 (a) and Fig. 1.24-left). To prevent from thermal and mechanical constraints, cold air was circulated in the gap between the casing and the cylindrical quartz tube. The cold air was finally injected through the combustor by means of dilution holes (located downstream of the burner) to cool down the exhaust gases (Figure 1.24-right).

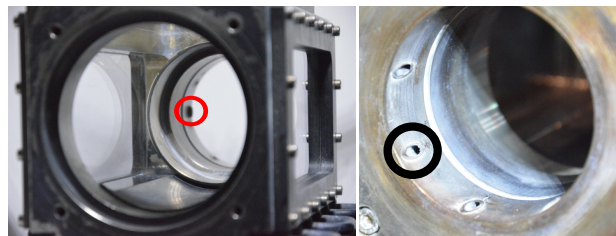


Figure 1.24: Photography of the combustion chamber casing. The TVC combustion chamber was inserted in the chamber. Left: view from the inlet. The red circle corresponds to the igniter location. Right: view from the rear. The black circle depicts one dilution hole used to gather cold air with burned gases.

The cavity region is shown in Fig. 1.23 (b). The mainstream flow consisted of a mixture of

air and methane ( $CH_4$ ) with a nominal air mass flow rate  $\dot{m}_m^o$  and a resulting equivalence ratio  $\phi_m$ . It flowed in the 10.5 mm high annular gap created between the forebody and the cylindrical quartz tube. Two injector systems were located inside the cavity. The upstream reactive flow (URF) injection system delivered a mixture of air and  $CH_4$  with a nominal air mass flow rate  $\dot{m}_c^o$  and an equivalence ratio  $\phi_c$ . This injection system was installed in the lower part of the upstream cavity face by means of a 1 mm annular slot. The DCA system discharged pure air by means of a 1 mm annular slot with a nominal mass flow rate  $\dot{m}_{DCA}$ . The latter was located on the downstream cavity face (8 mm below the cavity trailing edge). The injection system locations in the cavity were chosen in order to obtain a double vortex flow structure.

Table 1.2 summarizes the nomenclature used in this study.

Nomenclature	Correspondence	unity	Equivalence Ratio	
$\dot{m}_m^o$	main air mass flow rate	$g.s^{-1}$	$\phi_m$	$\phi_g$
$\dot{m}_m^F$	main fuel mass flow rate	$g.s^{-1}$		
$\dot{m}_c^o$	cavity air mass flow rate (URF)	$g.s^{-1}$	$\phi_c$	
$\dot{m}_c^F$	cavity fuel mass flow rate (URF)	$g.s^{-1}$		
$\dot{m}_{DCA}$	cavity air mass flow rate (DCA)	$g.s^{-1}$	-	

Table 1.2: Nomenclature used in the present study.

Table 1.3 gives the different surface area and the nomenclature used for the different bulk velocities.

Nomenclature	Correspondence	Unity	Surface area [m <sup>2</sup> ]
$U_m$	main bulk velocity	$m.s^{-1}$	$2.3 \times 10^{-3}$
$U_c$	cavity bulk velocity (URF)	$m.s^{-1}$	$7.6 \times 10^{-5}$
$U_{DCA}$	cavity bulk velocity (DCA)	$m.s^{-1}$	$1.4 \times 10^{-4}$

Table 1.3: Nomenclature used in the present study.

- **Exhaust line.** It was connected to the combustion chamber casing and carried burned gases to a vertical chimney (Fig. 1.25). A nozzle with a diameter of 20 mm and an adjustable valve were inserted in the exhaust line. This system was used to control the absolute pressure  $P_{glob}$  in the combustor. When the nozzle was choked (the valve was displaced with a stepping motor to vary the nozzle cross-section), the pressure adapted itself to ensure exhaust gases to flow normally. It also prevented from any external acoustic contributions coming from the chimney. Additional sonic nozzles were added in the main channel, at the entrance of the main plenum.

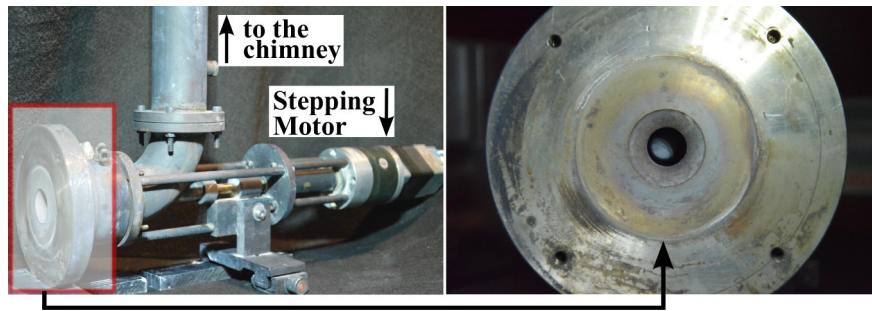


Figure 1.25: Details of the exhaust system. Left: overview. Right: sonic nozzle with the adjustable valve.

Figure 1.26 shows an overview of the TVC. In this study the cavity height was set to  $H_{aft} = 18.5$  mm, resulting in a cavity aspect ratio  $L_c / H_{aft} = 1.19$ .

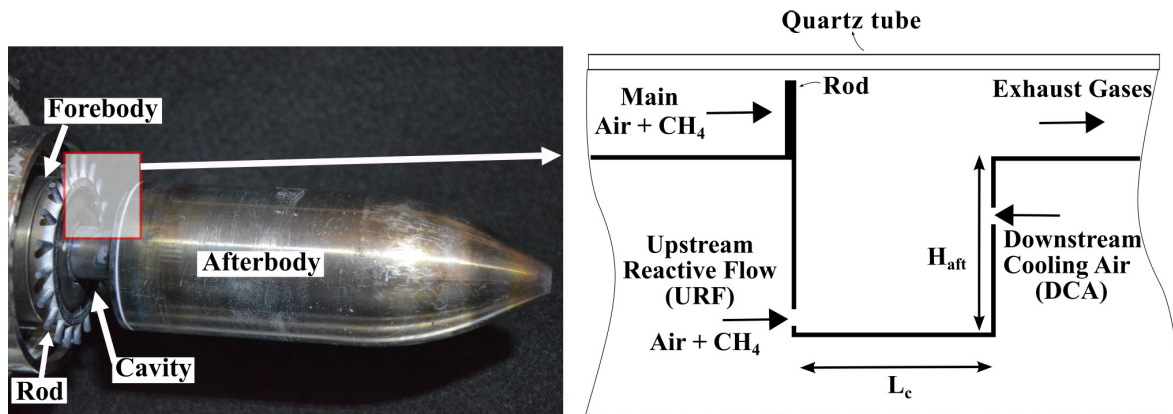


Figure 1.26: Left: schema of the TVC burner. right: details of the cavity region.  $H_{aft} = 18.5$  mm.

All mass flow rates were metered and controlled separately with six thermal mass flow controllers<sup>4</sup> (Fig. 1.27). A LabVIEW interface monitored all mass flow rates; that is, we were able to

<sup>4</sup>uncertainty of 1% when using the full scale.

set either the equivalence ratio, the air mass flow rate or the fuel mass flow rate of interests with a programmable ramp procedure. The mainstream air flow passed through an electric heater (nominal power of 18kW), and was monitored with a thermocouple located in the mainstream channel and by a proportional integral derivative (PID) controller. Absolute pressure  $P_{glob}$  was recorded with a static pressure sensor (Kistler 7061B ThermoComp) mounted on a waveguide system, 280 mm downstream from the cavity.

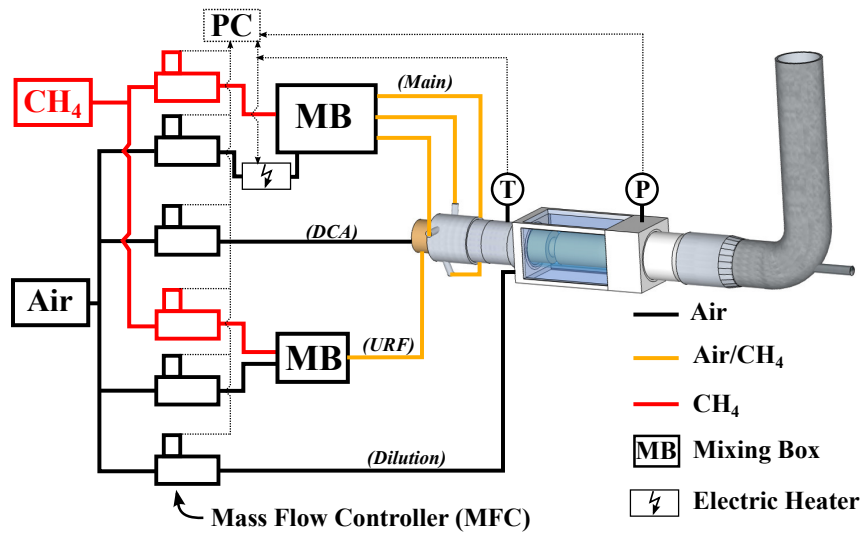


Figure 1.27: Schematic illustration of the TVC instrumentation



## Chapter 2

# Preliminary Investigation of Combustion Instabilities in a TVC

### Contents

---

<b>2.1</b>	<b>Background on flame stabilization and combustion instabilities . . .</b>	<b>34</b>
2.1.1	Flame stabilization in premixed flows . . . . .	34
2.1.2	Combustion instabilities . . . . .	39
2.1.3	Difficulty to predict combustion instabilities mechanisms . . . . .	44
<b>2.2</b>	<b>Diagnostics and Procedures . . . . .</b>	<b>45</b>
2.2.1	Acoustic measurements . . . . .	45
2.2.2	CH*-Chemiluminescence . . . . .	47
2.2.3	OH planar laser induced fluorescence (OH-PLIF) . . . . .	49
2.2.4	Phase-averaged measurements . . . . .	52
<b>2.3</b>	<b>Description of thermo-acoustic instabilities . . . . .</b>	<b>53</b>
2.3.1	Operating conditions . . . . .	53
2.3.2	Pressure Dynamics . . . . .	54
2.3.3	Combustion dynamics . . . . .	55
2.3.4	Flame Structure Dynamics . . . . .	58
2.3.5	Rayleigh Index Distribution . . . . .	60
<b>2.4</b>	<b>Concluding remarks . . . . .</b>	<b>62</b>

---

This chapter presents a general overview of combustion instabilities encountered in the present trapped vortex combustor (TVC). As mentioned in Chap. 1, extensive work has been performed on evaluating TVC performances to reduce pollutant emissions and to increase the range of flame stability. Remarkably, few studies have been focused on drastic operating conditions which could alter the combustor stability [192, 103].

In addition to recording numerous stable operating conditions, Burguburu and co-workers highlighted the existence of unstable operating conditions, associated with high-amplitude pressure oscillations [27]. Unfortunately, mechanisms leading to such conditions still need to be investigated. Therefore, this introductory chapter aims to:

- Provide a general background on flame stabilization and thermo-acoustics, with a focus on aerodynamic instabilities and possible interactions with heat release process.
- Introduce the different experimental tools and subsequent procedures used to characterize these instabilities.
- Present and discuss qualitatively one unstable operating condition in order to proceed with detailed measurements in Chap. 4.

The chapter starts with a review and challenges associated with flame stabilization in premixed combustion (Sec. 2.1.1). The presence of shear layers in real combustors naturally leads to combustion instabilities, which are introduced in Sec. 2.1.2. Section 2.2 describes the experimental setup, diagnostics and test conditions. Finally, we present a description of one combustion instability cycle and discuss the major phenomena encountered in the TVC (Sec. 2.3).

## 2.1 Background on flame stabilization and combustion instabilities

### 2.1.1 Flame stabilization in premixed flows

Because flow velocities in aero-engines are generally severe, special consideration is needed to determine conditions of flame stability. Flashback or blowoff are two critical examples arising

when the flame is not anymore stabilized [211, 91]. Specific methods are introduced to create a stabilization point/region in the burner and to ensure that the flame is spatially and temporally anchored.

### Diffusion vs. premixed flames

For clarity, we consider a laminar regime. A diffusion flame is defined as a flame in which the fuel and oxidizer are injected separately (non-premixed). Thus, the flame only develops in regions where enough mixing is achieved to obtain local stoichiometry. Because the internal structure of a laminar flame is greatly dependant on molecular diffusion, a diffusion flame cannot freely propagates [130], and mixing in the combustor is then critically important, (especially for pollutant emissions).

In contrast, a premixed flame consists in a premixed mixture of fuel and oxidizer entering the combustor. In this regime, the flame can freely propagate towards the fresh mixture, and mixing does not play a significant role. However, the flame location is much more difficult to predict (even more in turbulent conditions), and several studies showed that small disturbances in the incoming flow can tremendously affect the flame structure [39] and the resulting heat release rate. In real combustors, two-phase flows and separate injection systems lead to the existence of these two regimes in the primary zone, as depicted in Fig. 2.1. Because premixed flames have the advantage to suppress gas composition inhomogeneities in the combustor, this regime is described in the rest of this section.

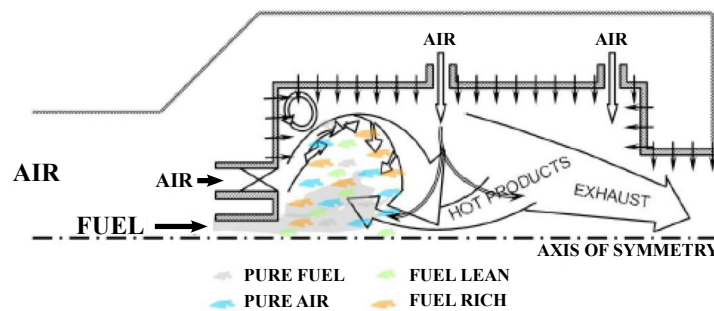


Figure 2.1: Combustion regimes in an aero-engine. Reproduced from [197].

### Basic concept: kinematic balance between flow and flame velocities

Kinematic balance between flow and flame speeds is the key element in premixed flame stabilization. A schematic illustration of three conditions is given in Fig. 2.2. If the flow velocity  $u_f$  exceeds the flame speed  $S_f$  (Fig. 2.2 (a)), the flame will blow off. In contrast, if the flame speed  $S_f$  exceeds the flow velocity  $u_f$ , the flame will propagate upstream (flashback, Fig. 2.2 (b)). When the flow velocity equals the flame speed, the flame will remain spatially located [139, 115]. Note that the present comments are focused on ideal planar laminar burning velocities but the same concept applies for real turbulent flames.

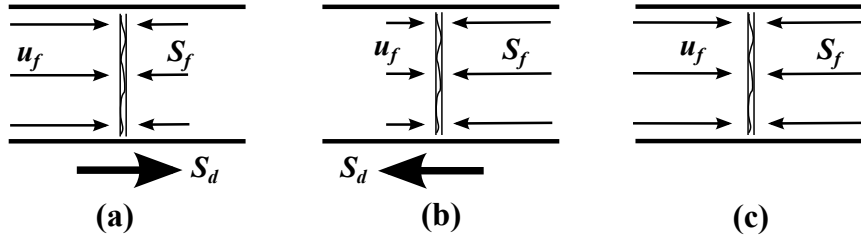


Figure 2.2: Schematic illustration depicting effects of kinematic balance between flow and flame velocities in a planar premixed flame propagating in a tube: (a) blowoff when  $u_f > S_f$ , (b) flashback when  $u_f < S_f$ , (c) stabilized when  $u_f = S_f$ .

### Common flame stabilization flow configurations in combustors

In order to obtain a good flame stabilization process, specific flow configurations are required in high-velocities combustors to balance flow and flame velocities. Shear layers (or mixing layers) are commonly used in combustors because mass, momentum, energy, and chemical species exchanges are favorable. But these flow configurations are intrinsically unstable (see Sec. 3.1.1). A basic example of a mixing layer is shown in Fig. 2.3(a) and consists in two merging streams, with different velocities and/or composition. The top flow could consist of premixed fresh gases and the bottom flow of hot products. Fluid entrainment, resulting from Kelvin-Helmoltz (KH) instabilities (described in Sec. 3.1.1) creates a mixing region which is accompanied by vortex shedding and vortex pairing processes. The latter are responsible for heat release oscillations [40] and proves that aerodynamic instabilities in reactive flows can result in combustion instabilities. Detailed studies showed that vortex shedding was an indirect source of combustion unsteadiness. In fact, vortices contribute to the entrainment process by engulfing pockets of gas whereas

turbulent mixing, primarily due to secondary instabilities, is responsible for mixing and heat release oscillations [121]. A brief and non-exhaustive list of practical methods commonly used in real combustors is provided hereafter:

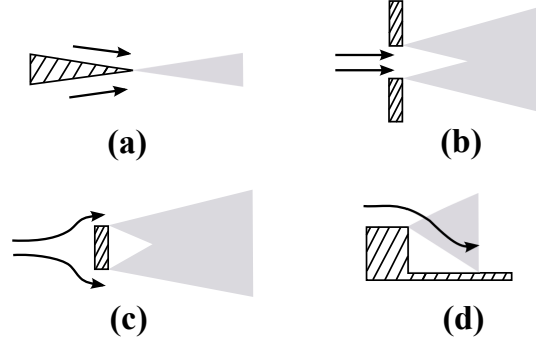


Figure 2.3: Schematic illustration of different methods used to stabilize flames. (a) splitter plate, (b) jet, (c) bluff body, (d) backward-facing step. Shear layer regions are depicted in gray.

- **Jets.** A large variety of jets are encountered in combustors, such as annular, coaxial, in cross flow, swirl, or featuring more complex features [89]. Separating shear layers develop from the exit of the jet, grow, and intersect; they can contribute to mixing with the ambient and with low-velocity recirculation zones of burned gases. Jets can be unstable with sufficient counterflow [106] or when heated [165], which is mostly the case in combustion applications. Jets are also subject to KH instabilities but other phenomena are encountered. Several important secondary instabilities occur far downstream of the injection location and makes the jet to become rapidly three-dimensional and even disorganized [238].

Jet in cross-flow is another application of great importance, especially in RQL combustors [138] or for wall-cooling engineering processes [137]. Velocity or momentum flux ratios of the jet to cross flow are conventional parameters which best describe this flow configuration [116, 209]. However, the detailed structure of a jet in cross-flow is relatively complex. In fact, many instabilities are present and interact each others. Figure 2.4 depicts a schematic illustration of a jet in cross-flow as well as the different vortices. The near-field of the shear layer between the jet and the cross-flow dominates the creation of counter-rotating vortices in the jet as well as horseshoe vortices around and in the wake of the jet [122].

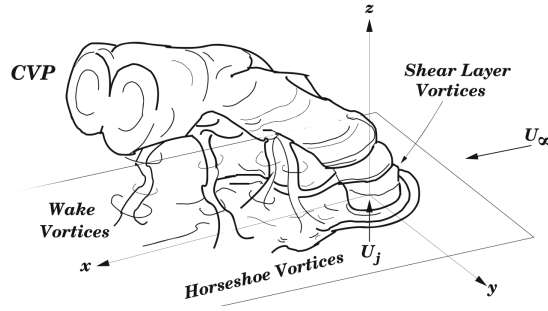


Figure 2.4: Schematic illustration of a jet in cross-flow structure, including the counter-rotative pair (CVP). Reproduced from Fric and Roshko [74].

- Bluff body and wakes.** Bluff bodies are used to create an artificial flow separation [151]. Wake regions are favorable for a flame to be anchored because of low-velocities and enhanced mixing. A schema is provided in Fig. 2.3(c) and depicts a rectangular piece inserted in the flow. Two shear regions are created behind the piece but the flow topology is more complex. Several stagnating vortices are established behind the bluff body. Even if shear regions are effectively present next to the bluff body trailing edge, an asymmetric vortex shedding process, referred to as Bénard von Karman (BVK) instability occurs far downstream and enables large fluid entrainment [181]. The frequency of the BVK instability is related to the Strouhal number and varies according to the bluff body shape (cylinder, "v-gutter", sharp edge, flat plate, etc.) [12].
- Swirl flows.** Swirl motion is commonly used in gas turbines to stabilize and ignite flames. It consists in providing an angular velocity to the axial incoming flow and to produce a central recirculation zone which provides the main flame stabilization mechanism. The swirl number [81] quantifies the ratio between the angular and axial momentum (cf. Eq. 1.1). However, several instabilities are associated with this complex flow topology. Remarkably, several authors pointed out the fact that all physical mechanisms highlighted were configuration specific [141, 105]. Because of the velocity gradient between the incoming flow and the ambient, KH instabilities develop in the shear layer regions, but classical mechanisms leading to the production of coherent structures are different in swirl flows: the combination of the azimuthal velocity and centrifugal instabilities leads to complex helical instabilities [227]. Vortex breakdown is another instability which occurs in the core of the flow, especially for high number swirl flows [83]. The precessing vortex core (PVC)

is also encountered in turbulent swirl flows, and is primarily due to the precession of the central vortex core around the injector axis [219]. Additional information can be found in [105].

- **Backward-facing steps and cavities.** These flow configurations are the subject of the present study but can be also found in dump combustors. Recirculation zones are created by a sudden expansion (e.g., entrance of the flow in the combustor). Particularity of these configurations is the reattachment of the shear layer on the outer wall, which induces a backflow recirculation zone serving as a stabilization source. Instabilities in backward-facing steps are driven by vortex shedding at the leading edge, which can greatly affect the recirculating region, behind the step [167]. The same applies for cavities but presence of the cavity trailing corner changes mechanisms leading to self-sustained processes (discussed later in Chap. 3).

To conclude, we showed in this section that many configurations used to stabilize flames in combustors were associated with a variety of aerodynamic instabilities. Coupling of these instabilities in inert conditions is not trivial and addition of heat release can lead to unsteady, drastic, and undesired phenomena, referred to as combustion instabilities.

## 2.1.2 Combustion instabilities

### Introduction and historical overview

Combustion instabilities denote large-amplitude sustained oscillations of one or several acoustic modes. In that case, instabilities are excited by a feedback loop between the combustion process itself and acoustic modes of the combustor. Occurrence of large-amplitude pressure and velocity oscillations result in severe operating conditions: high levels of vibration, inefficient heat transfers, mechanical loads, flashback, blowoff, or increased pollutant emissions. These undesired phenomena may also reduce the system lifetime (see [142] for case studies). Figure 2.5 depicts a classical schematic illustration of the different processes involved in combustion instabilities.

Fluctuations in velocity, temperature, pressure, or equivalence ratio induce a fluctuation in the heat release process (driving mechanisms). In turn, a feedback mechanism couples to these

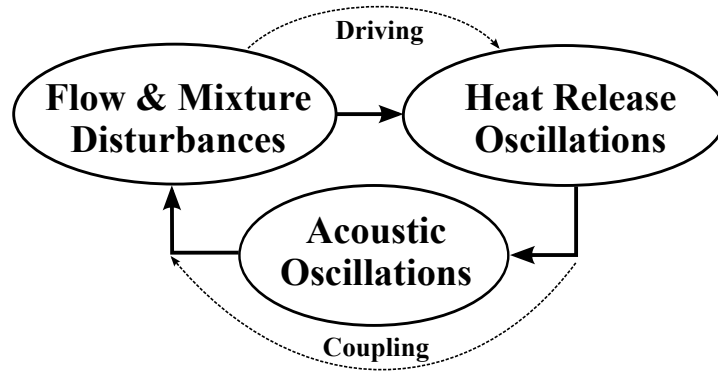


Figure 2.5: Schematic illustration of processes involved in combustion instabilities.

heat release oscillations, generates additional fluctuations and finally leads to a resonant self-sustained process. The feedback mechanism usually originates from pure acoustics; that is, heat release oscillations excite one or several natural acoustic modes of the combustor. However, oscillations may sometimes be associated with other mechanisms, such as convection processes (entropy waves) [166]. Because acoustic oscillations are excited by a thermal effect (combustion but also temperature gradients [218]), the observed phenomena are also named thermo-acoustic instabilities.

The first observation of these oscillations is attributed to Jones [109], who studied flames placed in tubes. Subsequent motivations appeared with the advent of large combustion systems, such as boilers, oil, and coal gas turbines [183]. Later, combustion instabilities have been encountered in liquid-fuel rockets; The F-1 engine that powered the Saturn rocket during the Apollo program exhibited pressure oscillations with an amplitude of the order of 138 bars! Similar observations were encountered in solid-propellant rockets [13], ramjet missiles, afterburners [46], and more recently with the advent of lean premixed combustors in aero-engines and gas turbines [142].

### Existence of combustion instabilities: acoustic energy balance

Because several processes are involved in the development of combustion instabilities, it is of great importance to predict the apparition of such phenomena. The coupling between heat release oscillations and pressure fluctuations can be explained with the acoustic energy bal-



ance [178], defined as

$$\frac{\partial e}{\partial t} + \nabla \cdot f_a = r, \quad (2.1)$$

where  $e$  is the local acoustic energy,  $f_a$  is the local flux term, and  $r$  is the local source term. The source term  $r$  in Eq. 2.1 is

$$r = \frac{\gamma - 1}{\gamma P_{glob}} p'(x, t) q'(x, t), \quad (2.2)$$

where  $P_{glob}$  is the mean pressure,  $p'$  is the fluctuating pressure,  $q'$  is the unsteady heat release, and  $\gamma$  is the polytropic index. Integration of Eq. 2.1 over the whole volume of the combustor  $V$  and over a period of oscillation  $\tau$  gives

$$\frac{d}{dt} \frac{1}{V} \int_V \frac{1}{\tau} \int_t^{t+\tau} e dt dV + \underbrace{\oint_A \left( \frac{1}{\tau} \int_t^{t+\tau} f_a dt \right) \cdot \vec{n} dA}_{\mathcal{F}} = \underbrace{\frac{1}{V} \int_V \frac{1}{\tau} \int_t^{t+\tau} r dt dV}_{\mathcal{R}}. \quad (2.3)$$

$\mathcal{R}$  represents the volume and period-averaged term source in Eq. 2.3 and can be written as

$$\mathcal{R} = \frac{1}{V} \int_V \frac{1}{\tau} \int_t^{t+\tau} \frac{\gamma - 1}{\gamma P_{glob}} p'(x, t) q'(x, t) dt dV. \quad (2.4)$$

Note that in Eq. 2.4, the coupling between  $p'$  and  $q'$  is important because it determines if energy is added to the system. Lord Rayleigh first stated the conditions under which an oscillatory heat-release process adds energy to the acoustic field [186], i.e.,

$$\mathcal{R} > 0. \quad (2.5)$$

Note in Eq. 2.5 that this criterion implies that if the pressure and the heat release oscillations are in phase (or within a  $\pm 90^\circ$  confidence interval), the term  $\mathcal{R}$  acts as a source term.

To conclude, occurrence of combustion instabilities results from a great coupling between pressure and heat release oscillations. This coupling can be also summarized with the Rayleigh

criterion. However, even if  $\mathcal{R} > 0$ , it does not necessarily lead to an unstable combustor. In fact, the energy added to the system must exceed losses, i.e.,  $\mathcal{R} > \mathcal{F}$  in Eq. 2.3 (primarily through boundaries). Because the estimation of losses is extremely difficult in complex geometries, the Rayleigh criterion is commonly used to assess the preponderance of the acoustic-combustion coupling.

Note that previous equations are valid in the linear regime; that is, the amplitude of instabilities must be reasonable (i.e.,  $p' < P_{glob}$ ). Note that models developed in linear regimes are useful but cannot be used anymore when amplitude of oscillations becomes large. In fact, during the appearance of combustion instabilities, the linear growth is controlled by the driving and damping processes, and an instability successfully grows for  $\mathcal{R} > \mathcal{F}$ . In contrast, when finite amplitudes are reached (e.g., instability growth rate almost null), non-linear processes are preponderant and the so called acoustic limit-cycle is attained [178, 142]. Many processes are nonlinearly dependant on the instability amplitude: convective terms in the Navier-Stokes equation, pressure-density relationship, non-linear processes occurring next to boundaries, etc. [45]. Many workers have considered non-linear processes in order to improve mathematical modeling and subsequent numerical computations [240]. However, most of the experimental data are obtained during the acoustic limit-cycle period. Thus, classical criteria (Rayleigh or Chu [36]) have to be used with care when analyzing results. **Note that in this study, we only performed measurements during the acoustic limit-cycle period and used criteria derived from linear theory to assess these combustion instabilities.**

### Causes of instabilities

The Rayleigh criterion relates pressure to heat release oscillations. However, the coupling path between heat-release and acoustic oscillations may involve complex processes. Ducruix et al. [53] argued the difficulty to determine the driving path between heat release and acoustic oscillations, and the coupling path between acoustic and heat release fluctuations. Candel gave a schematic illustration of the different possible interactions leading to combustion instabilities [29]. For instance, the coupling path can involve other processes, such as convection (entropy waves

reaching a nozzle, see [155]). Several fundamental coupling processes causing self-sustained oscillations have been highlighted and some of them are presented hereafter:

- **Equivalence-ratio oscillations.** Production of large-amplitude pressure oscillations in the combustor propagate in the upstream premixer section and may affect the air or fuel flow rates<sup>1</sup>. Thus, the reactive mixture entering the combustor is convected into the flame with an oscillatory equivalence ratio, and finally produces heat-release oscillations. Note here that both acoustic and convection processes are involved in the mechanism: the convection time needed to transport a disturbance into the flame as well as the coupling with acoustic modes of the combustor play important roles [41, 145]. Moreover, equivalence ratio oscillations have a greater effect in the lean regime because of larger flame speed variations, and consequently larger displacements of the flame front [146].
- **Vortex-flame interactions.** Flame stabilization methods described in Sec. 2.1.1 always imply presence of KH instabilities due to the presence of shear/mixing layers [187]. When these vortices are formed and shed (assuming that they consist of unburned gases), they entrain burned gases while being convected, ignite, and thus lead to sudden heat release oscillations. Vorticity oscillations, which are primarily due to aerodynamic instabilities can either induce flame area oscillations or directly affect mixing in the combustor [203, 177].
- **Entropy waves.** In this case, oscillations are not directly related to acoustics. In fact, unsteady combustion produces hot-gas pockets which are convected by the mean flow (entropy waves). The impact of an entropy wave on a nozzle can produce combustion noises and pressure waves, which finally travel upstream [155, 140]. This phenomenon is then based on a convective-acoustic phenomenology.
- **Flame-Area oscillations.** Variations of the flame area produce heat-release oscillations. Origins are numerous: aerodynamics and related instabilities can stretch the flame front whereas boundaries can also elongate the flame surface area [226, 56].

---

<sup>1</sup>propagation of acoustic waves in the premixer can also affect atomization of the liquid fuel and thus, affect the evaporation of droplets [44].

## Damping Processes

As mentioned in Sec. 2.1.2, dissipation processes (loss of acoustic energy through the combustor control volume) are critically important because they determine the existence of combustion instabilities. Three processes can be highlighted:

- **Walls and flow separation:** thermal and viscous effects dominate near walls. Thus, part of the incoming acoustic energy is converted into entropic or vortical fluctuations so that reflected acoustic waves have lower energies [142]. Recent studies even showed that wall temperatures had an important impact on the development of combustion instabilities [158].
- **Combustor boundaries:** acoustic energy can leave the system through inlets/outlets of the combustor (acoustic radiation) [213]. The dependence with the Mach number is quite important because it accounts in the reflexion coefficient amplitude [107].
- **Acoustic energy mode transfers:** because non-linear processes are preponderant during the acoustic limit cycle, transfer of acoustic energy from one excited mode to another one can lead to dissipation. These transfers are various; that is, they can occur from one specific tone to harmonics, or they can also be spectrally broadened [144].

### 2.1.3 Difficulty to predict combustion instabilities mechanisms

Studies in combustion instabilities are really challenging because they gather together several physical phenomena. However, coupling of several processes, which are time dependant (i.e., linear vs. limit-cycle regimes) makes the prediction of combustion instabilities in real gas turbines difficult.

Prediction of instability frequencies and their spatial structure is now quite easy because of the use of linear dynamics theory and the advent of numerical computations (e.g., Helmholtz solvers) [52].

Understanding of coupling and driving paths in the development of combustion instabilities is much more difficult because it requires information on the flow and mixture dynamics [29, 54].

Finally, acoustic limit-cycle physics involve non-linear processes and modeling these processes is

still a challenge nowadays [6, 170, 112].

In the next sections, we will qualitatively describe one combustion instability cycle (based on Burguburu experiments [27]) in order to gain preliminary insights about the possible mechanisms driving these drastic operating conditions (discussed in Chap. 4). We also introduce several diagnostics which are used to assess acoustics, heat release oscillations, and flame dynamics.

## 2.2 Diagnostics and Procedures

This section describes the different techniques used to characterize combustion instabilities. The phase-averaged procedure is also introduced and aims to reconstruct a cycle of instability with help of non time-resolved diagnostics.

### 2.2.1 Acoustic measurements

#### Pressure recordings

Pressure data were recorded using a dynamic piezoelectric pressure sensor (Kistler 7061B ThermoComp) operating with a range of measurements from 0 to 250 Bar, a sensitivity of 80 pC.Bar<sup>-1</sup>, and a natural frequency of 45 kHz. Because of the extreme temperatures in the combustor, the pressure sensor was mounted on a cooled-waveguide system (Fig. 2.6-left) 280 mm downstream from the cavity region. In order to prevent from any acoustic reflexions, the pressure sensor was flushed-mounted on a constant cross-section area pipe, and acoustic waves dissipation was achieved through a pipe of 10m in length, located downstream of the heat exchanger.

The pressure sensor was connected to a charge amplifier (Kistler 5011) with a scale of  $2 \cdot 10^{-2}$  bar/V. Two filters were integrated in this module: a low-pass filter with a cutoff frequency of 30 kHz was primarily used to suppress the natural frequency of the sensor, and a high-pass filter with a time constant of 0.1s removed the signal deviation during experiments. In addition, we daily corrected the voltage output signal deviation (scaled between 0 and 10 V), which was recorded on an acquisition card (National Instruments NI9201) controlled by the LabVIEW

software.

### Phase-shift correction

The location of the pressure sensor induced two phase shifts; that is, between the pressure produced in the cavity (main region of interest) and the location of the waveguide system 280 mm downstream, and between the parietal pressure of the combustor and the sensor location. These two shifts, assumed to be primarily due to acoustics, are depicted in Fig. 2.6-right and can be written as

$$\tau_{p'} = l_h/c_h^s + l_c/c_c^s. \quad (2.6)$$

$l_h$  is the distance between the cavity region and the location of the waveguide system,  $l_c$  is the distance between the entry of the waveguide system and the sensor location,  $c_h^s$  is the mean sound speed in the combustor, and  $c_c^s$  is the mean sound speed in the waveguide pipe. The two temperatures ( $T_h$  and  $T_c$ ) associated to the corresponding sound speeds were critically important to the characterization of thermo-acoustic oscillations. To calculate the sound speed in burned gases, we set the temperature  $T_h$  at 1700K in accordance with numerical computations of Merlin [160]. We also assumed that thermal equilibrium of the cooling system was reached (i.e.,  $T_c \approx 300\text{K}$ ). Table 2.1 summarizes parameters used to perform the temporal correction.

$l_h$	280 mm	$T_h$	1700K	$c_h$	818 m/s
$l_c$	20 mm	$T_c$	300K	$c_c$	344 m/s

Table 2.1: Details of parameters used to correct pressure records.

Sensitivity analysis showed that an estimation of temperatures with an uncertainty of  $\pm 400\text{K}$  led to an uncertainty of the order of  $1^\circ$  (taking the first acoustic period as a reference, see below).

### Spectral Analysis

A 5kHz acquisition rate was implemented and each record lasted for 60s. The power spectral density (PSD) distribution was calculated with the Welch algorithm [230]. We performed a sensitivity analysis in order to choose the best parameters; 300 windows with a 20% overlap, each windowed with a Hamming function. The final frequency resolution was  $\pm 5\text{Hz}$ . We checked

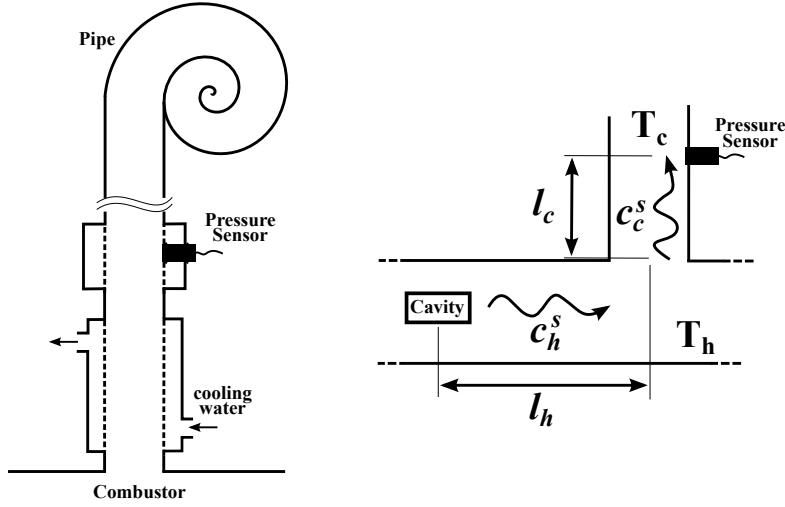


Figure 2.6: Left: schematic illustration of the waveguide system. Right: schema depicting the phase shift between the pressure produced in the cavity and pressure measured by the sensor.

that our signal processing was accurate by calculating the Parseval equality (for power), defined as

$$\lim_{\tau \rightarrow \infty} \frac{1}{\tau} \int_{-\tau/2}^{\tau/2} p'(t)^2 dt = \lim_{\tau \rightarrow \infty} \frac{1}{\tau} \int_{-\infty}^{+\infty} p'_{FFT}(f) p'^*_{FFT}(f) df. \quad (2.7)$$

$\tau$  is the characteristic period of the phenomenon of interest,  $p'(t)$  is the unsteady pressure trace, and  $p'_{FFT}(f)$  is the Fourier transform of  $p'(t)$ . Equation 2.7 gave an average error less than 2%. Finally, all measurements were scaled in sound pressure level (SPL in dB/Hz), i.e.,

$$SPL = 20 \log_{10} \left( \frac{\sqrt{G(f)}}{P_{ref}} \right), \quad (2.8)$$

where  $G(f)$  is the one-sided PSD, and  $P_{ref} = 2 \cdot 10^{-5}$  Pa is a reference acoustic pressure.

### 2.2.2 CH\*-Chemiluminescence

Vomume averaged heat release oscillations  $q'(t)$  were estimated by recording the spontaneous emission of the flame (or chemiluminescence).

## Background

Chemiluminescence is radiation naturally emitted by excited molecules  $M^*$  which spontaneously return to a lower energy state:



where  $h$  is the Planck's constant, and  $\nu$  is the emission frequency of the photon. The latter is characteristic of the molecule and transition it undergoes. Historically, Clark [38] first reported chemiluminescence measurements in flames and attempted to correlate these data to experimental variables. This ground work focused on four types of chemiluminescence:  $OH^*$ ,  $CH^*$ ,  $CO_2^*$ , and  $C_2^*$ , which are still commonly used nowadays in combustion studies. In fact, these radicals are found in flame regions and the chemiluminescence signal can be used as a rough estimator of heat release (assuming a premixed flame with a constant equivalence ratio) [182, 171, 87, 88]. More recent studies even showed a relation between the chemiluminescence signal and the location of the flame front [204]. However, Haber et al. mentioned that quantitative correlations between chemiluminescent measurements and heat-release were not obvious [82]. For instance, Najm et al. [168] pointed out that chemiluminescent analysis was limited under very high strain and high curvature flow regimes. In this study, two intrinsic issues made the analysis of the chemiluminescence delicate:

- The complex flame structure encountered in a TVC did not guarantee that the all reactants were burned through the flame front (in contrast with a conical bunsen flame). Thus, spatial analysis of chemiluminescence signal had to be considered with care.
- The equivalence ratio stratification between the cavity and the mainstream induced non-uniform local equivalence ratio, which was more difficult to analyze.

It was then impossible to directly correlate the chemiluminescence signal to heat-release oscillations. **Keeping in mind about this bias and for clarity, we use the term *heat release* in next sections.**



## Experimental setup

CH\* chemiluminescence was recorded on an intensified coupled charge device (ICCD) PI-MAX2 camera, with a resolution of  $512 \times 512 \text{ pix}^2$  and an acquisition rate of 10Hz. A visible lens (Nikon f/1.4 50mm) was equipped with a band-pass colored filter (Schott BG12), corresponding to the  $A^2\Delta^+ \leftarrow X^2\Pi$  CH\* transition ( $\lambda_{CH^*} = 431.4 \text{ nm}$ ).

### 2.2.3 OH planar laser induced fluorescence (OH-PLIF)

Location of burned and unburned gases was achieved with the OH-PLIF laser technique and by recording the OH fluorescence.

## Background

Fluorescence is the radiative deactivation of excited molecules through photon emission. Unlike chemiluminescence, laser-induced fluorescence (LIF) uses a laser excitation to populate the upper energy level state. The wavelength of the laser is tuned in accordance with a discrete transition of the molecule of interest [58, 125]. Several softwares can predict excitation and emission spectra<sup>2</sup> of molecules in order to adopt the best excitation/detection strategy. Note that these softwares can reproduce some biases of the experimental setup. Detailed information can be found in Appendix A.

### Strategy for OH fluorescence measurements

Optimization of the fluorescence signal was critically important. The strategy was three-folds:

- select an excitation wavelength in order to obtain a fluorescence signal less sensitive to the experimental conditions (i.e., temperature, pressure, and gas composition fluctuations).
- select a spectral range of fluorescence detection to improve the signal-to-noise ratio.

<sup>2</sup>These two names may be confusing. Excitation spectrum is obtained by measuring the fluorescence signal as a function of the laser wavelength. In that case, the signal is related to a specific transition of the molecule. In contrast, emission spectrum originates from a specific laser-excited state dispersed in a monochromator. Such dispersed fluorescence contains spectroscopic information (beyond the scope of our study) and can be used to adopt a collection strategy. Additional information in [59].

- minimize the scattered light by separating the fluorescence emission from the laser wavelength.

Because thermo-acoustic oscillations were investigated, the excitation wavelength and the corresponding fluorescence signal had to be as less sensitive as possible with temperature variations. The  $Q_1(5)$  ro-vibronic transition of the  $A^2\Sigma^+(\nu' = 0) \leftarrow X^2\Pi(\nu'' = 1)$  band ( $\lambda_{exc.} = 282.75\text{nm}$ ) was selected in accordance with Bresson [22]. This transition had the advantage to be isolated with regards to the excitation spectrum and facilitated the laser tuning procedure. Note that several studies already investigated benefits of this transition [4, 85]. We adopted a broadband collection strategy from 308 to 330 nm ( $\Delta\nu = 0$ ), which facilitated spectral filtering of the laser excitation  $\lambda_{exc.}$

## Experimental arrangement

A 10Hz Nd:Yag spectra physics laser operating at 532 nm with an average power of 1.7W, was used to pump a tunable dye laser (Sirah) supplied with Rhodamine 590 dye. The resultant output pulse energy was 15 mJ in the probe volume<sup>3</sup>. We made regularly adjustments to the excitation wavelength  $Q_1(5)$  using a laminar premixed  $CH_4$ /air flame. The resultant laser beam was expanded through a set of fused silica lenses (spherical  $f_1 = 500\text{mm}$ , cylindrical concave  $f_2 = -12.5\text{ mm}$ , cylindrical convex  $f_3 = 300\text{ mm}$ ) to form a collimated laser sheet of 30 mm in height. Fluorescence was collected on a 16 bits Intensified Coupled Charge Device (ICCD) PI-MAX3 with a resolution of  $512 \times 512\text{ pix}^2$  (a  $2 \times 2$  pixel binning was used to increase the signal-to-noise ratio). A Cerco f/1.4 45mm UV lens was mounted with an assembly consisting of a high-pass (Schott WG305) and a band-pass (Schott UG11) colored optical filters.

## OH image processing: flame front extraction

A pre-processing was applied to normalize raw images. The classical pre-processing steps were divided into two steps:

- **Background correction.** Reflexions (mainly due to elastic scattering) and electronic

---

<sup>3</sup>We performed tests at ambient temperature in order to evaluate losses through the two successive quartz windows. We assume that the temperature does not affect the transmittance yield.

noise from the camera intensifier were subtracted by averaging 300 images, recorded when the experiment was switched off.

- **Laser-sheet profile correction.** Because the laser beam had a non-homogeneous energy distribution, the resulting signal fluorescence was artificially modulated. To correct from these spatial energy variations, we filled the region of interest with a homogeneous mixture of acetone vapor and air and we averaged 500 images. Thus, it was possible to have access to the mean laser sheet profile. Finally, image correction was achieved by dividing the raw image by the mean laser sheet image.

The pre-processing steps can be summarized with the following equation:

$$I_{corr} = \frac{I_{raw} - \overline{I_{noise}}}{\overline{I_{laser}} - \overline{I_{noise}}}, \quad (2.10)$$

where  $I_{corr}$  is the processed image,  $I_{raw}$  is the raw image,  $\overline{I_{noise}}$  is the mean background image, and  $\overline{I_{laser}}$  is the mean laser profile image. Note that shot-to-shot laser-energy variations were not taken into consideration.

It is known that OH PLIF images are used to derive dynamics of flame fronts [136]. More specifically, the location of the steep gradient in OH signal can be used as an estimator of the flame front (separation of unburned and burned gases). However, because OH is relatively long lived molecule, it can persist in high-temperature burned gases. Thus, it was not possible to dissociate reaction regions (where OH were produced) from regions of burned gases (OH convection) in our configuration. **Keeping in mind this constraint, we use the term *flame front* to denote the interface between unburned and burned gases in the rest of the manuscript.**

Practically, we used a non-linear diffusive filter, followed with a classical Canny edge detection algorithm [30] (Matlab, image processing toolbox) with default parameters<sup>4</sup>. Note that more complex methods were referenced in the literature [216] but the present procedure was sufficient and gave good results. Finally, we used a thinning algorithm described in Lam et al. [131] to

---

<sup>4</sup>Low and high threshold values were set automatically, according to the highest gradient magnitude. The default standard deviation of the gaussian filter was  $\sigma = \sqrt{2}$  and its size was automatically set according to this value.

reduce the interface to one pixel width. Additional details can be found in Appendix B.

#### 2.2.4 Phase-averaged measurements

This procedure consisted in reconstructing the temporal evolution of an event with diagnostics which were not temporally resolved. Specifically, if an event has a duration  $t_e$  and the experimental diagnostic has a sampling rate  $f_d$  ( $t_d = 1/f_d$ ), the condition to temporally resolve the event must satisfy the following equation:

$$t_d < 0.5t_e. \quad (2.11)$$

Equation 2.11 expresses the Nyquist-Shannon sampling theorem [172, 205]. Despite the advent of high-speed systems (discussed in Chap. 4), investigation of high-frequency and transient phenomena remains complex. However, when the phenomenon is periodic, it is possible to use the phase-averaged based procedure to reconstruct the temporal evolution of the event with non-resolved diagnostics. A reference signal (most of the time with a relatively good acquisition rate) has to be chosen in order to phase other data. We chose in this study the dynamic pressure to phase our measurements (cf. Sec 2.2.1), and we implemented the procedure depicted in Fig. 2.7:

- Step 1 consisted in recording the reference signal trace and to identify the different cycles (i.e., starting and final time of each cycle). The beginning of each cycle was defined by the user (for example, when the signal was at maximum in Fig. 2.7). Then, pressure traces of each cycle were cut up and grouped into several bins (five bins in Fig. 2.7) and a phase angle  $\varphi$  was attributed to each of them, between 0 and 360°.
- Step 2 consisted in sorting data from other measurement techniques. Figure 2.7 depicts two red squares, which corresponds to two successive records. Note that the sampling rate was lower than the period of the phenomenon. Each record was then sorted in the corresponding bin.
- When the sorting procedure was completed, step 3 consisted in averaging all records contained within each bin.

This treatment lies on an *a posteriori* processing and two parameters can affect its accuracy: the width of one bin determines the temporal resolution whereas the amounts of records per bin determines the statistical convergence of data. It is evident that these two parameters are linked and results in a compromise. A sensitivity analysis showed that 15 bins, each having a  $24^\circ$  width, led to approximately 300 records within each bin with a good statistical convergence.

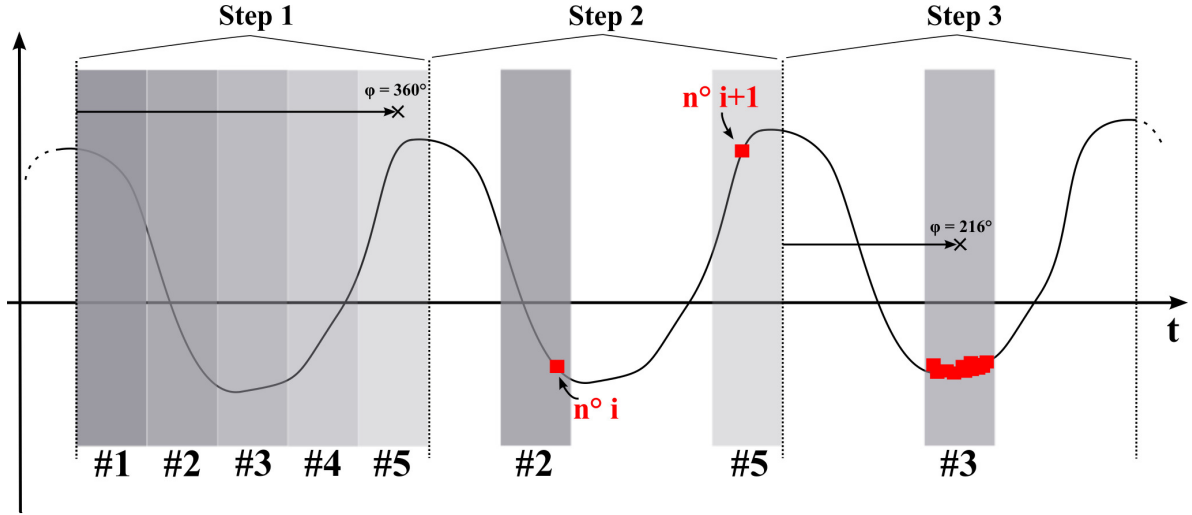


Figure 2.7: Schematic illustration of the phase-averaged procedure. Bins are depicted with grey filled rectangles (and numbering).

## 2.3 Description of thermo-acoustic instabilities

We are interested in giving a qualitative description of combustion instabilities encountered in our TVC by using the different diagnostics introduced previously.

### 2.3.1 Operating conditions

Details of the experimental setup are provided in Chap. 1. The mainstream air mass flow rate  $\dot{m}_m^o$  was  $21.54 \text{ g.s}^{-1}$  (bulk velocity of  $5.0 \text{ m.s}^{-1}$ ) and an equivalence ratio  $\phi_m$  of 0.8. The upstream reactive flow (URF) injection system delivered a nominal air mass flow rate  $\dot{m}_c^o$  of  $0.70 \text{ g.s}^{-1}$  (bulk air velocity of  $6.0 \text{ m.s}^{-1}$ ) and an equivalence ratio  $\phi_c$  of 3.0. The downstream cooling air (DCA) injection system generated a nominal air mass flow rate  $\dot{m}_{DCA}$  of  $1.0 \text{ g.s}^{-1}$  (bulk air velocity of  $3.6 \text{ m.s}^{-1}$ ). The nominal power of the TVC  $P_g$  was  $60 \text{ kW}$ , of which 83% were produced by the

main flame and the remaining 17% were produced by the cavity. Table. 2.2 summarizes operating conditions investigated in this chapter and selected from previous preliminary studies [27].

	Main	URF	DCA
Flow rate [g.s <sup>-1</sup> ]	22.54	0.82	1.0
Bulk velocity [m.s <sup>-1</sup> ]	5.0	6.0	3.6
$\phi$ [-]	0.8	3.0	0.0
fuel [g.s <sup>-1</sup> ]	1.0	0.12	0.0
$P_g$ [kW]	50	10	0
$P_{glob}$ [MPa]	0.17		

Table 2.2: TVC operating conditions.

### 2.3.2 Pressure Dynamics

Figure 2.8 depicts two time series of pressure fluctuations within the burner. The unstable condition (—, see Sec. 2.3.1), exhibited large and cyclic pressure fluctuations, with an amplitude measured at  $p'_{rms} = 1430$  Pa. In contrast, an example of a stable operating condition (.....) show that pressure fluctuation amplitude were reduced by 92 %, with no cyclic behavior anymore.

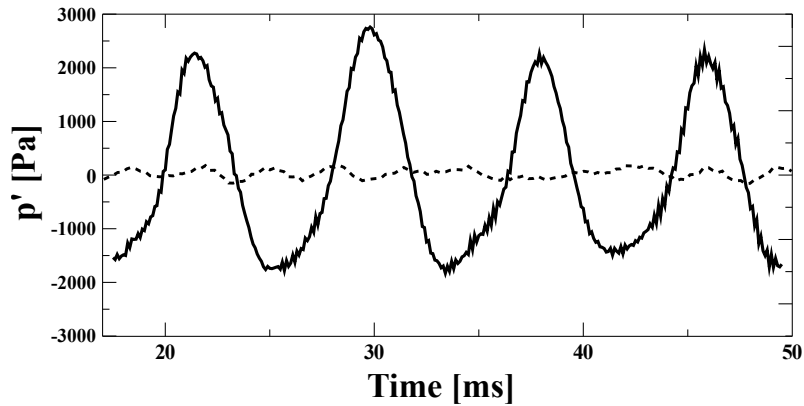


Figure 2.8: Time evolution of pressure fluctuations for an unstable condition (—) and a stable condition (....., additional details in Chap. 5).

The pressure fluctuation frequency spectrum of the unstable operating condition is presented in Fig. 2.9. Note the presence of several characteristic frequencies, with the most dominant at  $f_0 = 122$  Hz. Other characteristic frequencies were found and included 244, 366, 488 and 560 Hz, although their corresponding energies were decreasing. The harmonic relation between these spikes was evident and could be related to several acoustic modes of the geometry, non-linear

processes, and even more complex scenarios (i.e., coupling with convective modes).

Effects of these strong pressure oscillations may evidently affect the combustion process. Next section considers the combustion dynamics.

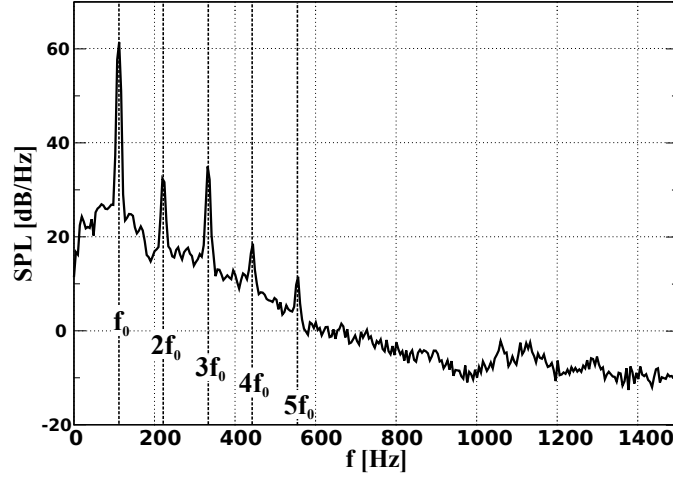


Figure 2.9: Pressure fluctuation frequency spectrum of the unstable operating condition.

### 2.3.3 Combustion dynamics

Phase-averaged  $\text{CH}^*$  fields are shown in Fig. 2.10. Two arrows are depicted in the first  $\text{CH}^*$  field (upper left image at  $12^\circ$ ) to recall the location of cavity injection systems. As a reminder, the range of phase angles (0 to  $360^\circ$ ) was divided into fifteen bins, each having a range of  $24^\circ$  and approximately 300 sorted  $\text{CH}^*$  images. Phases were locked according to the pressure signal, depicted at the bottom of the figure. Vertical lines indicate limits of each bin and red circles report the pressure value taken in each bin. Analysis of the instability cycle is arbitrarily chosen to start from the moment the dynamic pressure was null and started to increase.

Around the moment the pressure was null, the  $\text{CH}^*$  signal was quite important in the cavity and in the mainstream ( $\varphi$  between  $12$  and  $348^\circ$ ). The maximum of  $\text{CH}^*$  occurred at  $\varphi = 348^\circ$  and the signal was constantly decreasing when the pressure increased (i.e.,  $\varphi$  between  $12$  and  $108^\circ$ ). The presence of  $\text{CH}^*$  upstream of the rod indicated that the incoming fresh gases were ignited before reaching the cavity and proves that the tremendous heat release led to an intermittent flashback. With continually increasing pressure to its maximum, heat release progressively decreased to relatively low values ( $\varphi = 108^\circ$ ). We therefore assume that the burner was merely extinguished. Moreover, it is interesting to observe that the  $\text{CH}^*$  decayed

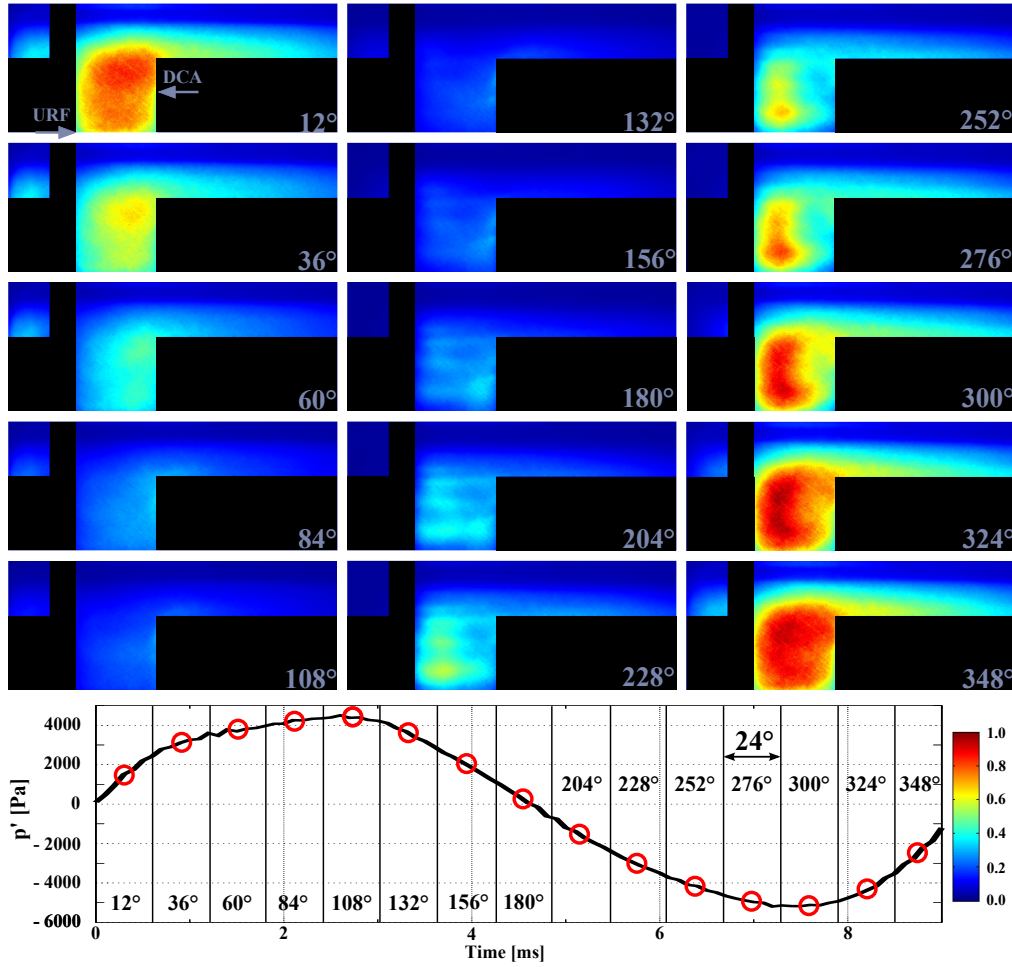


Figure 2.10: Phased-averaged  $\text{CH}^*$  fields with values of phase angle marked. Only the upper-half of the burner is represented and corresponds to the spatial average of the lower and upper parts of the burner to take into account any possible asymmetric effects. Pressure traces is shown at the bottom and also depicts the different bins used for the phase-averaged procedure.

faster on the upstream part of the combustor whereas  $\text{CH}^*$  signal was still persisting next to the cavity trailing edge. Thus, we conclude that burned gases were drained from the cavity toward the exit of the combustor, which also contributed to the extinction of the burner. When the pressure started decreasing, some  $\text{CH}^*$  radicals were appearing at the cavity base and in the surroundings of the DCA jet injection ( $\varphi = 132$  to  $228^\circ$ ).  $\text{CH}^*$  pockets appeared faster next to the upstream cavity face, which was in opposition with the  $\text{CH}^*$  decay observed in the first part of the instability cycle (i.e.,  $\varphi = 12$  to  $108^\circ$ ). Even if it was difficult to directly correlate the location of  $\text{CH}^*$  chemiluminescence to heat release, we suggest that the location of  $\text{CH}^*$  pockets were primarily controlled by the cavity flow dynamics and wake regions produced by the rods. When the pressure emerged from its minimum value, the  $\text{CH}^*$  signal was still increasing in the



upstream cavity region and became more intense ( $\varphi = 252$  to  $300^\circ$ ). At the same time,  $\text{CH}^*$  signal started to appear in the mainstream. Finally, when the pressure reached a null value again, the heat release rate was important in all the combustor and the cycle was over ( $\varphi = 300$  to  $348^\circ$ ).

Observations show that the cavity and the mainstream were not simultaneously ignited and had different behaviors. As explained previously, because the TVC is a staged combustor, interaction mechanisms between the rich and lean regions may necessarily control the combustion dynamics. Combined with the present analysis, we conclude from this sequence that the strong heat release oscillations may result in strong mass and heat transfers between the cavity and the mainstream. For this reason, next chapters are focused on this specific point to get detailed insights about these phenomena (i.e., Chap. 3 considers an inert flow whereas Chap. 4 treats the reactive flow).

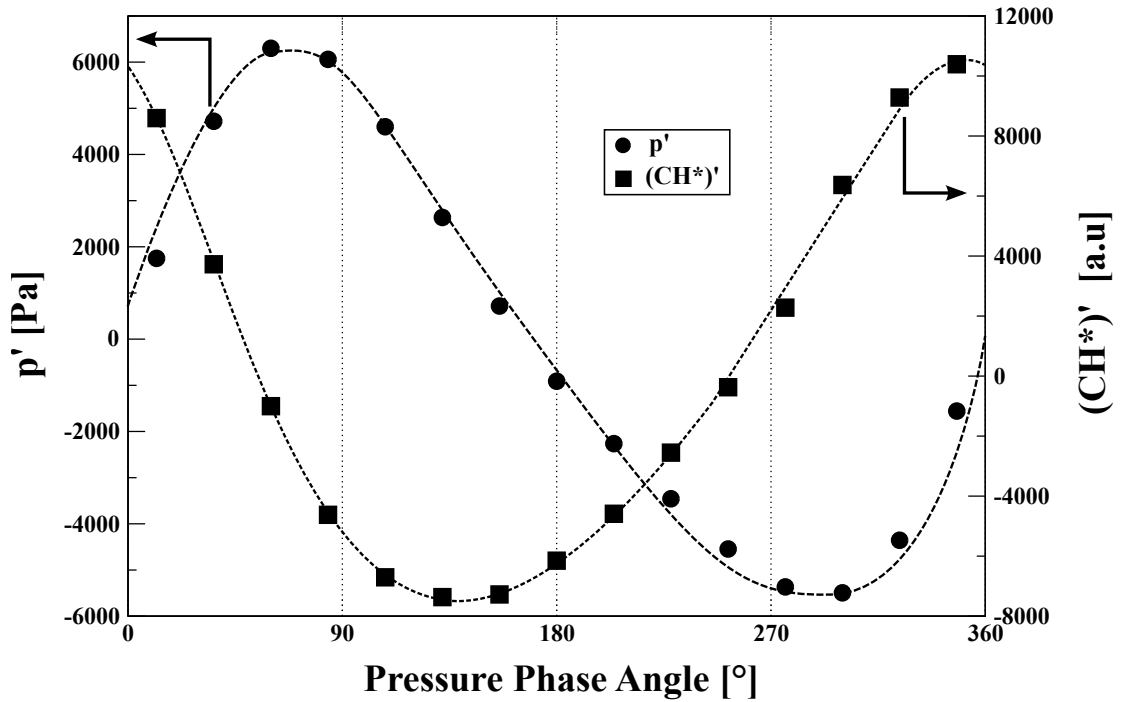


Figure 2.11: Phase-averaged pressure fluctuations ( $\bullet$ ) and total  $\text{CH}^*$  fluctuations ( $\blacksquare$ ). Informative dashed lines are depicted for clarity.

Figure 2.11 shows the phase-averaged evolution of global  $\text{CH}^*$  fluctuations and pressure fluctuations.  $\text{CH}^*$  fluctuations were estimated with the 300 images recorded in each bin whereas pressure fluctuation data corresponds to the red circles shown in Fig. 2.11. This figure clearly shows that pressure and heat release oscillations were coupled and harmonically oscillating. In

addition, the characteristic period of oscillation was roughly in agreement with the acoustic frequency  $f_0$  and confirmed that combustion dynamics was quite important. A rough estimation of this phase shift indicated that the Rayleigh criterion may be satisfied. Because of the phase-averaging procedure, the phase shift  $\varphi_{p'-q'}$  lied with a large uncertainty (at least  $\pm 24^\circ$ ). As mentioned in Sec. 2.1.2, the coupling between heat release and pressure fluctuations (Eq. 2.5) does not explain mechanisms affecting the combustion processes. Thus, it is crucial to have additional information regarding the flow dynamics (see Chap. 4).

### 2.3.4 Flame Structure Dynamics

In order to complete the findings highlighted in the previous section, we tracked the flame front dynamics. We recall here that because the geometry involved a large recirculation region and because the OH radical is a marker of burned and unburned gases, it was impossible to dissociate flame front regions (OH production) from regions of burned gases (OH convection). Keeping in mind about this constraint, we use the term "*flame front*" in this section to denote the interface between unburned and burned gases. However, information about the dynamics of burned and unburned gases could confirm that mass transfers occurring between the cavity and the mainstream were not optimized to stabilize a flame.

Figure 2.12 depicts fifteen instantaneous OH-PLIF images illustrating one combustion instability cycle (bins are identical to Fig. 2.10). Phase angles are recalled on each image and the white arrow depicts the location of the DCA injection system (located on the downstream cavity face). Note that this sequence of images is not temporally resolved.

When heat release was at minimum ( $\varphi = 132^\circ$ ), low amounts of burned gases were found exclusively in the cavity, forming isolated pockets, located at the interface with the mainstream and in the surroundings of the cavity injection systems. In contrast, no OH was found in the mainstream, then confirming that the main region was extinguished. When heat release started to increase ( $\varphi = 252^\circ$ ), the OH signal became more intense and more disorganised in the cavity. In addition, some OH pockets were observed in the mainstream, being more and more preponderant. When heat release was at maximum ( $\varphi = 324^\circ$ ), large amount of OH were found in the cavity and in the mainstream; at this point, the entire combustor was completely ignited. When

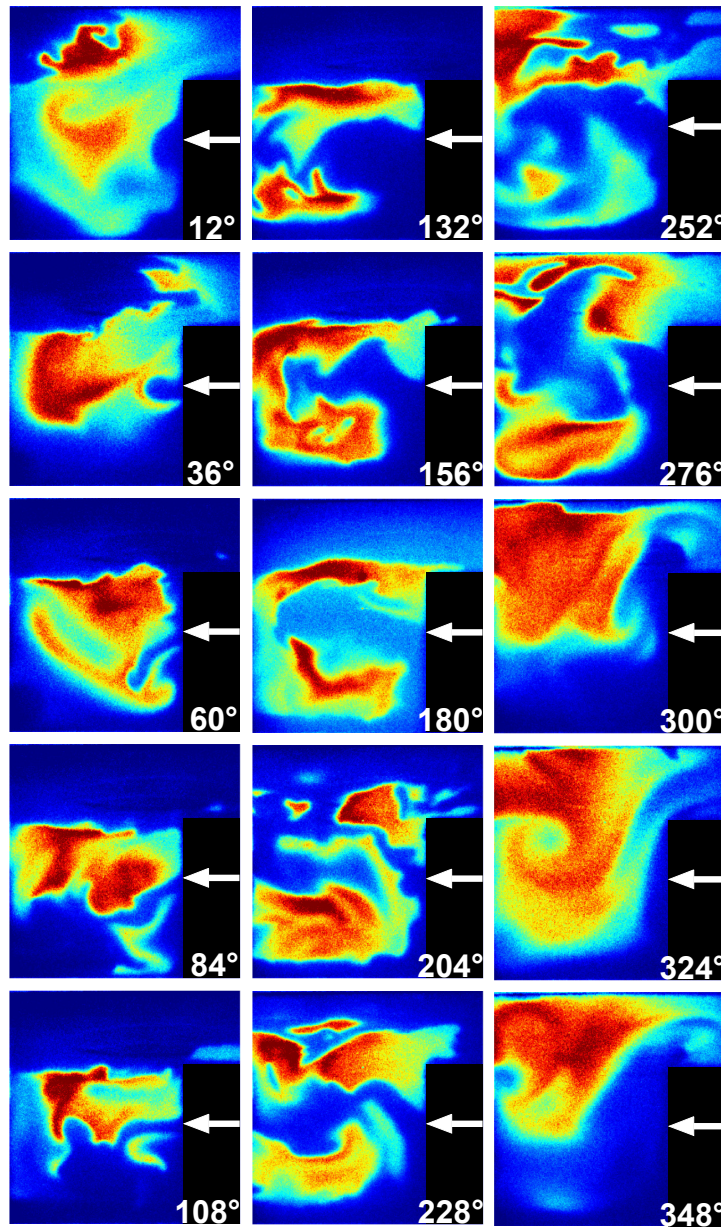


Figure 2.12: Instantaneous OH-PLIF images, illustrating specific instance of the combustion instability cycle. Phase angle values are identical to Fig. 2.10.

heat release started to decrease, the OH in the mainstream was disappearing ( $\varphi = 12\text{-}108^\circ$ ).

Note that the location of burned and unburned gases presented the same feature depicted in Fig. 2.10. In fact, the draining process was clearly visible between  $\varphi = 324^\circ$ , where burned gases were established in the mainstream as well as in the upstream cavity region, and at  $\varphi = 36^\circ$ , where some OH residuals were present in the downstream part of the mainstream and near the cavity trailing edge. The dynamics next to the DCA jet flow was also presenting interesting insights. The DCA air stream was clearly evident in the different images: it alternately flowed

in the cavity (e.g.,  $\varphi = 108^\circ$ ,  $132^\circ$ ,  $156^\circ$ , and  $180^\circ$ ) and in the mainstream (e.g.,  $\varphi = 252^\circ$ ,  $276^\circ$ , and  $300^\circ$ ). Between these two opposite behaviors, Fig. 2.12 shows that the DCA air stream was not flowing normally ( $\varphi = 36^\circ$ ), or even not flowing ( $\varphi = 324^\circ$ , and  $348^\circ$ ). This important jet dynamics consequently affected location of burned and unburned gases, and evidently showed that no flame stabilization regions were encountered in this unstable mode.

We conclude that location of burned and unburned gases was in agreement with previous remarks; that is, important dynamics of OH radicals were encountered in this unstable mode. It is clear that temporal evolution of OH signal may influence heat release oscillations. For this reason, temporal measurements were performed in Chap. 4 in order to link these oscillations to the unstable behavior of the combustor.

### 2.3.5 Rayleigh Index Distribution

Heat release and flame dynamics were greatly affected, and demonstrated the existence of instabilities. It was interesting to investigate regions amplifying or damping the instability. Consequently, we used the spatial Rayleigh index, which has been previously used by several workers [186, 147], and defined as

$$R(x, y) = \frac{1}{\tau} \int_{\tau} p'(x, y, t) q'(x, y, t) dt, \quad (2.12)$$

where  $R(x, y)$  is the Rayleigh index distribution,  $\tau$  is the period of the instability,  $p'$  is the local fluctuating pressure, and  $q'$  is the local heat release fluctuation. In-phase regions, indicating an amplification of the instability, result in positive Rayleigh values. In contrast, out-of-phase regions, indicating a damping of the instability, result in negative values. Because the wavelength of the pressure oscillation was much greater than the length of the flame<sup>5</sup>, the pressure was assumed to be spatially uniform over the region investigated, i.e.,  $p'(x, y, t) = p'(t)$ . Moreover, phase-averaged CH\* fields depicted in Fig. 2.10 represented the line-of-sight integrated chemiluminescence and did not reflect the planar heat release fluctuation distribution  $q'(x, y)$ .

<sup>5</sup>The wavelength associated to the first acoustic tone was estimated at 6 m, which is greatly larger than the combustor length (burned gases temperature of 1700K). Sensitivity analysis showed that the choice of burned gases temperature did not significantly change our conclusion.

Taking advantage of the present geometry, we assumed that the flame was axisymmetric and implemented an Abel deconvolution procedure to reconstruct the two-dimensional flame structure [47]. Again, because the flame was not perfectly axisymmetric, the upper and lower halves of each image were averaged prior to implementing the Abel deconvolution. An application of this procedure is given in Fig. 2.13.

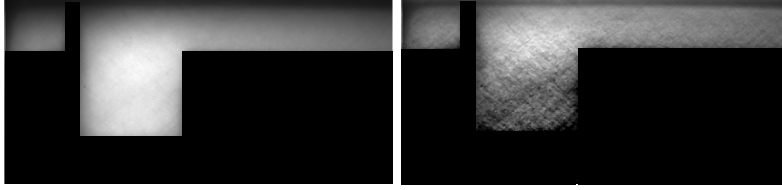


Figure 2.13: Example depicting the implementation of the Abel procedure. The image on the left corresponds to the volume averaged  $\text{CH}^*$  field. The corresponding deconvolved image is given on the right.

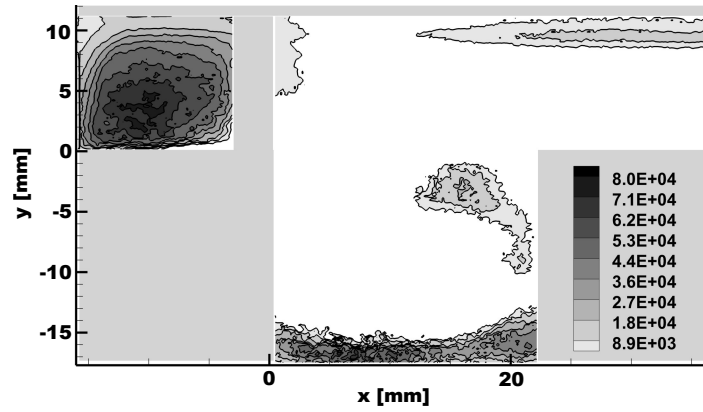


Figure 2.14: Rayleigh index distribution corresponding to the images show in Fig. 2.10.

The Rayleigh index distribution corresponding to the images shown in Fig. 2.10 is presented in Fig. 2.14. Note that only positive Rayleigh values are shown and that a color cutoff value was applied to blank negative values. Positive values were observed in the cavity and in the mainstream. In the cavity, amplifying regions were located in the surroundings of the URF jet injection and next to the cavity trailing edge where the DCA airflow was injected. As we mentioned when describing the instability cycle, injection systems could be critically important because they control the combustor aerodynamics. In addition, the chemical gas composition was quite extreme (i.e.,  $\phi_c = 3.0$  and  $\phi_m = 0.8$ ), and may result in specific and local conditions for ignition. In fact, we suggest that the DCA airflow may act as a moderator in the cavity to dilute and lower the rich equivalence ratio  $\phi_c$  injected by means of the URF jet flow until

stoichiometry regions appear.

In the mainstream, an amplification region was also found, upstream of the cavity. This region, highlighted in Fig. 2.10, showed great positive Rayleigh values and may also play an important role in sustaining the instability behavior. We propose then that the mainstream region, which consisted of a lean flammable mixture, may be intermittently burning and may produce a standing longitudinal acoustic wave.

Figure 2.14 also revealed large damping regions, especially far from the jet injection systems, being established in the middle of the cavity and slightly penetrating the main channel. Because these regions were located in the inner recirculation zone of the cavity, chemical and gas composition may be less fluctuating (primarily due to a better mixing process).

## 2.4 Concluding remarks

This study aimed to gain an improved understanding of the stabilization mechanisms involved in a complex TVC. For this reason, the combustor was voluntarily operated with drastic operating conditions, exhibiting thermo-acoustic oscillations. In order to guide our research strategy, this chapter was mainly focused on obtaining preliminary insights regarding the combustor dynamics.

We therefore took advantage of the self-excited pressure oscillations to extract phase-averaged information about the combustion dynamics, and flame dynamics. The pressure signal clearly showed large and periodic oscillations, with the existence of several discrete frequencies (underlying the presence of non-linear processes). The reconstruction of one combustion instability cycle confirmed that the combustor exhibited tremendous heat release oscillations and that location of burned and unburned gases was too disorganized to obtain a stable stabilization region for the flame. Remarkably, dynamics between the cavity and the mainstream was found to be independently quite different, but the resulting interactions may be the primary reason for the appearance of such instabilities. The Rayleigh index distribution revealed that the complex injection systems in the cavity and the associated chemical gas composition were driving the self-sustained instability, which in turn, may affect the inlet jet injection conditions, and finally

add energy to the system.

Both flow and flame dynamics were tremendously oscillating. Indeed, the complex geometry (i.e., a flow passing past a cavity), combined with complex injection systems (i.e., injections in the cavity), and complex chemical conditions (i.e., lean and rich regions), increased chances to obtain unfavorable operating conditions. As mentioned in Chap. 1, the natural flow unsteadiness of this geometry was extensively studied, but few were focused in reactive conditions. Unfortunately, mechanisms driving combustion instabilities are surely complex and coupled.

Based on the insights of this chapter, we decided to treat separately the contribution of each process as follows:

- Investigation of pure aerodynamic instabilities in Chap. 3 by treating the inert flow dynamics. In particular, effects of adding injection systems in the cavity and the resulting mass transfers between the lean and rich zone are considered.
- Characterization of the coupling between the flow, the flame and acoustics in reactive conditions (Chap. 4) in order to determine mechanisms piloting such instabilities.

## Chapter 3

# Aerodynamic stability of the shear layer in a TVC

### Contents

---

<b>3.1</b>	<b>Background on cavity flows . . . . .</b>	<b>66</b>
3.1.1	Free shear flows and associated instabilities . . . . .	66
3.1.2	Cavity flow dynamics . . . . .	69
3.1.3	Conclusion and challenging issues . . . . .	77
<b>3.2</b>	<b>Experimental setup of the inert trapped vortex combustor . . . . .</b>	<b>77</b>
<b>3.3</b>	<b>High-speed particle image velocimetry (HS-PIV) . . . . .</b>	<b>78</b>
3.3.1	Presentation of the technique . . . . .	78
3.3.2	Estimation of the accuracy of PIV . . . . .	79
<b>3.4</b>	<b>Global flow topology . . . . .</b>	<b>85</b>
3.4.1	Inlet flow characterization and operating conditions . . . . .	85
3.4.2	Qualitative description of the flow topology in an active and passive cavity . . . . .	87
3.4.3	Mass exchanges fluxes between the cavity and the mainstream flows . . . . .	89
3.4.4	Turbulent features . . . . .	94
3.4.5	Coherent Structures . . . . .	96
<b>3.5</b>	<b>Characterization of the flow separation shear layer . . . . .</b>	<b>99</b>
3.5.1	Self similar behavior . . . . .	99



---

3.5.2	Evolution of the shear layer thickness . . . . .	103
3.5.3	Effects of cavity flow injections on the shear layer location . . . . .	105
3.5.4	Momentum budget . . . . .	106
<b>3.6</b>	<b>Conclusion . . . . .</b>	<b>108</b>

---

In Chapter 2, a global observation of the TVC instability showed that a detailed understanding of flame stabilization mechanisms were still to be determined. The presence of a cavity in this concept involves a flow separation that naturally leads to the development of a shear layer. The latter is commonly used in combustion systems to improve mixing and stabilize flames. Unfortunately, shear layers are also prone to intrinsic aerodynamic instabilities (large-scale structures as well as broadband small-scale turbulence) which may affect the flame dynamics. For this purpose, this chapter only focuses on the inert flow structure, with an emphasis on the interactions between the cavity and the mainstream.

Because inert flows passing past passive cavities<sup>1</sup> have been studied for the course of many years in the aerodynamic community, it makes sense to review the different studies in order to understand the different mechanisms and to appreciate changes induced by the presence of mass injection systems in the cavity.

This chapter starts with a review of classical cavity studies in Sec. 3.1. Thus, Sec. 3.2 describes the experimental setup. Section 3.3 details the use of high-speed particle image velocimetry (HS-PIV) laser technique. Section 3.4 considers a global characterization of the flow structure arising with and without jet injection systems. Turbulence distribution, local mass exchanges between the cavity and the mainstream as well as presence of coherent structures are investigated. Finally, Section 3.5 is dedicated to the interfacial zone separating the cavity and the mainstream.

---

<sup>1</sup>Note that in this text, "passive cavity" refers to a cavity which do not have any injection systems (contrarily to an "active cavity").

### 3.1 Background on cavity flows

#### 3.1.1 Free shear flows and associated instabilities

Many fundamental and industrial configurations exhibit shear layers, such as jets, wakes or mixing layers. A schematic illustration is shown in Fig. 3.1 and consists in two parallel flows with different mean-velocities, separated by a thin plate. A free shear layer develops when the two flows come together, downstream of the separating leading plate. The term "free" means that no walls interfere with the shear flow development.

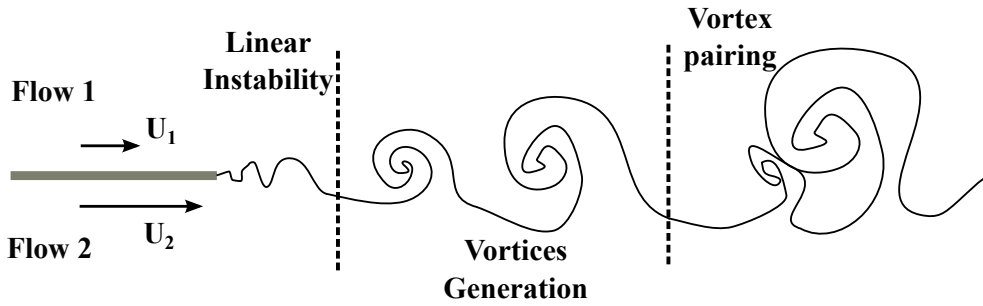


Figure 3.1: Schematic illustration of a free shear layer flow with the different steps leading to the creation of vortices.

For given aerodynamic conditions at the flow separation leading edge, velocity discontinuities stretch the separating surface between the two flows. As a result, pressure gradients appear and makes the flow to rollup. Appearance of these disturbances are amplified and leads to the creation of vortices. This mechanism is referred to as Kelvin Helmholtz (KH) instabilities [93, 123]. Even if this flow topology is naturally unsteady, its use in combustion chambers is unavoidable for mixing or flame stabilization [141]. In fact, Figure. 3.1 clearly shows that little fluid 1 is engulfed by fluid 2 in the vortex centroid, then increasing the mixing process.

Several early experimental works dealt with the amplification and development of velocity discontinuities in laminar conditions [163, 214]. Figure 3.2 depicts several illustrations of shear layer flow structures. Note that a repetitive pattern is visible and highlights the continuous process of vortices creation (also referred to as vortex shedding). Moreover, because one vortex travels in the wake of the preceding one, it has a faster velocity, and a vortex pairing process can appear (Fig. 3.2). The latter process makes the shear layer to thicken. Amplification of the interfacial instability and the production of larger vortical structures also facilitates the

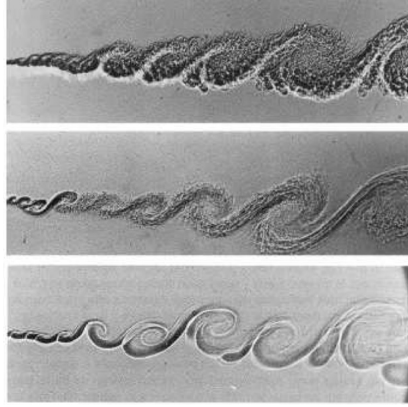


Figure 3.2: Shadowgraphs illustrating KH instabilities in a free shear layer (Nitrogen-Helium). Reproduced from Brown and Roshko [24].

transition to a turbulent flow topology [233].

Benney put in evidence the three-dimensional behavior of a shear layer [9]. He analytically demonstrated, with a non-linear analysis of the Navier Stokes equations, that vorticity was three-dimensional and that secondary smaller structures were created in the longitudinal direction. Bernal and Roshko experimentally confirmed the existence of a three-dimensional flow behavior [10]. As an example, a shear layer flow visualization is given in Fig. 3.3 and clearly demonstrates the existence of coherent structures, inserted in the rollup structures. Lasheras et al. [132, 133] argued that the three-dimensional behavior of a shear flow was related to a distortion of the vorticity pathlines and pointed out that initial boundary conditions at the separation leading edge were critically important. Another reason directly comes from the vortex pairing process, which modifies the relative velocity of vortices and destabilizes the whole flow.

Shear flows are regions where complex aerodynamic instabilities can initiate large-scale structures. The three-dimensional behavior of these instabilities makes easier its transition to a turbulent state while keeping its constituency. Several authors studied how a shear layer spatially and timely evolves (Winant & Browand [233], Davies & Yule [48], Roshko [194], Rockwell and Knisely [189]). Dimotakis & Brown [51] performed velocity autocorrelation measurements along the shear layer and observed a repetitive pattern with large variabilities. Based on these results, they suggested that the shear layer was influenced by the downstream conditions. In fact, because vortical structures are strengthened with the axial distance [233], they can exert an influence on the upstream flow, via the Bio-Savart induction law. This observation was found to be

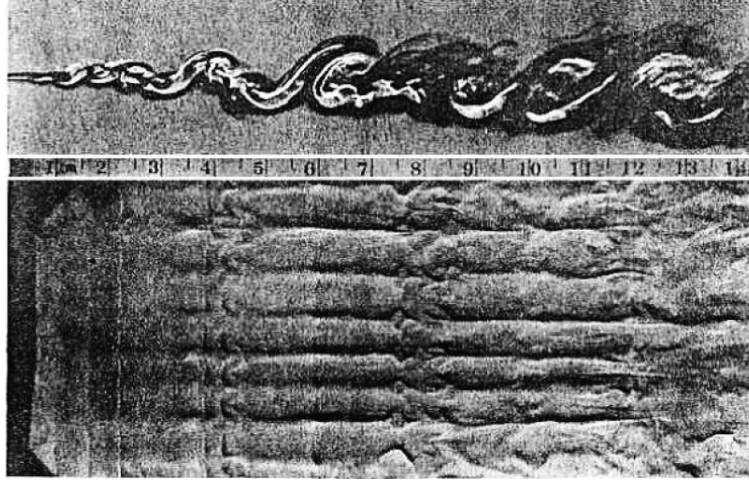


Figure 3.3: Superimposition of transverse and longitudinal rollers in a free shear flow. Reproduced from Bernal and Roshko [10].

true on a large range of Reynolds numbers [233, 23]. An example of preliminary measurements of Rockwell & Knisely is shown in Fig. 3.4.

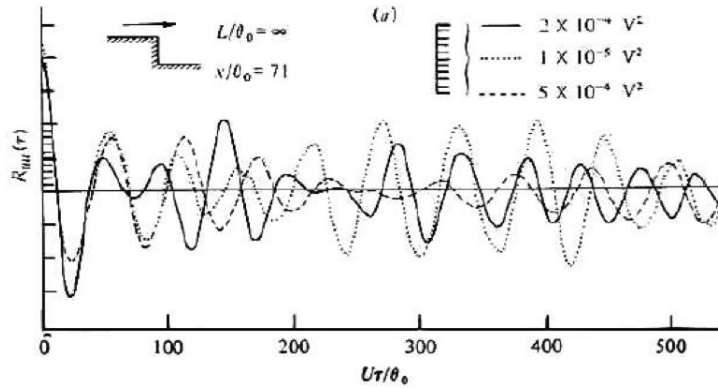


Figure 3.4: Autocorrelation functions of axial velocities measured in a free shear layer (backward-facing step flow). Reproduced from Rockwell & Knisely [189].

Large fluctuations in autocorrelation functions are visible but a feedback mechanism still sustains far downstream of the flow separation. Based on these observations, Rockwell & Knisely [189] argued that the insertion of an impingement corner could strengthen this feedback mechanism. The resulting velocity autocorrelation functions are shown in Fig. 3.5 and clearly demonstrates that the coherent organization of the flow was sustained all along the shear layer. However, at this time, authors were still wondering which mechanism(s) was responsible for such self-sustained flow dynamics [188, 239, 98].

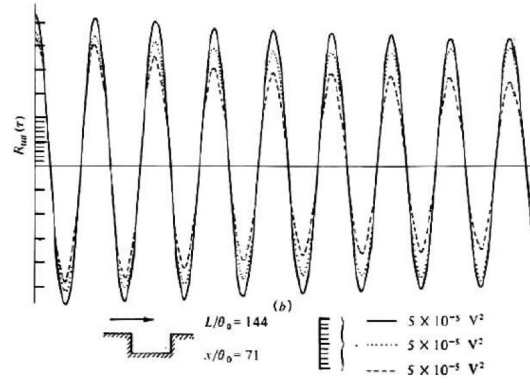


Figure 3.5: Autocorrelation functions of axial velocities in a shear layer developing above a cavity. Reproduced from Rockwell & Knisely [189].

### 3.1.2 Cavity flow dynamics

Subsonic<sup>2</sup> flows passing above cavities are encountered in many applications: landing systems and bomb bays in aircraft, cavity-like geometries in rivers, interstices between train carriages, etc. The incoming flow separates at the leading edge of the cavity, and a shear layer develops on top of the cavity (see Sec. 3.1.1). However, the presence of a cavity trailing corner, combined with the generation of vortical structures may induce large pressure and velocity oscillations. This unsteadiness can lead to undesired level of noises, vibrations and inefficient heat transfers. The complexity to study such flows is mainly due to the large amounts of parameters. Several studies attempted to classify such configurations.

#### Cavity classification

Most of cavities can be characterized by their length  $L$ , depth  $D$ , and width  $W$ . With these three information, cavities can be classified as:

- **Length to Depth ratio  $L/D$**

- $L/D < 1$ . The cavity is *deep*. One or several vortices can be established at the cavity base as well as the interfacial zone. The resonance modes are likely to occur along the transverse direction, exciting then the dead volume (Fig. 3.6-(a)).

- $L/D > 1$ . When  $L/D \approx 1$ , the shear layer does not interfere with the cavity. Only

<sup>2</sup>Supersonic flow studies are not treated in this study (see [8] for further information)

one stable recirculation zone is established (*open cavity*, Fig. 3.6-(b)). When  $5 < L/D < 10$ , several vortices are established in the cavity but the shear layer does not penetrate the cavity (*transitional cavity*, Fig. 3.6-(c)). For  $L/D > 10$ , the shear layer can interfere with the whole cavity. Thus, several recirculation zones appear in the longitudinal direction (*closed cavity*, Fig. 3.6-(d)).

- **Length to Width ratio  $W/L$**

As mentioned previously, shear layers can exhibit three-dimensional behaviors, especially when  $W/L < 1$ . In contrast, a large ratio  $W/L$  can reduce the development of secondary structures.

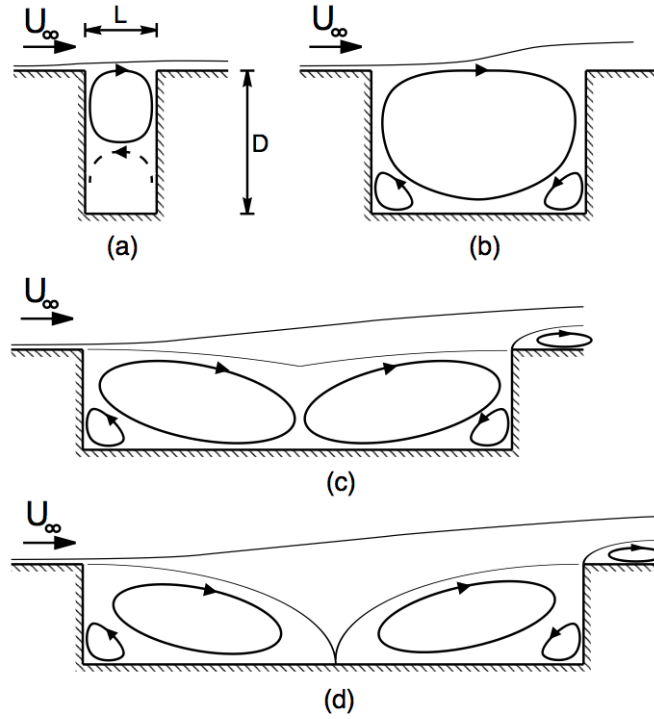


Figure 3.6: Cavity classification of length  $L$ , depth  $D$  and with a free flow speed  $U_\infty$ . (a): Deep cavity; (b): open cavity; (c): transitional cavity; (d): closed cavity. Reproduced from [34].

$L/D$				$W/L$	
$L/D < 1$	$L/D \approx 1$	$5 < L/D < 10$	$L/D > 10$	$W/L < 1$	$W/L > 1$
Deep	Open	Transitional	Closed	$\approx 2D$	$\approx 3D$

Table 3.1: Cavity classification in accordance with ratios  $L/D$  and  $W/L$

Roshko experimentally studied the laminar flow topology in a cavity for low-Mach conditions [193]. Effects of increasing the ratio  $L/D$  revealed the existence of a transition from a single trapped vortex topology to a more complex one, exhibiting several trapped vortices. However,

the literature reports several values of the ratio  $L/D$  for the transition from an *open* to a *closed* cavity [193, 200]. Several authors achieved to classify the different flow topologies. An example of the NASA classification (performed by Plentovich [176]) is shown in Fig. 3.7. He concluded that the ratio  $L/D$  was not sufficient to give an accurate classification, and demonstrated that the Mach number and ratio  $W/D$  had to be considered.

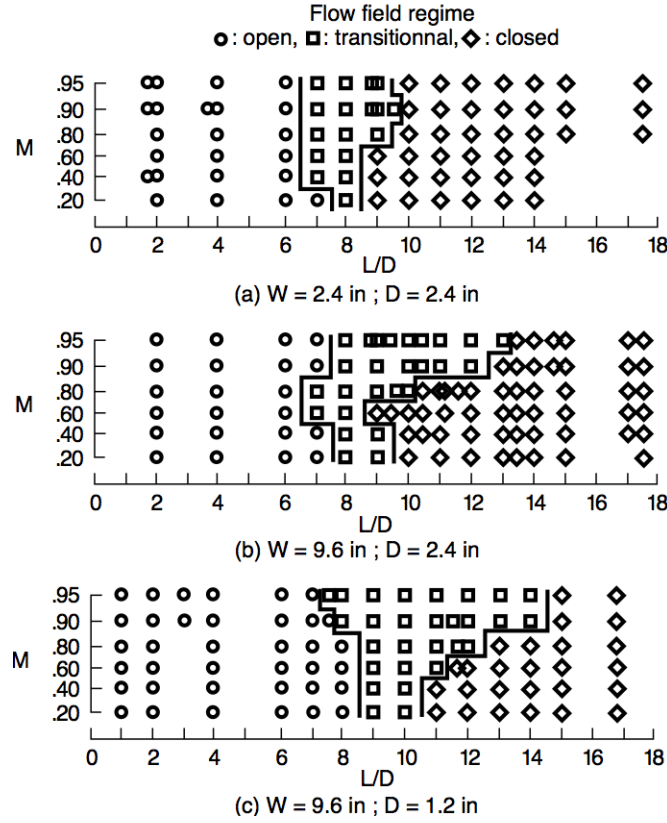


Figure 3.7: Cavity classification for different  $L/D$ ,  $W/D$ , and Mach numbers. Reproduced from Plentovich [176]

### Characterization of the feedback process

As mentioned previously, Rockwell and Knisely [189] introduced the concept that a feedback mechanism was driving self-sustained flow dynamics in cavities. The feedback loop is depicted in Fig. 3.8 and can be described as follows:

- A velocity difference appears at the cavity trailing edge and initiates the creation of a shear layer (see Sec. 3.1.1).
- The mean flow convects these instabilities, produces vortices, even of larger sizes. There-

fore, the shear layer spans and thickens.

- The shear layer reaches and impinges on the cavity trailing edge, which in turn creates another source of disturbances (see below).
- The disturbance created at the cavity trailing corner propagates upstream and can interact with the inlet conditions (upstream of the flow separation). For instance, Morkovin and Paranjape [164] analyzed the instability in a cavity as a back and forth process, with a characteristic convection time for coherent structures and another characteristic time needed for an acoustic wave to travel upstream.

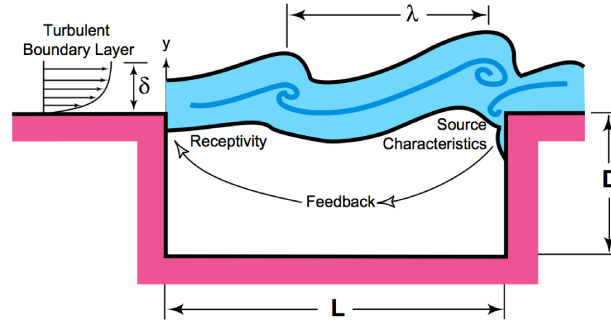


Figure 3.8: Illustration of the flow-induced resonance in a cavity. Reproduced from Cattafesta et al. [33]

Several feedback mechanisms have been highlighted in the literature (depending on the cavity dimensions or the Mach number) [190]. Three of them are presented hereafter:

- **Fluid-dynamic oscillations.** The flow within the cavity is disturbed by the shear layer impingement. Some patches of vorticity, mass or velocity disturbances may enter inside the cavity and create an unsteady motion. Then, the aerodynamic disturbance travels upstream and modifies the incoming boundary layer characteristics [190]. In fact, Rockwell and Knisely [189] related the observed instabilities to the way a vortex impinged on the cavity trailing edge. They found several possible scenarios for a given flow condition: complete entrance of the vortex in the cavity (complete clipping), impingement of the vortex leading to a partial clipping, or drained vortex (which does not enter the cavity). Lin and Rockwell [148] showed that a recirculation zone presenting a high level of unsteadiness, was more prone to affect the shear layer growth, the energy amplification and the development of secondary instabilities.



Ethembaoglu [68] showed that characteristic times associated to this mechanism did not have any harmonic relations. The incoming boundary layer characteristics were also found to play an important role in the development of such cavity instabilities. For instance, Gharib and Roshko [75] highlighted the existence of a critical value to observe cavity resonance (based on the cavity length and the upstream boundary layer momentum thickness). Sarohia [199] studied a laminar airflow condition and proposed a dimensionless parameter to describe the initiation of such instabilities. The latter was formed with the cavity length, the boundary layer thickness and the related Reynolds number. Note that some authors did not observe instabilities: measurements of Grace et al. [79] on an open cavity demonstrated a non-resonating cavity, and related this flow behavior to the smooth distribution of the interfacial Reynolds shear stress above the cavity.

- **Fluid-resonant oscillations.** This mechanism involves a coupling between acoustics and aerodynamics. Impingement of the shear layer on the cavity trailing edge can produce an acoustic wave, which in turn can intermittently affects upstream characteristics of the shear layer. It can also excites a resonant frequency of the cavity. Several classifications are found according to the nature of acoustic modes:

- Longitudinal fluid-resonant oscillations: they can be found in subsonic and supersonic flows. A pressure wave is produced when the shear layer impinges on the cavity trailing edge. The acoustic wave travels longitudinally and disturb the upstream flow conditions [32, 195].
- Transverse fluid-resonant oscillations: a *deep* cavity (i.e.,  $L/D < 1$ ) operating with a low Mach number ( $M < 0.2$ ) can be prone to the development of transverse modes. The upper part of the cavity is excited and a quarter wave acoustic mode usually takes place inside the cavity [25, 110]. These modes are more difficult to be highlighted when the cavity aspect ratio  $L/D$  is near unity.
- Helmholtz fluid-resonant oscillations: appearance of lower frequencies led several authors to consider the whole cavity as a characteristic volume and the associated cavity surface [55, 57].

- **Fluid-elastic oscillations.** This feedback is encountered when elastic edges are included

in the cavity. The latter can create vibrations, which in turn produce instabilities. In contrast to cavity which are subject to fluid-resonant oscillations, the amplification process comes directly from the vibrating structure, rather than the presence of the impingement object.

Several studies have been focused on cavity noises (especially for aeronautic applications). Note that few studies have considered "fluid-dynamic oscillations" cases, where a coupling with the flow dynamics is prevailing (low Mach number flows). The primary reason is that the energy associated to these oscillations is low compared to a direct acoustic feedback ("fluid-resonant oscillations"), and makes their detection more challenging.

### Parameters influencing cavity instabilities

Self-sustained oscillations encountered in cavities are dependent on several parameters such as the incoming boundary layer (laminar or turbulent), the incoming mainstream velocity and the cavity dimensions.

- **Boundary layer:** Rossiter [195] showed that an increase of the boundary layer thickness to cavity length ratio  $\delta_0/L$  led to an attenuation of excited modes (especially pressure oscillations). Similarly, a laminar boundary layer is prone to present larger oscillations compared to a turbulent boundary layer (especially for open cavities). Low Reynolds number  $Re_L$ , based on the cavity length  $L$ , also enhances effects of the boundary layer thickness [77] on the flow unsteadiness.
- **Cavity length and depth:** the ratio  $L/D$  leads to several phenomena. For low Mach flows and for ratios  $L/D$  lower than unity, the preponderant coupling is "fluid-resonant", with the appearance of a quarter standing wave in the cavity [176]. When the ratio is larger than unity, the "fluid-dynamics" coupling becomes preponderant. In addition, this coupling is more sensitive when mainstream velocities are increased. When the ratio  $L/D$  is much larger than unity (i.e.,  $L/D > 10$ ), the coherent motion disappears in favor of a broadband turbulent noise. Sarohia [200] even found that the influence of the cavity length  $L$  was enhanced when the boundary layer thickness was of the same order of magnitude than the cavity depth  $D$ .

- **Cavity Width:** the ratio  $L/W$  determines the two or three-dimensional behavior of the flow structure. When  $L/W > 1$ , the flow is considered to be two-dimensional whereas it is prone to be three-dimensional when  $L/W < 1$ . Surprisingly, characteristic frequencies of unstable cavities are not tremendously affected when the cavity is enlarged, and noise produced by such a cavity is decreased [159, 11]. The explanation is mainly due to the reduction of coherence between large structures (larger anharmonicity finally damps the overall instability process).
- **Mach number:** the mainstream velocity is of great importance on the nature of instabilities in cavities. Measurements of Forestier et al. [70, 71] showed that the larger the Mach number was (super or hypersonic), the greater influence it had. A similar conclusion is drawn when the cavity aspect ratio  $L/D$  is near unity: increase of the Mach number makes the oscillations to jump from a "fluid-dynamics" to a "fluid-resonant" regime. Plentovich et al. [176] concluded that the Mach number was quite important, in comparison to the cavity length  $L$ .

### Cavity modeling

The previous section put in evidence the existence of self-sustained oscillations. The strong relationship between the trailing and leading edges has been subject to the development of several models, in order to predict the unstable nature of cavities. A non-exhaustive list is provided hereafter:

- **Rossiter model:** he proposed a semi-empiric model for cavities subject to "fluid-resonant" oscillations, for an aspect ratio lying in a range  $1 < L/D < 4$ , and for moderate Mach numbers ( $0.4 < M < 0.9$ ) [195]. Considering that the acoustic frequency was directly related to the number of vortices shed at the leading edge, the model considered that the production of an acoustic wave corresponded to a vortex impingement at the cavity trailing edge, and could be mathematically written as

$$f_n = \frac{U_\infty}{L} \frac{n - \alpha}{M + 1/\kappa}, \quad (3.1)$$

where  $n$  corresponds to the number of vortices along the cavity,  $U_\infty$  is the mean flow veloc-

ity,  $L$  is the cavity length,  $\alpha$  is the phase shift appearing between the vortex impingement and the production of an acoustic wave,  $M$  is the Mach number, and  $\kappa$  is a coefficient taking into account the difference of velocities between the vortex and the mean flow. Values of  $\kappa$  and  $\alpha$  had to be adapted to fit experimental observations. Rossiter found experimental values for the coefficients  $\kappa$  [195] whereas Ahuja and Mendoza suggested several values of  $\kappa$  according to the size of the convected structures [3].

Several assumptions reduce the range of validity of this model. In fact, the sound speed  $c^s$  is assumed to be constant, then limiting its use in reactive conditions. Moreover, the parameter  $\kappa$  is assumed to be constant even if recirculation zones exist in the cavity. Finally, this model is not valid for large Mach numbers (i.e.,  $M > 1.2$ ) but Heller et al. [92] corrected the Rossiter formula as

$$f_n = \frac{U_\infty}{L} \frac{n - \alpha}{\frac{M}{1 + (\gamma - 1)/2} \cdot M^2 + 1/\kappa}. \quad (3.2)$$

- **Bilanin and Covert model:** They developed a model without any empirical constants, for Mach numbers lying between 0.6 and 3.0. They considered the shear layer as a thin sheet of vorticity and the trailing edge as a monopolar acoustic source. Therefore, the compressibility of the flow is taken into account. However, large deviations were found when Mach numbers were reduced below 0.6 [11].
- **Tam and Block model:** They proposed an analytical model, based on the Bilanin and Covert approach. The punctual exciting source located at the cavity trailing edge was replaced by reflections of acoustic waves at the cavity base [220]. This model has the advantage to take into account the cavity aspect ratio  $L/D$  and it can either predict a "fluid resonant" or a "fluid-dynamics" process. Results of this model were in agreement with Bilanin and Covert model as well as Rossiter experiments.
- **Howe model:** He introduced a more detailed model. Unlike Tam and Block or Bilanin and Covert models, interactions of the shear layer with edges are taken into account. The feedback process is also calculated by using three-dimensional Green functions (i.e., no presumed disturbances are introduced) [102, 100]. Results were in agreement with experimental measurements, especially for a Mach number lower than 0.2 [101].

### 3.1.3 Conclusion and challenging issues

Flows passing above cavities involve a complexity of physical phenomena. Due to the large amounts of parameters, there is no unified framework to understand mechanisms leading to self-sustained flow oscillations in a cavity. The feedback loop which affects the interfacial shear layer can be of different nature: acoustic, aerodynamic or purely vibrating. Remarkably, few studies have been focused on the aerodynamic feedback loop due to its difficulty to observe such instabilities. Consequently, cavity modeling is limited to a range of specific conditions. Another important point concerns effects of injecting mass directly in the cavity. Few studies are referenced in the literature and have been mainly motivated by the development of an active control procedure to suppress cavity tones. Sarohia and Massier [201] injected a steady mass flow rate at the base of the cavity and demonstrated that cavity tones were suppressed. Sarno and Franke studied steady and oscillatory mass injection. They concluded that the steady mass injection strategy was more efficient even if the pulsed injection produced good performances [198]. Vakili and Gauthier [224] obtained good levels of attenuation by injecting mass through porous plates, placed on the upstream face of the cavity. However, one issue still remains on consequences of mass transfers. In fact, assuming the cavity to be a confined region, injected mass must be necessarily drained out. We showed in Chap. 2 that combustion dynamics was surely affected by the important flow dynamics in the cavity. We suggest that mass transfers may be the primary reason. Thus, the rest of this chapter focuses on understanding relations between cavity injection systems, the shear layer, and the mainstream.

## 3.2 Experimental setup of the inert trapped vortex combustor

A detailed description of the TVC is provided in Chap. 1. The present section aims to recall the different geometries used in non-reactive conditions. A description of the cavity region is shown in Fig. 3.9.

Note that because we did not perform experiments under pressure, the transparent combustion chamber casing was removed as well as the exhaust portion. With no explicit remark, the cavity aspect ratio was kept constant to  $L_c/H_{aft} = 1.19$ . When the cavity was active, injections in the cavity were switched on (Fig 3.9 (b)). The upstream reactive flow (URF) consisted in

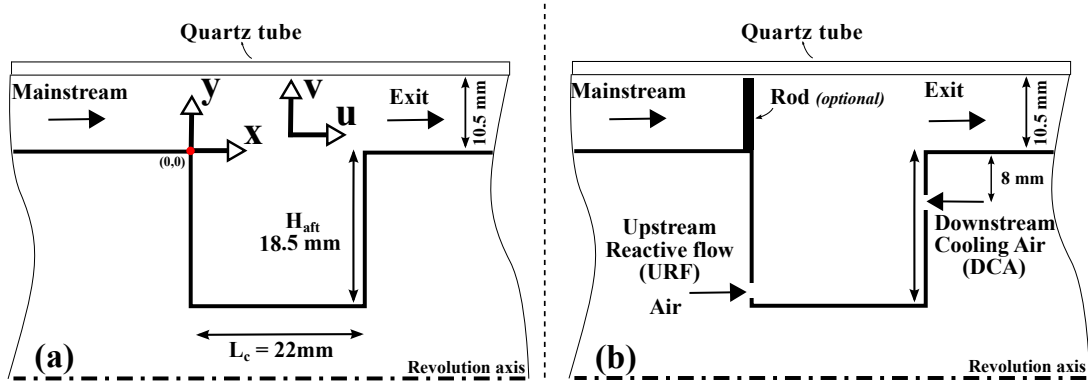


Figure 3.9: Cavity region arrangement used for inert studies. The burner was operated at ambient pressure  $P_{\text{glob}} = 0.1 \text{ MPa}$ . Two geometries were investigated: (a) a passive cavity with no mass injection systems in the cavity and, (b) an active cavity with two mass flow injection systems (by means of slots)

pure air (it was a premixed mixture of air and  $\text{CH}_4$  in reactive conditions). Note in Fig. 3.9 the nomenclature used for the two velocity components:  $u$  represented the axial velocity and  $v$  represented the radial velocity component.

### 3.3 High-speed particle image velocimetry (HS-PIV)

#### 3.3.1 Presentation of the technique

The PIV is a laser technique based on the Mie scattering and aims to determine an instantaneous velocity vector field. More precisely, its principle lies on extracting the displacement of particles which have been artificially seeded in the flow. A thin laser sheet illuminates the flow and the Mie scattering of particles is recorded on two images, taken at two distinct times (with a controlled delay  $\Delta t$ ). To have access to the quantitative vector fields, images are sampled using several interrogation windows<sup>3</sup> and the most likely displacement of particles is then evaluated. Thus, the velocity vector in each window is easily deduced as

$$\mathbf{u} = \frac{\Delta x_t^{t+\Delta t}}{\Delta t}. \quad (3.3)$$

where  $\mathbf{u}$  is the velocity vector estimated in one interrogation window and  $\Delta x_t^{t+\Delta t}$  is the sta-

<sup>3</sup>One interrogation window contains several pixels.

tistical displacement of particles in the window of interest. Note that the PIV does not calculate velocity of individual particles. Indeed, the statistical displacement  $\Delta x_t^{t+\Delta t}$  is estimated with a cross-correlation method [232] and the location of the correlation peak. The major challenge is to accurately estimate the correlation peak location, which best represents the relation between one image pair.

Thus, the PIV technique lies on a statistical treatment and the final velocity vector field is locally averaged (one vector for one interrogation window containing several particles). Because this technique indirectly assesses the local flow velocity, several biases can affect the error and uncertainty of PIV measurements [231]. Next sections gives an overview of the most relevant biases encountered with the PIV technique.

### 3.3.2 Estimation of the accuracy of PIV

#### Uncertainty of PIV

Several errors can bias the PIV technique: the flow seeding, signal-to-noise ratio, flow topology, out-of-plane particle motion, and the choice of an interrogation window can affect the final velocity vector field [231].

*Particle seeding:* the PIV technique assumes that particles are ideal flow tracers: they accurately follow the flow without being intrusive (aerodynamically or chemically). The Stokes number is commonly used to assess if particles are accurate tracers,

$$St = \frac{\tau_p}{\tau_t}. \quad (3.4)$$

The Stokes number is defined as the ratio of the particle relaxation time  $\tau_p$  to a characteristic turbulent time of the flow  $\tau_t$ . The characteristic time of the particle can be written as

$$\tau = \frac{\rho_d d_d^2}{18\mu_g}, \quad (3.5)$$

where  $\rho_d$  is the density of the particle,  $d_d$  is the diameter of the particle, and  $\mu_g$  is the dynamic viscosity of the flow [222]. Thus, smallest time scales of the fluid must be always greater than

the relaxation time of particles. Eq. 3.5 implies that the size distribution of particles should be as mono-disperse as possible.

The particle seeding density also plays an important role: Raffel et al. [184] carried out Monte Carlo computations and demonstrated that an increase of the particle seeding density from 5.2 to 32 led to a reduction in the measurement uncertainty (of a factor three).

The size of the imaged particle can affect the peak detection. In fact, Raffel et al. [184] showed that an optimum particle image diameter could reduce the uncertainty, whatever the interrogation window considered. He found that particle images larger than 2 pixels drastically reduced the peak locking bias<sup>4</sup> [180].

*Correlation peak determination:* because of the pixel discretization, an uncertainty of  $\pm 0.5$  pixel appears on the final peak location. Depending on applications, this error can significantly affect measurements. Several methods were developed in order to obtain a sub-pixel accuracy. For instance, use of curve-fitted functions<sup>5</sup> can give a final accuracy of 0.01 pixel [232]. Unfortunately, these methods require a minimum imaged particle size of 2 pixels [232].

*Spatial discretization:* because a statistical analysis is performed on each interrogation window, a minimum amount of particles is necessary in the region of study. The uncertainty was found to be increased when the size of the window was decreased [184]. Furthermore, increasing the amount of particles does not necessarily increase the accuracy of the measurement. In fact, more particles are prone to be lost from one image to another (especially next to boundaries of the window) and losses can also occur from an out-of-plane motion. Rouland [196] argued that the ideal displacement should be less than 30% of the interrogation window length. In order to take into account particle losses, windows are overlapped [135, 231] and it is still possible to vary the time delay  $\Delta t$  between the two images in order to roughly adjust the displacement of particles. Another issue is related to the flow topology. Determination of flow velocities in regions exhibiting large gradients makes the size (and the shape) of the interrogation window important. A compromise has then to be found in order to reduce the different biases while conserving a rather good flow fidelity.

---

<sup>4</sup>When the particle image size is too small, peak locking bias appears. Intentional defocus of the camera lens aims to slightly blurry the images and increase the size of the imaged particle.

<sup>5</sup>P arabolic or gaussian.



### Spatial resolution

As explained in the previous section, the spatial resolution of the PIV depends on the experimental setup and post-processing procedures used to extract velocity vector fields: largest scales directly depend on the size of the image whereas smallest ones are related to the size of one interrogation window [169]. Reducing the size of the interrogation window may increase the spatial resolution at small scales but Willert et al. [232] reported that the uncertainty was also increased.

Foucaut et al. [72] introduced an experimental technique based on a spectral analysis to determine the effective spatial range resolved by a specific PIV setup. This step is of great importance when analyzing detailed measurements (e.g., small structures, dissipation term in turbulence). The methodology implemented hereafter was used by Foucaut et al. [72] and Krawczynski [126] et al.. An example is given in Fig. 3.10 and depicts typical measured and decompensated energy spectra for the axial velocity fluctuations  $u'^6$ . The slight deviation at small scales between the two spectra demonstrates that the PIV had a low-pass effect on data and could not measure accurately small structures.

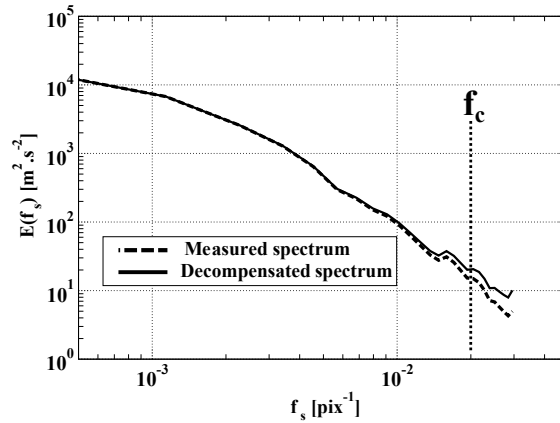


Figure 3.10: One dimensional cut in the 2D averaged spectrum, for measured (—) and decompensated (.....) spectra of the axial velocity fluctuation  $u'$ .

It is crucial to understand that when a measured spectrum is extracted (.....), noise is already included (additive as a first approach) and is altered by the PIV processing (convolution by a transfer function). Then, the following equation can be written as

<sup>6</sup>Spectra have been obtained with Liu et al. [150] and Krawczynski [127] methodology.

$$E_{PIV} = E_{TRUE} \cdot h(f_s), \quad (3.6)$$

where  $E_{PIV}$  is the measured energy spectrum,  $E_{TRUE}$  is the real energy spectrum, and  $h(f_s)$  is the transfer function of the PIV system. Therefore, with the determination of  $h(f_s)$ , it was therefore possible to have access to the real spectra  $E_{TRUE}$  with Eq. 3.6.  $E_{TRUE}$  corresponds to the continuous line in Fig. 3.10. Thus, the experimental procedure is twofold:

- *Determination of the PIV transfer function  $h(f_s)$* : Lourenco & Krothapalli [152] suggested to model the low-pass behavior of the PIV technique with a *sinc* function as

$$h(f_s) = \text{sinc}^2(X/2f_s). \quad (3.7)$$

$X$  is the size of the interrogation window, and *sinc* is the cardinal sine function corresponding to the Fourier transform of a unit step function. Results are given in Fig. 3.11 and shows the one dimensional cut in the 2D transfer function energy spectra for two different interrogation windows (i.e., 16x16 and 32x32  $pix^2$ ) and for two overlap values (i.e., 50 and 75%). The low-pass effect can be seen on all curves and structures smaller than the interrogation window cannot be resolved. By setting the cut-off frequency  $f_c$  when the energy is attenuated by -3 dB <sup>7</sup>, it is then possible to determine the spatial range resolved by the PIV. For instance, at 32x32  $pix^2$  and 50% overlap (○ in Fig. 3.11), the spatial range went from  $f_{max}$  (the largest structure given by the image size) to  $f_c$  (the smallest resolved scale). Note that increasing the overlap or decreasing the final interrogation window do not necessary lead to a better resolution as noise as also increased [72].

- *Decompensate the measured spectrum*: With Eq. 3.8, it was then possible to extract the real PIV spectrum as

$$E_{TRUE} = \frac{E_{PIV}}{h(f_s)}. \quad (3.8)$$

---

<sup>7</sup>Arbitrary choice.

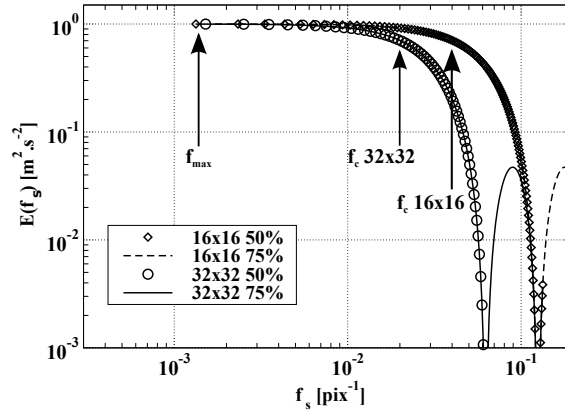


Figure 3.11: 1D cut in the 2D modeled transfer function energy spectra for two different interrogation windows (i.e.,  $16 \times 16$  and  $32 \times 32 \text{ pix}^2$ ) and for two overlap values (i.e., 50 and 75%).

The cut-off frequency which was obtained from the modeled PIV transfer function (Fig. 3.11) was reported on the decompensated spectrum in order to obtain the spatial resolution of the PIV system. The value of  $f_c$  is drawn in Fig. 3.10. The processing using an interrogation window of  $32 \times 32 \text{ pix}^2$  with a 50% overlap led to a small deviation between the measured and decompensated spectra (and without any additional corrections). Finally, the present measurements had a spatial resolution lying between 1.25 mm and 22 mm.

### Experimental arrangement

Temporal and spatial velocity measurements were achieved with HS-PIV. A 2.5 kHz double cavity Nd:YLF Laser (Darwin Dual, Quantronix) operating at 527nm gave two laser beams separated from 10 to 30  $\mu\text{s}$ , according to the flow conditions. Olive oil droplets were seeded through the different injection systems, and were controlled via a by-pass network to ensure a homogeneous seeding (Fig. 3.12(a)). The laser beams were expanded through a set of lenses to create a 35mm laser sheet in height. The collection system consisted of an high-speed camera (Photron Fastcam SA1.1) equipped with a Nikon f/2.8 105mm macro lens. The camera was operated at full resolution (i.e.,  $1024 \times 1024 \text{ pix}^2$ ) with a resulting magnification ratio of 40.8 pixel/mm. The HS-PIV image processing was achieved with a multi-pass interrogation window algorithm (dynamic Studio, Dantec) with a final size of  $32 \times 32 \text{ pix}^2$  (vector spacing of 0.8 mm). A total of 2728 images, corresponding to an acquisition time of 1.1s were recorded for each flow

condition<sup>8</sup>.

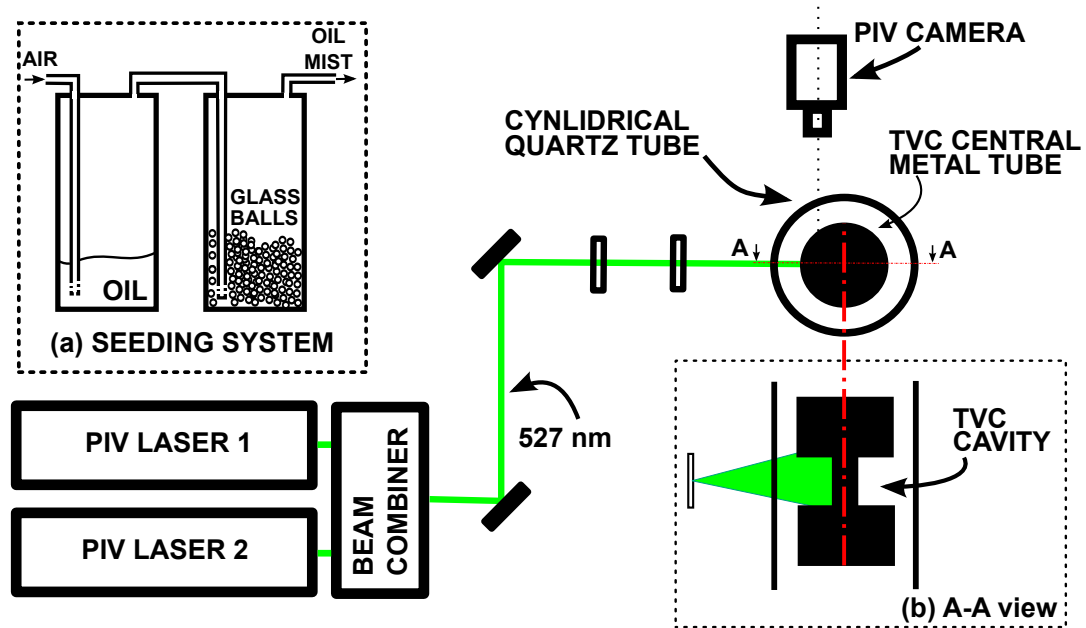


Figure 3.12: Schematic illustration of the HS-PIV in inert conditions. (a) apparatus used to seed the flow; (b) A-A view (from the camera)

<sup>8</sup>A parametric study on the number of images has been performed on the three first statistical moments (mean, standard deviation and skewness), in order to validate that a convergence was reached.

### 3.4 Global flow topology

In order to investigate the complex flow structure encountered in our TVC and have a better understanding of the combustion dynamics observed in Chap. 2, this section discusses the global characterization of a flow passing past a cavity. A comparison between a passive and an active cavity is given to appreciate effects of mass injection systems in the cavity. An investigation of turbulence levels as well as the existence of aerodynamic instabilities is conducted. A special attention is paid to quantify mass exchanges between the cavity and the mainstream.

#### 3.4.1 Inlet flow characterization and operating conditions

Inlet flow conditions at the cavity leading edge are of great importance because they can account for the development of instabilities [75]. For this reason, we took advantage of this characterization to validate our PIV measurements; that is, the mainstream mass flow rate was calculated *a posteriori* with the mean velocity vector field. Specifically, the radial profile of the mean axial velocity  $\bar{u}(y)$  was used with the following formula:

$$\dot{m}_m^o = \int_{\theta=0}^{\theta=2\pi} \int_{y=0}^{y=R} \rho_m^o \bar{u}(y) y dy d\theta = 2\pi \int_{y=0}^{y=R} \rho_m^o \bar{u}(y) y dy. \quad (3.9)$$

$\dot{m}_m^o$  is the mainstream flow rate of air,  $\theta$  is the angle around the revolution axis, and  $\rho_m$  is the density of the air in the mainstream. Because PIV data were obtained in one two-dimensional plane, the velocity profile  $\bar{u}(y)$  was assumed to be identical around the mainstream annular slot. Figure 3.13 shows a comparison between theoretical and calculated values. Note that the experimental error lied between 2-3%, which was considered to be negligible.

The upstream momentum thickness  $\theta_0$  was computed to characterize the upstream boundary layer. The latter is defined as

$$\theta_0 = \int_{-\infty}^{\infty} \frac{\bar{u}}{U_m} \left(1 - \frac{\bar{u}}{U_m}\right) dy. \quad (3.10)$$

$\bar{u}$  is the mean axial velocity and  $U_m$  is the mainstream bulk velocity. Because the present

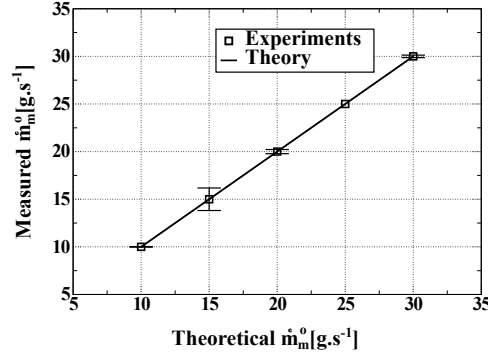


Figure 3.13: Mainstream mass flow rate calculation  $\dot{m}_m^o$  with PIV (Eq. 3.9). Comparison with theoretical values.

configuration was highly confined in comparison to most of previous studies,  $\theta_0$  was constant whatever the conditions and  $\theta_0 = 0.176$  mm.

Roshko found that for a fixed geometry, the mainstream velocity  $U_m$  controlled the apparition of coherent structures [75]. For this reason, we only considered varying the mainstream flow conditions while keeping cavity conditions and geometry constant. The configuration where no mass was injected in the cavity was named **NF** whereas the configuration with URF and DCA injection systems was named **2F**. Terms "active cavity" and "passive cavity" were used to denote the presence of injections (or not) in the cavity. Table 3.2 presents the operating conditions and the nomenclature used in the following sections.

Nomenclature	<b>NF</b>			<b>2F</b>		
	$\dot{m}_m^o$ [g.s <sup>-1</sup> ]	$U$ [m.s <sup>-1</sup> ]	$Re_h$	$\dot{m}_m^o$ [g.s <sup>-1</sup> ]	$U$ [m.s <sup>-1</sup> ]	$Re_h$
MAIN	10	3.8	2558	10	3.8	2558
	15	5.3	3500	15	5.3	3500
	20	7.8	5115	20	7.8	5115
	25	9.6	6475	25	9.6	6475
	30	10.8	7303	30	10.8	7303
DCA	0	0	0	1.0*	3.6	230
UCF	0	0	0	0.82*	6.0	385

Table 3.2: Nomenclature used for the inert investigation. **NF**: NOFLOWS (passive cavity); **2F**: 2FLOWS (active cavity). Reynolds numbers  $Re_h$  are based on the slot height  $h_m$ .  $U$  is the bulk velocity. \* These values have been chosen in accordance with the operating conditions given in Chap. 2 [235, 27].

### 3.4.2 Qualitative description of the flow topology in an active and passive cavity

Figure 3.14 presents the NF (top) and 2F (bottom) mean flow fields for a mainstream flow rate  $\dot{m}_m^o$  of  $30 \text{ g.s}^{-1}$ . Mean velocity vector fields are colored by the velocity magnitude (left), mean axial velocity  $\bar{u}$  (center), and mean radial velocity  $\bar{v}$  (right). Red arrows recall the location of the URF and DCA injection systems for the 2F configuration. In addition, streamlines are superimposed on the middle images.

Globally, the mainstream region was not significantly affected by the presence of the cavity neither flow injection systems. The shear layer zone also seemed to be confined to the interfacial zone separating the cavity from the main channel.

The NF configuration shows a single large clockwise vortex, locked in the cavity with a centroid located just above the cavity center ( $y_c = -6 \text{ mm}$ ). Note that this vortex was present for all mainstream mass flow rates and was mainly sustained by the partial entrainment of the main flow in the surroundings of the cavity trailing edge. Indeed, the flow intensity in this zone was higher in comparison to the whole cavity flow. Based on these observations, we conclude that this cavity was *open*, according to the classification of Plentovich [176].

When mass was injected in the cavity (i.e., DCA and URF), the mean flow topology radically changed (bottom images of Fig. 3.14). Similarly to the NF configuration, the mean topology was identical for all mainstream mass flow rates. However, differences appeared in the cavity, notably with the development of several vortices. In fact, two large counter-rotative vortices were retrieved, as described by Roquemoire et al. [192]: (1) a large anti-clockwise vortex at the cavity base, whereas (2) another one, more elongated, was located below the flow separation, inserted between the vortex (1) and the mainstream. In addition, a stagnation point (3) was clearly visible ( $x_{st} = 15 \text{ mm}$ ,  $y_{st} = -2 \text{ mm}$ ). The latter resulted from the competition between the DCA jet flow and the mainstream flow entrainment process. Upstream of the stagnation point (i.e.,  $x < 15 \text{ mm}$ ), the flow developed similarly to a passive cavity whereas beyond this point (i.e.,  $x > 15 \text{ mm}$ ), the DCA and URF flows became preponderant and greatly interfered with the shear layer. Corresponding radial mean velocities  $\bar{v}$  were relatively important next to

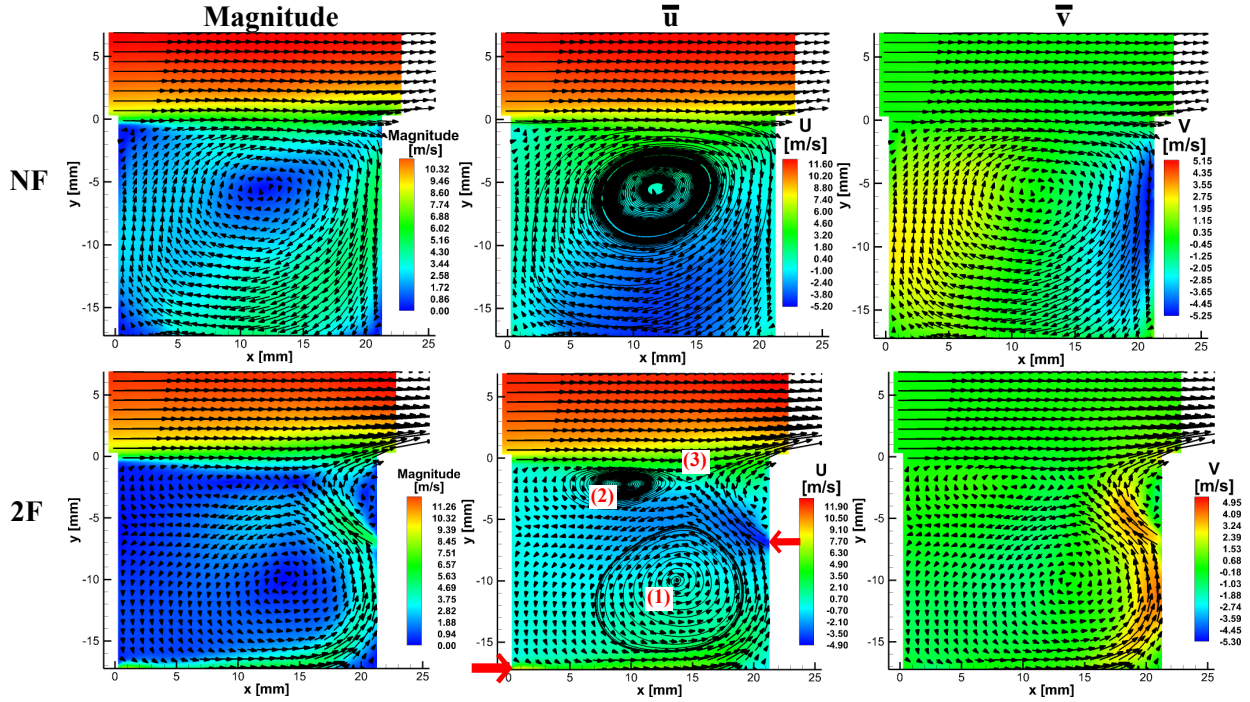


Figure 3.14: Mean velocity vector fields for the NF (top) and 2F (bottom). Mainstream mass flow rate  $\dot{m}_m = 30 g.s^{-1}$ . (left) Magnitude, (middle)  $\bar{u}$ , (right)  $\bar{v}$ .

the cavity trailing edge. Remarkably, instead of being oriented in the cavity, the DCA streamlines were slightly deflected towards the mainstream. The explanation for this jet behavior may come from the interaction with the URF flow. In addition to centrifugal effects, Tab. 3.2 shows that the URF flow had a momentum flux twice larger than the DCA flow.

To conclude, injection of mass inside the cavity radically changed the mean flow field. The interfacial zone of the 2F configuration was more affected by the cavity injection systems. Remarkably, the topology of both configurations was independent on the incoming mainstream mass flow rate  $\dot{m}_m^o$ . However, these qualitative insights did not enable us to assess the flow unsteadiness. Note that we did not vary conditions in the cavity but Burguburu et al. [27] highlighted several cavity flow structures, primarily piloted by the URF and mainstream bulk velocities.



### 3.4.3 Mass exchanges fluxes between the cavity and the mainstream flows

Hsu et al. [104] argued that when a vortex was locked inside the cavity, the resulting flow dynamics was quite stable but very little fluid was exchanged between the cavity and the mainstream. In order to enhance the flame stability in a TVC, Hsu directly added flow injection systems in the cavity to improve mass and heat transfers. This section focuses on assessing mass interactions between these two regions.

#### Definition of parameters

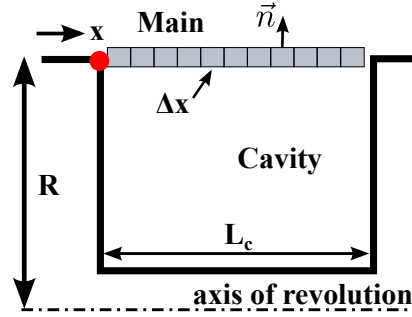


Figure 3.15: Schema presenting the calculation principle of local mass transfers along the interfacial zone between the cavity and the mainstream.

We used the radial velocity profile  $v(x, R)$  along the interfacial zone between the cavity and the mainstream (Fig. 3.15) to estimate mass flow transfers  $\Delta\dot{m}$ , defined as

$$\Delta\dot{m} = \int_{\theta=0}^{\theta=2\pi} \rho \mathbf{u} \cdot \mathbf{n} \Delta x R d\theta = 2\pi R \rho v(x, R) \Delta x, \quad (3.11)$$

where  $\Delta\dot{m}$  is the local mass transfer taken on a distance  $\Delta x$ ,  $\theta$  is the revolution angle along the axis of the burner,  $\rho$  is the density of air,  $R$  is the inner radius of the TVC combustor, and  $\mathbf{n}$  is a normal vector chosen to point out towards the main channel. Therefore, mass ejected from the cavity to the main channel accounted for a positive contribution and  $\mathbf{u} \cdot \mathbf{n} = v$ . Because velocity vector fields were discretized (cf. Sec. 3.3), a flat profile was considered in each window of length  $\Delta x$ . Moreover, the local mass transfer  $\Delta\dot{m}$  was integrated around a ring of radius  $R$ . Therefore, a normalized contribution was defined in order to take into account the mainstream flow variations:

$$Y = \frac{\Delta \dot{m}}{\dot{m}_m^o} \times 100. \quad (3.12)$$

With Eq. 3.12, mean and fluctuating information were derived, taking the mean and r.m.s profiles, and defined as

$$\bar{Y} = \frac{\overline{\Delta \dot{m}}}{\dot{m}_m^o} \times 100 \quad \& \quad Y^{rms} = \frac{\{\Delta \dot{m}\}^{rms}}{\dot{m}_m^o} \times 100. \quad (3.13)$$

### Bi-dimensional vs. three-dimensional flow field

As mentioned in Chap. 1, the TVC was designed in order to reduce boundary effects and asymmetries. We then investigated to what extent the flow was two-dimensional. Streamlines in Fig. 3.14 merged rapidly next to the vortex centroid and could indicate that the flow field was not perfectly two-dimensional. Therefore, we calculated all terms of the continuity equation, defined as

$$\frac{\partial \rho}{\partial t} + \text{div}(\rho \mathbf{u}) = 0. \quad (3.14)$$

Because the flow was incompressible (i.e.,  $\rho$  was constant) and that we obtained planar information with our PIV technique (i.e.,  $\mathbf{u} = [u, v]$ ), it was possible to write Eq. 3.14 in cylindrical coordinates as

$$\underbrace{\frac{\partial \bar{u}}{\partial x}}_{\text{grad}(u)} + \frac{1}{y} \underbrace{\frac{\partial (y\bar{v})}{\partial y}}_{\text{grad}(v)} = 0. \quad (3.15)$$

We considered the interface between the cavity and the main channel, and a mainstream mass flow rate  $\dot{m}_o^m$  of  $30 \text{ g.s}^{-1}$ . Therefore, because the total mass was unchanged (i.e., mass entering the cavity had to exit the cavity), the sum of the two left-hand side terms of Eq. 3.15 could be null. Results are plotted in Fig. 3.16, for the NF (left) and 2F (right) configurations. Note that their sum was not null, confirming that a third contribution was necessarily involved to balance this mass budget. **Therefore, we only considered two-dimensional data in**

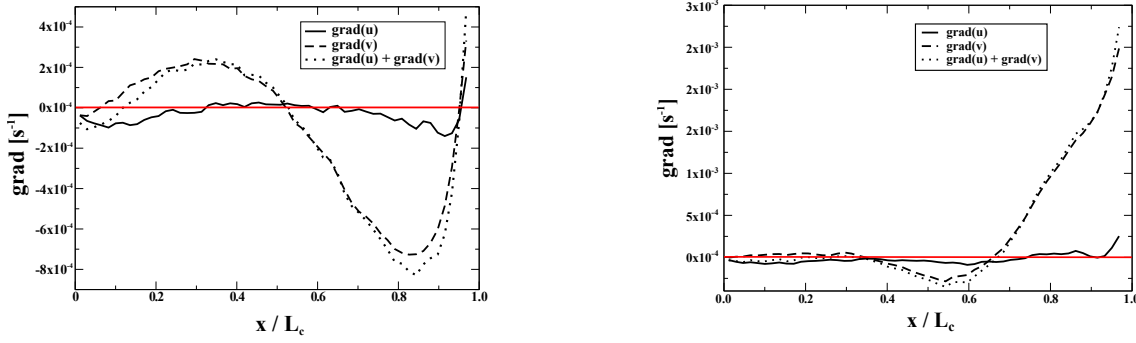


Figure 3.16: Validation of the continuity equation along the interface between the cavity and the main channel (red line). left: NF; right: 2F. Mainstream flow rate  $\dot{m}_o^m = 30 \text{ g.s}^{-1}$ .

the rest of this text while keeping in mind about the fact that the flow was surely three-dimensional.

### NF configuration

Figure 3.17 presents the normalized mass transfer profile  $\bar{Y}$  along the cavity, for different mainstream mass flow rates  $\dot{m}_m^o$ .

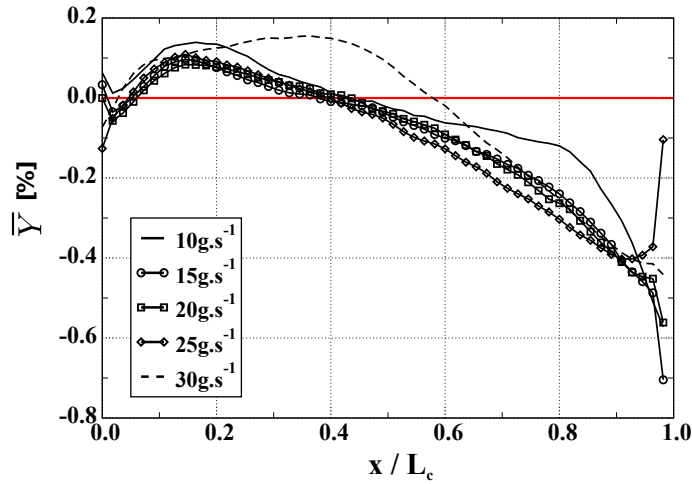


Figure 3.17: Normalized mean mass transfer profiles  $\bar{Y}$  along the cavity interface ( $y = 0 \text{ mm}$ ) for different mainstream flow rates  $\dot{m}_m^o$ . NF configuration.

Note that the different curves almost collapsed and had globally the same trend whatever the mainstream mass flow rate considered. Because the geometry was unchanged, the cavity aspect ratio seems to dictate local mass transfers.

Detailed analysis shows a large zone with negative values for  $x/L_c > 0.4$  and clearly put in evidence the mainstream mass entrainment process next to the cavity trailing edge. This phenomenon is comparable to the one highlighted by Rockwell [189]. The shear flow impingement upon the cavity trailing edge resulted in the well established vortex (see Fig. 3.14) and induced the strong clockwise recirculation zone. The latter also interacted with the mainstream: a slight ejection process was visible next to the cavity leading edge, when  $0.1 < x/L_c < 0.3$ .

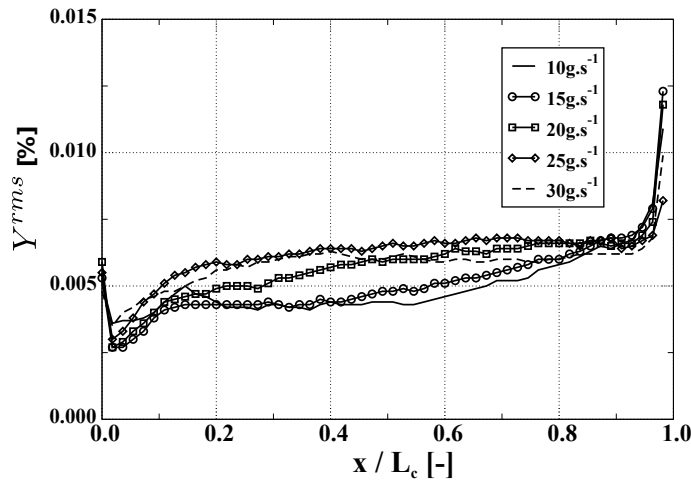


Figure 3.18: r.m.s of the mass transfer profile along the cavity interface ( $y = 0$  mm) for different mainstream flow rates. NF configuration.

Mass exchange fluctuations  $Y^{rms}$  along the cavity are depicted in Fig. 3.18. Again, the different curves had the same trend, even if values were not perfectly identical. Fluctuations were increased as the cavity trailing edge was reached: this was the proof that a large flow unsteadiness associated with the impingement of the shear layer occurred next to the trailing cavity corner.

## 2F configuration

Normalized mass transfer profiles  $\bar{Y}$  are shown in Fig. 3.19 for different mainstream mass flow rates  $\dot{m}_m^o$ .

Remarkably, all mass transfer profiles behaves differently from the NF configuration. In fact,

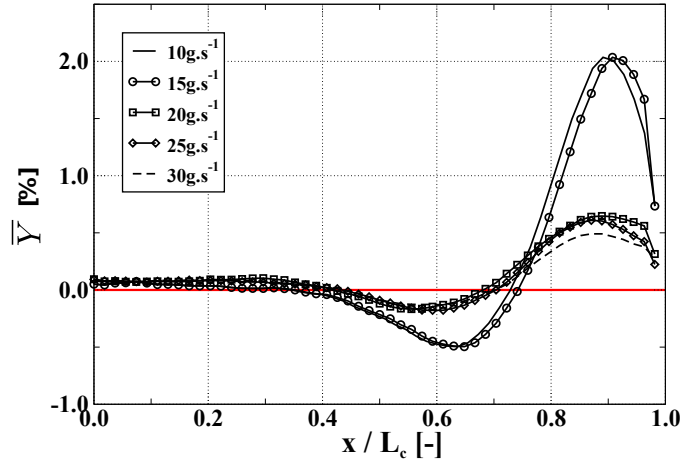


Figure 3.19: Normalized mean mass transfer profiles  $\bar{Y}$  along the cavity interface ( $y = 0$  mm) for different mainstream flow rates  $\dot{m}_m^o$ . 2F configuration.

most of mass transfers occurred in the second half of the cavity. For  $x/L_c < 0.4$ , almost no mass was exchanged whereas beyond this point, a strong mass ejection process was highlighted, especially next to the cavity trailing edge. As shown in Fig. 3.14, the URF and DCA flows were significantly affecting the interfacial shear layer for  $x/L_c > 0.8$ . In addition, the amplitude of the mass ejection process was dependent on the mainstream mass flow rate; a bifurcation occurred when  $\dot{m}_m^o$  was lying between 20 and 25  $g.s^{-1}$ . Below this critical value, mass exchanges were greatly important and location of this strong aerodynamic instability was in agreement with heat release dynamics (i.e.,  $CH^*$  traces) observed in Chap. 2.

This flow dynamics demonstrated that the strength of the main flow (or its impulsion) played a crucial role in confining the cavity flow dynamics and the resulting mass transfers. Furthermore, the appearance of the flow ejection process may necessarily affect the shear layer and deteriorate the different stabilization mechanisms.

Analysis of the corresponding r.m.s profiles  $Y^{rms}$  in Fig. 3.20 confirms that the reduction of the mainstream mass flow rate was accompanied with larger r.m.s values, and this observation was either confirmed with the flame dynamics (Chap. 2): increasing the mainstream flow rate may confine the location of burned gases at the flow separation and then improve flame stabilization. Figures 3.19 and 3.20 also shows that the flow unsteadiness was increased in comparison with the NF configuration, primarily due to the presence of cavity injection systems. We then consider

to further our analysis on characterizing turbulence and presence of coherent structures.

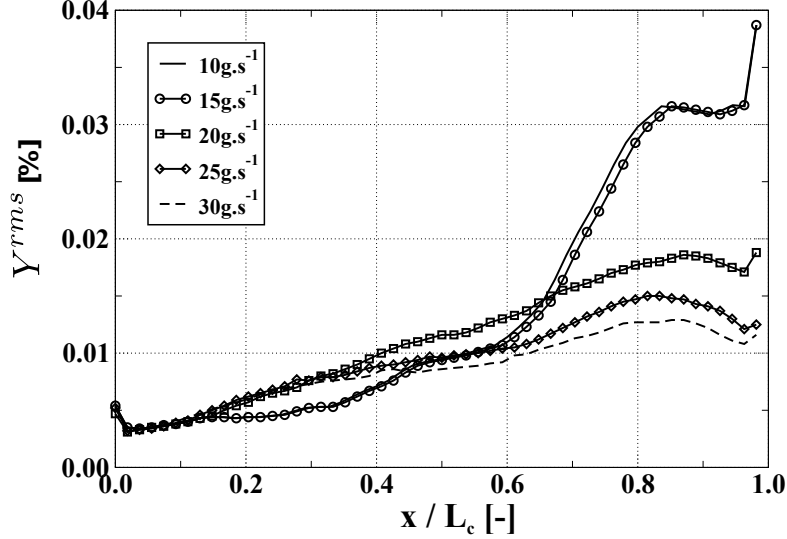


Figure 3.20: r.m.s of the mass transfer along the cavity interface ( $y = 0\text{mm}$ ) for different mainstream flow rates. 2F configuration.

### 3.4.4 Turbulent features

The previous section showed that the flow could present unsteady features when mass was directly injected in the cavity. Therefore, we analyzed velocity fluctuation properties.

First the isotropy level was investigated in order to assess if turbulence was preponderant in one preferential direction. Among others, the isotropy  $I_s$  is defined as

$$I_s = \frac{\overline{u'^2}}{\overline{v'^2}}. \quad (3.16)$$

$I_s$  relates the ratio between axial velocity fluctuations  $u'$ , and radial velocity fluctuations  $v'$ .

Figure 3.21 depicts the isotropy coefficient  $I_s$  for the NF (left) and 2F (right) configurations and for a mainstream flow rate  $\dot{m}_m^o$  of  $10\text{g.s}^{-1}$ . Axial fluctuations  $u'$  were largely preponderant at the interfacial zone separating the cavity from the main channel ( $u' \approx 2.5v'$ ), and this conclusion was true for the two configurations. However, for the 2F configuration, a sudden bifurcation in  $I_s$  values was found next to the cavity trailing edge. Indeed, we previously showed that this region

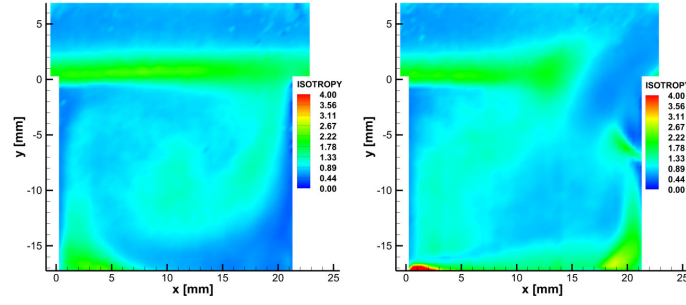


Figure 3.21: Isotropy coefficient  $I_s = \overline{u'^2}/\overline{v'^2}$  for a mainstream mass flow rate  $\dot{m}_m^o$  of  $10g.s^{-1}$ . Left: NF; Right: 2F.

was highly unstable, primarily due to the interactions between the cavity and the mainstream; the flow separation was mainly piloted by axial fluctuations ( $\overline{u'^2} \gg \overline{v'^2}$ ) until it encountered the surroundings of the cavity trailing edge, where radial fluctuations  $v'$  became preponderant. Because the mainstream flow was aerodynamically affected by this mass ejection, the mean axial velocity  $\bar{u}$  was compressed, which in turn produced large velocity fluctuations. Remarkably, the stagnation point highlighted in Fig. 3.14, corresponded to the bifurcation. Similarly to the flow structure, the isotropy distribution was not found to change when the mainstream flow rate was varied.

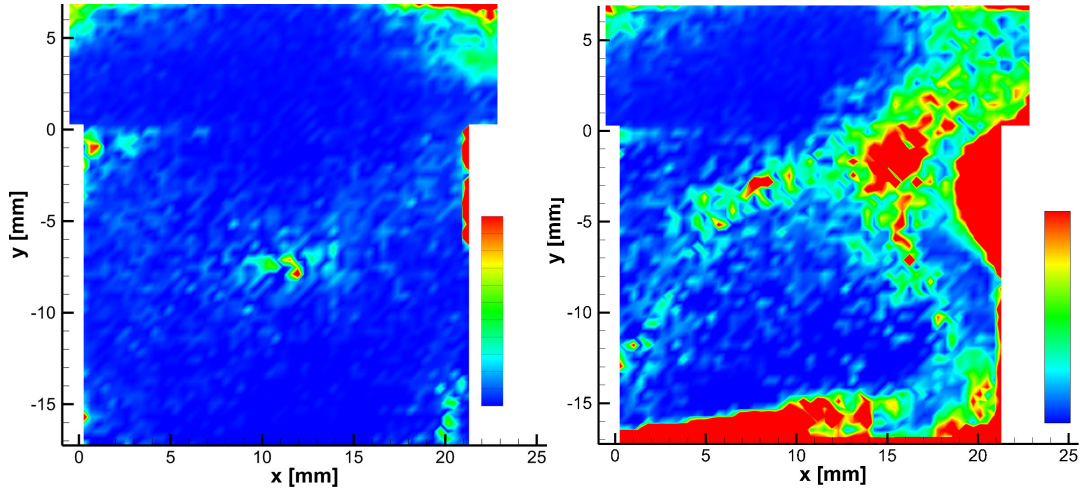


Figure 3.22: Turbulence intensity  $I_t = (u'^2 + v'^2)^{0.5}/(u^2 + v^2)^{0.5}$  for the NF (left) and 2F (right) configuration and for a mainstream mass flow rate  $\dot{m}_m^o$  of  $10g.s^{-1}$

Turbulence intensity, named  $I_t$ , was also investigated. It gives an information on the turbulence distribution, being defined as the ratio of the velocity fluctuation magnitude and the velocity magnitude:

$$I_t = \frac{\sqrt{u'^2 + v'^2}}{\sqrt{u^2 + v^2}}. \quad (3.17)$$

Figure 3.22 shows the  $I_t$  field encountered in the NF and 2F configurations, and for a main-stream flow rate  $\dot{m}_m^o$  of  $10g.s^{-1}$ . Regarding the 2F configuration, the turbulence intensity was preponderant next to the cavity trailing edge, in the surroundings of the stagnation point (presented previously, cf. Fig. 3.14), and next to the cavity injection systems. This confirms that the cavity featured a relatively high level of turbulence, which could effectively improve mixing in the pilot region (in reactive conditions). In contrast, the NF configuration had a quite low level of turbulence, primarily due to the presence of the stable vortex in the cavity [24].

### 3.4.5 Coherent Structures

We showed that the 2F configuration featured an important flow unsteadiness next to the cavity trailing edge. With high-speed measurements, it was possible to extract time series data and detect any coherent structures along the interfacial shear layer zone. Sarohia [199] studied effects of cavity dimensions (i.e., length, depth) to initiate such instabilities. He found that a minimum cavity length had to be reached to observe these oscillations. Similarly, he concluded that for an existing geometry, a minimum incoming velocity had to be reached with unchanged upstream conditions (which was the case here as  $\theta_0$  was constant due to the combustor confinement). In order to investigate the occurrence of coherent structures associated to a vortex shedding process, eight velocity time series were extracted along the cavity interfacial zone, and used to perform a spectral analysis. Figure 3.23 presents the different probe locations and the corresponding numbering. All probes were located at  $y = 0$  mm and the distance between two consecutive probe was 2.7 mm (slightly larger than the smallest resolved scale with PIV). We used a one-sided fast Fourier transform (FFT) with the Welch method [230]. The lowest resolved frequency was estimated in order to obtain at least ten coherent oscillations in the recorded signal whereas the maximum frequency only depended on the Nyquist cut-off frequency. This led to a resolved frequency range going from 28Hz to 1250Hz<sup>9</sup>.

Note that no coherent structures were observed for the NF configuration, whatever the range

---

<sup>9</sup>Tests were performed in order to determine the accurate parameter used in the Welch method. The Parseval equation (Eq. 2.7) was verified to validate our post-processing. A 2% deviation was found with 5 windows and a 60% overlap. This result was considered to be negligible.



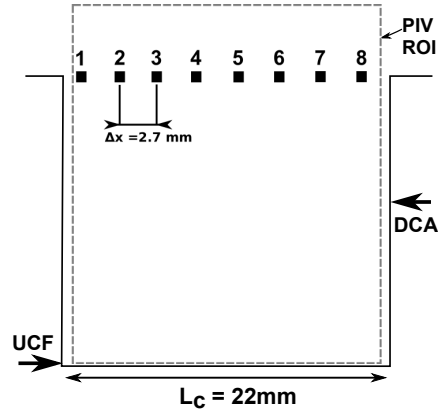


Figure 3.23: Scheme of the probe locations along the cavity interface.

of operating conditions investigated, and were in accordance with Sarohia [199] and Gharib [75] results; that is, the cavity length used here may be smaller than the critical one to initiate induced flow oscillations.

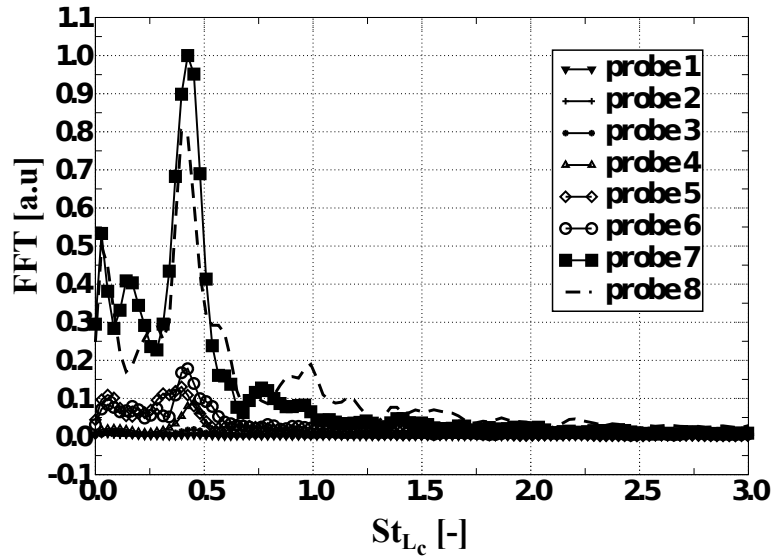


Figure 3.24: FFTs for the 2F configuration, with a mainstream mass flow rate  $\dot{m}_m^o$  of  $10g.s^{-1}$ .

Figure 3.24 depicts FFTs of radial velocity fluctuations  $v'$  in the 2F configuration, for a mainstream mass flow rate  $\dot{m}_m^o$  of  $10g.s^{-1}$ . Results are plotted as a function of the Strouhal number, defined as

$$St_{L_c} = \frac{fL_c}{U_m}. \quad (3.18)$$

$f$  is the frequency of the periodic phenomenon,  $L_c$  is the length of the cavity, and  $U_m$  is the mainstream bulk velocity. A coherent phenomenon is clearly visible next to the cavity trailing edge, especially at probes 7 and 8. This coherent phenomenon was appearing progressively as the probe was closer to the cavity trailing edge (a peak appeared at probe 5). The frequency of this coherent structure was 77 Hz. Remarkably, this instability was already highlighted by Burguburu et al. [27], but with another laser technique (i.e., laser doppler anemometry). Because the coherent motion was only preponderant in the second half of the cavity, the appearance of a vortex shedding process was unlikely. Nevertheless, a large-scale mass exchanges appeared between the cavity and the mainstream and may be the primary reason explaining this coherent flow unsteadiness. Unfortunately, the characteristic period of this aerodynamic instability was not matching the acoustic frequency observed in reactive conditions ( $f_0 = 122\text{Hz}$ ), and confirmed that coupling with combustion was more complex (cf. 2).

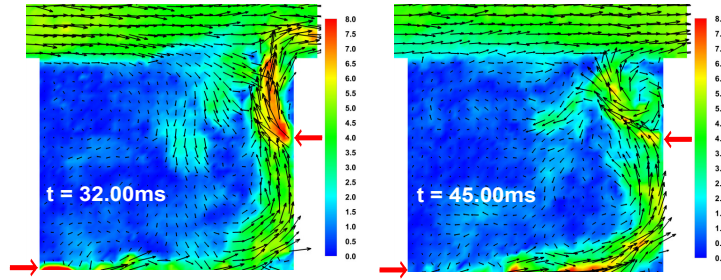


Figure 3.25: Two instantaneous PIV measurements for the 2F configuration. Main flow rate of  $10g.s^{-1}$ .

Visualization of two instantaneous velocity vector fields in Fig. 3.25, confirmed the previous conclusion: an ejection process occurred next to the cavity trailing edge. A strong cavity flow ejection was clearly evident at  $t = 32$  ms, disturbing largely the main channel, whereas at  $t = 45$  ms, it was oriented in the cavity, with almost no more interactions with the main channel. The characteristic period for this flow oscillation was in agreement with the Strouhal number  $St_{L_c}$  depicted in Fig. 3.24.

We suggest that the mainstream flow rate (or its impulsion) may have a great importance in the annihilation of such flow oscillation. Figure 3.26 reports the evolution of the first mode extracted at probe 7, and for several mainstream flow rates. The frequency of oscillations as well as their amplitudes were lowered and finally disappeared in the turbulence broadband spectrum when the mainstream flow rate was increased. The cavity flow oscillation was damped when the

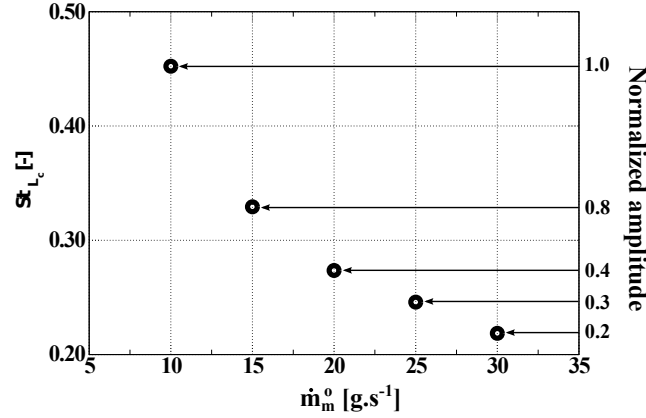


Figure 3.26: Evolution of the Strouhal number  $St_{L_c}$  (1<sup>st</sup> mode) with the main mass flow rate

mainstream velocity was increased and was surely due to an impulsion balance which confined the cavity. Note that this simple design rule will be useful in next chapters (in particular in Chap. 5)

### 3.5 Characterization of the flow separation shear layer

Coherent oscillations which were highlighted in the 2F configuration were interacting with the interfacial shear layer. This section aims to investigate the latter zone in order to give a more detailed analysis and characterize effects of cavity injection systems.

#### 3.5.1 Self similar behavior

As described in Sec. 3.1.1, the present flow separation consisted in a turbulent shear layer and has received extensive attention [179]. However, some differences appear in our present experiment; that is, because the present geometry was highly confined, several modifications necessarily occurred [111]. To illustrate this concept, Fig. 3.27 depicts several profiles of the mean axial velocity  $\bar{u}$  taken in the middle of the cavity ( $x/L_c = 0.5$ ) and for different mainstream mass flow rates (NF configuration).

Axial velocity profiles far away from the shear layer (i.e.,  $y \neq 0$  mm) were not constant due to the presence of walls. This was even more true in the cavity where the presence of recirculation zones affected aerodynamics. We therefore concluded that a classical approach to treat the shear layer with two infinite velocities was not possible in our conditions. Analysis of profiles

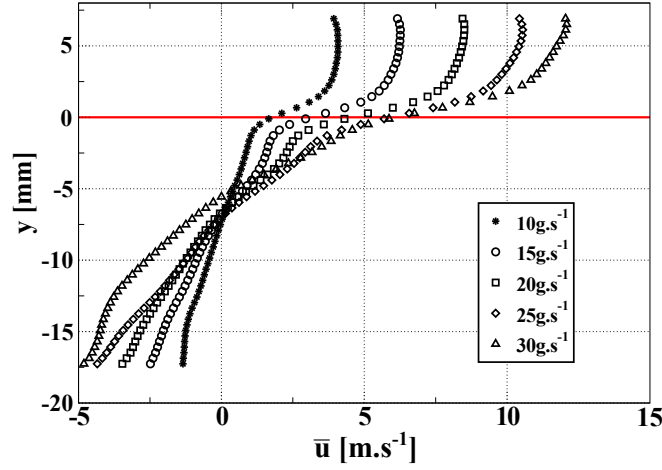


Figure 3.27: Mean axial velocity profiles  $\bar{u}(x/L_c = 0.5)$  for the NF configuration and for several main flow rates. Profiles extracted at  $x/L_c = 0.5$

show that the larger the mainstream flow rate was, the more strengthened the cavity recirculation velocity was. At this point, it was interesting to see if the shear layer was self-similar by using scaled variables introduced by Pope [179]:

$$\zeta = [y - \bar{y}(x)] / \delta(x) \quad \& \quad f(\zeta) = [\bar{u} - U_c] / U_s. \quad (3.19)$$

$\bar{y}(x)$  is a radial reference position, and  $\delta(x)$  is a characteristic flow width defined as

$$\begin{cases} \delta(x) = y_{0.9}(x) - y_{0.1}(x) \\ y_\alpha(x) := U_l + \alpha(U_h - U_l). \end{cases} \quad (3.20)$$

$U_c$  is the characteristic convection velocity, and  $U_s$  is the characteristic difference velocity, all based on two constant infinite velocities  $U_h$  and  $U_l$  (Fig. 3.28):

$$\begin{cases} U_c = 0.5(U_h + U_l) \\ U_s = U_h - U_l. \end{cases} \quad (3.21)$$

Figure 3.29 shows different axial scaled velocity profiles, taken along the cavity in the NF configuration. The mainstream mass flow rate  $\dot{m}_m^o$  was  $30 \text{ g.s}^{-1}$  and scaling parameters were chosen as follows:  $U_h$  was the axial bulk velocity, calculated in the main channel, and  $U_l$  was set

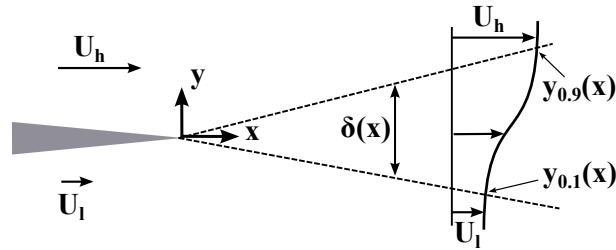


Figure 3.28: Schematic illustration depicting a typical shear layer and notations used to define the self-similar concept.

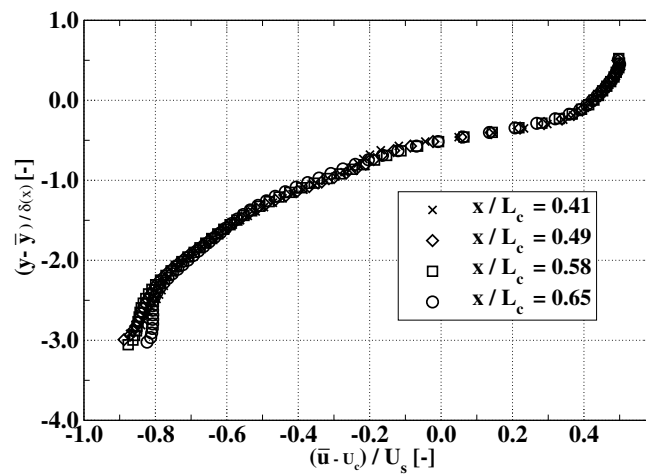


Figure 3.29: Scaled mean axial profiles, according to Pope [179], for a mainstream mass flow rate of  $30 \text{ g.s}^{-1}$

to a null value<sup>10</sup>. The graph shows that the resulting scaled profiles collapsed in the middle of the cavity, corresponding to approximately 30 to 40% of the total length of the cavity (i.e.,  $0.41 < x / L_c < 0.65$ ). Thus, the self-similarity was not valid next to the cavity walls, as Sarohia [199] concluded for a passive cavity. In addition, this result also shows that the shear layer was not altered at all by boundary effects in the middle of the cavity and could be assimilated to a classical free shear layer. Self-similar behavior was observed for all mainstream mass flow rate investigated in this study and was only valid in the middle of the cavity.

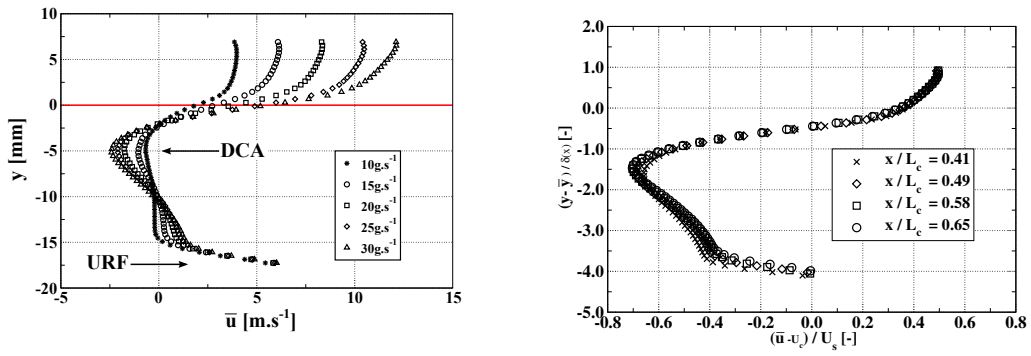


Figure 3.30: (Left) Axial mean velocity  $\bar{u}$  profiles for the 2F configuration and for several mainstream flow rates. Profiles extracted at  $x/L_c = 0.5$ . (Right) Scaled axial profiles for a main mass flow rate of  $30g.s^{-1}$ , at different locations.

The same methodology was performed for the 2F configuration. Cavity flow injections are clearly visible in Fig. 3.5.1-left: the URF injection systems, located at the cavity base, was not altered by the mainstream flow whereas some differences appeared for the DCA jet. This flow feature can be explained as follows: because the flow dynamics was more confined in the cavity when the mainstream flow rate increased (Sec. 3.4.3), it resulted in a higher jet penetration. Scaled profiles are shown in Fig. 3.5.1-right, and similarly to the NF configuration, profiles collapsed in the middle of the cavity. This shows that for a certain range along the cavity, effects of jet injection systems in the cavity did not tremendously alter the shear layer flow topology.

<sup>10</sup>Because the cavity flow structure resulted from an internal recirculation, we assumed the infinite cavity velocity to be null.

### 3.5.2 Evolution of the shear layer thickness

Insights about the spatial shear layer enlargement is of great importance in combustion because it can determine the level of mixing. The momentum thickness is commonly used to assess the shear layer growth, i.e.,

$$\theta = \int_{-\infty}^{\infty} \left\{ \frac{1}{4} - \left( \frac{u - \bar{u}}{\Delta u} \right)^2 \right\} dy. \quad (3.22)$$

An ambiguity appears in Eq. 3.22. Again, the difference of velocities  $\Delta u$  is defined with two constant velocities. Because the confinement and the recirculation flow in the cavity were not negligible in our case, this quantity could be greatly biased. Dimotakis [51] and Rowley [228] derived the vorticity thickness  $\delta_{\omega}^0$  and found that this parameter was a good estimator to assess the shear layer thickness growth,

$$\delta_{\omega}^0 = \frac{\Delta u}{|d\bar{u}/dy|_{max}}. \quad (3.23)$$

Note in Eq. 3.23 that the vorticity thickness  $\delta_{\omega}^0$  is calculated with a local measurement of the maximum shear and does not use the entire velocity profile. Rowley adapted Eq. 3.23 by replacing the velocity difference  $\Delta u$  by one infinite velocity. In the present study, the following formula was used:

$$\delta_{\omega} = \frac{\bar{u}_{max}}{|d\bar{u}/dy|_{max}}. \quad (3.24)$$

The evolution of the vorticity thickness (defined in Eq. 3.24) is shown in Fig. 3.31 for the NF configuration and for different mainstream mass flow rates  $\dot{m}_m^o$ . Note that when the mainstream mass flow rate was increased, the spreading rate (corresponding to the slope of the vorticity thickness) was almost constant all along the cavity. Moreover, the larger the mainstream mass flow rate was, the larger the spreading rate was, which could enhance the mixing process. All curves reached a maximum of vorticity thickness at  $x/L_c \approx 0.8$  and then collapsed rapidly due

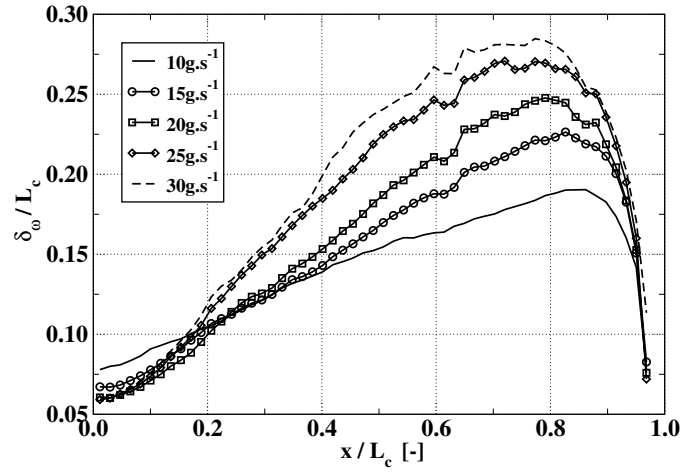


Figure 3.31: Evolution of the vorticity thickness  $\delta_\omega$  along the cavity, for the NF configuration and for different mainstream mass flow rates  $\dot{m}_m^o$ .

to the presence of the cavity trailing edge. The latter annihilated the development of the shear layer. Quantitative values of spreading rates were quite in agreement with the literature, even if it was intrinsically difficult to compare our results [51].

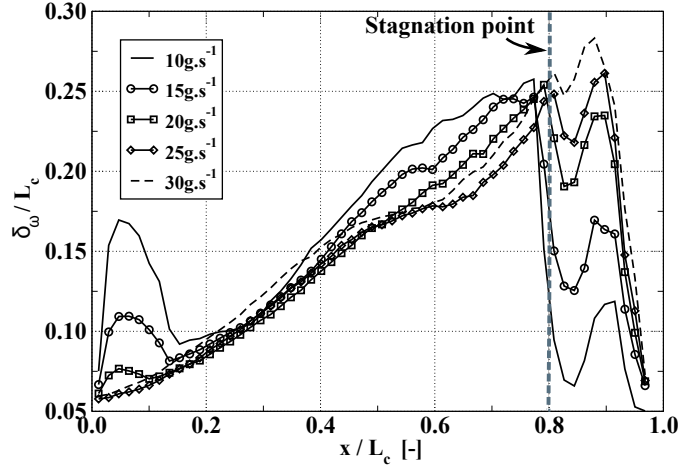


Figure 3.32: Evolution of the vorticity thickness  $\delta_\omega$  along the cavity, for the 2F configuration and for different main mass flow rates.

The evolution of the shear layer thickness along the cavity, for the 2F configuration and for different mainstream mass flow rates, are depicted in Fig. 3.32. Contrarily to the NF configuration, the shear layer spreading rate almost remained constant when the mainstream mass flow rate was increased. In fact, as shown in Fig. 3.5.1-left, the recirculation zone in the cavity remained unaffected by the mainstream conditions and partially controlled the shear layer region.



Thus, the development of the shear layer was almost the same. Next to the cavity trailing edge, the presence of the stagnation point at  $x/L_c \approx 0.8$  is clearly visible: curves were completely damped beyond this point and no conclusion was possible because this zone was subject to important interactions between the cavity and the shear flow.

### 3.5.3 Effects of cavity flow injections on the shear layer location

The previous section focused on the spreading rate and thickness of the shear layer. We now consider the spatial shear layer flow behavior. Many studies have been carried out on evaluating the shear layer locus  $y_{0.5}$ , defined as

$$y_{0.5} \leftrightarrow \frac{\bar{u}(y_{0.5})}{U_h} = 0.5. \quad (3.25)$$

This parameter was found to be a good estimator to spatially locate the shear layer. According to previous studies (Browand [23], Sarohia [199], Rockwell [189], Roshko [75]), the locus of a classical free shear layer was found to lie above the  $y=0$  line.

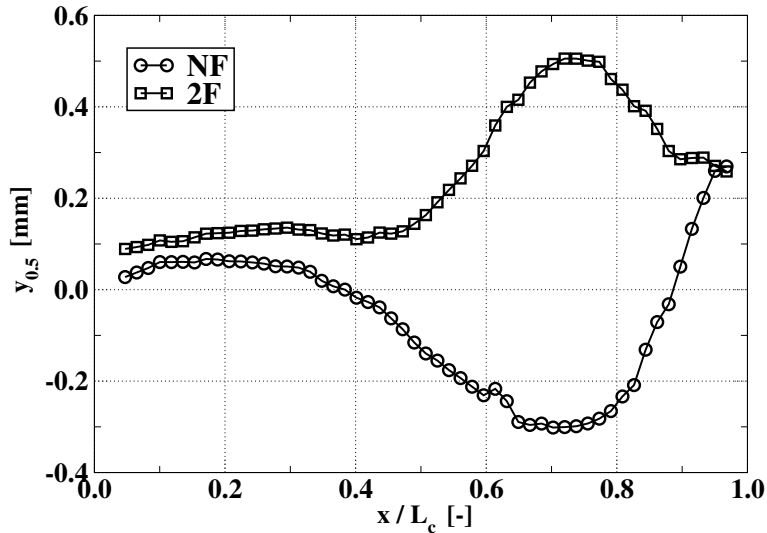


Figure 3.33: Comparison of locus  $y_{0.5}$  for the NF and 2F configurations, for a mainstream mass flow rate  $\dot{m}_m^o$  of  $10g.s^{-1}$

Figure 3.33 depicts the evolution of the shear layer locus  $y_{0.5}$  along the cavity, for the NF and 2F configurations and for a mainstream flow rate  $\dot{m}_m^o$  of  $10g.s^{-1}$ . Contrarily to previous results on passive cavities, the locus in the NF configuration was located above ( $x/L_c < 0.4$ ) and below

the y-0 line ( $0.4 < x/L_c < 0.9$ ). Because the experiment was highly confined, the shear layer was forced to penetrate and enlarge itself in the cavity. Note that for  $x/L_c \approx 1.0$ , the shear layer seemed to reattach the y-0 line, primarily due to the presence of the cavity corner. Note that the larger the mainstream flow rate was, the stronger the cavity vortex was (determined by the mass entering the cavity), which limited the shear layer penetration below the y-0 line. The 2F configuration shows that its locus was, in major part, located above the cavity (especially for  $0.6 < x/L_c < 0.8$ ). This confirms that the cavity had a stronger recirculation zone, reinforced by the continuous jet injection systems. Because mass injected in the cavity was forced to exit the cavity region, the shear layer was blocked and even slightly displaced in the main channel.

### 3.5.4 Momentum budget

As mentioned in previous sections, because the shear layer zone was largely unsteady, it is then important to understand in details interaction mechanisms occurring between the mean flow structure and the observed flow fluctuations. For this reason, almost all terms of the Navier Stokes momentum equation were calculated in order to highlight preponderant effects. First, a classical Reynolds decomposition was implemented on velocities, leading to the mean Reynolds equations (presented here for the axial velocity  $u$ ):

$$\frac{\partial \bar{u}}{\partial t} + \bar{u} \frac{\partial \bar{u}}{\partial x} + \bar{v} \frac{\partial \bar{u}}{\partial y} + \overline{u' \frac{\partial u'}{\partial x}} + \overline{v' \frac{\partial u'}{\partial y}} = -\frac{1}{\rho} \frac{\partial \bar{p}}{\partial x} + \nu \frac{\partial^2 \bar{u}}{\partial x_i \partial x_i}. \quad (3.26)$$

We made some assumptions to simplify Eq. 3.26. The flow was considered to be steady while viscous effects were neglected. The flow was incompressible (inert conditions and low-mach number) and because the geometry was axisymmetric, a strong hypothesis on a purely two-dimensional flow was done:

- $H_1$ : Quasi steady flow
- $H_2$ : Viscous stress neglected
- $H_3$ : Incompressibility
- $H_4$ :  $\bar{w} \approx 0$  (out-of-plane velocity).

The following equations were derived (because of  $H_4$ , the equation for the  $w$  component is not displayed):

$$\left\{ \begin{array}{l} \underbrace{\bar{u} \frac{\partial \bar{u}}{\partial x}}_{T_{uu}} + \underbrace{\bar{v} \frac{\partial \bar{u}}{\partial y}}_{T_{vu}} + \underbrace{\overline{u' \frac{\partial u'}{\partial x}}}_{R_{uu}} + \underbrace{\overline{v' \frac{\partial u'}{\partial y}}}_{R_{vu}} = \underbrace{-\frac{1}{\rho} \frac{\partial \bar{p}}{\partial x}}_{\text{Grad}(P)} \\ \underbrace{\bar{u} \frac{\partial \bar{v}}{\partial x}}_{T_{uv}} + \underbrace{\bar{v} \frac{\partial \bar{v}}{\partial y}}_{T_{vv}} + \underbrace{\overline{u' \frac{\partial v'}{\partial x}}}_{R_{uv}} + \underbrace{\overline{v' \frac{\partial v'}{\partial y}}}_{R_{vu}} = \underbrace{-\frac{1}{\rho} \frac{\partial \bar{p}}{\partial y}}_{\text{Grad}(P)} \end{array} \right. \quad (3.27)$$

Note that the mean pressure gradient on the right hand side of Eq. 3.27 could not be measured experimentally and was therefore deduced from other terms. Moreover, because the budget momentum did not give any interesting trends in the radial direction, we did not present these results in the text.

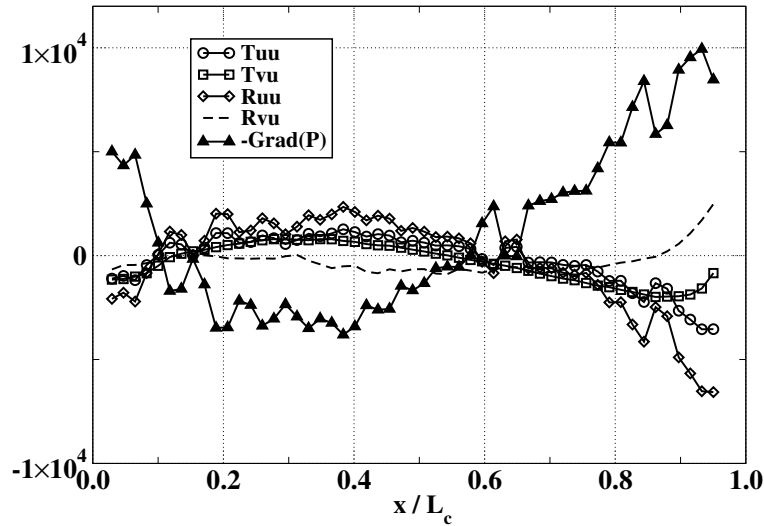


Figure 3.34: Different terms of the momentum equation budget for the NF configuration. Main flow rate of  $30 g.s^{-1}$

Figure 3.34 depicts the different terms of Eq. 3.27 along the interface separating the cavity and the main channel, for an incoming mainstream mass flow rate of  $30 g.s^{-1}$ . The mean pressure gradient is clearly the preponderant term, being negative for  $0.15 < x/L_c < 0.6$ . This region corresponded to entrainment of mass from the cavity to the main channel. Because the shear layer had an unsteady behavior, the normal Reynold's term  $R_{uu}$  was larger in this zone compared to the  $R_{vu}$  term. Thus, all fluctuations were primarily created by the axial velocity  $u$ . In contrast, an opposite effect was found next to the cavity trailing edge. In fact, the presence of the corner drastically increased the mean pressure gradient. At the same time, the term

$Rvu$  became preponderant whereas the  $Ruu$  term was lowered. Thus, the production of flow unsteadiness was more prone to be done via the radial component, and put in evidence the interaction of the cavit flow dynamics with the mainstream, via the shear layer.

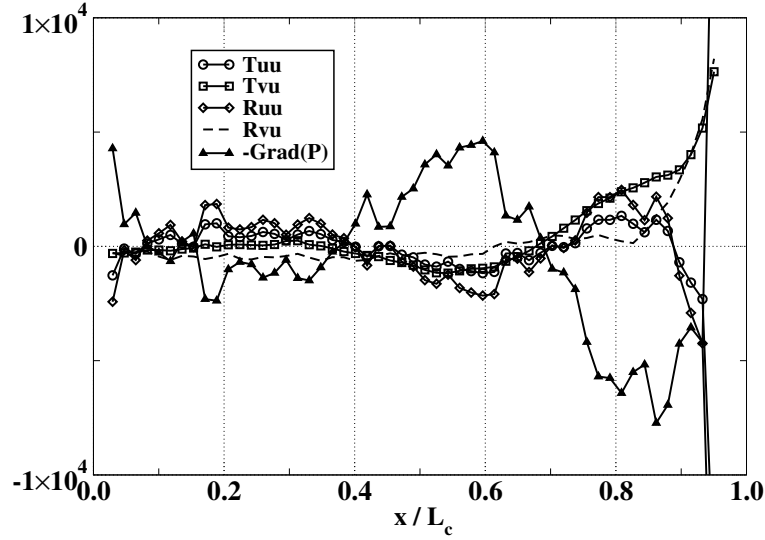


Figure 3.35: Different terms of the momentum equation budget for the 2F configuration. Main flow rate of  $30gs^{-1}$

A similar graph is shown in Fig. 3.35, for the 2F configuration and for a mainstream mass flow rate of  $30 g.s^{-1}$ . Most part of physical phenomena occurred in the second-half of the cavity, next to the cavity trailing edge. The mean pressure gradient was found to be slightly negative, for  $0.1 < x/L_c < 0.4$ , and was related to the vortex (2) depicted in Fig. 3.14. Then, for  $0.4 < x/L_c < 0.6$ , the mean pressure gradient increased due to the fluid compression caused by the stagnation point. Finally, for  $x/L_c > 0.7$ , this term was negative due to the flow ejection process from the cavity. Considering the convection process, beyond the stagnation point,  $Tvu \gg Tuu$ : the convection of the the axial velocity  $\bar{u}$  was controlled by the radial velocity  $\bar{v}$  and confirmed the interaction of the cavity flow dynamics with the shear layer. Similarly, the Reynold's term  $Rvu$  was also preponderant in comparison to the  $Ruu$  term.

### 3.6 Conclusion

Based on global observations of thermo-acoustic oscillations in Chap 2, this chapter was exclusively focused on the inert aerodynamics which was encountered in a trapped vortex combustor. The primary reason was that several studies emphasized that flows passing past cavities were

quite unstable due to the separating shear layer. Besides, effects of direct flow injection systems in the cavity have received less attention in the literature. Then, we focused our investigation on (1) characterize the flow dynamics, turbulence, mass exchanges, shear layer behavior, and (2) address modifications caused by the addition of flow injection systems in a passive cavity.

Results showed that no self-sustained cavity oscillations (related to a continuous vortex shedding process) were encountered in this study. Effects of adding several injection systems in the cavity resulted in the production of multiple, counter-rotating vortices as well as a stagnation point at the interface between the cavity and the mainstream. Mass exchanges between the cavity and the main channel were enhanced, featuring an unsteady flapping phenomenon. The latter was found to be controlled by the mainstream velocity, which improved the cavity confinement. Thus, the isotropy and the turbulent intensity were drastically increased.

Despite the confinement and the cavity jets, a focus on the separated shear flow put in evidence that the shear flow was self-similar far away from the walls. In the case of an active cavity, the shear layer growth and its location were remarkably piloted by the cavity injection systems and were quite independent of the mainstream conditions. Eventually, a momentum budget demonstrated that the cavity jets favored radial exchanges next to the cavity leading edge.

Several insights have been highlighted regarding the advantages to anchor a flame in a TVC:

- The main velocity controls the flow stability, especially by confining the cavity. When the mainstream momentum was reduced, an aerodynamic instability was encountered next to the cavity trailing edge and affected the interfacial shear layer: the latter could contribute to the appearance of combustion instabilities.
- The presence of multiple vortices makes the cavity to be a good mixer and flame-holder candidate. Moreover, flow injection systems favorize moderate radial transfers, and the stagnation point also creates a low velocity zone and thus may increase the mixing rate.

In summary, this flow configuration remains quite complex. Note that the results presented

here are highly configuration specific. Thus modification of the injection systems should also be considered but evidently results in numerous possibilities. Moreover, addition of heat release may amplify, modify, or damp instabilities observed in this chapter. Therefore, next chapter is focused on considering the addition of combustion in this geometry.

## Chapter 4

# Temporal and Spatial analysis of Flow-Flame-Acoustic Interactions

### Contents

---

<b>4.1</b>	<b>Experimental methods</b>	<b>112</b>
4.1.1	Advanced high-speed laser diagnostics	112
<b>4.2</b>	<b>Experimental methods</b>	<b>113</b>
4.2.1	10kHz OH-Planar Laser Induced Fluorescence system	113
4.2.2	Reactive 2.5kHz Particle Image Velocimetry system	115
4.2.3	Pressure and Photomultiplier	115
4.2.4	Synchronisation and Measurement Duration	116
<b>4.3</b>	<b>Data Processing</b>	<b>117</b>
4.3.1	Flame front extraction	117
4.3.2	Coherent velocity field filtering	117
4.3.3	Proper orthogonal decomposition (POD)	119
<b>4.4</b>	<b>Mechanisms of combustion instabilities</b>	<b>121</b>
4.4.1	Global Rayleigh Index	121
4.4.2	Phenomenological description of self-excited oscillations	123
4.4.3	Effects of acoustics on the flow field	126
4.4.4	Effects of flow dynamics on the unsteady combustion process	131

---

4.4.5	Resulting mass transfers at the interface between the cavity and the mainstream . . . . .	133
<b>4.5</b>	<b>Scenario for combustion instabilities in the present TVC . . . . .</b>	<b>136</b>
<b>4.6</b>	<b>Concluding Remarks . . . . .</b>	<b>137</b>

---

Chapter 2 highlighted the existence of large pressure oscillations in our combustor. In order to separate effects of the flow unsteadiness and heat release oscillations, we then performed a detailed study on the inert flow dynamics in Chap. 3. Aerodynamic instabilities were highlighted, mainly originated from jet injection systems located next to the cavity trailing edge. Results showed that this flow instability could be annihilated by increasing the mainstream momentum and confining the cavity. We continue our investigation by treating the additional physical processes associated with the presence of a flame in our trapped vortex combustor. Despite the difficulty to fully understand mechanisms leading to operating conditions exhibiting combustion instabilities, the aim of this chapter is to gain finer information about the flow-flame-acoustic coupling and to propose a possible scenario leading these instabilities.

In order to assess the flame-flow-acoustic interactions, we took advantage of high-speed optical diagnostics in order to perform a spatial and temporal analysis. Data enabled to extract temporal and frequential information but also transient or rare events. This chapter uses high-speed particle image velocimetry (PIV) and OH-planar laser induced fluorescence (OH-PLIF) to record simultaneous measurements of the flow unsteadiness and the flame structure.

Advanced experimental methods are presented in Sec. 4.1, followed by specific data and processing procedures (Sec. 4.3). An analysis of one combustion cycle is provided in Sec. 4.4 as a preliminary approach. The flame-flow-acoustic interactions are then investigated in the rest of this section in order to present a mechanism that best describes these combustion instabilities.

## 4.1 Experimental methods

### 4.1.1 Advanced high-speed laser diagnostics

Because flow and flame dynamics must be both temporally and spatially resolved, high-speed laser imaging diagnostics promise to be a well-adapted strategy to obtain measurements for



stringent operating conditions. As mentioned by Bohm et al. [18, 16], the advent of Q-switched, all-solid-state, diode-pumped lasers and the emergence of complementary metal oxide semiconductor (CMOS) camera technologies made it possible to transfer planar optical diagnostic methods to the multi-kilohertz regime. However, the energy delivered into the probe volume is reduced to a few mJ, which dramatically reduces the sensitivity of the laser diagnostics. Moreover, because the camera's resolution decreases as the repetition rate is increased, a compromise must be made between the temporal and spatial resolutions. Among the available high-speed optical diagnostics, high-speed OH-PLIF [114] and PIV [223] methods have proved to be suitable for combustion applications. Recent studies have relied on these laser diagnostics to investigate unsteady or transient mechanisms in academic turbulent flames and conventional gas turbine combustors for various scenarios: local extinction associated with vortex-flame interactions in opposed-jet flames [17], re-ignition in a jet diffusion flame [210], flame blowout in swirl combustion [211], PVC and flashback in LPP swirl flames [21], flame kernel development in a GT, and ignition processes in internal combustion engines [20, 175].

To our knowledge, few studies involving laser diagnostics have been implemented on TVC geometries. For instance, Meyer et al. [162] was the first to perform optical diagnostics on the two-dimensional US Air Force TVC. He coupled a 10Hz PIV system with a 10Hz OH-PLIF system to roughly characterize the flow topology and flame structure. More recently, Jin et al. [108] performed PIV measurements in order to validate turbulence models for numerical computations. However, no studies have been reported on dual high-speed laser diagnostics this complex geometry, and even more, exhibiting strong instabilities.

## 4.2 Experimental methods

This section describes the dual measurement technique for the apparatus and setup presented in Fig. 4.1. For clarity, details of each diagnostic are presented independently.

### 4.2.1 10kHz OH-Planar Laser Induced Fluorescence system

A high-speed OH-PLIF system operating at a repetition rate of 10kHz was used to study flame dynamics and to record the hydroxyl radical (OH) in the flame. A 10 kHz Nd-YAG-laser (Edge-

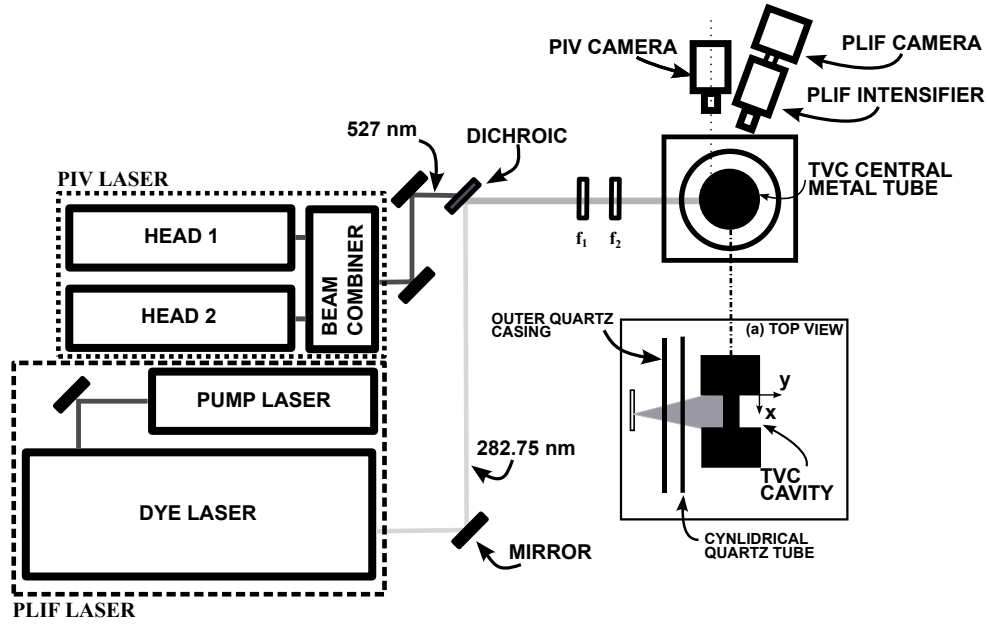


Figure 4.1: Schematic representation of the dual measurement technique.

Wave IS2011-E) operating at 532nm with an average power of 100W was used to pump a tunable dye laser (Sirah Credo) supplied with Rhodamine 590 dye. The frequency-doubled pulse energy was  $460\mu\text{J}/\text{shot}$  and the resultant energy was  $130\mu\text{J}/\text{shot}$  in the probe volume. The excitation wavelength was tuned to the  $Q_1(5)$  ro-vibronic transition of the  $A^2\Sigma^+(\nu' = 0) \leftarrow X^2\Pi(\nu'' = 1)$  band ( $\lambda = 282.75\text{nm}$ ). We made daily adjustments to the excitation wavelength using a laminar premixed  $\text{CH}_4/\text{air}$  flame. The resultant laser beam was overlapped with the PIV beam by using a dichroic mirror and was expanded through a set of fused silica lenses (spherical lens  $f_1 = 1000\text{mm}$ , and cylindrical lens  $f_2 = -20\text{mm}$ ) to form a laser sheet of 30 mm in height (Fig. 4.1). The detection system consisted of an external image intensifier (HighSpeed IRO, LaVision) connected to a CMOS-camera (Fastcam SA1) with a resolution of  $512 \times 512 \text{ pix}^2$  (21.5 pix/mm magnification ratio). The UV lens (100mm f/2 B-Halle Nachfl. GmbH) was mounted on a Scheimpflug system because the camera was titled at a  $15^\circ$  angle (away from the laser sheet normal) due to the central metal body and the presence of the PIV camera. The intensifier gate was set to 500 ns, and background noise arising from elastic scattering of the particles used for PIV was reduced with a high-pass colored optical filter (Schott WG305). We adopted a broadband collection strategy from 308 to 330 nm with a bandpass colored filter (Schott UG11). Spatial correction and normalization of the laser sheet profile was taken into account and corrected by filling the combustion chamber with a homogeneous mixture of acetone vapor and air.

The optical distortion caused by the oblique viewing angle and the curved face of the quartz tube was systematically corrected by measuring the transfer function prior to performing the experiments. We obtained this transfer function by comparing the image of a calibration plate inserted into the region of interest with the associated theoretical grid marks (implemented with Davis software, LaVision).

#### 4.2.2 Reactive 2.5kHz Particle Image Velocimetry system

High-speed PIV system operating at a repetition rate of  $2.5\text{kHz}$  was used to study flow dynamics. The repetition rate resulted in a compromise imposed by the spatial resolution of the camera used in this study. A double cavity Nd:YLF laser (Darwin Dual, Quantronix) operating at  $527\text{nm}$  fired two laser beams,  $15\text{ }\mu\text{s}$  apart (each cavity was operating at  $2.5\text{kHz}$ ). The laser beams were transmitted and combined with the UV laser beam through the dichroic mirror and expanded through the same lenses used for the PLIF beam. We used  $\text{ZrO}_2$  particles, with a 99% purity and a median diameter of  $1\text{ }\mu\text{m}$ , to seed the various flow injection conditions (generated by means of several fluidized beds). Light scattering was collected on a  $5\text{kHz}$  high-speed CMOS-camera (Phantom V10) equipped with a Nikon f/2.8 105mm lens. The camera was set to a resolution of  $480 \times 480\text{ pix}^2$ , resulting in a 24 pixel/mm magnification ratio. We then paired the images to estimate the velocity fields. In this study, PIV image processing was performed with a multi-pass interrogation window algorithm (DynamicStudio, Dantec) resulting in a final interrogation window of  $32 \times 32\text{ pix}^2$  and a 50% overlap. A coherent filter was applied to correct isolated false vectors. In addition, we quantified the spatial limitations of the PIV technique in accordance with previous studies by Foucaut et al. [72] and Krawczynski et al. [126], resulting in a spatial resolution scales lying between 2.13mm and 18mm.

#### 4.2.3 Pressure and Photomultiplier

A dynamic pressure sensor (Kistler 7061B ThermoComp<sup>®</sup>,  $10\text{ kHz}$  sampling rate) was mounted on a waveguide system, 280 mm downstream from the cavity region (Fig. 1.23(a)). Spatial offset was taken into account by applying a temporal correction, considering that the shift occurred

mainly because of a propagating acoustic wave. To calculate the sound speed in the burned gases, the estimated temperature was set at 1700K in accordance with [160]<sup>1</sup>. We used one-sided power spectral density (PSD) with the Welch method for the acoustic mode detection [230]. Results are given as sound pressure levels (SPL, units in  $dB.Hz^{-1}$ ) with a frequency resolution of  $\pm 5$  Hz. Temporal fluctuations in the heat release were collected on a 10 kHz sampling rate photo multiplier tube (PMT, Hamamatsu 6780-20) with a selected photocathode of 0.15nA low dark current. The output signal of the PMT was amplified with a Hamamatsu C7319 pre-amplifier ( $10^6$  gain). A BG12 band-pass optical filter was used to record spontaneous CH\* emission, thus providing a good estimator for the heat release rate [168, 182].

#### 4.2.4 Synchronisation and Measurement Duration

	PLIF	PIV	Pressure and CH* sensors
Rate of acquisition [ $kHz$ ]	10	2.5	10
Duration of acquisition [ $s$ ]	2.18	6.0	6.0
Total amount of data	21,829	15,000	60,000
Amount of data used for coupling	5,400	15,000	15,000

Table 4.1: Acquisition rates and amount of processed data.

Table 4.1 summarizes acquisition rates and amounts of processed data for all measurement techniques. To obtain a reasonable signal-to-noise ratio, we relied on nonidentical acquisition rates for each measurement technique. OH-PLIF images were recorded with a 10kHz repetition rate, whereas velocity vector fields were acquired with a 2.5kHz repetition rate. The combined analysis thus resulted in an artificially deteriorated to a lower sampling rate; only one out of every four PLIF images was extracted. Nevertheless, all data were saved for use in conjunction with pressure and heat release measurements. Note that the acquisition of pressure, heat release and PLIF measurements was achieved between the two successive shots of the PIV laser. We performed a parametric study of the number of images used for the first three statistical moments (mean, standard deviation, and skewness) to confirm that convergence was achieved with the present data.

<sup>1</sup>This temperature is critically important to the characterization of thermo-acoustic oscillations. Sensitivity analysis has shown that an estimation of the temperature of burned gases with an uncertainty of  $\pm 400K$  leads to a phase shift of less than  $1^\circ$  (taking the fundamental acoustic period as a reference).

### 4.3 Data Processing

It is important to develop robust and automatic post-processing tools to manage the large amounts of data obtained with kHz systems. The following section provides descriptions of various routines developed to analyze the coupling between flow structure, heat release, and acoustics.

#### 4.3.1 Flame front extraction

We developed an image-processing tool to automate flame front detection and derive other quantities from the OH-PLIF recordings. Prior to the use of a edge-detection algorithm, pixel-to-pixe noise contained in the images was suppressed using a nonlinear diffusive filter (NLDF). More details can be found in appendix B.

We remind that because the geometry involved a large recirculation region and because OH is a chemical marker of burned and unburned gases, it was impossible to dissociate flame front regions (OH production) from regions of burned gases (convection of OH). Keeping in mind this constraint, we continue in using the term *flame front* to denote the interface between unburned and burned gases in the following sections.

#### 4.3.2 Coherent velocity field filtering

We observed that velocity oscillations in the TVC burner were superimpositions of a coherent low frequency signal on a broadband noise (primarily turbulence-induced). Assuming that the low frequency fluctuations were mainly acoustics-induced, we chose to adopt a triple decomposition to dissociate these two contributions:

$$u(x, y, t) = \bar{u}(x, y) + \tilde{u}(x, y, t) + \tilde{u}'(x, y, t), \quad (4.1)$$

where  $\bar{(\cdot)}$ ,  $\tilde{\cdot}$ , and  $\tilde{\cdot}'$  represent time-averaged, deterministic, and random components of the velocity, respectively [141] (Fig. 4.2 (a)).

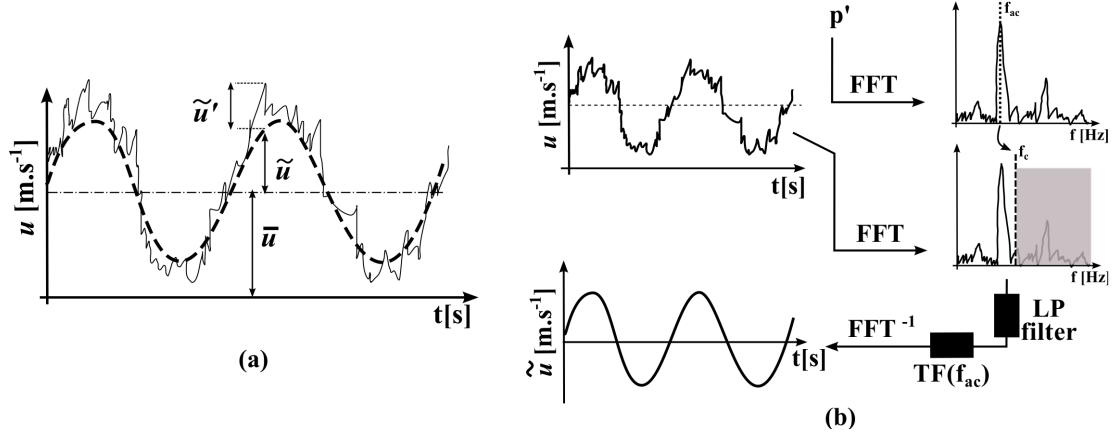


Figure 4.2: Triple decomposition principle. (a) Definition of variables. (b) Implementation procedure for the triple decomposition using an acoustic cutoff frequency  $f_c$ .

Practical use of this equation in turbulent flows is complicated by the variability of the deterministic component in time ("phase jitter") or in amplitude ("nonlinear") [?]. However, coherent velocity fluctuations in the present investigation were relatively accurate and without ambiguity, pulsating at the same acoustic frequency  $f_{ac}$ . Figure 4.2 (b) depicts the procedure used to automatically implement the triple decomposition. The temporal evolution of local velocities was recorded, and a 2<sup>nd</sup> order Butterworth low-pass filter (good band-pass ripple and short transition band) was applied to this time series. The cutoff frequency  $f_c$  was slightly higher than the corresponding fundamental acoustic tone, which was detected through pressure measurements (i.e.,  $f_c = f_0 + 5Hz$ ). Unfortunately, filtering is known to induce an artificial temporal shift that is incompatible with triple decomposition. We estimated the induced temporal shift  $\varphi_{u,\tilde{u}}$  between the raw signal  $u$  and the filtered signal  $\tilde{u}$  with a transfer function  $TF$  as follows:

$$\varphi_{u,\tilde{u}} = \Im[TF(f_{ac})] \text{ with } TF(f_{ac}) = \frac{P_{u,\tilde{u}}}{P_{u,u}}, \quad (4.2)$$

where  $P$  is the power spectral density estimated with the Welch method. The transfer function was calculated at the acoustic frequency  $f_0$ . The temporal shift was then used to temporally readjust the filtered signal.

### 4.3.3 Proper orthogonal decomposition (POD)

Because coherent structures could be a driving source for combustion instabilities (e.g., vortex-flame interactions, see Sec. 2.1.2), determination of their spatial characteristics is a critical issue. For instance, several acoustic frequencies could be associated to the presence of simultaneous coherent structures in the combustor, and may contribute differently on the combustion process. The POD is a post-processing technique which was introduced by Lumley in 1967 to investigate coherent structures in turbulent flows [153]. Compared to classical detection techniques (e.g., Fourier or wavelet transforms) [19], this method do not need an *a priori* criterion to assess coherent structures and relies on the energy associated to flow oscillations. In our case, it could be useful to perform this treatment in order to reveal the existence of several coherent structures, their spatial characteristics, and their energy contributions. A brief overview of this technique is given hereafter.

#### Classical POD decomposition

The main idea of the classical POD technique is to decompose a variable of interest  $\mathbf{u}$  as

$$\mathbf{u} = [u(t), v(t)] \approx \sum_{k=1}^K a_k(t) \Phi_k(\mathbf{x}), \quad (4.3)$$

where  $\mathbf{u}$  is a vector containing the velocity components,  $\Phi_k(\mathbf{x})$  are space functions,  $a_k(t)$  are time coefficients, and  $K$  is a positive integer used to approximate the variable of interest  $\mathbf{u}$ . At this point, several parameters need to be defined. Space functions  $\Phi_k$  are usually defined *a priori* (e.g., *sin* or *cos* functions in the case of a Fourier transform). In contrast, the POD directly uses the original data  $\mathbf{u}$  and an energetic criterion to estimate these functions. Mathematically, it corresponds to maximize the projection of the variable of interest  $u$  on the space function  $\Phi$

$$\frac{\langle |(u, \Phi)|^2 \rangle}{\|\Phi^2\|}, \quad (4.4)$$

where  $\langle . \rangle$  is a temporal average operator,  $(.,.)$  is the inner product, and  $\| . \|$  is the

norm. An additional constraint can be defined to make these functions orthonormal two by two, i.e.,  $(\Phi_k, \Phi_{k'}) = \delta_{kk'}$ . Thus, functions  $\Phi_k$  span an optimized subspace, where the orthogonal projection of original variables  $u$  are maximized. Eq. 4.4 can be rewritten into the Fredholm integral as

$$\int_{\mathcal{D}} \bar{R}(x, x') \Phi(x') dx' = \lambda \Phi(x), \quad (4.5)$$

where  $\mathcal{D}$  is the domain where data are analyzed. Eq. 4.5 corresponds to a classical eigenvalues problem (i.e.,  $Ax = \lambda x$ ), and  $\lambda$  are eigenvalues associated to eigenfunctions  $\Phi$ . The averaged correlation matrix  $\bar{R}(x, x')$  is defined as

$$\bar{R}(x, x') = \frac{1}{N} \sum_{n=1}^N R_{ij}^n(x, x') = \frac{1}{N} \sum_{n=1}^N u_i^n(x) u_j^n(y), \quad (4.6)$$

where  $N$  is the amount of data (e.g., number of instantaneous vector fields),  $R_{ij}^n(x, x')$  is the velocity correlation matrix, and  $u_i$  and  $u_j$  are velocity components according to indices  $i$  and  $j$ <sup>2</sup>. Resolution of Eq. 4.5 provides eigenfunctions  $\Phi$  and eigenvalues  $\lambda$ . therefore, time coefficients  $a_k(t)$  can be easily determined with the following expression:

$$a_k(t) = (u(\mathbf{x}, t), \Phi_k(\mathbf{x})). \quad (4.7)$$

Note that  $a_k(t)$  represents the amplitude of the projection of the data on the space function  $\Phi_k$ .

## POD mode reconstruction

Eigenvalues which are extracted when solving Eq. 4.5 correspond to the contribution of the turbulent kinetic energy contained in the  $k^{th}$  mode [42], and the total turbulent kinetic energy can be retrieved as

$$\sum_{k=1}^{+\infty} \lambda_k = E. \quad (4.8)$$

---

<sup>2</sup> $u_1 = u$  and  $u_2 = v$  in the case of two-dimensional data.



With Eq. 4.9, it is then possible to reconstruct the flow by keeping the most energetic modes:

$$u(x, t) = \sum_{k=1}^M a_k(t) \Phi(x), \quad (4.9)$$

where  $M$  is an integer which is chosen in order to minimize loss of information. It is common to define  $M$  such that 75% of the total kinetic energy is retrieved [185].

Finally, the first modes can highlight the spatial behavior of a coherent structure [49]. Note that in the present study, we used the classical method described previously<sup>3</sup>.

## 4.4 Mechanisms of combustion instabilities

As described in Chap. 3, several processes can drive combustion instabilities. Results given were mainly simple observation of the combustor dynamics. However, this dynamics is greatly related to aerodynamic instabilities, which may couple with the combustion process, and finally the combustor acoustics. A schema in Fig. 4.3 recalls this relationship [29] and the following subsections are focused on understanding mechanisms involved in combustion instabilities with an emphasis on the main controlling parameters.

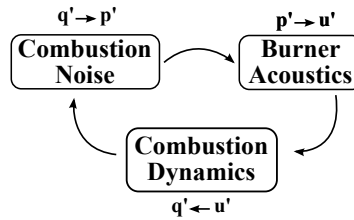


Figure 4.3: Schema illustrating the feedback process involved in combustion instabilities.  $p'$ : unsteady pressure,  $q'$ : unsteady heat release,  $u'$ : velocity fluctuations.

### 4.4.1 Global Rayleigh Index

In contrast with Chap. 2, it is possible to precisely calculate the global Rayleigh index with temporal measurements, and to confirm the coupling between acoustics and heat release process.

Figure 4.4 depicts time series of pressure (left axis) and heat release fluctuations (right axis)

<sup>3</sup>Many studies usually use the "snapshot" method introduced by Sirovich [206, 207, 208] to reduce computation costs due to the calculation of the correlation matrix. In our case, we used the Matlab software which was optimized for matrix calculations.

within the burner. Note that the pressure time series have been corrected in accordance with Sec. 2.2.1. Although these fluctuations are distinctly harmonic, they also present nonlinear features (i.e., they are not perfectly sinusoidal).

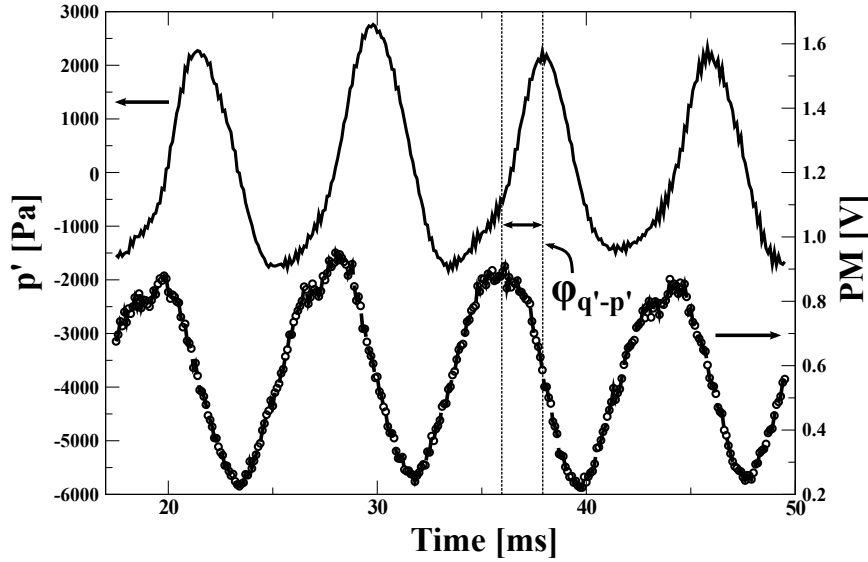


Figure 4.4: (a) Pressure signal from dynamic sensor (left axis), and CH\* radical intensity (right axis).

Equation 2.4 gives the volume and period-averaged term source  $\mathcal{R}$  in Eq. 2.3. Note that our pressure and PMT records provided a space-averaged information. Moreover, because the fundamental acoustic wavelength  $\lambda_1^4$  was longer than the cavity length, the pressure was assumed to be constant in this region (i.e.,  $p'(x, y, t) = p'(t)$ ). The same principle applies to heat release oscillations (i.e.,  $q'(x, y, t) = q'(t)$ ). The term  $\mathcal{R}_1$ , expressed as

$$\mathcal{R}_1 = \frac{1}{\tau} \int_t^{t+\tau} p'(t)q'(t)dt, \quad (4.10)$$

was then calculated from measurements and used to verify the Rayleigh criterion. Mathematically, this criterion also corresponds to the phase shift between the two signals and had a value of  $\varphi_{q'-p'} = 72^\circ$  (see Fig. 4.4). This value, with a confidence interval of  $\pm 90^\circ$ , indicated that pressure and heat release fluctuations were in phase and finally added energy to the system.

<sup>4</sup>We estimated a rough acoustic wavelength corresponding to the fundamental acoustic frequency  $f_{ac}$ . Taking an average burned gas temperature of 1800K, we found a value of the order of 7 m.

The corresponding pressure and heat release spectra are presented in Fig. 4.5 and show large peaks at identical frequencies <sup>5</sup>.

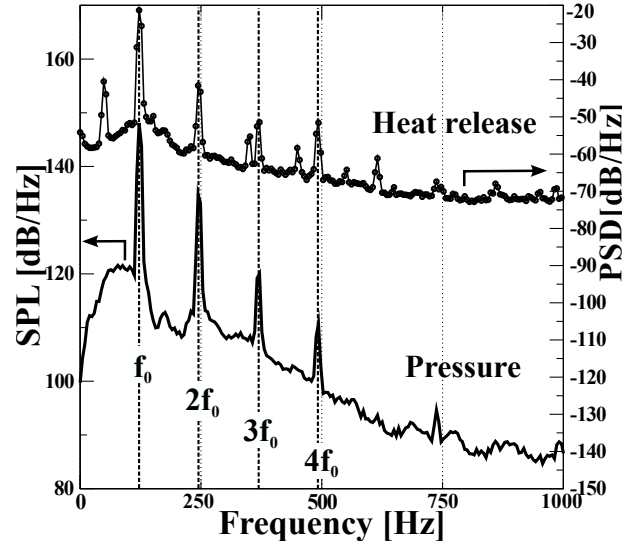


Figure 4.5: Pressure (left axis) and heat release (right) spectra.

The fundamental acoustic frequency occurred at  $f_0 = 122 \text{ Hz}$ , whereas the following spikes were found to be harmonics (cf. Sec. 2.3.2).

We conclude that the combustor acoustics and the combustion process couple and can drive the observed thermo-acoustic instabilities. However coupling mechanisms are rarely direct and result in both temporal (coherent structures) and spatial (size and energy associated with these coherent structures) effects on the flow field. Both approaches are investigated hereafter.

#### 4.4.2 Phenomenological description of self-excited oscillations

Figure 4.6 depicts a sequence of instantaneous OH-PLIF and PIV measurements corresponding to the operating conditions presented in Tab. 2.2. The figure illustrates instantaneous coupling of velocity vector fields colored by their corresponding magnitudes and locations of burned gases (OH signal in greyscale). The corresponding pressure and  $\text{CH}^*$  values are given in the graph on the right in Fig. 4.6 (numbered red dots). The region of interest relative to the entire burner

<sup>5</sup>The first peak of the heat release (at  $50 \text{ Hz}$ ) does not have any physical significance and occurs merely due to electromagnetic interferences between the PMT amplifier system and the electrical network.

is given in the upper right schema. The axial and radial velocity components  $u$  and  $v$  are also defined.

When the unsteady pressure was null and the unsteady heat release was at maximum (Fig. 4.6 #1), the flow located in the downstream part of the cavity was radially ejected towards the main channel. Although this flow behavior was decreasing, it continued to be observed, as depicted in Fig. 4.6 #2. This ejection process had a tremendous effect: It blocked the mainstream flow and created a region of low velocities. Burned gas locations were also altered by this ejection process. The three subsequent snapshots (Fig. 4.6 #3, #4, and #5) highlight a totally different behavior. The ejection process disappeared when pressure was at maximum and heat release decreased. In fact, effect of pressure was quite visible and affected the whole flow field: velocities were relatively low, without any preponderant flow topology.

In contrast, the axial mainstream velocity  $u$  was constantly increasing in snapshots #6, #7, and #8; they clearly show that the main channel flowed without being blocked anymore when pressure was almost at minimum. Consequently, burned gases located above the cavity were drained towards the exhaust line so that few traces were found in this region. Simultaneously, several vortices and recirculation zones appeared in the developing flow in the cavity. At this point, burned gases were well established in the shear layer at the interface between the main channel and the cavity. With continually increasing pressure (snapshot #8, #9, and #10), the ejection process, which started to penetrate the main flow, became apparent and the cycle was over.

We conclude from this sequence that an intense flow instability, located in the downstream part of the cavity, greatly modified the flow, the heat release rate, and the dynamic pressure. Note that this coherent instability was located next to the DCA jet injection which may be flapping. Moreover, the absence of periodic vortex shedding confirmed that jet injections inside the cavity modified the conventional mechanism observed in these type of geometries [5]. We therefore assume that the alternation between a cavity presenting several vortices and almost no flows is due to a jet flow modulation. In turn, the local gas composition is altered and induce the pressure and heat release oscillations.

Specifically, the DCA jet flow modulation, being alternately pointing in the cavity and in the

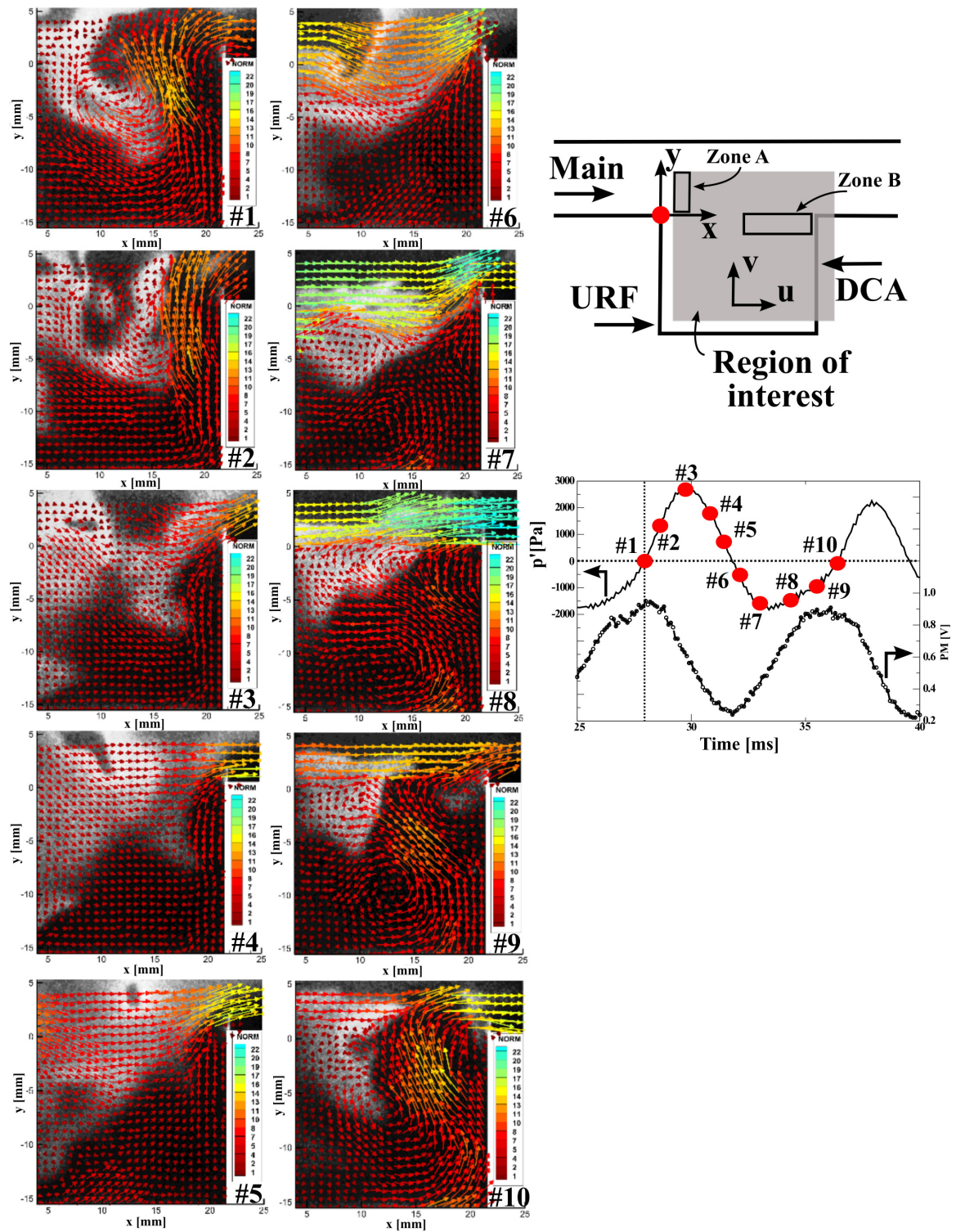


Figure 4.6: Simultaneous OH traces and velocity measurements (colored according to magnitude) for an individual pressure cycle.

main channel, was greatly affecting the cavity flow topology. This phenomenon, referred to as *jet flapping*, affected the dynamics of the large vortex located in the lower cavity region (centroid at  $x = 13$  mm,  $y = -12$  mm). Injected into the cavity (Fig. 4.6 #7), the DCA jet strengthened the vortex, but deflected towards the main flow, the DCA jet enabled the cavity to be drained (cf. #10).

#### 4.4.3 Effects of acoustics on the flow field

The strong flow fluctuations observed in Sec. 4.4.2 are the consequences of the burner acoustics. Thus, it is important to determine if acoustics is the primary source of these instabilities, assess if this coupling is either local or global, and to estimate corresponding spatial structures.

Figure 4.7 presents the PSD of the axial velocity fluctuation  $u'$ . These energy spectra are based on two distinct zones: zone A located in the main channel and zone B located in the cavity (cf. Fig. 4.6). The figure clearly shows that the acoustic peaks were retrieved with the same energy regardless of the considered zone. The first peak  $f_0 = 122\text{Hz}$  is considerably more pronounced, even if the following spikes are clearly visible. In zone A, the coherent axial oscillation was an indirect indicator of the *jet flapping* mechanism, which alternately penetrated and blocked the mainstream flow. The energy spectrum of zone B (cavity) demonstrates that thermo-acoustic oscillations affected the cavity region. Thus, the global flow sensitivity to thermo-acoustic oscillations may suggest that a high-amplitude pulsed combustion regime was encountered in the present configuration.

Consequently, the total turbulence energy may be the result of a coherent contribution, mainly due to acoustics, and a broadband term, due to the turbulence itself. We used the triple decomposition to dissociate these two contributions and estimate their respective energies (see Sec. 4.3.2). Results are shown in Fig. 4.8, depicting the ratio of total velocity fluctuation energy spectra of  $(\tilde{u}(x, y, t) + \tilde{u}'(x, y, t))$  to the filtered energy spectra  $(\tilde{u}'(x, y, t))$ . Because there is no evidence that the flow is isotropic, four 1D-cuts of 2D-energy spectra are given. Axial and radial  $u'$  and  $v'$  velocity spectra are plotted according to two spatial wave numbers (corresponding to the axial  $\vec{u}$  and radial  $\vec{v}$  directions).

Note the relative similarity of the four ratios of energy spectra, regardless of the direction

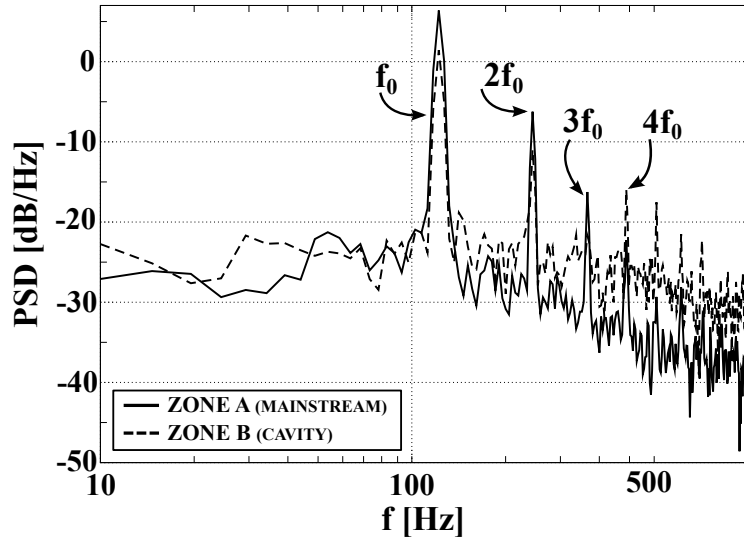


Figure 4.7: Power spectrum density of the axial velocity fluctuation  $u'$ , taken in zone A (mainstream) and zone B (cavity). Refer to Fig. 4.6 for the nomenclature.

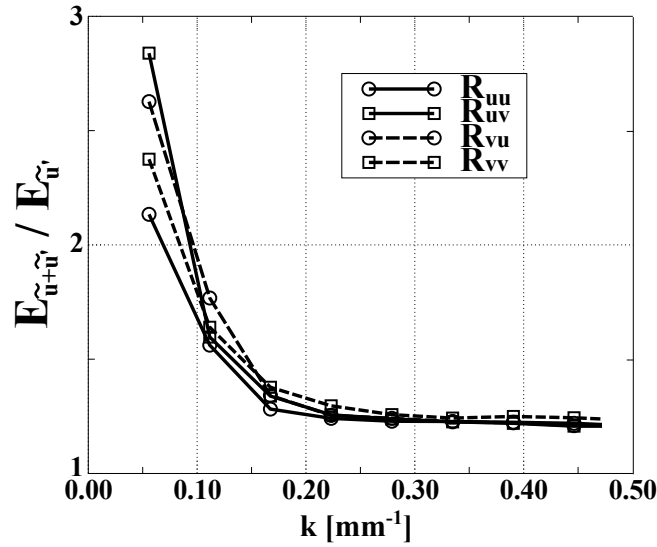


Figure 4.8: Comparison between total energy spectra ( $\tilde{u} + \tilde{u}'$  or  $\tilde{v} + \tilde{v}'$ ) and filtered energy spectra ( $\tilde{u}'$  or  $\tilde{v}'$ ) using triple decomposition.  $R_{uv}$  corresponds to the ratio of the energy spectra of the axial component  $u$  in the radial direction  $\vec{y}$ .

and the velocity component considered. The deterministic energy associated with the acoustics thus had an isotropic impact on the entire flow field. More precisely, the ratios of the energy spectra were larger for large scales with a deterministic contribution  $E_{\tilde{u} + \tilde{u}'}$  that was up to three times greater than the pure turbulence  $E_{\tilde{u}'}$ . At fine scales, the level of this contribution rapidly dropped to a plateau with a value of 1.2, demonstrating the existence of an equal contribution

of acoustics and pure turbulence energies. As a result, a continuous energy transfer may break up large-scale structures due to acoustics in order to be transferred to smaller turbulent scales. This observation confirms that the flow induced a tremendous global pulsed combustion regime behavior.

Because the whole burner was apparently pulsing and that no discrete peaks appeared in the turbulence spectrum, we performed a POD analysis with the PIV velocity vector fields to investigate the existence of a spatial event associated to the different observed frequencies (see Sec. 4.3.3). The normalized energy of the 10 first POD modes is shown in Fig. 4.9, for the axial and radial velocity components. It is clearly visible that most of the energy was contained in the first mode, which accounted for 73% of the total turbulent kinetic energy. The two first modes contained more than 80% of the total energy and could be representative of the different coherent structures in the TVC. Note that the energy distributions were similar for the axial and radial velocity component, and confirms that acoustics had an isotropic effect on the whole flow field.

Thus, we performed a POD reconstruction by keeping the two first modes. The r.m.s of each velocity fluctuation component is shown in Fig. 4.10. The first mode shows that axial fluctuations were quite important in the mainstream. This flow behavior was associated to the alternate *jet flapping* penetration and the resulting mainstream blockage effect. The latter process was also visible next to the cavity trailing edge and confirms that the mutual interaction between these two flows was driving the instability. The second mode presents high level of axial fluctuations at the flow separation between the cavity and the mainstream. The latter were due to the presence of large axial velocity gradients but also resulted from the *jet flapping*.

Figure 4.11 shows the evolution of the axial velocity  $u_{k=1,2}$  (reconstructed with the two first POD modes) in the main channel (zone A, see Fig. 4.6). In addition, pressure fluctuation and heat release fluctuation time series are superimposed on the graph. Note that the pressure fluctuation and the axial velocity are almost out-of-phase. In fact, when the pressure was at maximum, the *jet flapping* was effective and blocked the mainstream. In contrast, when the pressure was minimum, the axial velocity was almost maximum. In the mean time, heat release was increasing due to the cavity flow dynamics. Note that the different variables were not perfectly sinusoidal and was the primary reason for the appearance of harmonics.



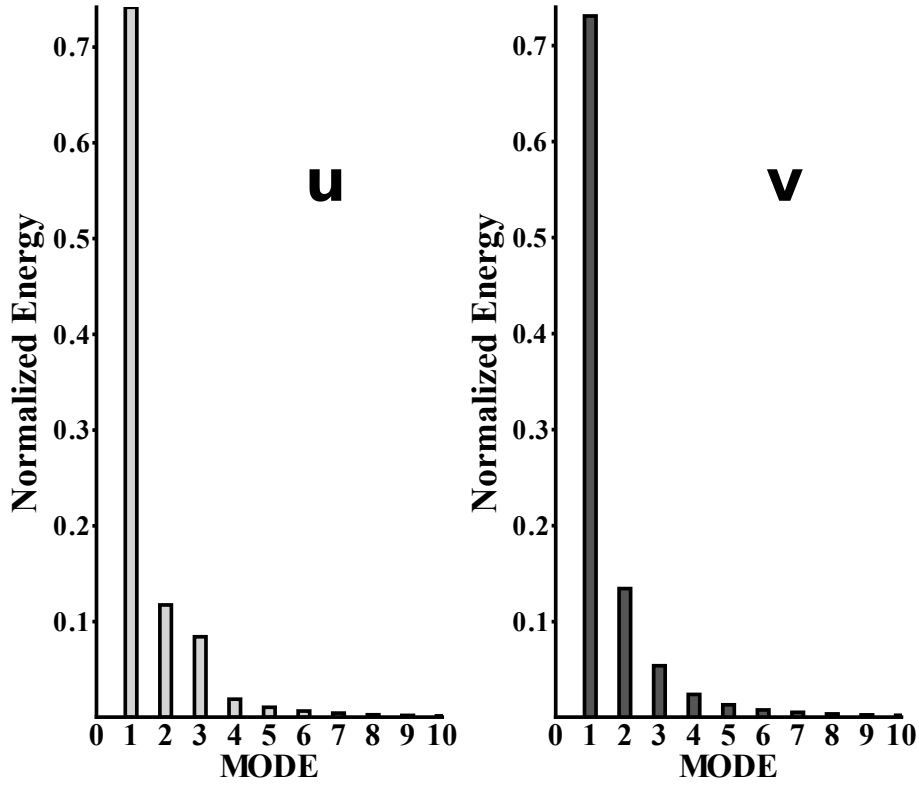


Figure 4.9: Normalized energy of POD modes for the axial and radial velocity component

We definitively conclude that the *jet flapping* mechanism was the only preponderant mechanism driving the flow dynamics and then thermo-acoustic oscillations. Harmonics were primarily due to non-linear processes<sup>6</sup>.

The complex instability found in the TVC evidently resulted from the coupling between heat release rates and dynamic pressure oscillations. Consequently, flow dynamics were overall affected, as revealed by alternating bursts in the cavity and in the mainstream. Specifically, the *jet flapping* mechanism that appeared in the cavity, combined with the pressure oscillations, may have been responsible for these instabilities because it modified the establishment of the cavity flow and shear layer region. This pulsed regime was simply estimated with the G number, defined as

<sup>6</sup>Measurements were recorded during the acoustic limit cycle.

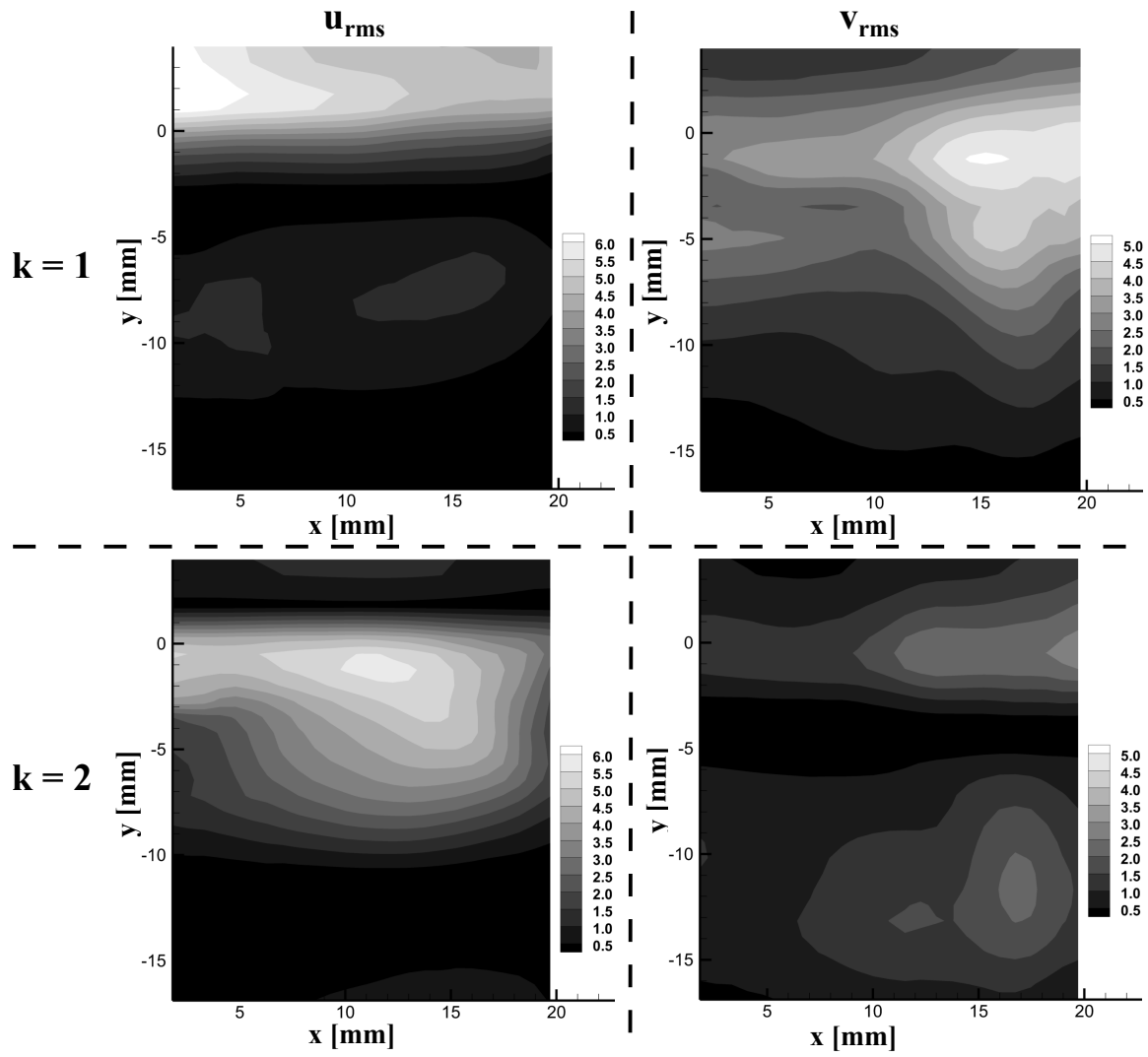


Figure 4.10: r.m.s velocity component fields, calculated from the first and second POD modes. Top: 1<sup>st</sup> mode. Bottom: 2<sup>nd</sup> mode. Left:  $u_{rms}$ . Right:  $v_{rms}$

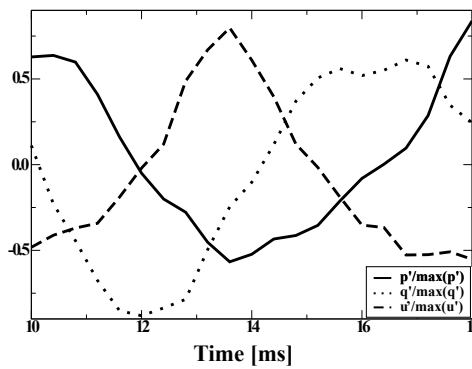


Figure 4.11: Temporal history of the reduced pressure, heat release, and axial reconstructed velocity (with the two first modes).

$$G = \frac{\sqrt{v_B^2}}{\sqrt{u_A^2}}, \quad (4.11)$$

where subscripts  $A$  and  $B$  denote the considered zone (Fig. 4.6).  $G$  gives the ratio of magnitude between the radial and the axial velocity in the cavity and the mainstream region. The ratio provides temporal information regarding the coupling of the *jet flapping* process with the two regions (similar to a jet in cross-flow).

Figure 4.12 depicts the behavior of  $G$  with time. Note that the  $G$  time series measurements is periodic, oscillating with the same acoustic frequency  $f_0$ . This graph also exhibits two dominant zones for  $G > 1$  and  $G < 1$ , respectively. The radial cavity velocity  $v_B$  was preponderant compared with the axial mainstream flow for  $G > 1$ .

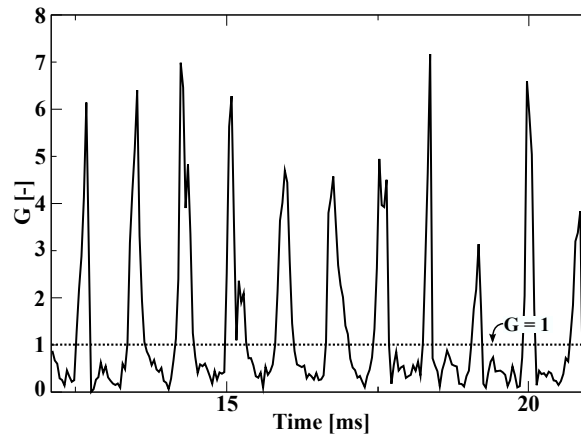


Figure 4.12: Time series measurements of  $G$  parameter.

#### 4.4.4 Effects of flow dynamics on the unsteady combustion process

This section considers the possible driving effects of flow field disturbances on heat release oscillations (Fig. 4.3). It is well known that fluctuations in the flow field (cf. Fig. 4.7) can induce oscillatory mixture compositions [146]. In the present study, the phase shift between local velocity fluctuations (e.g.,  $u'$  and  $v'$ ) and global heat release was estimated based on the assumption

that the entire flow field is affected by acoustics<sup>7</sup>. Results are shown in Fig. 4.13, depicting phase shifts  $\varphi_{u'-q'}$  and  $\varphi_{v'-q'}$  (expressed in degrees). Globally, the existence of in-phase and out-of-phase regions shows that the heat release rate was affected by local flow modulations. Figure 4.13(a), depicting the phase shift  $\varphi_{u'-q'}$ , shows that the region next to the URF jet (zone \* in Fig. 4.13 (a)) was in phase with the heat release fluctuation. Because this jet transported fuel and was modulated by thermo-acoustic oscillations, it necessarily implies an unsteady local equivalence ratio, which controlled the heat release rate. In contrast, an out-of-phase region was observed in the mainstream, demonstrating that the latter flowed normally when the heat release was at minimum. Figure 4.13(b) shows the phase shift for the radial velocity fluctuation  $v'$ . The *jet flapping* mechanism is clearly visible in the downstream part of the cavity; it was in phase with the heat release process.

We conclude that oscillations of the cavity jet surroundings in phase with the heat release rate controlled the combustion process. Because the equivalence ratio  $\phi_c$  of the URF flow was larger than the upper flammability limits, an interaction with the DCA jet necessarily resulted in local stoichiometric regions that led to ignition. This behavior implies a thermal gas expansion, which drained the cavity and deflected the DCA jet towards the mainstream.

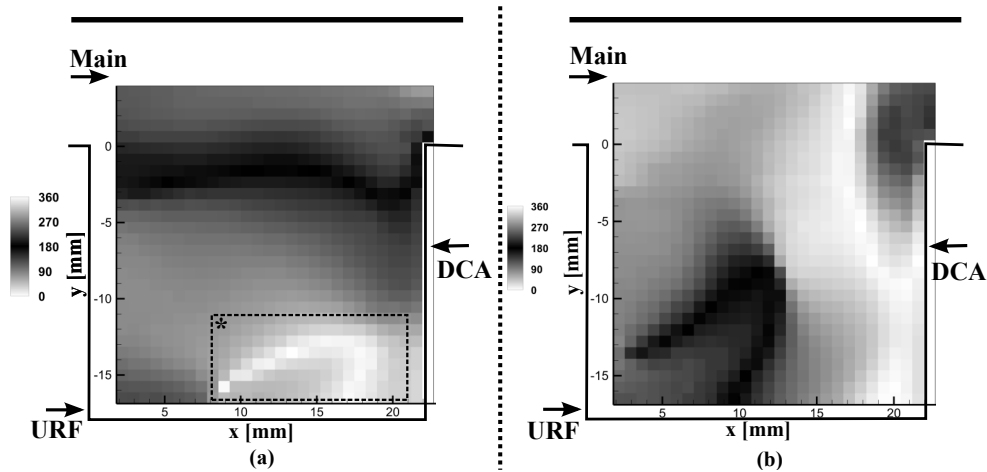


Figure 4.13: Phase shift between global heat release and velocity fluctuations: a)  $\varphi_{u'-q'}$  (axial fluctuation). b)  $\varphi_{v'-q'}$  (radial fluctuation).

<sup>7</sup>We verified the present assumption by determining the power spectrum density for each vector so that the phase shift was estimated at the first acoustic tone  $f_{ac}$ , following the methodology described in Sec. 4.3.2

#### 4.4.5 Resulting mass transfers at the interface between the cavity and the mainstream

The alternate preponderance of cavity and mainstream flows, which occurred primarily because of an inhomogeneous equivalence ratio within the cavity, necessarily resulted in inefficient mass transfers between these two regions. In order to understand how the flow affected mass transfers and consequently flame stability, we performed a simultaneous analysis of the flow and OH fields at the interface between the cavity and the mainstream. The spatial composition of gases in a premixed flame can be estimated with the mean progress variable, defined as

$$\bar{c} = \frac{\bar{T} - T_u}{T_b - T_u}. \quad (4.12)$$

In Eq. 4.12, the mean progress variable is defined as a normalized temperature [174], where unburned gases have a temperature  $T_u$ , and burned gases have a temperature  $T_b$ . Thus,  $\bar{c}$  changes from zero to unity; unburned gases correspond to  $\bar{c} = 0$ , whereas  $\bar{c} = 1$  corresponds to burned gases. In this study, we experimentally approximated the definition of  $\bar{c}$  with the following definition [35]:

$$\bar{c} = \langle \mathfrak{B}(I_{OH}) \rangle. \quad (4.13)$$

Practically, we phased raw OH PLIF images with respect to the pressure signal (using 10 bins to discretize one combustion instability cycle). Then, for each class, we binarized each OH PLIF image with the operator  $\mathfrak{B}$ , and averaged results. Respective phased mean radial velocity fields were also extracted to have access to the flow dynamics and then, obtain a qualitative description of mass transfers between the cavity and the mainstream.

Figures 4.14 a), b), and c) illustrate three specific instances of bin information. Their positions along the combustion instability cycle are recalled on the lower right pressure signal. Each graph depicts the conditioned mean radial velocity  $v_m$  (red curve) along the interface (black dashed line), superimposed on the field of the corresponding mean progress variable  $\bar{c}$ .

Note that in Fig 4.14 a), when the pressure was almost null, substantial positive velocities

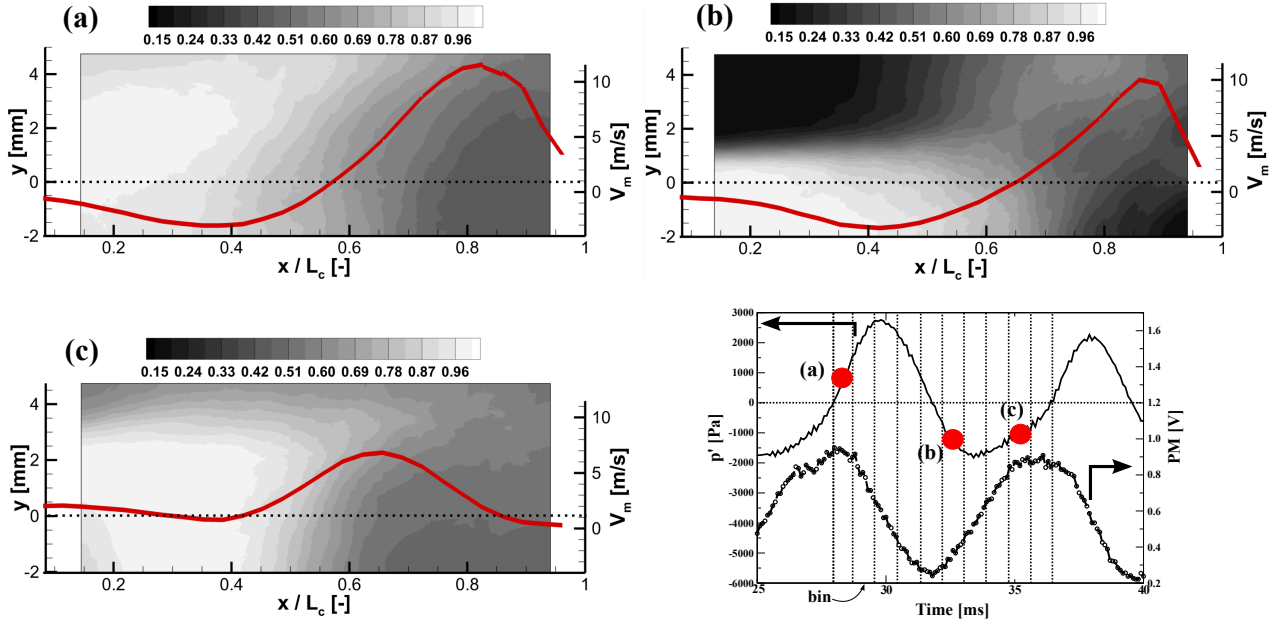


Figure 4.14: Conditioned mean radial velocity  $v_m(x, y = 0 \text{ mm})$  (red curve) superimposed on the corresponding mean progress variable  $\bar{c}$  fields (grayscale). (a)  $0^\circ < \varphi < 36^\circ$ . (b)  $180^\circ < \varphi < 216^\circ$ . (c)  $288^\circ < \varphi < 324^\circ$ . The lower right pressure signal recalls the position of each graph along the combustion instability cycle (red dots).

(up to  $12 \text{ m.s}^{-1}$  at  $x/L_c = 0.82$ ) were observed in the downstream part of the cavity for  $x/L_c > 0.55$ . For  $x/L_c < 0.55$ , velocities were negative so that the mainstream entered the cavity. Figure 4.6#1 reveals the *jet flapping* mechanism that alternately penetrated and blocked the mainstream. Concerning the corresponding mean progress variable field, low  $\bar{c}$  values in the *jet flapping* region are evidence that the air from the DCA jet was drained considerably from the mainstream and no longer participated in the mixing process within the cavity.

Figure 4.14 b) corresponds to the minimum of heat release (see Fig. 4.6#7). The behavior observed for  $\bar{c}$  differed considerably. Low values of  $\bar{c}$  in the mainstream region indicated that the lean flame was no longer ignited. Moreover, the region of high  $\bar{c}$  values was confined to the cavity, allowing the mainstream to flow unimpeded. Surprisingly, the mean velocity profile exhibits a similar trend to the one in Fig. 4.14 a). However, because the heat release was globally at minimum, we propose an alternative explanation for the observed trend: The main flow suddenly expanded and thus entered the cavity. The presence of burned gases in the cavity then forced the main flow to exit the burner through a constriction, which would explain the positive velocities next to the downstream cavity edge.

Figure 4.14 c) shows the end of the cycle, when the pressure tended to a null value (cf. Fig. 4.6#9). The whole mean velocity profile was positive, demonstrating that, as the heat release increased, thermal expansion pushed gases from the cavity to the mainstream. The existence of the *jet flapping* mechanism in the velocity profile became apparent at  $x/L_c = 0.65$ . Consequently, the main velocities began to decrease and were eventually drastically blocked. The  $\bar{c}$  field is similar to the one in Fig. 4.14 a) although it contains lower values in the mainstream and next to the downstream cavity corner.

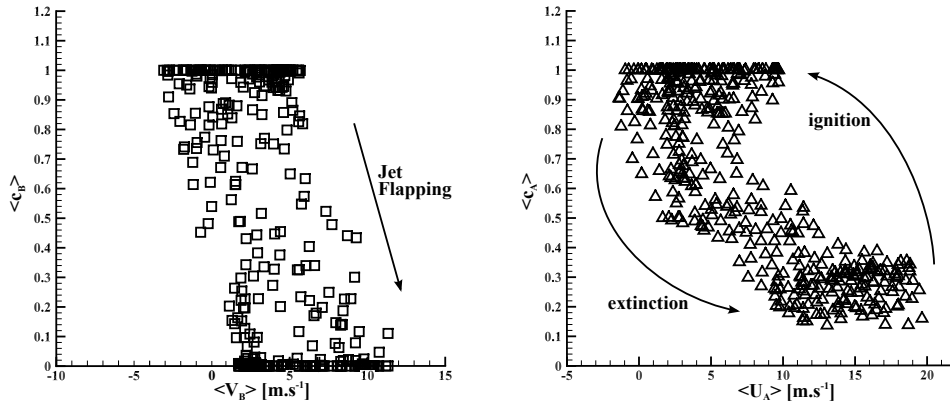


Figure 4.15: scatter plots of the spatially averaged progress variables with the corresponding averaged velocity component. 2000 instantaneous data. Left: data extracted in zone A and axial velocity. Right: data extracted in zone B and radial velocity

These spatial information showed that large mass transfers occurred at the interface between the cavity and the mainstream and may result in a poor flame stability. In order to demonstrate that the main flame was intermittently located above the cavity, Fig. 4.15 depicts instantaneous progress variables  $c$  and corresponding flow velocities in zone A and B. We chose to plot the radial velocity in zone B (averaged on the zone) in Fig. 4.15-left. The scatter plot present a bimodal distribution for  $\langle c_B \rangle = 0$  and  $\langle c_B \rangle = 1$ . In addition, when  $\langle c_B \rangle = 0$  (i.e., fresh gases), the radial velocity was increased and was related to the jet flapping. Thus, the jet flapping instability was effectively draining fresh gases. In contrast, low radial velocity were associated to values of  $\langle c_B \rangle$  close to unity. Consequences of these alternate mass transfers were visible in the mainstream. Figure 4.15-right shows instantaneous progress variables  $\langle c_A \rangle$  and corresponding axial velocity in zone A (averaged on the zone). Again, a bimodal distribution

was found, with an segregation between  $\langle c_A \rangle = 1$  and  $\langle c_A \rangle = 0.25$ . When the mainstream was ignited ( $\langle c_A \rangle = 1$ ), axial velocities were quite low and was mainly due to the cavity thermal gas expansion. When the mainstream was flowing normally (i.e., high axial velocities),  $\langle c_A \rangle$  was reduced to  $\langle \bar{c}_A \rangle \approx 0.25$ . This shows that when the cavity thermal expansion was over, the mainstream was draining burned gases and that no flame was stabilized above the cavity.

#### 4.5 Scenario for combustion instabilities in the present TVC

Our instantaneous analysis of a combustion instability cycle demonstrated a strong coupling between acoustic and heat release fluctuations. Remarkably, the mechanism driving combustion instabilities was found to differ from the conventional idea that the heat release oscillations were primarily related to a periodic vortex shedding in these type of geometries.

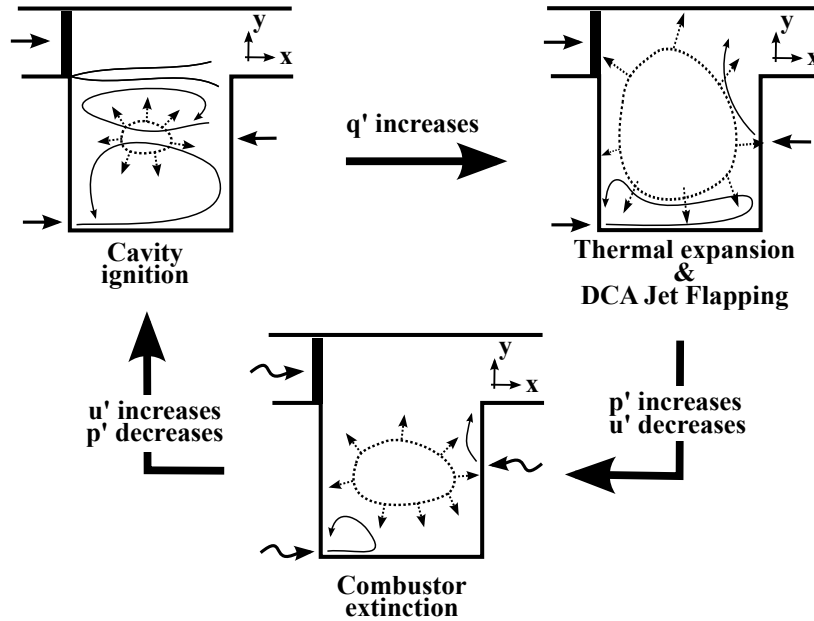


Figure 4.16: Schematic illustration of the mechanism of combustion instabilities encountered in the present TVC.

Figure 4.16 presents the mechanism that best explains the present data set:

- First, cavity jet injections circulated normally and efficient mixing enabled to create and ignite a stoichiometric region in the cavity. At this moment, the DCA jet injection was injected into the cavity and heat release was constantly increasing. Moreover, the main-



stream was flowing normally and a shear layer was established.

- Second, the cavity ignition became violent, mainly due to the cavity confinement. Consequently, the DCA jet was deflected towards the mainstream and resulting thermal gas expansion was annihilating the whole flow topology.
- Third, in parallel to the *jet flapping* aerodynamic instability, we suppose that the pressure increase may induce a flow rate oscillation, which in turn may disturb both cavity and mainstream flow dynamics and cause the burner extinction. Note that because the combustor was premixed, the flow rate modulation was related to variations in equivalence ratios.
- Fourth, the cavity flow dynamics started to establish as the heat release was at minimum and the cycle was over.

## 4.6 Concluding Remarks

This chapter was focused on investigating a stringent operating condition presenting large pressure oscillations. the main objective was to determine a possible scenario for these instabilities in order to obtain guidelines for a faster design.

To assess the flow-flame-acoustic interactions, we implemented dual PIV and OH PLIF measurements to examine the flow-flame-acoustics coupling. In order to process these large amounts of collected data, several image-processing routines were developed to automatically post-process the numerous images, extract flame contours (based on OH gradients), binarize images, and quantify energy contributions of deterministic and random velocity fluctuations.

We showed that the entire flow field was highly sensitive to acoustics. In particular, the *jet flapping* aerodynamic instability became apparent, flapping at the same acoustic frequency and alternately penetrating and blocking the mainstream flow. A spatial analysis showed that the energy associated with the acoustic-induced coherent motion was injected via large scale structures even if the whole energy cascade was affected. The POD analysis confirmed that this flow instability was exclusively driving and controlling the combustor dynamics.

Effects on the flame stabilization induced large and inefficient mass transfers between the cavity

and the mainstream. These transfers affected both aerodynamics and local equivalence ratio. As a result, the shear layer region was weakened and was not able mix and anchor the incoming lean main mixture.

We showed in Chap 2 that the pure flow instability could be annihilated by increasing the cavity confinement. This conclusion was confirmed (and even more true) with the presence of heat release and related thermal gas expansion. In addition, control of the local equivalence ratio within the cavity seemed to be critically important to establish a temporal and spatial stable recirculation zone that could produce a constant mass of burned gases. This conclusion is in agreement with numerical studies of Merlin [160], who also recommended to reduce spatial fluctuations of the progress variable in the cavity and at the flow separation.

From this analysis, several guidelines can be highlighted in order to obtain to a stable combustor:

- Obtain a sufficient mainstream momentum to ensure a good confinement of the cavity.
- Design injection systems in the cavity in order to obtain a relatively fast mixing, and the continuous presence of a pilot flame. For instance, modifications of the actual injection system could give better level of performances.
- Adopt a smarter stratification strategy to prevent steep variations of equivalence ratios between the cavity and the mainstream.

## Chapter 5

# Global analysis of the TVC burner

### Contents

---

<b>5.1</b>	<b>Experimental tools . . . . .</b>	<b>140</b>
5.1.1	Pressure energy $E_p$ . . . . .	140
5.1.2	Pollutant emissions . . . . .	141
<b>5.2</b>	<b>TVC performances . . . . .</b>	<b>142</b>
5.2.1	Effect of the mainstream flow momentum . . . . .	142
5.2.2	Importance of the cavity for flame stabilization . . . . .	145
5.2.3	Cavity equivalence ratio $\phi_c$ . . . . .	146
5.2.4	TVC momentum ratio . . . . .	147
5.2.5	Conclusion of the sensitivity study . . . . .	149
<b>5.3</b>	<b>Determination of criteria to predict flame stability . . . . .</b>	<b>149</b>
5.3.1	Definition of stability transition . . . . .	150
5.3.2	Importance of the cavity power $P_c$ . . . . .	151
5.3.3	Mainstream-cavity interactions . . . . .	154
<b>5.4</b>	<b>Characteristics of a stable point of operation . . . . .</b>	<b>156</b>
<b>5.5</b>	<b>Conclusion . . . . .</b>	<b>161</b>

---

Chapter 2 through 4 focused on the physical processes involved in a trapped vortex combustor geometry operating in an unstable mode. Inert investigations showed that a flow instability in the cavity was interfering with the shear layer region. Therefore, we recommended an improvement

of the cavity confinement by increasing the mainstream momentum (Chap. 3). This fact was confirmed in reactive conditions, primarily due to the presence of chemical reactions and thermal gas expansion and oscillations in flow rates and mixture composition. Moreover, we pointed out the necessity to modify injection systems in the cavity to optimize mixing and obtain a continuous production of burned gases (Chap. 4).

This chapter takes advantages of the previous detailed laser measurements to evaluate and improve global performances of the TVC. In particular, determination of stability maps to obtain a stable and low polluting mode is of interest. Thus, we adopt the following approach:

- Investigate the sensitivity of several parameters which may greatly improve the combustor dynamics.
- Based on the previous item, determine stability maps, trends, and dimensionless parameters to characterize the combustor.
- Validate these findings with detailed measurements of one stable operating condition.

Because fine data are not of interest in this chapter, simple diagnostics and global criteria are used (Sec. 5.1). Effects of some parameters (geometry, chemical composition and aerodynamics) are investigated to estimate their sensitivity in terms of pollutant emissions and flame stability (Sec. 5.2). Section 5.3 introduces dimensionless parameters which may be suitable to predict the TVC stability and finally, Sec. 5.4 presents detailed characteristics of one stable operating condition.

## 5.1 Experimental tools

### 5.1.1 Pressure energy $E_p$

Pressure fluctuations were measured with a 5 kHz sampling rate 7061B Kistler dynamic pressure sensor (cf. Sec. 2.2.1). Global burner acoustics was characterized by integrating the area under the power spectral density spectrum as

$$E_p = \int_0^{+\infty} PSD(f)df. \quad (5.1)$$

$E_p$  is the pressure energy in  $Pa^2$ . This energy does not correspond to the acoustic energy but is used as an estimator in the present study. The pressure power spectral density (PSD) spectrum was determined with a one-sided algorithm using the Welch method.

### 5.1.2 Pollutant emissions

Pollutant emissions were measured with two portable gas analyzers. A PG 250 Horiba unit was used for CO and  $NO_x$  measurements, and a MEXA 11170 HFID unit was measuring UHC concentrations. The sample probe was placed in the exhaust gas line, downstream of the adaptive nozzle (see Sec. 1.4):

- $NO_x$  were measured with the chemiluminescence method. The sample gas reacted with injected ozone  $O_3$  and the resulting radiation emission (chemiluminescence between 600 and 1300 nm) produced from the excited specie was proportional to the  $NO_x$  concentration in the sample gas. Prior to the measurement,  $NO_2$  molecules were converted into  $NO$  to reduce quenching effects.
- $CO$  was measured with the non-dispersive infrared absorption method. In fact, an infrared laser beam was going through the the gas sample and measurements of the absorption was directly correlated to the  $CO$  concentration.
- $UHC$  were measured with a flame ionization detector. A hydrogen flame burned organic compounds to produce ions. The concentration of these ions was directly proportional to the amount of organic compound.

Prior to the measurements, a 30 minute warm-up period was necessary to heat all feeding lines. Then, a zero calibration was performed with nitrogen, followed by a span calibration, using a standard mixture of gases. This procedure was done daily. Because the response time of the different sensors was within 45 s, we recorded the different data after 60 s.

All results were given in parts-per-millions (*ppm*) and transformed into an emission index in this study, defined as the ratio of the emitted specie mass to the mass of fuel ( $g.kg_F^{-1}$ ). Note that the TVC was fueled with  $CH_4$ .

## 5.2 TVC performances

We showed in Chap. 4 that the alternate location of the DCA jet, mainly due to thermal gas expansion, led to a local oscillatory equivalence ratio and produced strong heat release oscillations. In order to prevent from these instabilities, two solutions were suggested: (1) vary the composition and velocity of the different cavity injection systems or (2) change the injection strategy to obtain a favorable cavity flow structure. These two solutions were tested hereafter. Jet conditions could be easily varied with the different flowmeters, and we added a refractory piece of steel to radially deflect the DCA jet flow in the mainstream. Note that we intentionally deflect this jet in order to ensure a good cooling of the cavity trailing edge. This new injection was named  $I_1$  whereas the original injection system was named  $I_0$ . A schematic illustration is depicted in Fig. 5.1.

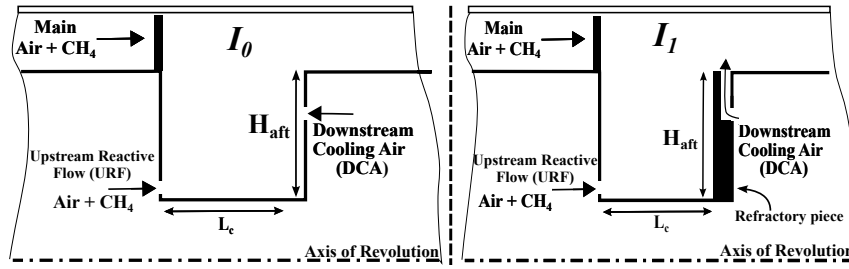


Figure 5.1: Schematic illustration of the two cavity injection systems  $I_0$  (left) and  $I_1$  (right). The cavity aspect ratio  $L_c / H_{aft}$  was unchanged.

### 5.2.1 Effect of the mainstream flow momentum

We first investigated the cavity confinement by increasing the mainstream flow momentum (Chap. 4). Combination of moderate mass interactions with a stable location of the mixing region at the flow separation between the cavity and the mainstream should improve the TVC performances.

Effects of increasing the main bulk velocity  $U_m$  were then evaluated using two approaches:

- Increase the mainstream temperature  $T_{air}$  while keeping a constant flow rate of air  $\dot{m}_m^o$ . The mainstream density was lowered and balanced by a velocity variation.
- Increase the mainstream flow rate of air  $\dot{m}_m^o$  at constant power  $P_g$  (constant fuel flow rate).

The mainstream bulk velocity  $U_m$  was directly varied but also resulted in variations of the main equivalence ratio  $\phi_m$ .

Note here that conditions in the cavity were kept constant.

### Variation of the mainstream temperature $T_{air}$

Figure 5.2 shows the pressure energy  $E_p$  when increasing the mainstream temperature  $T_{air}$ . Results are given for two cavity injection systems, and for two equivalence ratios (i.e., the mainstream air flow rate  $\dot{m}_m^o$  was varied). Cavity operating conditions were kept constant, in accordance to Tab. 2.2.

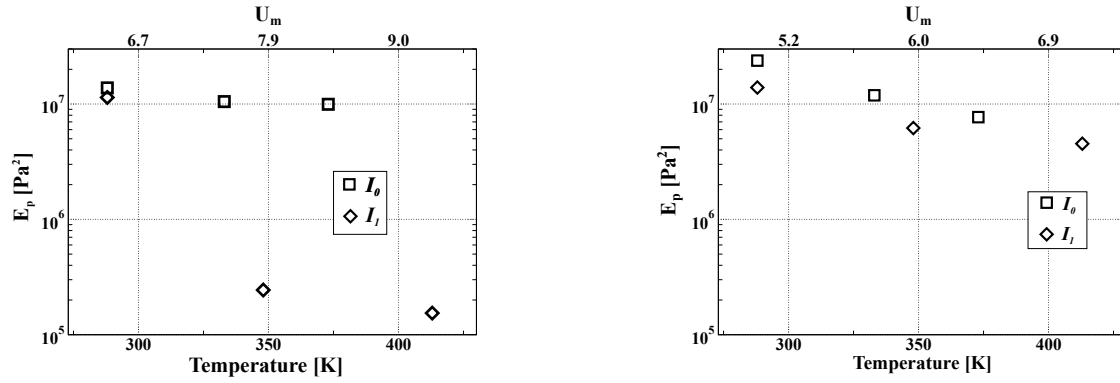


Figure 5.2: Pressure energy  $E_p$  as a function of the mainstream temperature  $T_{air}$ . Left:  $\phi_m = 0.60$ ,  $\dot{m}_m^o = 28.7 \text{ g.s}^{-1}$ ; Right:  $\phi_m = 0.80$ ,  $\dot{m}_m^o = 21.6 \text{ g.s}^{-1}$ .  $P_g = 60\text{kW}$ ,  $\phi_c = 3.0$ ,  $\dot{m}_c^o = 0.7 \text{ g.s}^{-1}$ . Mass flow rates are given at ambient temperature.

Because the experiments were performed at constant air mass flow rates, and at constant power, the velocity  $U_m$  necessarily increased with temperature to balance density variations. For instance, the mainstream bulk velocity  $U_m$  was increased by an order of 30% between 288 and 413 K at  $\phi_m = 0.80$ .

All data show a decrease of  $E_p$  when the main air temperature was increased. However, a bifurcation occurred for  $\phi_m = 0.60$  (Fig. 5.2-left). The  $I_1$  system (Fig. 5.1) resulted in a pressure energy almost 100 times lower than the  $I_0$  system and was remarkably not observed when  $\phi_m$  was 0.8 (Fig. 5.2-right). We conclude that the original injection system  $I_0$  was not efficient and did not improve the cavity confinement. In addition, when using the  $I_1$  system, a minimum equivalence ratio combined with a relatively high mainstream velocity had to be reached in order

to confine the cavity and reduce pressure oscillations. This shows that chemical and aerodynamic conditions are of importance. Note that increasing the mainstream air temperature also resulted in modifications of the medium, and may also affect acoustics (e.g., sound speed).

### Variation of the mainstream air flow rate $\dot{m}_m^o$

In order to confirm the bifurcation observed in Fig. 5.2-left, we directly increased  $\dot{m}_m^o$  at constant power ( $\phi_m$  was automatically decreased). Note that data shown in this section are performed at  $T_{air} = 413K$ . This test provided two advantages: on one hand, lower flame temperatures to reduce  $NO_x$  emissions and, on the other hand, higher bulk velocities in order to increase the cavity confinement. Figure 5.3 shows the pressure energy when the main bulk velocity

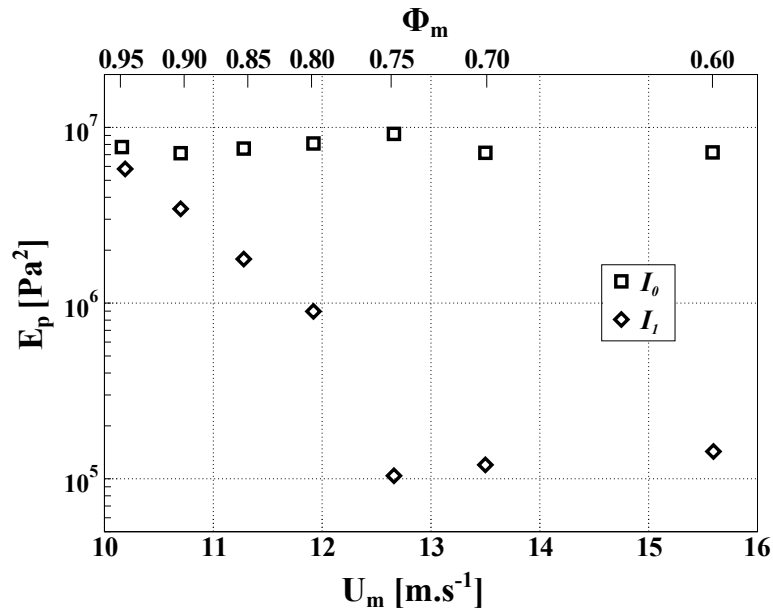


Figure 5.3: Pressure energy  $E_p$  as a function of the main bulk velocity  $U_m$ . Corresponding main equivalence ratios  $\phi_m$  are given on the secondary x-axis.  $P_g = 60kW$ .  $T_{air} = 413K$ ,  $\phi_c = 3.0$ ,  $\dot{m}_c^o = 0.7 \text{ g.s}^{-1}$

$U_m$  was increased. Results are provided for the two injection systems and the corresponding main equivalence ratio  $\phi_m$  is given on the secondary x-axis. Similarly to the previous results, a bifurcation occurred at high mainstream velocities  $U_m$  for the injection system  $I_1$ . In contrast, the original system  $I_0$  proved to be unstable whatever the operating conditions we investigated. Again, the combination of a minimum main velocity and its corresponding equivalence ratio



may increase the cavity confinement and then reduce pollutant emissions.

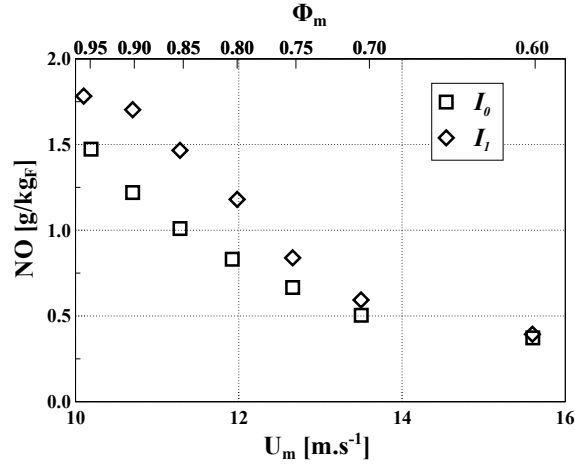


Figure 5.4:  $NO$  emissions as a function of the main bulk velocity  $U_m$ , for the two cavity injection systems. Corresponding main equivalence ratios  $\phi_m$  are given on the secondary x-axis.  $P_g = 60\text{kW}$ .  $T_{air} = 413\text{K}$ ,  $\phi_c = 3.0$ ,  $\dot{m}_c^o = 0.7\text{ g.s}^{-1}$ .

The latter were measured and Fig.5.4 shows the evolution of  $NO_x$  emissions when  $U_m$  was increased, for the two injection systems. Benefit of lowering  $\phi_m$  is clearly evident because of the reduction of the flame temperature. Both systems gave globally the same  $NO_x$  emissions, decreasing to a value of  $0.4\text{ g/kg}_F$  but the effectiveness of the  $I_1$  system is clear in Fig. 5.5. In fact, the  $I_0$  system presented higher CO and UHC values when  $U_m$  was increased and confirmed results shown in Chap 4: the combustor arrangement produced a pulsed combustion regime associated with an alternate ignited and extinguished operating conditions. Then, important quenching and production of unburned gases were evident. In contrast, the  $I_1$  system had a large range of operating condition with low CO and UHC. From these data, we conclude that a compromise can be found to balance all pollutant emissions with the  $I_1$  injection system. The low emission window (Fig. 1.2 for the  $I_1$  system can be found between  $\phi_m = 0.70$  and  $0.80$ .

### 5.2.2 Importance of the cavity for flame stabilization

The previous section showed the importance of the injection system to confine the cavity and to prevent from sudden thermal gas expansion. In addition, for a given mainstream power  $P_m$ , a minimum mainstream velocity  $U_m$  had to be reached to obtain a stable configuration and low

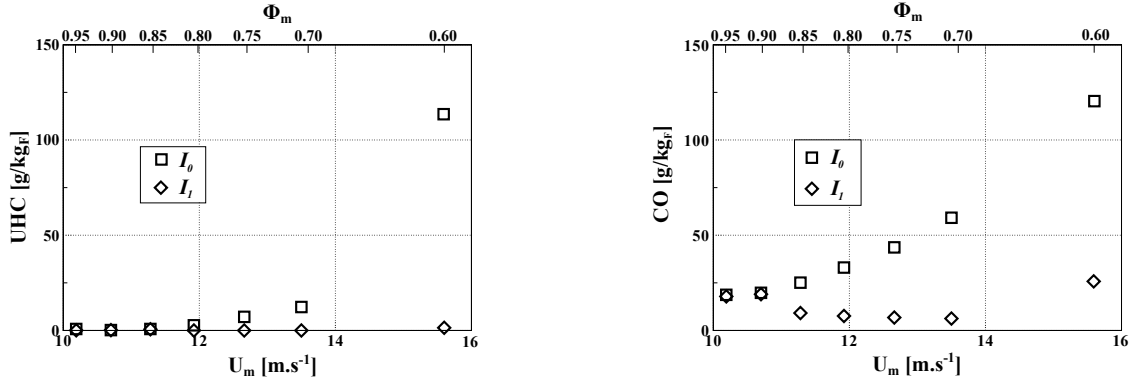


Figure 5.5: CO and UHC emissions as a function of the main bulk velocity  $U_m$ , for two cavity injection systems. Corresponding main equivalence ratios  $\phi_m$  are given on the secondary x-axis.  $P_m = 50\text{kW}$ .  $\phi_c = 3.0$ ,  $\dot{m}_c^o = 0.7 \text{ g.s}^{-1}$ .

pollutant emissions. However, these trends were true for one set of cavity operating conditions. In this section, the mainstream conditions were set ( $\phi_m = 0.7$ ,  $T_{air} = 413\text{K}$ ,  $U_m = 13.7 \text{ m.s}^{-1}$ ,  $P_{main} = 50\text{kW}$ ) and we studied several cavity parameters in order to highlight variables likely to be optimized.

### 5.2.3 Cavity equivalence ratio $\phi_c$

Figure 5.6 presents the pressure energy  $E_p$  when the cavity equivalence ratio  $\phi_c$  (calculated with the URF flow composition, cf. Chap. 1) was increased. Similarly to the previous section, a bifurcation occurred when the injection system was changed and when  $\phi_c$  was increased. The  $I_0$  system was unstable in comparison to the  $I_1$  system. The latter was found to be more stable around  $\phi_c = 3$ , but the observed parabolic trend highlights two opposite effects: at low  $\phi_c$ , the cavity may not produce enough radicals and may not stabilize the main flame whereas at high  $\phi_c$ , the potential chemical energy from the rich flow may produce a steep mixture stratification not favorable for a continuous ignition. These two extreme configurations resulted in a pulsed combustion regime.

The  $I_1$  injection system clearly gave better results and we chose to focus on this injection in the next sections. In addition, the cavity equivalence ratio was set to  $\phi_c = 3.0$  in the rest of the study.

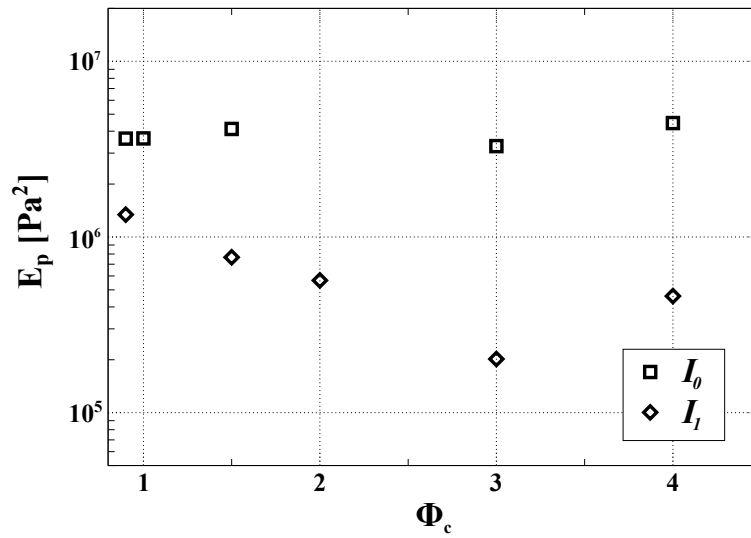


Figure 5.6: Pressure energy  $E_p$  as a function of the cavity equivalence ratio  $\phi_c$ .  $P_m = 50\text{kW}$ ,  $\phi_m = 0.7$ ,  $T_{air} = 413\text{K}$ .

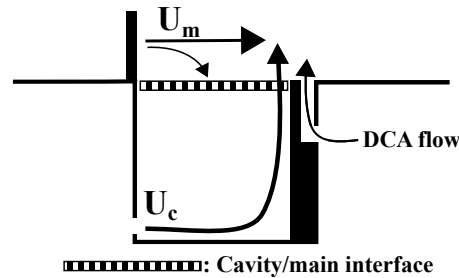


Figure 5.7: Schematic illustration of the jet cross-flow like flow. Arrows represent the different flow pathlines.

#### 5.2.4 TVC momentum ratio

We highlighted that quality of mass exchanges was of great importance to achieve a good mixing at the interface between the cavity and the mainstream. Figure. 5.7 shows that the URF cavity flow was directly interacting with the mainstream, and that aerodynamics may play an important role in the location of the mixing region.

In fact, the URF flow was injected at the the bottom of the upstream cavity face, impinged the downstream cavity face and was deflected towards the main channel. Thus, we could model

this flow topology to a jet in cross-flow and we introduced the dimensionless number  $J$ , defined as

$$J = \frac{\rho_m U_m^2}{\rho_c U_c^2}, \quad (5.2)$$

where  $J$  is the jet momentum flux between the mainstream and the cavity flows<sup>1</sup>,  $U_c$  is the bulk velocity of the URF injection system, and  $\rho_c$  is the density of the URF mixture. In the present experiments, because the mainstream momentum was unchanged,  $J$  was only varied with the cavity jet momentum. The bulk cavity flow  $U_c$  was varied with a constant  $\phi_c = 3.0$ , the cavity power  $P_c$  slightly varied ( $\pm 5\%$ ).

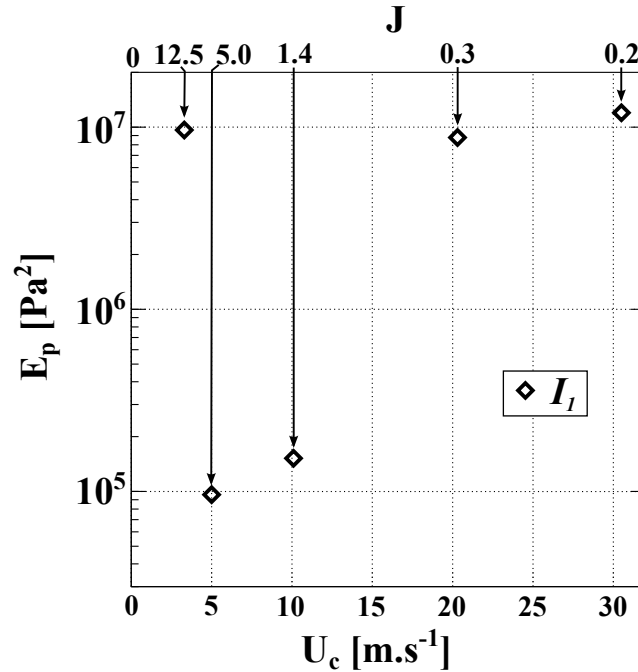


Figure 5.8: Pressure energy  $E_p$  as a function of the URF cavity bulk velocity. Results given for the  $I_1$  injection system.

Figure 5.8 depicts the pressure energy  $E_p$  when the cavity bulk velocity  $U_c$  was increased. The mainstream operating conditions were unchanged and results are given for the  $I_1$  injection system. The corresponding values of  $J$  is given on the secondary x-axis.

Data show a stable configuration at  $J_{min} = 5.0$  whereas the burner was unstable for lower or higher values of  $J$ . We then propose an explanation for the observed trend: the cavity flow rate readily penetrated the mainstream flow when  $J$  was higher than  $J_{min}$ . In contrast, the

<sup>1</sup>This parameter is well used to study and characterize jet in cross flows but is defined differently in comparison to a classical jet in cross flow [116]

mainstream flow entered and mixed with the cavity flow when  $J$  was lower than  $J_{min}$ . When the optimum value of  $J$  was not reached, mixing regions were likely to occur either in the cavity or in the mainstream (Fig. 5.7).

### 5.2.5 Conclusion of the sensitivity study

Based on the detailed insights, we evaluated the sensitivity of several parameters in order to obtain a stable TVC (in terms of flame stability and pollutant emissions). We conclude that the location of the mixing region is critically important and highly depends on the injection system strategy: modification of the DCA injection system was found to give better performances. Moreover, the range of stable operating conditions seemed to be both controlled by aerodynamics and chemical conditions: a relatively high cavity equivalence ratio in the cavity, combined with a sufficient mainstream flow velocity led to a stable combustor. These results are in agreement with Burguburu [27], who argued that a large cavity equivalence ratio combined with a relatively important mainstream velocity were confining the cavity flow structure and then creating a stable source of flame stabilization.

## 5.3 Determination of criteria to predict flame stability

The aim of this section is to highlight some control laws which could be used to predict stable operating conditions, and to prevent the occurrence of thermo-acoustic oscillations in such a combustor. We took advantages of all insights gained with detailed laser diagnostics (Chap 4) and results from previous sections in order to introduce dimensionless parameters which may be most appropriate for early-design rules.

Because the  $I_1$  injection system gave good results in terms of stability, this geometry is only investigated hereafter.

### 5.3.1 Definition of stability transition

We performed several experiments to determine an automatic, rapid, and robust criterion to obtain a transition between unstable and stable operating conditions.

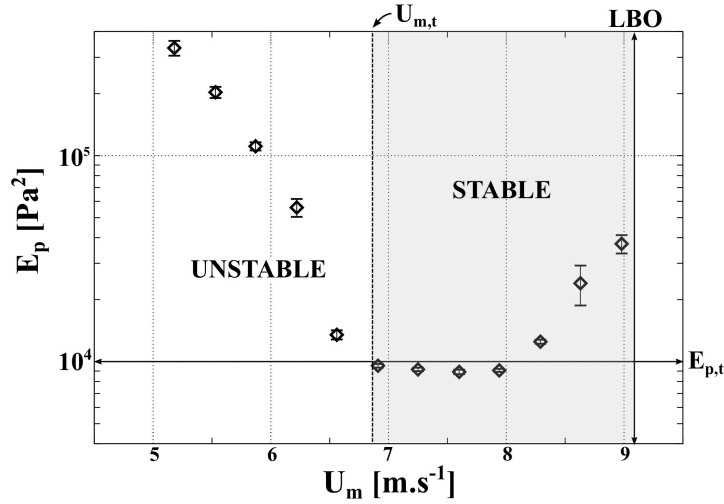


Figure 5.9: Example depicting the pressure energy criterion  $E_{p,t}$  used to determine the transition to a stable regime. Pressure energy  $E_p$  as a function of the main bulk velocity  $U_m$ .  $P_g = 15$  kW,  $\phi_c = 3.0$ .

Figure 5.9 depicts the pressure energy  $E_p$  as a function of the main bulk velocity  $U_m$ . The TVC power was  $P_g = 15$  kW, and the cavity equivalence ratio  $\phi_c$  was 3.0. Data showed a rapid decrease of the pressure energy when  $U_m$  was increased, reaching a plateau at  $E_p \approx 10^4$  Pa<sup>2</sup> for  $U_m > 7.0$  m.s<sup>-1</sup>. The slight increase observed for  $U_m > 8$  m.s<sup>-1</sup> was related to the LBO limit, which resulted in local flame extinctions rather than thermo-acoustic oscillations. Thus, the stability criterion between an unstable and stable flame was chosen when the pressure energy reached a plateau at  $E_{ac,t} = 10^4$  Pa<sup>2</sup>. All subsequent parameters were estimated in accordance with this critical value. For instance, the transitional mainstream bulk velocity  $U_{m,t}$  was determined with the following relation:

$$U_{m,t} = U_m \cap E_{p,t} \quad (5.3)$$

This criterion was tested for all the experiments several times and was found to be intrin-

sically robust (uncertainty less than 9%). Because we were only interested in thermo-acoustic oscillations, we intentionally included data until LBO was reached (even if  $E_p$  was increased).

Because mass exchanges were of great importance to achieve a good mixing at the interface between the cavity and the mainstream, the URF cavity flow was directly interacting with the mainstream. In fact, the URF flow was injected at the bottom of the upstream cavity edge, impinged the downstream cavity edge and was deflected towards the main channel. Thus, we could model this flow topology to a jet in cross-flow and we introduced the dimensionless transitional jet-momentum flux  $J_t$  to obtain a stable combustor, and defined as

$$J_t = \frac{\rho_m U_{m,t}^2}{\rho_c U_{c,t}^2}. \quad (5.4)$$

$\rho_m$  is the density of the lean mixture in the main channel, and  $\rho_c$  is the density of the URF rich mixture in the cavity. This parameter is well used to study and characterize jet in cross flows but is defined differently in comparison to a classical jet in cross flow [116]. We also introduced a transitional stratification ratio  $S_t$ , defined as

$$S_t = \frac{\phi_{c,t}}{\phi_{m,t}}. \quad (5.5)$$

This parameter is well used in stratified configurations or when flows are not perfectly mixed [217].

### 5.3.2 Importance of the cavity power $P_c$

This section aims to investigate effects of the cavity power  $P_c$  on the combustor stability. As a preliminary experiment, the cavity power was fixed at  $P_c = P_c^* = 3.5\text{kW}$ . The experiment consisted in adapting the mainstream bulk velocity  $U_m$  (for different mainstream powers  $P_m$ ) to reach a sufficient level of cavity confinement, and obtain a stable combustor. Measurements were scaled with the combustor power ratio  $P_m / P_c^*$  and dimensionless parameters introduced in the previous section (cf. Eqs ??).

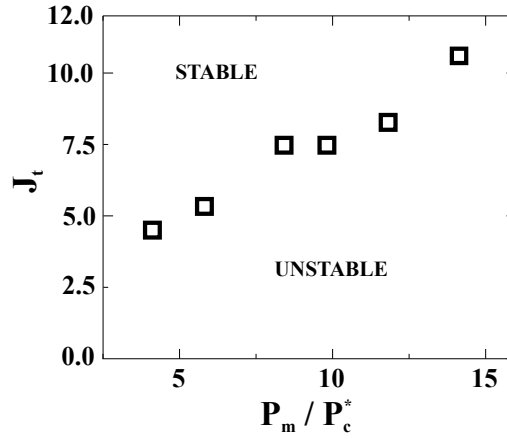


Figure 5.10: Stability map scaled with transitional jet momentum flux  $J_t$ , for different power ratios  $P_m / P_c$  while keeping fixed conditions in the cavity ( $P_c = 3.5$  kW,  $\phi_c = 3.0$ ,  $U_c = 3.6$  m.s<sup>-1</sup>)

Figure 5.10 depicts the evolution of the transitional values  $J_t$  when increasing the power ratio  $P_m / P_c^*$ . Because conditions in the cavity were unchanged (i.e.,  $P_c$ ,  $\phi_c$ , and  $U_c$ ) in this experiment,  $J_t$  values were obtained by varying the mainstream conditions, and the transitional jet momentum ratio was then defined as

$$J_t = \frac{\rho_m U_{m,t}^2}{\rho_c U_c^2}. \quad (5.6)$$

First, the stable range of operating conditions was reached for values of  $J_t$  higher than unity and confirmed the need to confine the cavity by increasing considerably the mainstream momentum flux. Second,  $J_t$  values had a quasi-linear dependance with the ratio  $P_m / P_c^*$ . Note that the increase of the main bulk velocity  $U_m$  was accompanied by an increase of the wake region behind the rods, which in turn, improved mass exchanges and finally flame stabilization. We conclude that cavity conditions automatically determined the amount of mainstream momentum needed to achieve a good confinement of the cavity. However, because we operated the combustor in a premixed mode, chemical parameters had also be optimized.

Thus, we investigated the transitional stratification ratio  $S_t$ , defined here as

$$S_t = \frac{\phi_c}{\phi_{m,t}}. \quad (5.7)$$



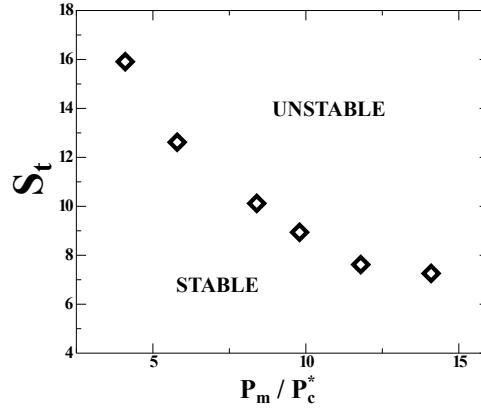


Figure 5.11: Stability map scaled with transitional  $S_t$  values, for different power ratios  $P_m / P_c$  while keeping fixed conditions in the cavity ( $P_c = 3.5$  kW,  $\phi_c = 3.0$ ,  $U_c = 3.6$  m.s<sup>-1</sup>)

Again, because the cavity conditions were fixed,  $S_t$  values were determined only by varying the mainstream conditions. Results are depicted in Fig. 5.11 and corresponds to the same operating conditions of Fig. 5.10. Lower values of  $S$  led to a stable combustor, and this trend was even pronounced for higher values of  $P_m / P_c^*$ . Note that values of  $S_t$  were always higher than unity and proves that the concept of using rich and lean regions was efficient in our case. In addition, the level of stratification was dependent on the mainstream power: at low powers  $P_m$ , stratification was high to improve the lean flame stabilization whereas at high powers  $P_m$ , a moderate stratified flow was sufficient to stabilize main flame. This result is in agreement with the literature. In fact, previous investigations showed that mainstream flows were almost not fueled (i.e., low  $P_m$  conditions) and with a relatively high cavity equivalence ratio [104, 128].

The previous results were obtained for one set of operating conditions within the cavity ( $P_c^* = 3.5$  kW). We repeated the previous experiment for several cavity power  $P_c^*$  (i.e., 1.0, 2.0, and 3.5 kW). The latter was adjusted with the fuel flow rate  $\dot{m}_c^F$  in order to maintain a constant aerodynamics. Therefore, cavity equivalence ratios  $\phi_c$  were automatically adjusted. Results are depicted in Fig. 5.12, as a function of the power ratio  $P_m / P_c^*$ .

The evolution of  $J_t$  values were similar to the first experiment. Increasing the power ratio  $P_m / P_c^*$  also increased the transitional value of  $J_t$ . Remarkably, this trend was even more pronounced for larger cavity power  $P_c^*$  and demonstrates the need to enhance the cavity confinement when the cavity power was increased. In fact, when referring to the combustion instability scenario (Fig. 4.16), thermal gas expansion was the mechanism destabilizing the whole flow structures

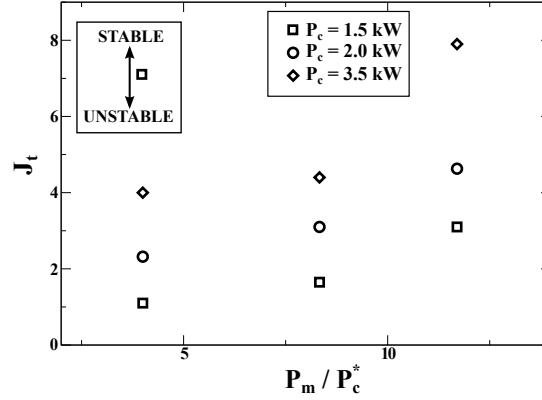


Figure 5.12: Stability map as a function of the power ratio  $P_m / P_c$  and for different cavity equivalence ratios. Constant aerodynamics within the cavity,  $U_c = 3.6 \text{ m.s}^{-1}$ .

and may be related to the chemical energy injected in the cavity.

We conclude that the confinement of chemical reactions occurring in the cavity was critical and could be obtained by increasing the mainstream momentum flux. In addition, smart values of the equivalence ratio stratification have also to be obtained in order to take advantage of the rich pilot region. Remarkably, low mainstream powers led to wider stable modes. Thus, aerodynamic and chemical interactions may play an important role in the flame stabilization. Therefore, we investigated the interactions between the cavity and the mainstream in the next section.

### 5.3.3 Mainstream-cavity interactions

We considered the whole combustor in order to highlight any relationship between the mainstream and cavity regions, which may be useful for a smart early-design. Thus, the cavity power  $P_c^*$  was set to 3.5 kW and we adjusted the cavity equivalence ratio by means of the cavity air flow rate  $\dot{m}_c^o$  (i.e., aerodynamics was now changed).

Figure 5.13 shows the transitional cavity bulk velocities  $U_{c,t}$  as a function of different mainstream bulk velocities  $U_m$ , and for several power ratios  $P_m / P_c^*$ . Note that all data had a linear feature: for fixed cavity conditions, the stable region of the combustor was encountered when the mainstream flow rate was increased. This confirmed the necessity to balance the different jet momentum fluxes to confine the cavity and to locate the mixing region at the interface between the cavity and the mainstream. Remarkably, all data collapsed whatever the power ratio  $P_m / P_c^*$  considered and could be useful for design laws.

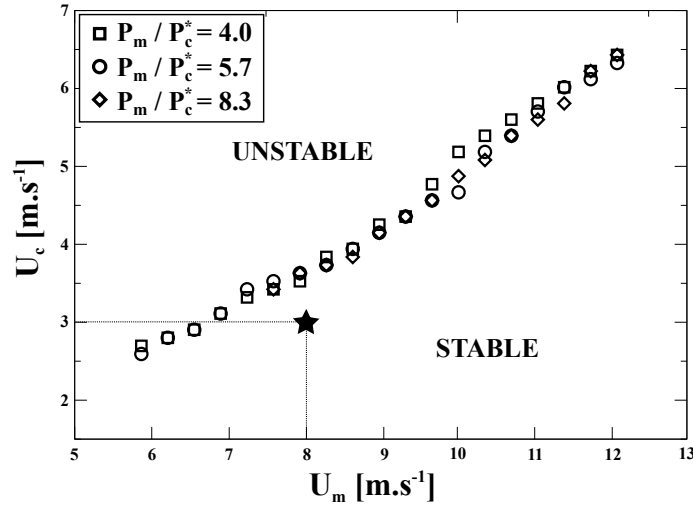


Figure 5.13: Transitional cavity bulk velocities obtained for different mainstream velocities  $U_m$  and for different power ratios  $P_m / P_c$ .  $P_c = 3.5$  kW

Calculation of the different equivalence ratios  $\phi_{m,t}$  and  $\phi_{c,t}$  are reported in Fig. 5.14 as a function of the mainstream bulk velocity  $U_m$ . The stratification values obtained for each power ratio were quite independent of  $U_m$ . Thus, for a given mainstream bulk velocity and a given mainstream power, it was possible to obtain the corresponding transitional stratification ratio  $S_t$  and predict the cavity conditions  $\phi_c$  and  $U_c$ .

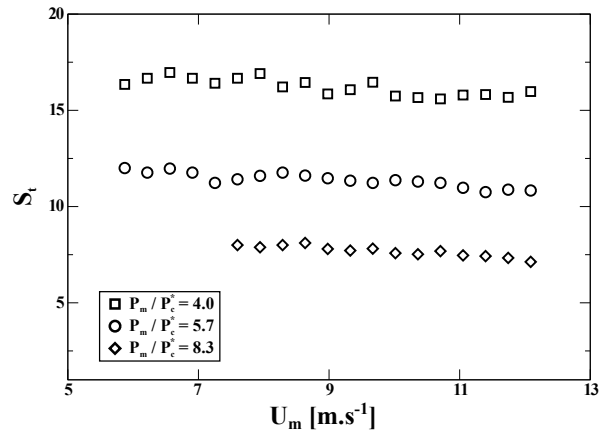


Figure 5.14: Values of  $S_t$  a function of the mainstream bulk velocity  $U_m$  and for different power ratios. Values corresponding to transitional values obtained in Fig. 5.13

Considering that the transitional stratification values were quite constant for each power ratio, it was possible to directly obtain a control law between these two quantities (Fig. 5.15).

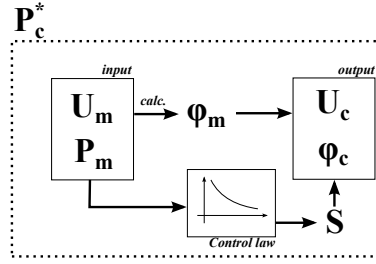


Figure 5.15: Simplified schematic illustration of a design procedure with a given cavity power  $P_c^*$ .

As an example, if the mainstream velocity  $U_m$  was set to  $9 \text{ m.s}^{-1}$  with a power ratio  $P_m / P_c = 5.7$  ( $P_c = 3.5 \text{ kW}$  and  $P_m = 11.5 \text{ kW}$ ), the corresponding stratification ratio was 11.7. Thus a cavity equivalence ratio  $\phi_c = 1.9$  and a cavity bulk velocity  $U_c = 5.6 \text{ m.s}^{-1}$  may lead to a stable burner.

To conclude, we showed that the cavity confinement was critically important to obtain a stable combustor. The cavity power was primarily controlling the stability but a set of aerodynamic conditions was also necessary to ensure a stable combustion process (i.e., locate the mixing region at the interface between the cavity and the mainstream). Note that these correlations are only valid for the cavity power  $P_c^* = 3.5 \text{ kW}$ .

## 5.4 Characteristics of a stable point of operation

In accordance with the previous sections, we performed detailed laser measurements (see Chap. 4) of a stable operating condition. Table 5.1 summarizes operating conditions investigated hereafter, chosen in accordance with Fig. 5.13 (star symbol). Note that the DCA flow rate was deflected with the refractory metal piece, the mainstream air flow rate  $\dot{m}_m^o$  was increased to  $24.6 \text{ g.s}^{-1}$  with a constant power of  $50 \text{ kW}$ , and the URF flow rate  $\dot{m}_c^o$  was reduced to  $0.41 \text{ g.s}^{-1}$  with a constant cavity equivalence ratio  $\phi_c = 3.0$ . This resulted in a slight decrease of the nominal power of the combustor to  $53.5 \text{ kW}$ .

Figure 5.16 depicts a sequence of instantaneous OH-PLIF and PIV measurements corresponding to the operating conditions in Tab. 5.1. The figure illustrates instantaneous coupling of velocity vector fields colored by their corresponding magnitudes and locations of burned gases (OH signal in greyscale). Left column depicts data recorded in the rod middle plane RM (plane

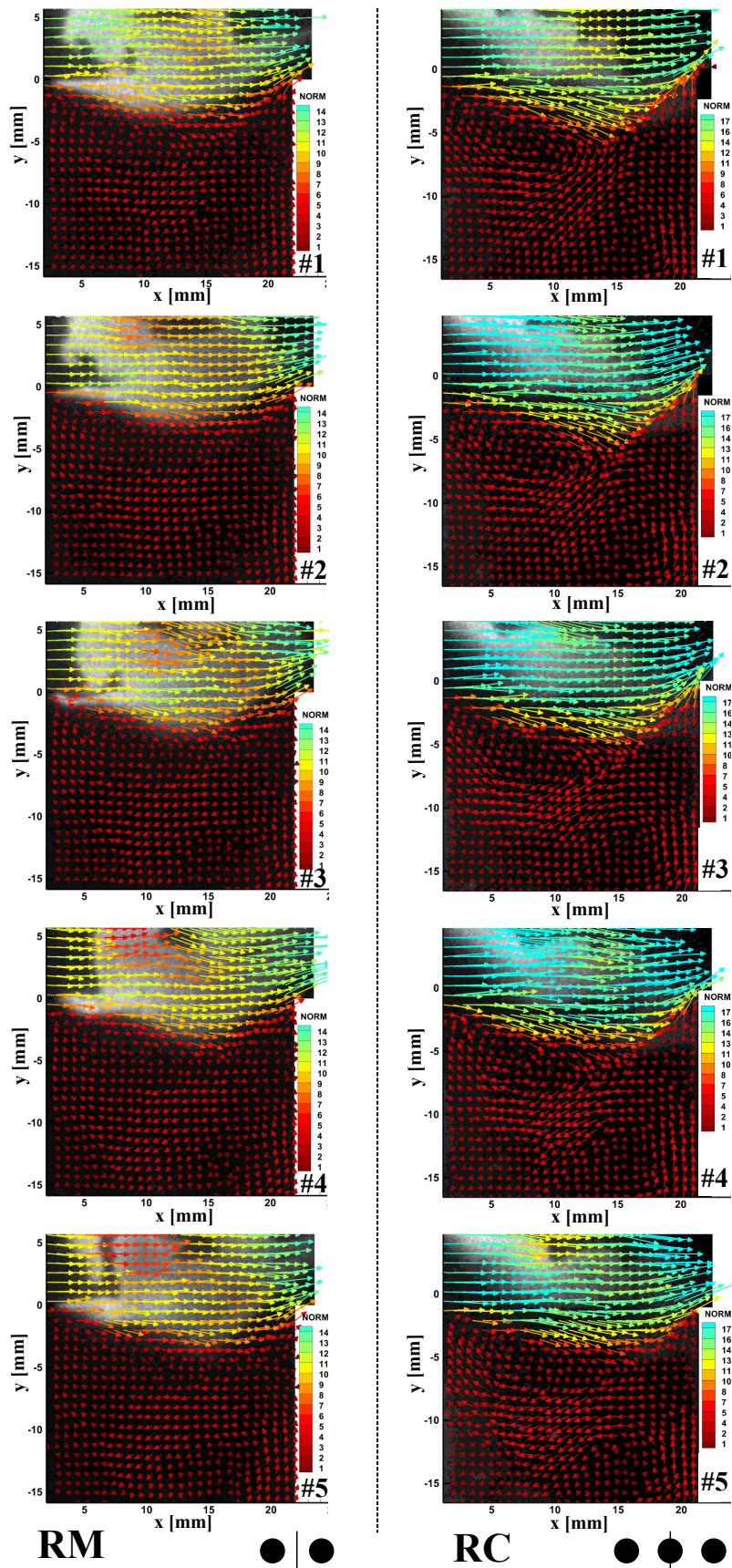


Figure 5.16: Simultaneous OH traces and velocity measurements (colored according to magnitude). Time between two instantaneous records was  $400\mu\text{s}$ . Left: rod middle plane RM; Right: rod center plane RC. • at the bottom represents rods and vertical line corresponds to the plane of interest.

	Main	URF	DCA
Flow rate [g.s <sup>-1</sup> ]	25.6	0.41	1.0
Bulk velocity [m.s <sup>-1</sup> ]	8.0*	3.0	3.6
$\phi$ [-]	0.7	3.0	0.0
fuel [g.s <sup>-1</sup> ]	1.0	0.06	0.0
Power [kW]	50	3.5	0
$P_{glob}$ [MPa]	0.17		

Table 5.1: TVC operating conditions. \* The mainstream air was heated up to 413K.

between two rods) and the right column shows data recorded in the rod center plane RC (plane crossing one rod).

In contrast with Fig. 4.6, the different snapshots are quite similar. Velocities in the cavity were quite constant with the presence of two counter-rotative vortices whereas the mainstream flowed normally. Burned gases were spatially located around  $y = 0$  mm and in the whole mainstream, proving that the main flame was constantly ignited and stabilized. Remarkably, no OH traces were found in the cavity (negative y-values), and demonstrated that mixing of gases were located in the shear layer region, at the interface between the mainstream and the cavity. Because the URF jet was directly injected in the cavity with an equivalence ratio  $\phi_c$  larger than the upper flammability limit, the flame was then sustained in regions exhibiting local stoichiometry.

However, some differences in the location of burned gases were visible between the two planes of interest. In the RM plane (Fig. 5.16-left), burned gases were located in two specific regions:

- A long and thin ligament of burned gases was always located all along the interface at  $y = 0$  mm. The latter acted as a pilot flame, resulting from the mixing with cavity gases.
- A wrinkled flame front was established for  $y > 3$  mm and with an axial location lying between 5 and 10 mm. The lean incoming mixture flow was continuously ignited.

Note that a zone of unburned gases was inserted between these two regions ( $0 \text{ mm} < y < 3 \text{ mm}$  and  $x < 7 \text{ mm}$ ) and was primarily due to the flow separation. In fact, for  $y \approx 0$  mm, the incoming mainstream flow first mixed with cavity gases to produce the pilot flame and the production of combustion radicals enabled the main flame to be ignited downstream of the cavity leading edge ("rearward" ignition mechanism).

Figure 5.17-left depicts the corresponding mean OH-PLIF field in the two planes of interest.

The two flames are clearly visible: the pilot flame, stabilized at the flow separation, and the main flame, developing in the main channel. Both regions are recalled as well as the "rearward" mainstream ignition mechanism.

Instantaneous data in the rod center plane RC (Fig. 5.16-right) shows that burned gases were located in the wake region, downstream of the rod. Only one region of burned gases was visible and resulted from a direct migration of combustion radicals in the mainstream and the subsequent flow ignition. Mean OH-PLIF field is shown in Fig. 5.17-right, and shows that the main flame was shifted towards the rod. We then suggest that this flame gathered the pilot and main flame at the same location. Note that, even with the presence of the rod, mainstream velocities were remarkably homogeneous, with small radial component and similar to the RM plane data. This behavior was not explained and confirms again that three-dimensional effects were preponderant.

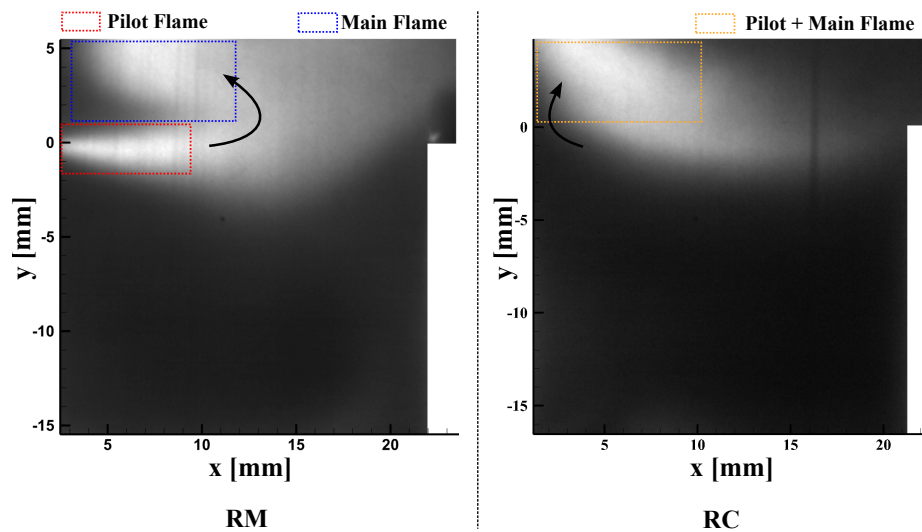


Figure 5.17: Mean OH field for the stable configuration. Left: rod middle plane RM; Right: rod center plane RC. Flame regions are depicted with colored dashed rectangles.

In order to assess in details the coupling between the two flames observed in the RM plane (Fig. 5.16-left), we considered two zones, depicted in Fig. 5.18-left and we extracted a set of coupled and spatially averaged a set of progress variables  $\langle c_{main} \rangle$  and  $\langle c_{pilot} \rangle$ <sup>2</sup>. Figure 5.18 shows a scatter plot of 400 instantaneous  $(\langle c_{pilot} \rangle, \langle c_{main} \rangle)$  pairs. The plot clearly show that values of  $\langle c_{pilot} \rangle$  were most of the time close to unity and demonstrates that this flame was

<sup>2</sup>The surface area was identical in each zone.

spatially established at the flow separation between the cavity and the mainstream. In contrast, the broadened distribution of the corresponding values of  $\langle c_{main} \rangle$  shows that the location of the main flame was spatially fluctuating, primarily due to the local conditions. In fact, the "rearward" mechanism may embed local mixing and turbulence but could not be explained in details with the present data. However, values of  $\langle c_{main} \rangle$  were never lower than 0.2, thus proving that the flame front was relatively well established, primarily due to the presence of the stable pilot flame.

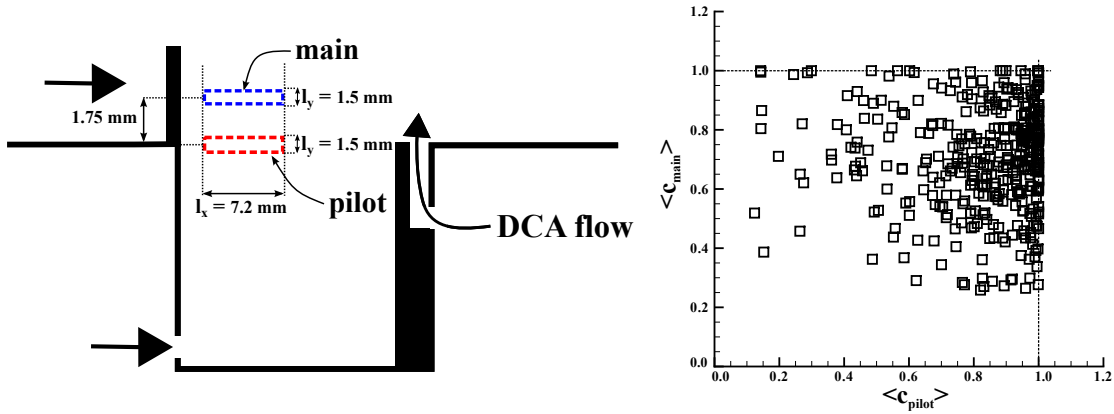


Figure 5.18: Left: zones considered in the pilot and the main flame to estimate the spatial average of the progress variable  $\langle c \rangle$ . Right: scatter plot of the progress variable  $\langle c \rangle$  (spatially averaged) taken in the pilot and in the main region for 2000 instantaneous binarized OH-PLIF data.

These complementary effects are confirmed in Fig. 5.19. It shows four scatter plots of the spatially averaged progress variables with the corresponding velocity components. The two scatter plots at the top of Fig. 5.19 shows that values of  $\langle c_{pilot} \rangle$  were correlated with the mean axial and radial velocities in the pilot region. In addition, values of  $\langle c_{pilot} \rangle$  were segregated towards unity. In contrast, the two scatter plots at the bottom exhibited a broadened behavior with no real correlation. In fact, axial and radial velocities were affected by turbulence, which broadened values of  $\langle c_{main} \rangle$  (axial broadening in Fig. 5.19). The vertical broadening may be explained by the mixing process as well as interactions between the pilot and main regions. We then conclude that the main flame sustainment was primarily due to the presence of a stable pilot flame region, and a weaker pilot flame may not be favorable to the ignition and main flame stabilization. In our case, even if values of  $\langle c_{main} \rangle$  were largely distributed, a successful ignition was encountered, mainly due to the fact that the mean progress variable  $\langle \bar{c}_{main} \rangle$  in the downstream part of the combustor was close to unity (not shown here).



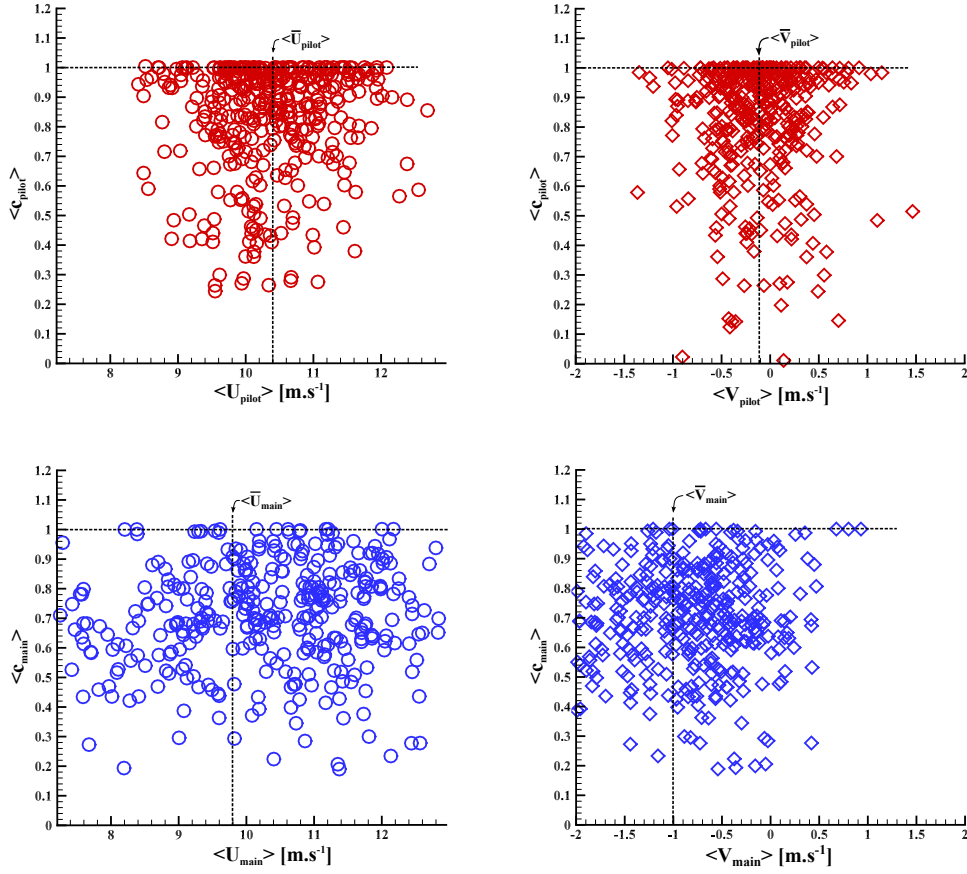


Figure 5.19: Scatter plots of the spatially averaged progress variable with the corresponding averaged velocity components. Top:  $\langle c_{pilot} \rangle$ ; Bottom:  $\langle c_{main} \rangle$

## 5.5 Conclusion

This chapter aimed to determine main parameters controlling the combustor stability and to highlight simple design rules. Even if the results presented in this study are only valid for our burner geometry, detailed insights determined in previous chapters were validated with global investigations. In fact, the cavity thermal expansion was reduced by obtaining a sufficient mainstream velocity combined with a relatively high stratification ratio. Moreover, introduction of dimensionless parameters resulted in a quite simple control law, but was found to be dependant on the cavity power  $P_c$ . Future works should consider validating this trend for several cavity conditions.

Based on this study, we investigated in details a stable point of operation. The main flame was spatially located above the cavity, primarily due to the presence of a pilot flame at the flow

separation between the cavity and the mainstream. However, the three-dimensional behavior of the burner was confirmed, showing different flame structures according to the plane of interest. These results are partially confirmed in comparison to the literature. Even if the geometry and the operating conditions were not identical, parametric studies of Burguburu [27] effectively showed that the establishment of two counter-rotative vortices in the cavity was contributing to the flame stability. In addition, he showed that wake regions in the mainstream (produced by the rods) were primarily improving mass exchanges between the cavity and the mainstream and thus stabilizing the flame. Merlin [160] performed numerical computations with larger mainstream flow rates and effectively observed an improvement in the flame stabilization. However, alternate cavity draining processes were still present (with a reduced preponderance), which was not the case in with the  $I_1$  system. This definitely proves that the injection systems strategy is critically important.

Pollutant emissions are given in Tab. 5.2 for the unstable and stable operating conditions.

	Unstable	Stable
NOx [g/kg <sub>F</sub> ]	48	40
CO [g/kg <sub>F</sub> ]	91	6
UHC [g/kg <sub>F</sub> ]	24	≈0
E <sub>p</sub> [Pa <sup>2</sup> ]	2.4.10 <sup>7</sup>	9.6.10 <sup>3</sup>

Table 5.2: Pollutant emissions for the stable and unstable operating conditions.

The pressure energy was reduced by an order of  $\approx 200$ .  $NO_x$  emissions were relatively constant whereas  $CO$  and  $UHC$  were dramatically reduced between the unstable and stable case. In fact, pulsed combustion led to an alternation between a completely ignited and a completely extinguished combustor, thus affecting  $CO$  and  $UHC$  rather than  $NO_x$  (mainly produced at high temperatures).

## Chapter 6

# Conclusion and recommendations for future works

The general framework of this study was focused on the reduction of pollutant emissions in aero-engines. Indeed, this thesis was part of an European project which was supporting the next 2020 goals set by the ACARE.

The main challenge of this project was to lead a disruptive research on high-potential combustor technologies which could meet the future stringent regulations on pollutant emissions. Thus, the objectives were three-folds: (i) consider innovative combustor technologies which demonstrated important capabilities in previous european programmes (i.e., TECC, TLC, etc.) to (ii) develop faster and smarter design methodologies and make easier their integration in real engines while reducing design times, and (iii) optimize and validate these methodologies with experimental data.

In this study, we experimentally investigated a new combustor technology, named trapped vortex combustor (TVC), which uses lean combustion and cavity-based flame holders. In comparison with avanded swirl-stabilized combustors, the TVC demonstrated good performances in terms of pollutant emissions and operating conditions but very few studies focused on the mechanisms of flame stabilization. The objective of this thesis was twofold:

- Investigate the different mechanisms of flame stabilization involved in this innovative ge-

ometry, and crucial parameters which could be used for early-design rules.

- Produce detailed database to validate numerical computations and design methodologies.

We took advantage of a TVC, which was designed and commissioned at the laboratory. Because the combustor exhibited some unstable operating conditions, we decided to focus our investigation on these drastic conditions in order to be able to prevent them during development programmes. In addition, this choice was also driven by the fact that only two studies mentioned the existence of such unstable conditions.

As a preliminary study, a global and qualitative investigation of one unstable operating condition was performed to assess the behavior of periodic instabilities. Results were phased-averaged with regards to pressure records. Analysis of one cycle of instability (with CH\* chemiluminescence, and OH-PLIF) showed that heat release oscillations, and spatial location of burned and unburned gases were tremendous in whole combustor. In turn, mass transfers between the cavity and the main channel inevitably deteriorated possibilities to stabilize a flame above the cavity. In addition, heat release and pressure oscillations were almost in-phase and confirmed that the burner was exhibiting thermo-acoustic oscillations. The spatial distribution of the Rayleigh index also revealed that injection systems were controlling the development of these instabilities. Based on these preliminary results, we argued that the natural flow unsteadiness arising in this geometry (i.e., flow passing past a cavity) and the presence of a flame were the two mechanisms which led to the presence of combustion instabilities. Thus, we decided to treat separately these two effects in order to highlight the driving and coupling processes and eventually propose some control laws.

Investigation of the inert TVC aerodynamics was achieved with high-speed PIV, and aimed to determine the major flow instabilities, primarily caused by the impingement of the shear layer on the downstream cavity corner. In addition, effects of direct mass injection in the cavity was addressed by studying local mass transfers between the cavity and the mainstream. Although results found were highly configuration specific (e.g., cavity aspect ratio was kept constant), the global analysis of the flow topology remarkably revealed that no self-sustained cavity

oscillations were found in this geometry. In contrast, addition of mass in the cavity modified the cavity flow structure, creating several vortices and stagnation regions. It also affected local turbulence, especially next to the cavity trailing edge. We finally highlighted the existence of a flow instability, which disturbed the interfacial shear layer. The latter was mainly due to the cavity jet injections and was found to be controlled by the mainstream flow.

A detailed analysis showed that the shear layer was featuring a self-similar behavior far away from the cavity walls, even in the case where mass was directly injected in the cavity. A budget momentum confirmed that the region next to the cavity trailing edge was quite active, by favorizing radial exchanges of momentum between the cavity and the mainstream.

We concluded that classical cavity instabilities were not observed in our TVC and that addition of injection systems in the cavity was enhancing turbulence, mass transfers with the main channel but also risks of coherent structures interacting with the shear region.

Addition of heat release and the occurrence of self-excited pressure oscillations were investigated by implementing dual PIV and OH-PLIF measurements to examine the flow-flame-acoustics interactions. To our knowledge, it was the first time that these techniques were implemented in this type of geometry and therefore was technically challenging. Several image-processing routines were developed to automatically post-process the numerous images, extract flame contours (based on OH gradients), binarize images, and quantify energy contributions of deterministic and random velocity fluctuations.

Our instantaneous analysis of a combustion instability cycle demonstrated and confirmed a strong coupling between acoustic and heat release fluctuations. Similarly to the inert studies, mechanisms driving combustion instabilities were found to differ from classical flame-vortex interactions encountered in backward-facing steps or dump combustors. In fact, a strong flow instability, referred to as *jet flapping*, and located next to one injection system in the cavity, was found to be in-phase with the pressure oscillations and to disturb the whole flow topology. Spatial analysis revealed that this coherent motion was associated to a large-scale event and a POD analysis confirmed that this *jet flapping* was clearly the primary mechanism involved in combustion instabilities.

Consequence of this coherent mechanism was important: large and inefficient mass transfers

between the cavity and the mainstream. In particular, composition of the exchanged gases alternated between completely burned and unburned gases, which finally led to a pulsed combustion regime and weakened the flame stabilization.

We then concluded that aerodynamics between the cavity and the main channel could be a critical parameter to spatially locate the mixing region produce a stable recirculation zone for an efficient flame stabilization. We therefore argued that modifications of the injection systems in the cavity could produce better performances.

Based on these detailed measurements and insights, we therefore performed a global analysis of the TVC in order to validate (or not) if we could obtain a stable range of operating conditions and if we could highlight some design rules to predict the burner stability. For this purpose, simple diagnostics were used, such as pressure records and gas analyzer. Results demonstrated that stable modes were highly configuration specific: the original injection strategy was found to be unstable on a large range of operating conditions whereas modification of the injection strategy in the cavity gave better performances in terms of flame stability and pollutant emissions. In addition, the mainstream momentum was definitively found to be the primary stabilizing parameter: because the chemical energy injected in the cavity was paramount for an efficient flame stabilization, a sufficient confinement was also needed to counter the thermal gas expansion. Remarkably, an extended range of stable operating conditions was achieved with a low mainstream power. Note that stable operating conditions exhibited low pollutant emissions, especially regarding CO and UHC.

Among others, we highlighted a simple design rule, based on a specific cavity power: a linear relation between the cavity and mainstream velocities, thereby making possible to predict the combustor stability, independently of the main channel combustor power.

This work pointed out the complexity to study such a combustor and even to draw general recommendations because of the presence of several physical processes, which were certainly configuration specific. Among others, staged combustion (RQL type), stratified configuration, flow passing above a cavity, complex injection strategy. Individual treatment of each process may

be considered as a first approach but it is clear that new physical mechanisms will arise when combining these simple processes. In view of the results of this thesis, several recommendations are given hereafter:

- Perform an accurate characterization of the acoustic modes and their spatial structures (i.e., longitudinal, transverse, azimuthal, etc.) by using a Helmholtz solver. Insights would inform about the contribution of acoustic modes in combustion instabilities, and separate combustor instabilities from the system contribution.
- Continue the treatment initiated in Chap. 5 to obtain more design rules. Investigation of several cavity powers should confirm the design trend and also possible limitations.
- Because our measurements were performed during the limit-cycle period, investigate the linear growth period occurring when the combustor switch from one stable to one unstable mode (high-speed measurements were performed but not treated yet...).
- Access to the flame structure remains of great importance. Because the geometry involved large recirculation zones, choice of an alternative tracer (i.e.,  $CH_2CO$ ) should be more accurate than OH measurements.
- Understand in details the internal mechanisms of mixing in the cavity and their interactions with the mainstream. Indeed, experimental access to the mixture fraction field and local equivalence ratio fields is unavoidably in order to confirm our data and optimize choices of injection system strategy.
- Investigation of flows passing past cavities have always considered unconfined geometries (i.e., large mainstream height). It should be interesting to see how the confinement affects the mixing and the occurrence of cavity oscillations.
- Our TVC had a surface to volume ratio of 220 ! Thus, flame-walls interactions, quenching, and resulting heat transfers must play a crucial role on the flame stability and pollutant performances.
- Optimization of the injection systems as well as the whole geometry. This task is quite difficult (and open) in view of the large amounts of parameters to vary and the choice of an universal criterion for the optimization.

## Appendices



## Appendix A

# Laser-Induced Fluorescence Spectroscopy

### A.1 Quantum Mechanics

Internal energy  $E_{int}$  of a molecule can be divided into vibrational  $E_{vib}$ , rotational  $E_{rot}$ , and electronic  $E_{elec}$  energies:

$$E_{int} = E_{vib} + E_{rot} + E_{elec}. \quad (\text{A.1})$$

We assume that energy levels associated to a molecule are quantized: each quantum state has one quantum number, energy, and angular momentum. As a result, transitions in energy are also discrete and correspond to the energy absorbed or emitted by photons. This fact can be expressed with the Planck's law as

$$\Delta E = E_{upper} - E_{lower} = h\nu, \quad (\text{A.2})$$

where  $\Delta E$  is the energy of one photon associated to the  $E_{lower} \leftrightarrow E_{upper}$  transition,  $h$  is the Planck's constant, and  $\nu$  is the frequency of the photon. We also assume that quantum mechanics defines selection rules, which result in a range of allowed and forbidden transitions. Figure ??

depicts a schematic illustration of the energy quantization. Additional details can be found in [84, 95, 96, 99].

## A.2 Transfer processes

An illustration of a simplified treatment, depicted in Fig. A.1, displays the different transfer processes between the lower energy state  $E_1$  and the upper energy state  $E_2$ .

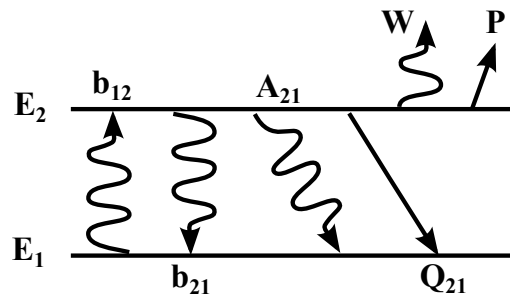


Figure A.1: Schematic illustration of a two-level energy diagram. Several transfer processes are presented.

$b_{12}$  is the absorption rate (e.g. laser source),  $b_{21}$  is the stimulated emission rate which directly undergoes to the lower state,  $A_{21}$  is the rate for spontaneous emission and which accounts for the fluorescence,  $Q_{21}$  is the collisional quenching (de-excitation based on inelastic collisions with other molecules),  $W$  is the photo-ionization, and  $P$  is the predissociation. Transfer processes, depicted in Fig. A.1, are the subject of several models in order to relate LIF signals to several properties (concentration [86], temperature, and pressure [134, 157]) of the absorbing species.

## A.3 Laser excitation spectroscopy

Laser excitation spectroscopy is a means of detecting the absorption process of a molecule (i.e., resonant wavelengths fluorescence) and to choose a strategy for the excitation. The experimental setup is shown in Fig. A.2.

The laser is tuned to a specific wavelength  $\lambda_{exc.}$  and the output laser beam goes through a controlled medium (i.e., laminar flow seeded with enough molecules of interest in order to

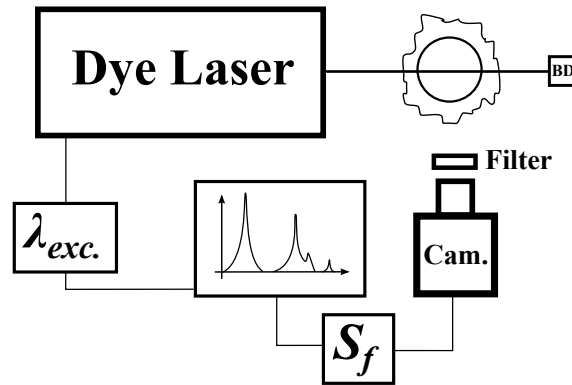


Figure A.2: Typical experimental arrangement for laser excitation spectroscopy.  $\lambda_{exc.}$  is the tunable wavelength of the dye laser,  $S_f$  is the fluorescence signal collected on the intensified camera (cam.), and BD is a beam dump.

obtain a homogeneous concentration). Thus, a portion of the fluorescence  $S_f$  is collected on the intensified camera. A filter is used to reduce the scattered laser light. This procedure is repeated for several laser wavelength  $\lambda_{exc.}$  and it is then possible to determine the experimental laser excitation spectrum of the molecule of interest. When the laser is off-resonance with the molecule, no fluorescence is produced, whereas intensity peaks denote resonant wavelengths.

Another feature of this experiment consists in comparing the experimental laser excitation spectrum to the theoretical one in order to take into account the potential wavelength shift which may occur in the dye laser.

The resolution is critically important in laser excitation spectroscopy. In fact, each transition theoretically refers to a line in a spectrum, with a given wavelength. However, these lines in real spectra are broadened, then having a spectral width. Several phenomena can contribute to line broadening effects:

- **Natural broadening.** It is the consequence of the Heisenberg uncertainty principle, which relates uncertainty of the energy levels to their respective lifetimes. Thus, the spectral uncertainty  $\Delta\lambda_N$  (subscript  $N$  indicates Natural) is

$$\Delta\lambda_N = 2\pi c\tau, \quad (\text{A.3})$$

where  $c$  is the speed of light and  $\tau$  is the lifetime to return to the ground state. In the absence of non-radiative routes (i.e., predissociation or quenching), the lifetime is primarily due to spontaneous emission.

- **Doppler Broadening.** It is the consequence of thermal movements of molecules in the medium. In fact, if a molecule has a velocity component in the same direction of the light source, there will be a shift in the line wavelength (similar to the Doppler effect). Assuming that the medium is at thermal equilibrium, the velocity distribution of all molecules can be described with a Maxwell-Boltzmann distribution and each velocity class is associated to a Doppler shift, then leading to a broadening  $\Delta\lambda_D$  (subscript D indicates Doppler) given by

$$\Delta\lambda_D = \lambda_0 \left( \frac{8kT\ln 2}{mc^2} \right), \quad (\text{A.4})$$

where  $\lambda_0$  is the wavelength of transition,  $k$  is the Boltzmann constant,  $T$  is the temperature of the medium, and  $m$  is the mass of the molecule. It is interesting to see that Doppler broadening is smaller for heavier molecules and is increased in the visible and ultraviolet regions.

- **Collisional (Pressure) broadening.** It is the consequence of increasing pressure, which in turn increases the collisions between molecules. Consequently, the lifetime of an energy level can be considerably reduced (via the Heisenberg uncertainty principle) and leads to a broadening  $\Delta\lambda_C$  given by

$$\Delta\lambda_C = P \sum_i \chi_i 2\gamma_i, \quad (\text{A.5})$$

where  $P$  is the pressure of the medium,  $\chi_i$  is the mole fraction of each perturber specie  $i$ , and  $\gamma_i$  is the collisional coefficient between the specie of interest and the specie  $i$ . Note that the collisional coefficient  $\gamma_i$  is dependant of the temperature of the medium.

Note that other mechanisms of broadening can be encountered in specific conditions. For instance, the Stark broadening is preponderant in plasmas (see [120]).

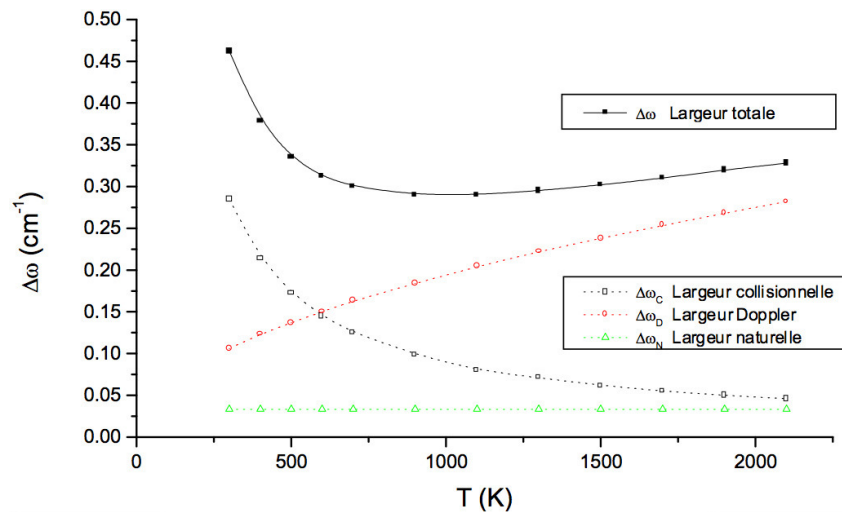


Figure A.3: Influence of the temperature on the Doppler, collisional, and natural broadening widths. Results given for the OH molecule ( $Q_1(5)$  line). Reproduced from [22].

Moreover, the instrumental resolution is a factor limiting the spectral resolution. In fact, the spectral width of the laser  $\Delta\lambda_L$  and its overlap with one transition can also affect the measured lineshape. In order to compare the experimental laser excitation spectrum to the theory, we used the LIFBASE software [154]

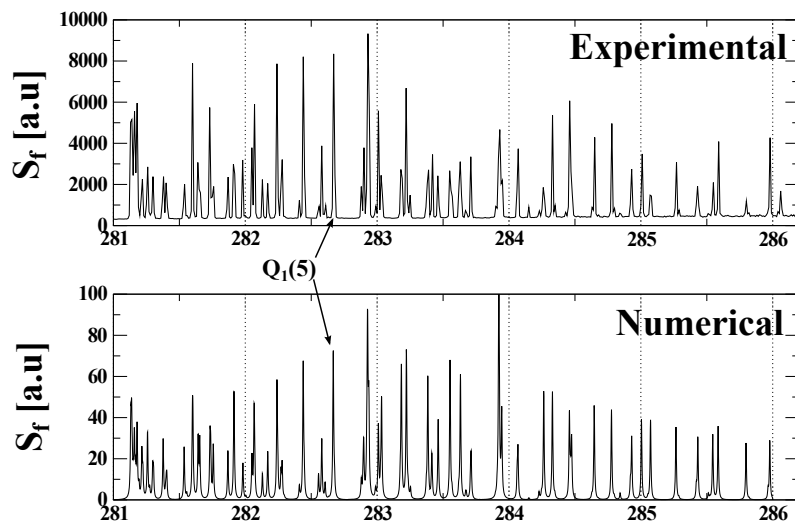


Figure A.4: Experimental and theoretical laser excitation spectrum of the OH molecule in a laminar burner.  $P=1$  bar,  $T=2000$  K. The fluorescence signal was obtained by averaging 100 images and by taking the mean value of a defined region of interest ( $40 \times 40 \text{ pix}^2$ ). The wavelength interval between two measurements was 0.01 nm.

Because we were interested in recording images with a large signal-to-noise ratio, a broadband collection strategy was adopted for the fluorescence signal (see Chap. 2). A particular attention was paid to not overlap the excitation wavelength  $\lambda_{exc}$  with the collected band. Figure A.5 depicts a numerical emission spectrum of the OH radical, which was excited at the specific wavelength  $\lambda_{exc}$  [80]. Note that the collection band was spectrally separated from the excitation wavelength.

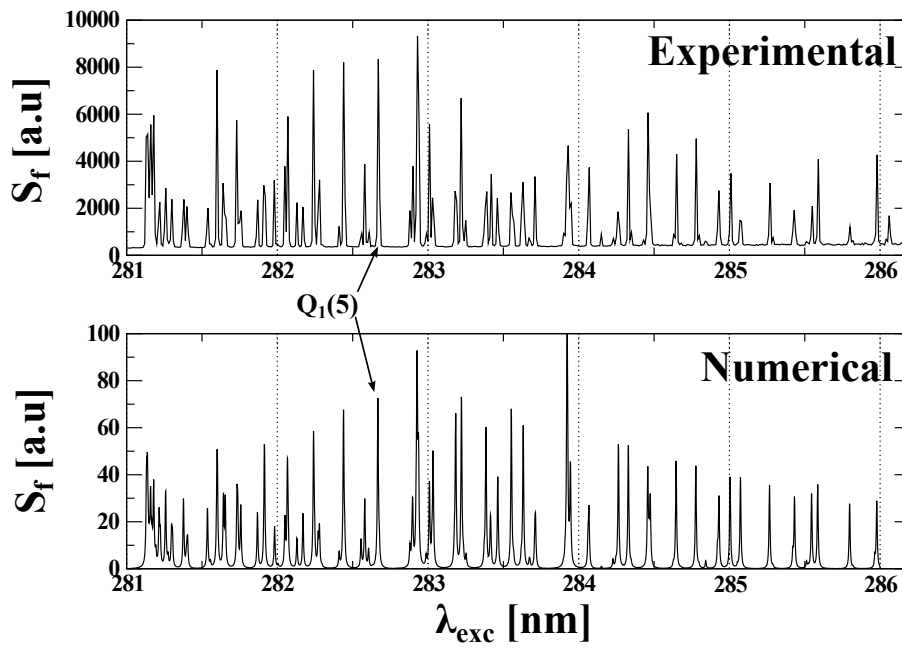


Figure A.5: Theoretical emission spectrum of the OH molecule.  $P = 1$  bar,  $T = 2000$ K, and  $\lambda_{exc} = 282.75$  nm [80].

## Appendix B

# Estimation of the local flame curvature

In order to estimate curvature pdfs (see Chap.2), we developed an automatic and robust processing tool (using Matlab software) to process the large amount of OH images without any parameter adaptation.

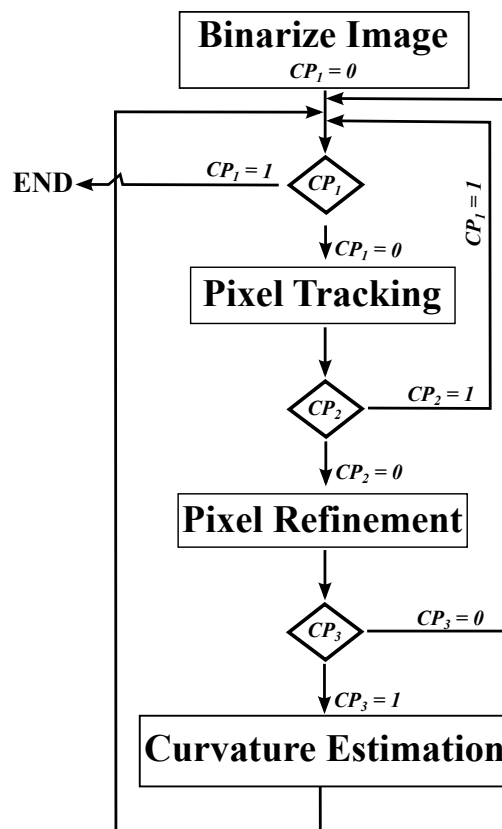


Figure B.1: Schematic illustration of the curvature estimation procedure.

A schematic illustration of the algorithm is presented in Fig. B.1 and can be divided into four steps:

- **Flame front detection.** As mentioned in Sec. 2.2.3, a non-linear diffusive filter (NLDF) [229] was applied to the corrected raw images OH images. The NLDF filter was defined as

$$\partial_t I = \nabla \cdot (D \nabla I), \quad (\text{B.1})$$

$I$  is the intensity of a pixel, and  $D$  is the local diffusivity, defined in accordance with [173] as

$$D(\|\nabla I\|) = \frac{1}{\sqrt{1 + \frac{\|\nabla I\|^2}{\lambda^2}}}. \quad (\text{B.2})$$

$\|\nabla I\|$  is the local intensity gradient (updated at each time iteration), and  $\lambda$  is a weight coefficient. This filter has the advantage to be non-linear; that is, diffusion was not identical according to the local intensity gradient  $\|\nabla I\|$ . In our case, Eq. B.2 smoothed high frequency noise while conserving large scale information with a low attenuation (Fig. B.2).

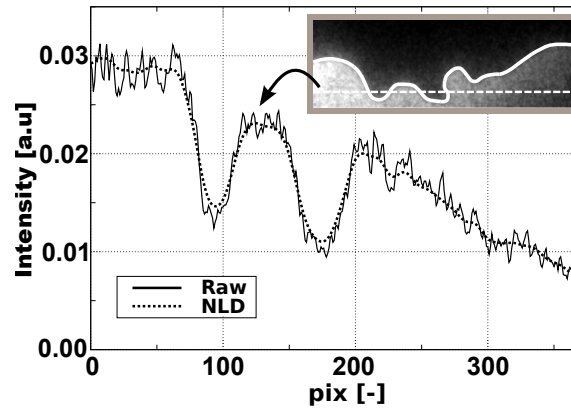


Figure B.2: Extracted intensity profile of a raw and a filtered OH-PLIF image.

Note that choosing an anisotropic conductivity (i.e., the flux  $D \nabla I$  is not anymore parallel to the local intensity gradient  $\nabla I$ ) did not enhance the quality of the detection.

Thus, the output of this subroutine consisted in interface pixels; that is, a pixel with a value of unity corresponded to the location of the interface between burned and unburned gases whereas other pixels had a null value. An example is given in Fig. B.3. Note that the controlling parameter 1 ( $CP_1$ ) was initialized to 0, thus allowing to access to the next



subroutine.

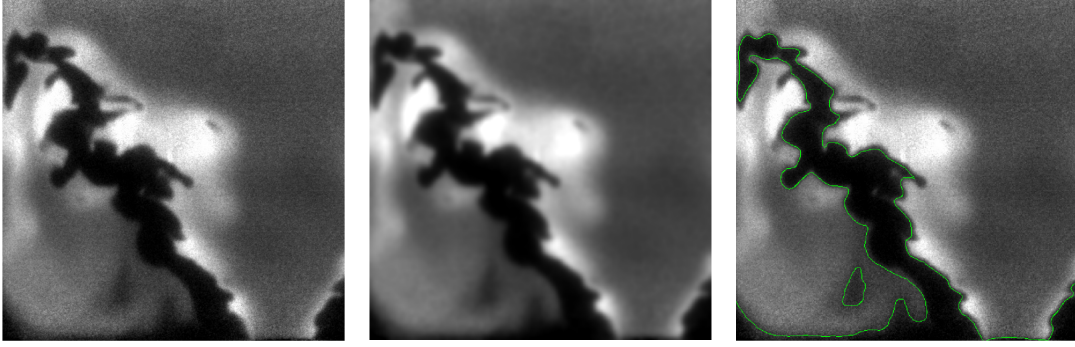


Figure B.3: Procedure used to extract the flame front from a raw OH PLIF image. Tests were performed on a swirl combustor. left: corrected raw image; middle: image after the NLD filter; right: flame front (green line) superimposed on the corrected raw image.

- **Pixel tracking.** This subroutine was used to detect and save interface pixels of one single flame front and their corresponding coordinates. A probe was displaced along the matrix of the image, starting from the top left corner and the record started when on interface pixel was found. At this point, a curvilinear variable  $s$  was initialized. A 8x8 directional matrix algorithm was then used in order to record the following pixel interface until the end of the flame front.

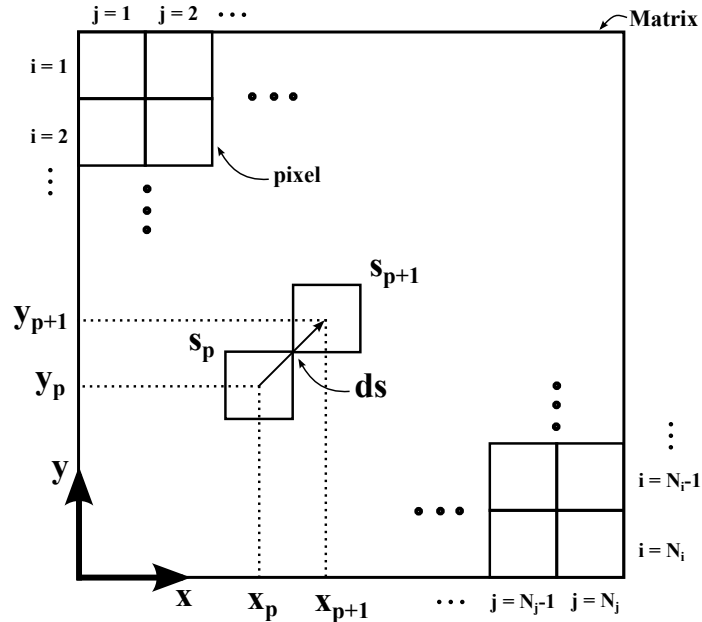


Figure B.4: Schematic illustration of pixel tracking procedure.

Because the pixels were indexed in a matrix (line and row indices,  $i$  and  $j$ , respectively), a particular care was paid to attribute spatial coordinates  $x_p$  and  $y_p$  (in mm) as

$$\begin{aligned} x_p &= (j-1)l_{pix} + 0.5l_{pix} \\ y_p &= (N_i - i + 1)l_{pix} + 0.5l_{pix}, \end{aligned} \tag{B.3}$$

where  $l_{pix}$  is the length of one pixel in mm, and  $N_i$  is the number of lines of the matrix. These coordinates were recorded with respect to the curvilinear variable  $s$ , which was also incrementally increased by the distance between two pixel centers  $\delta s^1$ .

At the end of the procedure, the two discrete functions  $x(s)$  and  $y(s)$  outputs were sent to the next subroutine. In the case that no more fronts were present in the image, the functions  $x(s)$  and  $y(s)$  were empty. Thus, the controlling parameter 1 and 2 were set to 1 ( $CP_2 = CP_1 = 1$ ), involving the program to stop.

- **Pixel refinement.** The two discrete functions  $x(s)$  and  $y(s)$  were artificially resampled in order to reduce stiff variations from one pixel to another. The barycenter of two adjacent pixels was calculated to insert an additional sample. This procedure allowed to resample as many time the functions but was not found to be critically important in the final results. The controlling parameter 3 consisted in checking that the number of points were sufficiently high to estimate the local curvature. In our case, a minimum flame front length with ten times more than the minimum size (i.e., 15 pixels, see hereafter) was set in order to suppress small contributions. The controlling parameter 3 was set 0 if this criterion was not meet, and the flame front was ignored.
- **Curvature estimation.** This last subroutine enabled to calculate the local flame curvature. Polynomials were locally fitted to the  $x(s)$  and  $y(s)$  functions<sup>2</sup> with defined neighboring pixels (Fig. B.5 (a)). Then, the mathematical curvature was calculated based on the fitted functions as

$$H_{math} = \frac{|x'y'' - y'x''|}{(x'^2 + y'^2)^{3/2}}, \tag{B.4}$$

where  $x$  and  $y$  are the fitted functions,  $x'$  and  $y'$  are the first order derivatives, and  $x''$  and  $y''$  are the second order derivatives. Finally the physical curvature  $H$ , being positive if the

---

<sup>1</sup>The distance between two pixel centers was  $l_{pix}$  in the case the two pixels were vertically or horizontally adjacent, and  $\sqrt{l_{pix}}$  for the remaining cases.

<sup>2</sup>Note that the indexation with  $s$  was chosen in order to prevent from non mono-valued functions (i.e.,  $y \neq f(x)$ ) and subsequently issues in fitting.

flame front is convex towards the reactants, was automatically determined by multiplying the mathematical curvature  $H_{math}$  with the sign of the dot product between the local intensity gradient vector  $\vec{G} = \nabla I$  and the radius of curvature  $\vec{R}$  (Fig. B.5 (b)).

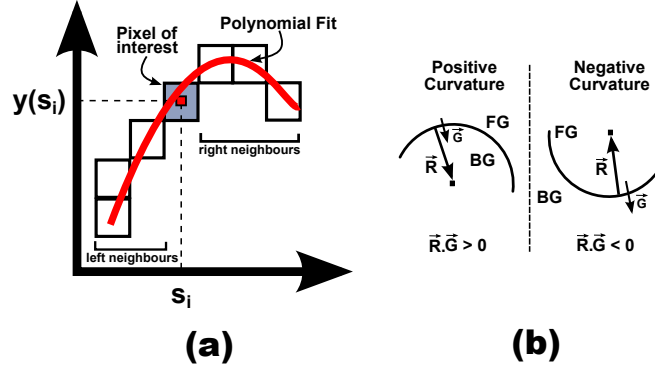


Figure B.5: Schematic illustration of the curvature estimation procedure. (a) Example of fitting process on the discrete function  $y(s)$ . (b) Automatic criterion used to determine the physical curvature  $H$ , where BG are burned gases, FG are fresh gases,  $\vec{G}$  is the local intensity gradient vector, and  $\vec{R}$  is the local radius of curvature.

It is important to note that the flame curvature was estimated, based on a fit process. The order of the fit, and the number of neighbours were found to be critically important. Thus, a sensitivity analysis was performed on synthetic images with known curvatures (i.e, circles with several radii<sup>3</sup>).

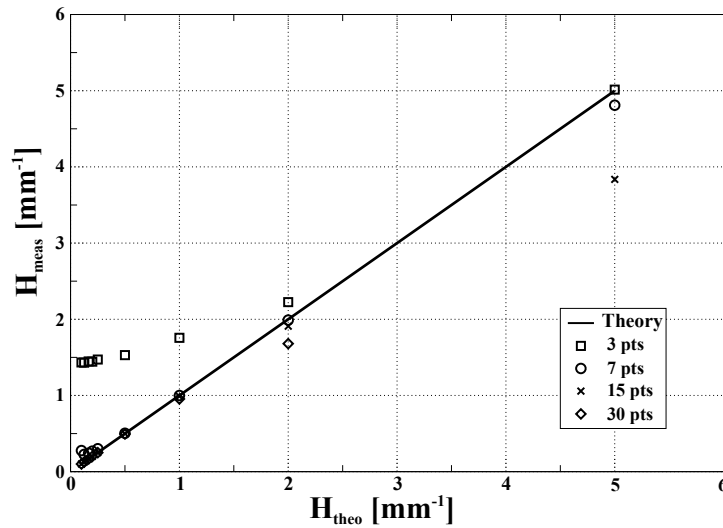


Figure B.6: Sensitivity analysis based on the number of pixels used for the fit.

Figure B.6 presents the estimation of different curvature circles, using different neighbouring pixels (with 3rd order polynomial fits and no resampling). Note that the large deviation for small

<sup>3</sup>The curvature of a circle with a radius  $R$  is  $1/R$ .

---

curvatures (i.e., large radii) with few neighbouring pixels demonstrated the preponderance of pixel-to-pixel digitization noise (step functions). In contrast, deviations for large curvatures (i.e., small radii), mainly for high number of neighbouring pixels, highlighted the effect of smoothing which underestimated small scale information.

# Bibliography

- [1] Independent experts  $NO_x$  review and the establishment of medium and long term technology goals for  $NO_x$ . ICAO doc 9887. Technical report, International civil aviation organization, 2006.
- [2] K. AGARWAL, S. KRISHNA, and R. RAVIKRISHNA. Mixing enhancement in a compact trapped vortex combustor. *Combustion Science and Technology*, 185(3):363–378, 2013.
- [3] K. AHUJA and J. MENDOZA. Effects of cavity dimensions, boundary layer and temperature on cavity noise with emphasis on benchmark data to validate computational aeroacoustic codes. Technical report, NASA contractor report 4653, 1995.
- [4] M. ALDEN, H. EDNER, G. HOLMSTEDT, S. SVANBERG, and T. HOGBERG. Single-pulse laser-induced OH fluorescence in an atmospheric flame, spatially resolved with a diode array detector. *Appl. Opt.*, 21:1236–1240, 1982.
- [5] H. ALTAY, R. SPETH, D. HUDGINS, and A.F.GHONIEM. Flame-vortex interaction driven combustion dynamics in a backward-facing step combustor. *Combustion and Flame*, 156:1111–1125, 2009.
- [6] K. BALASUBRAMANIAN and R. SUJITH. Thermoacoustic instability in a rijke tube: Non-normality and nonlinearity. *Physics of Fluids*, 20(044103), 2008.
- [7] S. BARBOSA, P. SCOUFLAIRE, and S. DUCRUIX. Time resolved flowfield, flame structure and acoustics characterization of a staged multi-injection burner. *Proceedings of the Combustion Institute*, 32(2):2965–2972, 2009.
- [8] A. BEN-YAKAR and R. HANSON. Cavity flame-holders for ignition and flame stabilization in scramjets: an overview. *Journal of Propulsion and Power*, 17(4):869–877, 2001.

- 
- [9] D. BENNEY. A non-linear theory for oscillations in a parallel flow. *J. Fluid Mech.*, 10(02):209–236, 1961.
- [10] L. BERNAL and A. ROSHKO. Streamwise vortex structures in plane mixing layers. *J. Fluid Mech.*, 170(1):499–525, 1986.
- [11] A. BILANIN and E. COVERT. Estimation of possible excitation frequencies for shallow rectangular cavities. *AIAA Journal*, 11:347–351, 1973.
- [12] R. BLEVINS. *Flow-induced vibration*, volume 2nd ed. FL: Krieger Publishing Company, 2001.
- [13] F. BLOMSHIELD. Historical perspective of combustion instability in motors: case studies. In *AIAA*, pages 2001–3875, 2001.
- [14] D. BLUNCK, D. SHOUSE, C. NEUROTH, R. BATTELLE, A. LYNCH, B. SEKAR, J. ZELINA, T. ERDMANN, D. BURRUS, R. HOWARD, A. BRIONES, D. RICHARDSON, and A. CASWELL. Experimental and computational studies of an Ultra-Compact Combustor. In *ASME turbo Expo 2013*, pages GT2013–94372, San Antonio, USA, June 3-7 2013.
- [15] D. BLUNCK, D. SHOUSE, C. NEUROTH, A. LYNCH, T. ERDMANN, D. BURRUS, J. ZELINA, D. RICHARDSON, and A. CASWELL. Experimental studies of cavity and core flow interactions with application to Ultra-Compact Combustors. *Journal of Engineering for Gas Turbines and Power*, 136(9):091505, 2014.
- [16] B. BOHM, D. GEYER, M. GREGOR, C. HEEGER, A. NAUERT, C. SCHNEIDER, and A. DREIZLER. Advanced Laser Diagnostics for Understanding Turbulent Combustion and Model Validation. In *Flow and Combustion in Advanced Gas Turbine Combustors*, volume 1581, chapter 4, pages 93–160. Springer, 2013.
- [17] B. BOHM, C. HEEGER, I. BOXX, W. MEIER, and A. DREIZLER. Time-resolved conditional flow field statistics in extinguishing turbulent opposed jet flames using simultaneous highspeed PIV/OH-PLIF. *Proceedings of the Combustion Institute*, 32(2):1647–1654, 2009.
- [18] B. BOHM, C. HEEGER, R. GORDON, and A. DREIZLER. New Perspectives on turbulent Combustion: Multi-Parameter High-Speed Planar Laser Diagnostics. *Flow Turbulence*

- Combustion*, 86:313–341, 2011.
- [19] J. BONNET, J. DELVILLE, M. GLAUSER, R. ANTONIA, D. BISSET, D. COLE, H. FIEDLER, J. GAREM, D. HILDBERG, J. JEONG, N. KEVLAHAN, L. UKEILEY, and E. VINCENDEAU. Collaborative testing of eddy structure identification methods in free turbulent shear flows. *Experiments in Fluids*, 25:197–225, 1998.
- [20] I. BOXX, C. CARTER, M. STOHR, and W. MEIER. Study of the mechanisms for flame stabilization in gas turbine model combustors using khz laser diagnostics. *Experiments in Fluids*, 54(5):1–17, 2013.
- [21] I. BOXX, M. STOHR, C. CARTER, and W. MEIER. Temporally resolved planar measurements of transient phenomena in a partially pre-mixed swirl flame in a gas turbine model combustor. *Combustion and Flame*, 157(8):1510–1525, 2010.
- [22] A. BRESSON. *Techniques d’imagerie quantitatives : fluorescence induite par laser appliquée aux écoulements et aux combustions*. PhD thesis, University of Rouen, 2000.
- [23] F. BROWAND and P. WEIDMAN. Large scales in the developing mixing layer. *J. Fluid Mech.*, 76:127–144, 1976.
- [24] G. BROWN and A. ROSHKO. On the density effects and large structure in turbulent mixing layers. *J. Fluid Mech.*, 64(04):775–816, 1974.
- [25] J. BRUGGEMAN, A. HIRSHCHBERG, M. V. DONGEN, A. P. J. WIJNANDS, and J. GORTER. Self-sustained aero-acoustic pulsations in gas transport systems: experimental study of the influence of closed side branches. *Journal of sound and vibration*, 150:371–393, 1991.
- [26] J. BURGUBURU. *Etude expérimentale de la stabilité d’une flamme dans une chambre de combustion aéronautique par recirculation de gaz brûlés et par ajout d’hydrogène*. PhD thesis, INSA Rouen, 2012.
- [27] J. BURGUBURU, G. CABOT, B. RENOU, A. BOUKHALFA, and M. CAZALENS. Flame stabilization by hot products gases recirculation in a Trapped Vortex Combustor. In *Proceedings of the ASME*, pages GT2012–68451, Copenhagen, Denmark, June 11–15 2012.

- 
- [28] D. BURRUS, A. JOHNSON, W. ROQUEMORE, and D. SHOUSE. Performance assessment of a prototype Trapped Vortex Combustor concept for a gas turbine applications. In *ASME Turbo Expo 2001*, pages GT2001-0087, Atlanta, USA, July 16-19 2001.
- [29] S. CANDEL. Combustion dynamics and control : Progress and challenges. *Proceedings of the Combustion Institute*, 29(1):1-28, 2002.
- [30] J. CANNY. A computational approach to edge detection. In *IEEE Trans Pattern anal Mach Intell*, volume 8, pages 679-698, 1986.
- [31] L. CASALINO and D. PASTRONE. Optimization of an advanced open rotor engine for civil transport. In *50th AIAA/ASME/SAE/ASEE Joint Propulsion Conference*, pages 1-12, 2014.
- [32] L. CATTAFESTA, S. GARG, M. CHOUDHARI, and F. LI. Active control of flow-induced cavity resonance. In *28th AIAA Fluid Dynamics Conference*, volume AIAA-1997-1804, Snowmass Village, CO, 1997.
- [33] L. N. CATTAFESTA, D. R. WILLIAMS, C. ROWLEY, and F. ALVI. Review of active control of flow-induced cavity resonance. In *AIAA*, 2003.
- [34] L. CHATELLIER. *Modélisation et contrôle actif des instabilités aéroacoustiques en cavité sous écoulement affleurant*. PhD thesis, Poitiers University, 2001.
- [35] T. CHEW, R. BRITTER, and K. BRAY. Laser tomography of turbulent premixed bunsen flames. *Combustion and Flame*, 75(2):165-174, 1989.
- [36] B. CHU. On the energy transfer to small disturbances in fluid flow (part I). *Acta Mechanica*, pages 215-234, 1965.
- [37] I. Civil Aviation Organization. <http://www.icao.int/>.
- [38] T. CLARK. Studies of OH, CO, CH and  $C_2$  adiation from laminar and turbulent propane-air and ethylene air flames. Technical report, NACA Technical Note, 1958.
- [39] P. CLAVIN. Dynamic behavior of premixed flame fronts in laminar and turbulent flows. *Prog. Energy Combust. Sci.*, 11:1-59, 1985.



- 
- [40] C. COATS. Coherent structures in combustion. *Combustion and Flame*, 22(5):427–509, 1996.
- [41] J. COHEN, B. WAKE, and D. CHOIR. Investigations of instabilities in a lean, premixed step combustor. *Journal of Propulsion and Power*, 19:81–88, 2003.
- [42] L. CORDIER and M. BERGMANN. Proper Orthogonal Decomposition: an overview. In *Lecture series 2002-04 on post-processing of experimental and numerical data*. Von Karman Institute for Fluid dynamics, 2002.
- [43] M. CORDIER. *Allumage et propagation de flammes dans les écoulements fortement swirlés: études expérimentales et numériques*. PhD thesis, INSA Rouen, 2013.
- [44] L. CROCCO and S. CHENG. *Theory of Combustion Instability in Liquid Propellant Rocket Motors*. Butterworths Scientific Publications, London, 1956.
- [45] F. CULICK. Non-linear growth and limiting amplitude of acoustic oscillations in combustion chambers. *Combust. Sci. Technol.*, 3(1):1–16, 1971.
- [46] F. CULLICK. Combustion instabilities in liquid-fueled propulsion systems-an overview. In *AGARD*, 1977.
- [47] C. DASCH. One Dimensional Tomography: a Comparison of Abel, Onion-Peeling, and Filtered backprojection Methods. *Appl. Optics*, 31(8):1146–1152, 1992.
- [48] P. DAVIES and A. YULE. Coherent structures in turbulence. *J. Fluid Mech.*, 69:513–537, 1975.
- [49] J. DELVILLE, L. UKEILEY, L. CORDIER, J. BONNET, and M. GLAUSER. Examination of large-scale structures in a turbulent plane mixing layer. part 1. Proper Orthogonal Decomposition. *Journal of Fluid Mechanics*, 391:91–122, 1999.
- [50] I. Design Methodologies for Low PollutAnt Combustors for Aero-Engines. <http://www.impact-ae.eu/>.
- [51] P. DIMOTAKIS and G. L. BROWN. The mixing layer at high Reynolds number: large-structure dynamics and entrainment. *J. Fluid Mech.*, 78(3):535–560, 1976.

- 
- [52] A. DOWLING. The calculation of thermoacoustic oscillations. *Journal of sound and vibration*, 180(4):557–581, 1995.
- [53] S. DUCRUIX. *Combustion instabilities in gas turbine engines: operational experience, fundamental mechaniss, and modeling*, chapter 9, pages 179–212. American Institute of Aeronautics and Astronautics, inc, 2005.
- [54] S. DUCRUIX, T. SCHULLER, D. DUROX, and S. CANDEL. Combustion dynamics and instabilities: elementary coupling and driving mechanisms. *Journal of Propulsion and Power*, 19(5):722–734, 2003.
- [55] W. DUHAM. Flow-induced cavity resonance in viscous compressible and incompressible fluids. In *4th symposium on naval Hydrodynamics. Ship propulsion and hydrodynamics*, volume ACR-73, page 939, Washington D.C, 1962.
- [56] D. DUROX, F. BAILLOT, G. SEARBY, and L. BOYER. On the shape of flames under strong acoustic forcing: a mean flow controlled by an oscillating flow. *J. Fluid Mech.*, 350:295–310, 1997.
- [57] L. EAST. Aerodynamically induced resonance in rectangular cavities. *Journal of sound and vibration*, 3(3):277–287, 1966.
- [58] A. ECKBRETH. *Laser diagnostics for combustion temperatures and species*. Godon and Breach Publishers, Amsterdam, 2nd edition edition, 1996.
- [59] A. ELLIS, M. FEHER, and T. WRIGHT. *Electronic and Photoelectron Spectroscopy: Fundamentals and Case Studies*. Cambridge University Press, 2005.
- [60] I. Energy Agency. *Energy Technology Perspectives*. OECD Publishing, 2008.
- [61] I. Energy Agency. *World Energy Outlook*. OECD Publishing, 2008.
- [62] I. Energy Agency. *Transport Energy and CO<sub>2</sub>: Moving towards Sustainability*. OECD, 2009.
- [63] A. et al. Trapped Vortex Combustion Chamber. Patent US 8 322 142 B2, December 2012.
- [64] B. et al. Gas Turbine Engine Combustor Can with Trapped Vortex Cavity. Patent US 6 951 108 B2, October 2005.

- 
- [65] B. et al. Combustor assembly with trapped vortex cavity. Patent EP 2 626 635 A2, August 2013.
- [66] B. et al. Ejector purge of cavity adjacent exhaust flowpath. Patent US 8 726 670 B2, June 2014.
- [67] K. et al. Trapped Vortex Combustor. Patent US 7 003 961 B2, February 2006.
- [68] S. ETEMBABAOGLU. *On the fluctuating flow characteristics in the vicinity of gate slots*. PhD thesis, University of Trondheim, 1973.
- [69] Q. for performance: The evolution of modern aircraft. <http://history.nasa.gov/SP-468/ch10-3.htm>.
- [70] N. FORESTIER, P. GEOFFROY, and L. JACQUIN. Etude expérimentale des propriétés instationnaires d'une couche de mélange compressible sur une cavité: cas d'une cavité ouverte peu profonde. Technical Report Rt22/00153, DAFE, ONERA, 2003.
- [71] N. FORESTIER, P. GEOFFROY, and L. JACQUIN. the mixing layer over a deep cavity at high subsonic speed. *J. Fluid Mech.*, 475:101–145, 2003.
- [72] J. FOUCAUT, J. CARLIER, and M. STANISLAS. PIV optimization for the study of turbulent flow using spectral analysis. *Meas. Sci. Technol.*, 8:1427–1440, 2004.
- [73] J.-P. FRENILLOT. *Etude phénoménologique des processus d'allumage et de stabilisation dans les chambres de combustion turbulente swirlées*. PhD thesis, INSA Rouen, 2011.
- [74] T. FRIC and A. ROSHKO. Vortical structure in the wake of a transverse jet. *Journal of Fluid Mechanics*, 279:1–47, 1994.
- [75] M. GHARIB and A. ROSHKO. The effect of flow oscillations on cavity drag. *J. Fluid Mech.*, 177(10):510–530, 1987.
- [76] A. GHONIEM, S. PARK, A. WACHSMAN, A. ANNASWAMY, D. WEE, and H. M. ALTAY. Mechanism of combustion dynamics in a backward-facing step stabilized premixed flame. *Proceedings of the Combustion Institute*, 30:1783–1790, 2005.

- 
- [77] X. GLOERFELT. Aeroacoustic computations of high-reynolds number cavity flows on staggered grids. In *12th AIAA/CEAS Aeroacoustics conference*, pages 2006–2433, Cambridge, Massachusetts, 2006.
- [78] P. GOKULAKRISHNAN, M. RAMOTOWSKI, G. GAINES, C. FULLER, R. JOKLIK, L. ESKIN, M. KLASSEN, and R. ROBY. A novel low  $\text{No}_x$  lean, premixed, and prevaporized combustion system for liquid fuels. *Journal of engineering for gas turbines and power*, 130(5):051501, 2008.
- [79] S. GRACE, W. DEWAR, and D. WROBLEWSKI. Experimental investigation of the flow characteristics within a shallow wall cavity for both laminar and turbulent upstream boundary layers. *Experiments in Fluids*, 36:791–804, 2004.
- [80] F. GRISCH. Private communication. 2014.
- [81] A. GUPTA, D. LILEY, and N. SYRED. *Swirl flows*. Abacus Press, 1984.
- [82] L. HABER, U. VANDSBURGER, W. SAUNDERS, and V. KHANNA. An experimental examination of the relationship between chemiluminescent light emissions and heat-release rate under non-adiabatic conditions. Technical report, DTIC Document, 2001.
- [83] M. HALL. Vortex breakdown. *Annual review of fluid mechanics*, 4:195–218, 1972.
- [84] R. HANSON. *Introduction to spectroscopic diagnostics to gases course*. Stanfor University, 2001.
- [85] R. HANSON, A. CHANG, and D. DAVIDSON. Modern shock tube methods for chemical studies in igh temperature gases. In *AIAA thermophysics*, San Antonio, USA, 1988.
- [86] R. HANSON, J. SEITZMAN, and P. PAUL. Planar Laser Fluorescence Imaging of Combustion Gases. *Appl. Phys. B*, 50:441–454, 1990.
- [87] Y. HARDALPUAS and M. ORAIN. Local measurements of the time-dependent heat release rate and equivalence ratio using chemiluminescent emission from a flame. *Combustion and Flame*, 139(3):188–207, 2004.

- 
- [88] Y. HARDALUPAS, C. PANOUTSOS, and A. TAYLOR. Spatial resolution of a chemiluminescence sensor or local heat-release rate and equivalence ratio measurements in a model gas turbine combustor. *Exp. Fluids*, 49(4):883–909, 2010.
- [89] W. HAWTORNE, D. WEDDELL, and H. HOTTEL. Mixing and combustion in turbulent jets. *Proceedings of the Combustion Institute*, 3(1):266–288, 1948.
- [90] J. HAYNES, D. MICKA, B. HOJNACKI, C. RUSSELL, J. LIPINSKI, B. SHOME, and M. HUFFMAN. Trapped Vortex Combustor performance for heavy-duty gas turbines. In *Proceedings of the ASME*, pages GT2008–50134, Berlin, Germany, June 9-13 2008.
- [91] C. HEEGER, R. GORDON, M. TUMMERS, T. SATTELMAYER, and A. DREIZLER. Experimental analysis of flashback in lean premixed swirling flames: upstream flame propagation. *Exp. Fluids*, 49(4):853–863, 2010.
- [92] H. HELLER, D. HOLMES, and E. COVERT. Flow-induced pressure oscillations in shallow cavities. *Journal of sound and vibration*, 18(4):545–546, 1971.
- [93] H. HELMHOLTZ. On the discontinuous movements of fluids. *Monthly reports of the Royal Prussian Academy of Philosophy in Berlin*, 23:215–288, 1868.
- [94] R. HENDRICKS, D. SHOUSE, W. ROQUEMORE, D. BURRUS, B. DUNCAN, R. RYDER, A. BRANKOVIC, N.-S. LIU, J. GALLAGHER, and J. HENDRICKS. Experimental and computational study of Trapped Vortex Combustor sector rig with Tri-pass diffuser. Technical memorandum 212507, NASA, 2004.
- [95] G. HERZBERG. *Atomic spectra and Atomic Structure*. Courier Dover Publications, 1944.
- [96] G. HERZBERG. *Molecular spectra and molecular structure: Spectra of diatomic molecules*, volume 1. Van Nostrand Company, 1950.
- [97] M. HISHIDA, T. FUJIWARA, and P. WOLANSKI. Fundamentals of rotating detonations. *Swihoek Waves*, 19:1–10, 2009.
- [98] C. HO and N. NOSSEIR. Dynamics of an impinging jet. part 1. the feedback phenomenon. *J. Fluid Mech.*, 105:119–142, 1981.
- [99] J. HOLLAS. *Modern Spectroscopy*. John Wiley & Sons, 2004.

- 
- [100] M. HOWE. Edge, cavity and aperture tones at very low mach numbers. *J. Fluid Mech.*, 220(1):61–84, 1997.
- [101] M. HOWE. Mechanism of sound generation by low mach number flow over a wall cavity. *J. Sound Vib.*, 273:103–123, 2003.
- [102] M. S. HOWE. The influence of mean shear layer on unsteady aperture flow, with application to acoustical diffraction and self-sustained cavity oscillations. *J. Fluid Mech.*, 71(4):125–146, 1981.
- [103] K. HSU, C. CARTER, V. KATTA, and W. ROQUEMORE. Characteristics of combustion instability associated with Trapped-Vortex burner. In *37th AIAA Aerospace Sciences Meeting and Exhibit*, pages 99–0488, Reno, NV, USA, January 11-14 1999.
- [104] K. HSU, L. GOSS, D. TRUMP, and W. ROQUEMORE. Characteristics of a Trapped Vortex Combustor. *Journal of Propulsion and Power*, 14(1):57–65, 1998.
- [105] Y. HUANG and V. YANG. Dynamics and stability of lean-premixed swirl-stabilized combustion. *Progress in Energy and Combustion Science*, 35:293–364, 2009.
- [106] P. HUERRE and P. MONKEWITZ. Local and global instabilities in spatially developing flows. *Ann. Rev. Fluid Mech.*, 22(1):473–537, 1990.
- [107] U. INGARD and V. SINGHAL. Effect of flow on the acoustic resonances of an open ended duct. *Journal of the Acoustical Society of America*, 58(4):788–793, 1975.
- [108] Y. JIN, X. HE, J. ZHANG, B. JIANG, and Z. WU. Numerical investigation on flow structures of a laboratory-scale trapped vortex combustor. *Applied Thermal Engineering*, 66(1–2):318–327, 2014.
- [109] A. JONES. Singing flames. *Journal of the Acoustical Society of America*, 16(4):254–266, 1945.
- [110] W. M. JUNGOWSKI, K. BOTROS, and W. STUDZINSKI. Cylindrical sidebranch as one generator. *Journal of sound and vibration*, pages 265–285, 1989.
- [111] M. JUNIPER. The effect of confinement on the stability of two-dimensional shear flows. *J. Fluid Mech.*, 565(1):171–195, 2006.

- 
- [112] L. KABIRAJ and R. SUJITH. Nonlinear self-excited thermoacoustic oscillations: intermittency and flame blowout. *Journal of Fluid Mechanics*, 713:376–397, 2012.
- [113] K. KAILASANATH. Recent developments in the research on pulse detonation engines. *AIAA Journal*, 41(2), 2003.
- [114] C. KAMINSKI, J. HULT, and M. ALDEN. High repetition rate planar laser-induced fluorescence of OH in a turbulent non-premixed flame. *Applied Physics B*, 68:757–760, 1999.
- [115] A. KANURY. *Introduction to combustion phenomena*. Gordon and Breach Science Publishers, 1975.
- [116] A. KARAGOZIAN. Transverse jets and their control. *Progress in Energy and Combustion Science*, 36(5):531–553, 2010.
- [117] V. KATTA and W. ROQUEMORE. Numerical studies on Trapped Vortex Combustor. In *32nd AIAA/ASME/SAE/ASEE Joint Propulsion Conference*, pages 96–2660, Lake Buena Vista, FL, USA, July 1-3 1996.
- [118] V. R. KATTA and W. ROQUEMORE. Numerical studies on Trapped Vortex Combustor for stable combustion. *Journal of engineering for gas turbines and power*, 120(1):60–68, 1998.
- [119] V. R. KATTA and W. ROQUEMORE. Study on Trapped Vortex Combustor- Effect of Injection on Flow Dynamics. *Journal of Propulsion and Power*, 14(3):273–281, 1998.
- [120] D. KELLEHER. Stark broadening of visible neutral helium lines in a plasma. *Journal of Quantitative Spectroscopy and Radiative Transfer*, 25(3):191–220, 1981.
- [121] J. KELLER, L. VANEVELD, D. KORSCHETT, G. HUBBARD, A. GHONIEM, J. DAILY, and A. OPENHEIM. Mechanisms of instabilities in turbulent combustion leading to flashback. *AIAA Journal*, 20(2):254–262, 1982.
- [122] R. KELSO, T. LIM, and A. PERRY. An experimental study of round jets in cross-flow. *J. Fluid Mech.*, 306:111–144, 1996.

- 
- [123] L. KELVIN. Hydrokinetic solutions and observations. *Philosophical magazine*, 42:362–377, 1871.
- [124] K. Koenig and A. Roshko. An experimental study of geometrical effects on the drag and flow field of two bluff bodies separated by a gap. *J. Fluid Mech.*, 156:167–204, 1985.
- [125] K. KOHSE-HOÏGHAUS. Laser techniques for the quantitative detection of reactive intermediates in combustion systems. *Prog. Energ. Combust.*, 20:1–203, 1994.
- [126] J. KRAWCZYNSKI, B. RENOU, and L. DANAILA. The structure of the velocity field in a confined flow driven by an array of opposed jets. *Physics of Fluids*, 22(4):045104, 2010.
- [127] J. F. KRAWCZYNSKI. *La structure du champ de vitesse dans un réacteur à jets opposés. Caractérisation du mélange turbulent*. PhD thesis, Université de Rouen, 2007.
- [128] P. E. KUMAR and D. MISHRA. Numerical modeling of an axisymmetric Trapped Vortex Combustor. *Int. J. Turbo Jet-Engines*, 28:41–52, 2011.
- [129] P. E. KUMAR and D. MISHRA. Numerical simulation of cavity flow structure in an axisymmetric trapped vortex combustor. *Aerospace Science and Technology*, 21(1):16–23, 2011.
- [130] K. KUO. *Principle of combustion*. John Wiley & Sons, 2005.
- [131] L. LAM, S. LEE, and C. SUEN. Thinning methodologies- a comprehensive survey. In *IEEE Trans Pattern anal Mach Intell*, volume 14, pages 869–885, 1992.
- [132] J. LASHERAS, J. CHO, and T. MAXWORTHY. On the origin and evolution of stream-wise vortical structures in a plane, free shear layer. *J. Fluid Mech.*, 172(1):231–258, 1986.
- [133] J. LASHERAS and H. CHOI. Three-dimensional instability of a plane free shear layer: an experimental study of the formation and evolution of streamwise vortices. *J. Fluid Mech.*, 315(1):175–221, 1988.
- [134] N. LAURENDEAU. Temperature measurements by light-scattering methods. *Prog. Energy Combust. Sci.*, 14(2):147–170, 1988.



- 
- [135] B. LECORDIER, D. DEMARE, L. VERVISCH, J. REVEILLON, and M. TRINITE. Estimation of the accuracy of piv measurements for turbulent flow studies by direct and numerical simulation of multi-phase flow. *Meas. Sci. Technol.*, 12(1382–1391), 2001.
- [136] J. LEE, K. KIM, and D. SANTAVICCA. Effect of injection location on the effectiveness of an active control system using secondary fuel injection. *Proceedings of the Combustion Institute*, 28(1):739–746, 2000.
- [137] A. LEFEBVRE. *Gas Turbine Combustion*. CRC Press, 1998.
- [138] A. LEFEBVRE and D. BALLAL. *Gas Turbine Combustion: Alternative Fuels and Emissions*. Taylor and Francis, 2010.
- [139] B. LEWIS and G. V. ELBE. *Combustion, Flames and Explosions of Gases*. 3rd ed. Academic Press, 1987.
- [140] M. LEYKO, F. NICLOUD, and T. POINSOT. Comparison of direct and indirect combustion noise mechanisms in a model combustor. *AIAA Journal*, 47(11):2709–2716, 2009.
- [141] T. LIEUWEN. *Unsteady combustor physics*. Cambridge University Press, 2012.
- [142] T. LIEUWEN and V. Y. (Eds). *Combustion Instabilities in Gas Turbine engines. Operational Experience, Fundamental mechanisms, and Modelling*, volume 210. American Institute of Aeronautics and Astronautics, 2005.
- [143] T. LIEUWEN, V. McDONNELL, E. PETERSEN, and D. SANTAVICCA. Fuel flexibility influences on premixed combustor blowout, flashback, autoignition, and stability. *Journal of engineering for gas turbines and power*, 130(1):11506, 2008.
- [144] T. LIEUWEN, Y. NEUMEIER, and R. RAJARAM. Measurements of incoherent acoustic wave scattering from turbulent premixed flames. *Proceedings of the Combustion Institute*, 29(2):1809–1815, 2002.
- [145] T. LIEUWEN, H. TORRES, C. JOHNSON, and B. ZINN. A mechanism of combustion instability in lean premixed gas turbine combustors. *Journal of engineering for gas turbines and power*, 123:182–189, 2001.

- 
- [146] T. LIEUWEN and B. ZINN. The role of equivalence ratio oscillations in driving combustion instabilities in Low NO<sub>x</sub> gas turbines. In *Proceedings of the Combustion Institute*, volume 27, pages 1809–1816, 1998.
- [147] T. LIEUWEN and B. ZINN. On the experimental determination of combustion process driving in an unstable combustor. *Combust. Sci. Technol.*, 157:111–127, 2000.
- [148] J. LIN and D. ROCKWELL. Organized oscillations of initially turbulent flow past a cavity. *AIAA Journal*, 39:1139–1151, 2001.
- [149] B. LITTLE and R. WHIPKEY. Locked vortex afterbodies. *J. Aircraft*, 16(5):296–302, 1979.
- [150] S. LIU, C. MENEVEAU, and J. KATZ. On the properties of similarity sub-grid scale models as deduced from measurements in a turbulent jet. *J. Fluid Mech.*, 275:83, 1994.
- [151] J. LONGWELL, E. FROST, and M. WEISS. Flame stability in bluff body recirculation zones. *Ind. Eng. Chem.*, 45(8):1629–1633, 1953.
- [152] L. LOURENCO and A. KROTHAPALLI. True resolution piv, a mesh free second order accurate algorithm. In *10th International symposium on applications of laser techniques to fluid mechanics*, Lisbon, Portugal, 2000.
- [153] J. LUMLEY. The structure of inhomogeneous turbulent flows. *Atmospheric turbulence and radio wave propagation*, 64:166–178, 1967.
- [154] J. LUQUE and D. CROSLEY. Lifbase: database and spectral simulation for oh a-x, od a-x, no a-x and d-x, ch a-x, b-x, and c-x. Technical report, SRI report M001, 1996.
- [155] F. MARBLE and S. CANDEL. Acoustic disturbance from gas non-uniformity convected through a nozzle. *Journal of sound and vibration*, 55:225–243, 1977.
- [156] G. MARTINS. *Etude de la combustion pauvre prémélangée prévaporisée avec les effets du préchauffage et de la pression*. PhD thesis, INSA Rouen, 2006.
- [157] B. MCMILLIN, J. PALMER, and R. HANSON. Temporally resolved, two-line fluorescence imaging of NO temperature in a transverse jet in a supersonic crossflow. *Appl. Opt.*, 32:7532–7545, 1993.

- 
- [158] D. MEIJA, L. SELLE, R. BAZILE, and T. POINSOT. Wall-temperature effects on flame response to acoustic oscillations. *Proceedings of the Combustion Institute*, xxx(xxx):xxx, 2014.
- [159] J. MENDOZA and K. AHUJA. The effects of width on cavity noise. *Journal of Aircraft*, 14(9):833–837, 1995.
- [160] C. MERLIN. *Simulation numérique de la combustion turbulente: Méthode de frontières immergées pour les écoulements compressibles, application à la combustion en aval d’une cavité*. PhD thesis, INSA Rouen, France, 2012.
- [161] C. MERLIN, P. DOMINGO, and L. VERVISCH. Large Eddy Simulation of turbulent flames in a Trapped Vortex Combustor (tvc) - A flamelet presumed-pdf preserving laminar flame speed. *C.R. Mecanique*, 340:917–932, 2012.
- [162] T. MEYER, M. BROWN, S. FONOV, L. GOSS, J. GORD, D. SHOUSE, V. BELOVICH, W. ROQUEMORE, C. COOPER, E. KIM, and J. HAYNES. Optical diagnostics and numerical characterization of a Trapped-Vortex Combustor. In *AIAA*, pages AIAA–2002–3863, 2002.
- [163] A. MICHALKE. The instability of free shear layers: a survey of the state of the art. *Dsch. Luft- & Raumfahrt. Mitteilung*, 70-04, 1970.
- [164] M. MOKOVIN and S. PARANJAPE. On the acoustic excitation of shear layer. *Z. Flugwiss*, 8/9(2):328–335, 1971.
- [165] P. MONKEWITZ and K. SOHN. Absolute instability in hot jets. *AIAA Journal*, 26(8):911–916, 1988.
- [166] E. MOTHEAU, F. NICOUD, and T. POINSOT. Mixed acoustic-entropy combustion instabilities in gas turbines. *Journal of Fluid Mechanics*, 749:542–576, 2014.
- [167] H. NAJM and A. GONHIEM. Numerical simulation of the convective instability in a dump combustor. *AIAA Journal*, 29:911–919, 1991.
- [168] H. NAJM, P. PAUL, C. MUELLER, and P. WYCKOFF. On the adequacy of certain experimental observables as measurements of flame burning rate. *Combustion and Flame*,

- 113(3):312–332, 1998.
- [169] J. NOGUEIRA, A. LECUONA, and P. RODRIGUEZ. Limits on the resolution of correlation piv iterative methods. fundamentals. *Exp. Fluids*, 39:305–313, 2005.
- [170] N. NOIRAY, D. DUROX, T. SCHULLER, and S. CANDEL. A unified framework for nonlinear combustion instability analysis based on the flame describing function. *Journal of Fluid Mechanics*, 615(1):1391–1398, 2008.
- [171] V. NORI and J. SEITZMAN. CH\* chemiluminescence modeling for combustion diagnostics. volume 32, pages 895–903. Proceedings of the Combustion Institute, 2009.
- [172] H. NYQUIST. Certain topics in telegraph transmission theory. volume 47, pages 617–644. Proceedings of the IEEE, IEEE.
- [173] P.CHARBONNIER, L. BLANC-FERAUD, G. AUBERT, and M. BARLAUD. Two deterministic half-quadratic regularization algorithms for computed imaging. In *Image Processing, 1994. Proceedings. ICIP-94., IEEE International Conference*, volume 2, pages 168–172. IEEE, 1994.
- [174] N. PETERS. *Turbulent Combustion*. Cambridge University Press, 2000.
- [175] B. PETERSON, D. REUSS, and V. SICK. On the ignition and flame development in a spray-guided direct-injection spark-ignition engine. *Combustion and Flame*, 161(1):240–255, 2014.
- [176] E. PLENTOVICH, R. STALLINGS, and M. TRACY. Experimental cavity pressure measurements at subsonic and transonic speeds. Technical Report 3358, NASA Technical Paper, 1993.
- [177] T. POINSOT, A. TROUVE, D. VEYNANTE, S. CANDEL, and E. ESPOSITO. Vortex-driven acoustically coupled combustion instabilities. *J. Fluid Mech.*, 177:265–292, 1987.
- [178] T. POINSOT and D. VEYNANTE. *Theoretical and Numerical Combustion*. RT Edwards, Inc., 2012.
- [179] S. POPE. *Turbulent Flows*. Cambridge University Press, 2000.

- 
- [180] A. PRASAD, R. ADRIAN, C. LANDRETH, and P. OFFUTT. Effect of resolution on the speed and accuracy of particle image velocimetry interrogation. *Exp. Fluids*, 13:105–116, 1992.
- [181] A. PRASAD and C. WILLIAMSON. The instability of the shear layer separating from a bluff body. *J. Fluid Mech.*, 333:375–402, 1997.
- [182] R. PRICE, I. HURLE, and T. SUGDEN. Optical studies of the generation of noise in turbulent flames. volume 12, pages 1093–1102. Proceedings of the Combustion Institute, 1969.
- [183] A. PUTNAM. *Combustion Driven Oscillations in Industry*. American Elsevier Publishers, New York, 1971.
- [184] M. RAFFEL, M. WILLERT, and J. KOMPENHANS. *Particle Image Velocimetry, a practical guide*. Springer-Verlag, 1998.
- [185] S. RAVIDRAN. A reduced-order approach for optimal control of fluids using Proper Orthogonal Decomposition. *International journal for numerical methods in Fluids*, 34:425–448, 2000.
- [186] J. RAYLEIGH. *The Theory of Sound*, volume 2. 1945.
- [187] P. RENARD, D. THEVENIN, J. ROLON, and S. CANDEL. Dynamics of flame/vortex interactions. *Progress in Energy and Combustion Science*, 26:225–282, 2000.
- [188] D. ROCKWELL. Oscillations of impinging shear layers. *AIAA Journal*, 21(5):645–664, 1983.
- [189] D. ROCKWELL and C. KNISELY. The organized nature of flow impingement upon a corner. *J. Fluid Mech.*, 93(03):413–432, 1979.
- [190] D. ROCKWELL and E. NAUDASCHER. Review – Self-sustaining oscillations of flow past cavities. *Trans A.S.M.E, J. Fluids Engng*, 100:152–165, 1978.
- [191] Z. RONGSHUN and F. WEIJUN. Experimental study of entrainment phenomenon in a trapped vortex combustor. *Chinese Journal of Aeronautics*, 21(1):63–73, 2013.

- 
- [192] W. ROQUEMORE, D. SHOUSE, D. BURNS, A. JOHNSON, C. COOPER, B. DUNCAN, K. HSU, V. KATTA, G. STURGESS, and I. VIHINEN. Trapped Vortex Combustor concept for gas turbine engines. In *39th AIAA Aerospace Sciences Meeting and Exhibit*, pages 2001–0489, Reno, NV, USA, January 8–11 2001.
- [193] A. ROSHKO. Some measurements of flow in a rectangular cutout. Technical Report TN-3488, NACA Technical Note, 1955.
- [194] A. ROSHKO. Structure of turbulent shear flows: a new look. *AIAA Journal*, 14:1349–1357, 1976.
- [195] J. ROSSITER. Wind tunnel experiments of the flow over rectangular cavities at subsonic and transonic speeds. Technical report, Aeronautical Research Council Reports and Memoranda, 1964.
- [196] E. ROULAND. *Etude et développement de la technique de vélocimétrie par intercorrélation d'images de particules. Application aux écoulements en tunnel hydrodynamique*. PhD thesis, University of Rouen, 1994.
- [197] S. SAMUELSEN. *Conventional Type Combustion*. NETL, 2006.
- [198] R. SARNO and M. FRANKE. Suppression of flow-induced pressure oscillations in cavities. *J. Aircraft*, 31(1):90–96, 1994.
- [199] V. SAROHIA. *Experimental and analytical investigation of oscillations in flows over cavities*. PhD thesis, California Institute of Technology, Pasadena, 1975.
- [200] V. SAROHIA. Experimental investigation of oscillations in flows over shallow cavities. *AIAA Journal*, 15(7), 1977.
- [201] V. SAROHIA and P. MASSIER. Control of cavity noise. *J. Aircraft*, 14(9):833–840, 1977.
- [202] R. SAWYER. Science based policy for addressing energy and environmental problems. *Proceedings of the Combustion Institute*, 32(1):45–56, 2009.
- [203] K. SCHADOW and E. GUTMARK. Combustion instability related to vortex shedding in dump combustors and their passive control. *Progress in Energy and Combustion Science*, 18:117–132, 1992.

- 
- [204] T. SCHULLER, D. DUROX, and S. CANDEL. Dynamics of and noise radiated by a perturbed impinging premixed jet flame. *Combustion and Flame*, 128(1):88–110, 2002.
- [205] C. SHANNON. Communication in the presence of noise. volume 37, pages 10–21. Proceedings of the IRE, IEEE.
- [206] L. SIROVICH. Turbulence and the dynamics of coherent structures. part 1: Coherent Structures. *Quarterly of Applied Mathematics*, XLV(3):561–571, 1987.
- [207] L. SIROVICH. Turbulence and the dynamics of coherent structures. part 2: Symmetries and transformations. *Quarterly of Applied Mathematics*, XLV(3):573–582, 1987.
- [208] L. SIROVICH. Turbulence and the dynamics of coherent structures. part 3: Dynamics and scaling. *Quarterly of Applied Mathematics*, XLV(3):583–590, 1987.
- [209] S. SMITH and M. MUNGAL. Mixing, structure and scaling of the jet in crossflow. *J. Fluid Mech.*, 357:83–122, 1998.
- [210] A. STEINBERG, I. BOXX, C. ARNDT, J. FRANCK, and W. MEIER. Experimental study of flame-hole reignition mechanisms in a turbulent non-premixed jet flame using sustained multi-kHz PIV and crossed-plane OH PLIF. *Proceedings of the Combustion Institute*, 33(1):1663–1672, 2011.
- [211] M. STOHR, I. BOXX, C. CARTER, and W. MEIER. Dynamics of lean blowout of a swirl-stabilized flame in a gas turbine model combustor. *Proceedings of the Combustion Institute*, 33(2):2953–2960, 2011.
- [212] C. STONE and S. MENON. Simulation of fuel-air mixing and combustion in a Trapped Vortex Combustor. In *38th AIAA Aerospace Sciences Meeting and Exhibit*, pages 2000–0478, Reno, NV, USA, January 10-13 2000.
- [213] W. STRALHE. On combustion generated noise. *J. Fluid Mech.*, 49:399–414, 1971.
- [214] J. STUART. Nonlinear stability theorem. *Ann. Rev. Fluid Mech.*, 3:347–370, 1971.
- [215] G. STURGESS and K. HSU. Entrainment of mainstream flow in a Trapped Vortex Combustor. In *35th AIAA Aerospace Sciences Meeting and Exhibit*, pages 97–0261, Reno, NV, USA, January 6-10 1997.

- 
- [216] M. SWEENEY and S. HOCHGREB. Autonomous extraction of optimal flame fronts in oh planar laser-induced fluorescence images. *Appl. Optics*, 48(19):3866–3877, 2009.
- [217] M. SWEENEY, S. HOCHGREB, and R. BARLOW. The structure of premixed and stratified low turbulence flames. *Combustion and Flame*, 158(5):935–948, 2011.
- [218] G. SWIFT. *Thermoacoustics*. Acoustical society of america, New York, 2002.
- [219] N. SYRED, W. FICK, T. O'DOHERTY, and A. GRIFFITHS. The effect of the precessing vortex core on combustion in a swirl burner. *Combustion Science and Technology*, 125:139–157, 1997.
- [220] C. TAM and P. W. BLOCK. On the tones and pressure oscillations induces by flow over rectangular cavities. *J. Fluid Mech.*, 89((part 2)):373–399, 1978.
- [221] B. TAUPIN. *Etude de la combustion turbulente à faible richesse, haute température et haute pression*. PhD thesis, INSA Rouen, 2003.
- [222] C. TROPEA, A. YARIN, and J. FOSS. *Springer handbook of experimental fluid mechanics*, volume 1. Springer, 2007.
- [223] A. UPANIETKS, J. DRISCOLL, and S. CECCIO. Cinema particle imaging velocimetry time history of the propagation velocity of the base of a lifted turbulent jet flame. *Proceedings of the Combustion Institute*, 29:1897–1903, 2002.
- [224] A. VAKILI and C. GAUTHIER. Control of cavity flow by upstream mass-injection. *J. Aircraft*, 31(1):169–243, 1994.
- [225] D. VAUCHELLES. *Etude de la stabilité et des émissions polluantes des flammes turbulentes de prémélange pauvre à haute pression appliquées aux turbines à gaz*. PhD thesis, INSA Rouen, 2004.
- [226] H. Y. WANG, C. LAW, and T. LIEUWEN. Linear response of stretch-affected premixed flames to flow oscillations. *Combustion and Flame*, 156:889–895, 2009.
- [227] S. WANG, S. HSIEH, and V. YANG. Unsteady flow evolution in swirl injector with radial entry. I. Stationary conditions. *Physics of Fluids*, 17(045106), 2005.



- 
- [228] M. WEI and C. ROWLEY. Low-dimensional models for a temporally evolving free shear layer. *J. Fluid Mech.*, 618:113–134, 2009.
- [229] J. WEICKERT. A review of nonlinear diffusion filtering. In *Scale-space Theory in Computer Vision*, 1997.
- [230] P. WELCH. The use of Fast Fourier Transform for the estimation of power spectra: a method based on time averaging over short, modified periodograms. volume 15, pages 70–73. IEEE Transactions on Audio and Electroacoustics, 1967.
- [231] J. WESTERWHEEL. Fundamentals of digital particle image velocimetry. *Meas. Sci. Technol.*, 8:1379–1392, 1997.
- [232] C. WILLERT and M. GHARIB. Digital particle image velocimetry. *Exp. Fluids*, 10(181–193), 1991.
- [233] C. WINANT and F. BROWAND. Vortex pairing: The mechanism of turbulent mixing layer growth at moderate reynolds number. *J. Fluid Mech.*, 63(2):237–255, 1974.
- [234] A. WULFF and J. HOURMOUZIADIS. Technology review of aeroengine pollutant emissions. *Aerospace Science and Technology*, 8:557–572, 1997.
- [235] P. XAVIER, G. CABOT, B. RENOU, A. BOUKHALFA, and M. CAZALENS. Towards Low-NO<sub>x</sub> operation in a complex burner. Optimization of an annular Trapped Vortex combustor. In *Proceedings of the ASME*, pages GT2013–94704, San Antonio, USA, June 3-7 2013.
- [236] F. XING, W.-J. FAN, Y.-Y. LIU, Z.-J. KONG, and M.-L. YANG. Ignition and lean blow out performance of tvc with different fuel-air matching forms. *Journal of Propulsion Technology*, 29(4), 2008.
- [237] G. XING, R.-C. ZHANG, W.-J. FAN, Y.-Y. LIU, and Y.-Q. YAN. Experimental study on single/fuel-lean trapped vortex combustor ignition and limit blow-out at different main air and mix air temperatures. *Journal of Aerospace Power*, 23(12):2280–2285, 2008.
- [238] A. YULE. Large-scale structures in the mixing layer of a round jet. *J. Fluid Mech.*, 89(3):413–432, 1978.

- 
- [239] S. ZIADA and D. ROCKWELL. Vortex-leading-edge interaction. *J. Fluid Mech.*, 118:79–107, 1982.
- [240] B. ZINN and E. POWELL. Nonlinear combustion instability in liquid-propellant rocket engines. *Proceedings of the Combustion Institute*, 13(1):491–503, 1971.